Steen Brøndsted Nielsen Jean Ann Wyer *Editors*

Photophysics of Ionic Biochromophores



Physical Chemistry in Action

Steen Brøndsted Nielsen • Jean Ann Wyer Editors

Photophysics of Ionic Biochromophores



Editors
Steen Brøndsted Nielsen
Jean Ann Wyer
Faculty of Science and Technology
Department of Physics and Astronomy
Aarhus University
Aarhus
Denmark

ISSN 2197-4349 ISSN 2197-4357 (electronic)
ISBN 978-3-642-40189-3 ISBN 978-3-642-40190-9 (eBook)
DOI 10.1007/978-3-642-40190-9
Springer Heidelberg New York Dordrecht London

Library of Congress Control Number: 2013950272

© Springer-Verlag Berlin Heidelberg 2013

This work is subject to copyright. All rights are reserved by the Publisher, whether the whole or part of the material is concerned, specifically the rights of translation, reprinting, reuse of illustrations, recitation, broadcasting, reproduction on microfilms or in any other physical way, and transmission or information storage and retrieval, electronic adaptation, computer software, or by similar or dissimilar methodology now known or hereafter developed. Exempted from this legal reservation are brief excerpts in connection with reviews or scholarly analysis or material supplied specifically for the purpose of being entered and executed on a computer system, for exclusive use by the purchaser of the work. Duplication of this publication or parts thereof is permitted only under the provisions of the Copyright Law of the Publisher's location, in its current version, and permission for use must always be obtained from Springer. Permissions for use may be obtained through RightsLink at the Copyright Clearance Center. Violations are liable to prosecution under the respective Copyright Law.

The use of general descriptive names, registered names, trademarks, service marks, etc. in this publication does not imply, even in the absence of a specific statement, that such names are exempt from the relevant protective laws and regulations and therefore free for general use.

While the advice and information in this book are believed to be true and accurate at the date of publication, neither the authors nor the editors nor the publisher can accept any legal responsibility for any errors or omissions that may be made. The publisher makes no warranty, express or implied, with respect to the material contained herein.

Printed on acid-free paper

Springer is part of Springer Science+Business Media (www.springer.com)

Preface

Spectroscopy of isolated biomolecular ions in vacuo has within the last decade or so become a highly active research field, both for experimentalists and theorists, made possible by the development of advanced instrumental apparatus and the steady increase in more powerful computers. The field is highly interdisciplinary including researchers in chemistry, physics, and molecular biology. Absorption spectra of isolated ions shed light on the intrinsic electronic structures without perturbations from say water molecules, counter ions, nearby charges, or polar amino acids. A comparison with spectra of the chromophores in their natural environment then allows one to identify possible perturbations. Spectra at the same time provide important benchmarks for quantum chemical calculations of electronically excited states, which is still a non-trivial task. Not only absorption spectra but also fluorescence spectra are excellent indicators of environmental effects. In this volume, we focus on spectroscopy of protein chromophores, amino acids and peptides, to whole proteins and DNA nucleotides and oligonucleotides. Dissociation channels and timescales for deexcitation and dissociation are also discussed in detail, as they shed important light on energy-flow processes within the isolated biomolecular ion; indeed, small molecular ions with few degrees of freedom are destined to break apart after photoexcitation due to the absence of a heat bath (energy sink). As all systems included here are ionic, mass spectrometry in combination with lasers are used for the experiments. Experimental techniques to measure spectra and theoretical methods commonly employed are described with a discussion on limitations and advantages.

Our book comprises 11 chapters each written by one or more experts in the topic. The book is organised as follows: At the beginning of the book, even before the General Introduction, there are explanatory pages (Concepts) for non-experts in the field where we briefly describe electric- and magnetic-field sectors used as ion deflectors, photophysical processes illustrated by Jablonski diagrams, molecular orbital theory, solvatochromic shifts of electronic transitions, peptide and nucleic acids structures, and nomenclature regarding peptide fragmentation. Our hope is that with these sections, the book shows potential to be used for graduate teaching courses in photobiology and not just for researchers within the field. The second chapter is a brief introduction by one of us (Brøndsted Nielsen) discussing

vi Preface

biochromophore ions and the role of microenvironments such as water or nearby charge sites. The chapter ends by touching upon possible future directions for the field. In the next chapter, Wyer introduces the experimental techniques used for performing gas-phase spectroscopy of ions with emphasis on ion storage rings and other home-built ion beam set-ups as these are less well described in the literature. It is certainly true that no experiment is perfect, and Wyer discusses the advantages and disadvantages with different set-ups, differences between positive and negative ions and importantly what to be cautious about when interpreting experimental results. In the next chapter by Rubio and Wanko, theoretical methods that are commonly employed to describe these rather big systems are presented. Also here the methods are carefully evaluated and their performances relative to each other are discussed. The subsequent chapters deal with actual biochromophores and their photophysics. The chapter by Andersen and Bochenkova gives an overview of the GFP chromophore anion and its absorption spectrum; this spectrum from 2001 was the first to be obtained for an isolated biochromophore ion. The authors discuss the competition between electron photodetachment and internal conversion, which is an issue that needs to be considered for anions whose detachment energies are within the absorption band. The next chapter by Brøndsted Nielsen deals with the detection of light emitted from photoexcited chromophore ions (dyes), which is even harder experimentally than obtaining an absorption spectrum. Still fluorescence spectroscopy has proven to be a very strong tool for monitoring structures of isolated biomolecular ions. Wyer and Brøndsted Nielsen summarise in the following chapter the increasing amount of data on porphyrin and heme ions and their complexes with amino acids and NO and compare results with protein spectra. Also two-laser experiments are discussed allowing one to record spectra of long-lived photoexcited ions. Spectra of whole proteins are presented in the next chapter by Antoine and Dugourd, where either heme or aromatic amino acid residues are the absorbing species. The authors demonstrate the importance of the charge state in obtaining action spectra, and from two-laser experiments they nicely succeed in performing spectroscopy on radical species. Dedonder, Féraud, and Jouvet provide a comprehensive review of the field of spectroscopy of protonated amino acids and small peptide ions, both at room temperature and at low temperature, with emphasis on the fast dissociation channels that are operative when the ions are electronically excited and that compete with internal conversion to the electronic ground state; their relative importance is measured from photodissociation of the ions in an electric field. The number of fragments formed in a dissociation process is found from coincidence experiments considering momentum conservation. Timescales for the deexcitation processes are established from femtosecond pump-probe laser experiments. Their work nicely demonstrates how experimental results and theoretical ones go hand in hand in obtaining the deepest level of understanding. DNA and RNA nucleotides and oligonucleotides are the focus of the chapter by Weber, Marcum, and Brøndsted Nielsen who in detail discuss UV-induced fragmentation channels, timescales for dissociation after photoexcitation and whether dissociation is statistical or nonstatistical, and finally electronic spectra (both absorption and photoelectron spectra). In this chapter the complex role of multiple light absorbing Preface vii

species is also considered. In all of these works either visible or UV light was used for the experiments. In the final chapter by Schlathölter and Hoekstra, recent work in extending the wavelength region to the vacuum ultraviolet is presented, and the importance of this region is clearly emphasised by work on peptide ions.

Let us end by saying that the chosen topics for this volume present a selection of important scientific contributions that *we* believe have been made to this rapidly increasing field. They are of course biased by our own interests, and other important work could have been covered, *e.g.* the electronic properties of simpler molecular ions isolated *in vacuo* that were earlier explored. However, we hope that the reader has got an impression after reading all the chapters of the rich possibilities that exist to form and study complicated and fragile ions *in vacuo*, and that, most importantly, new fundamental science is learned from such work. We would like to take the opportunity to thank all the authors who have contributed to this volume and in our opinion have made this volume a most timely one and one of very high quality.

Aarhus, June 25, 2013

Steen Brøndsted Nielsen and Jean Ann Wyer

Abbreviations

A Acceptor

Adenine

ADE Adiabatic Detachment Energy

AI Auto Ionising

AMP Adenosine MonoPhosphate ATP Adenosine TriPhosphate

BBO Barium BOrate

BIRD Blackbody Infrared Radiative Dissociation

C Cytosine

CA Connection-Atom

CAD Collisional Activated Dissociation (high energy, > keV)

CAM Coulomb-Attenuation Method

CASSCF Complete Active Space Self-Consistent Field

CC Coupled Cluster
CE Crown Ether
CI Conical Intersection

CID Collision Induced Dissociation (low energy, <100 eV)

CIS Configuration Interaction Singles
CPE Chemical Potential Equilibration

CT Charge Transfer CW Continuous Wave

D Donor

Dye

DDCI Difference-Dedicated Conical Intersection

DFT Density Functional Theory DMSO DiMethylSulfOxide

DNA DeoxyriboNucleic Acid

EA Electron Affinity

EBE Electron Binding Energy
ECD Electron Capture Dissociation
EDD Electron Detachment Dissociation

x Abbreviations

EGP Effective Group Potential

ELISA ELectrostatic Ion Storage ring in Aarhus

EOM Equation-Of-Motion

EPD Electron Photodetachment Dissociation

ESA ElectroStatic Analyser
ESI ElectroSpray Ionisation
ETD Electron Transfer Dissociation

FC Franck Condon FCO Frozen-Core Orbital

FOIS First-Order Interacting Space

FRET Förster Resonance Energy Transfer

FT-ICR Fourier Transform Ion Cyclotron Resonance

FWHM Full Width Half Maximum

G Guanine

GFP Green Fluorescent Protein

GGA Generalised Gradient Approximation

GHO Generalised Hybrid-Orbital HBN Hydrogen-Bonded Networks

HF Hartree Fock

HOMO Highest Occupied Molecular Orbital

IC Internal Conversion
ICR Ion Cyclotron Resonance

IE Ionisation Energy

IMS Ion Mobility Spectrometry

IR InfraRed

IRMPD InfraRed MultiPhoton Dissociation

ISC InterSystem Crossing

IVR Intramolecular Vibrational Redistribution

KER Kinetic Energy Release

KID keV Ion-induced Dissociation

LCAO Linear Combination of Atomic Orbitals

LDA Local Density Approximation
LIAD Laser Induced Acoustic Desorption

LSCF Local Self-Consistent Field

LUMO Lowest Unoccupied Molecular Orbital
MALDI Matrix Assisted Laser Desorption Ionisation

MBPT Many-Body Perturbation Theory

MCP MicroChannel Plate MD Molecular Dynamics

MECI Minimum-Energy Conical Intersections

MeCN Acetonitrile MeOH Methanol

MIKE Mass-analysed Ion Kinetic Energy

MM Molecular Mechanics MO Molecular Orbital Abbreviations

MR Multi-Reference

MP Møller Plesset (perturbation theory)

MS Mass Spectrometry

Nd:YAG Neodymium-doped Yttrium Aluminium Garnet NEXAMS Near Edge X-ray Absorption Mass Spectrometry

NIM Normal Incidence Monochromator NMR Nuclear Magnetic Resonance OPO Optical Parametric Oscillator

PA Proton Affinity

PAAA Protonated Aromatic Amino Acid

PD PhotoDetachment

PES PhotoElectron Spectroscopy

Potential Energy Surface

PGM Plane Grating Monochromator PID Photo-Induced Dissociation PMT PhotoMultiplier Tube

PP ProtoPorphyrin IX

PSD Position Sensitive Detector

Post Source Decay

PT Proton Transfer

Perturbation Theory

PYP Photoactive Yellow Protein
QCP Quantum-Capping Potential
QET Quasi-Equilibrium Theory
QM Quantum Mechanical
RCB Repulsive Coulomb Barrier
RET Resonance Energy Transfer

RF RadioFrequency
Rh Rhodopsin

RNA RiboNucleic Acid

RRKM Rice Ramsperger Kassel Marcus (rate constant expression)

R-TOF Reflectron Time Of Flight

S Singlet state

SDS Sodium Dodecyl Sulfate
SED Secondary Emission Detector
SF Statistical Fragmentation
SID Surface Induced Dissociation
SOMO Single Occupied Molecular Orbital

SORCI Spectroscopy-Oriented Conical Intersection

T Thymine

Triplet state Tryptophan

TCNQ TetraCyaNoQuinodimethane

TD-DFT Time-Dependent Density Functional Theory

TOF Time Of Flight

xii Abbreviations

U Uracil UV UltraViolet

VAD Vibrational AutoDetachment

VC Vibrational Cooling

VDE Vertical Detachment Energy

VFRAD Vibrational Feshbach Resonance AutoDetachment

Vis Visible

VUV Vacuum UltraViolet XC eXchange Correlation

Contents

1	Steen Brøndsted Nielsen and Jean Ann Wyer	1
2	Introduction and New Aspects	11
3	Experimental Techniques	21
4	Theoretical Methods	45
5	Photo-initiated Dynamics and Spectroscopy of the Deprotonated Green Fluorescent Protein Chromophore	67
6	Fluorescence from Gas-Phase Biomolecular Ions	105
7	Spectroscopy of Ferric Heme and Protoporphyrin IX Ions In Vacuo	117
8	UV-Visible Absorption Spectroscopy of Protein Ions Rodolphe Antoine and Philippe Dugourd	141
9	Excited-State Dynamics of Protonated Aromatic Amino Acids Claude Dedonder, Géraldine Féraud, and Christophe Jouvet	155
10	UV Photophysics of DNA and RNA Nucleotides <i>In Vacuo</i> : Dissociation Channels, Time Scales, and Electronic Spectra J. Mathias Weber, Jesse Marcum, and Steen Brøndsted Nielsen	181
11	Action Spectroscopy of Gas-Phase Peptide Ions with Energetic Photons	209
Ind	lov.	227

General Concepts

Steen Brøndsted Nielsen and Jean Ann Wyer

1.1 **Electrostatic and Magnetic Fields**

An ion with mass m, charge q and velocity v that encounters an electromagnetic field, composed of an electric field E and/or a magnetic field B, will experience the Lorentz force $F = q(E + v \times B)$. For both electrostatic parallel plate and cylindrical deflectors the potential difference V required to redirect an ion is dependent on the kinetic energy to charge ratio of the ion (Figs. 1.1 and 1.2). On the other hand, the magnitude of a magnetic field needed to deflect an ion along a radius of curvature r depends on the momentum to charge ratio of the ion (Fig. 1.3).

As the centripetal force is perpendicular to the direction of motion, the speed remains constant. Since the particle takes a circular path within the cylindrical deflectors, the angle of deflection is simply the angle, θ , subtended by the deflectors.

As the force on a moving charge due to the magnetic field is perpendicular to the velocity, the ion will take a circular path with no change in its kinetic energy.

1.2 **Nucleic Acid Building Blocks**

Nucleic acids are composed of nucleotides. Each building block contains a furanose sugar, a phosphate group and a base (Fig. 1.4). In DNA the sugar is deoxyribose while in RNA it is ribose, and the bond that links the sugar and the base together is called the glycosidic bond. The DNA bases are adenine (A), guanine (G), thymine (T), and cytosine (C), and the RNA bases are adenine, guanine, cytosine and uracil (U) (Fig. 1.5). An example of a DNA homopolymer of adenine (oligonucleotide) is shown in Fig. 1.6. The DNA double helix is formed when two complementary strands come together according to the specific binding of A with T and G with C (Watson-Crick base pairs, Fig. 1.5). Guanine-rich DNA strands can form G-quadruplex

Department of Physics and Astronomy, Aarhus University, Aarhus C 8000, Denmark e-mail: sbn@phys.au.dk; jeanwyer@phys.au.dk

S.B. Nielsen (⋈) • J.A. Wyer

Fig. 1.1 Deflection of an ion using parallel plates: $V = \frac{E_{kin}}{a} \frac{2 d \tan \theta}{L}$

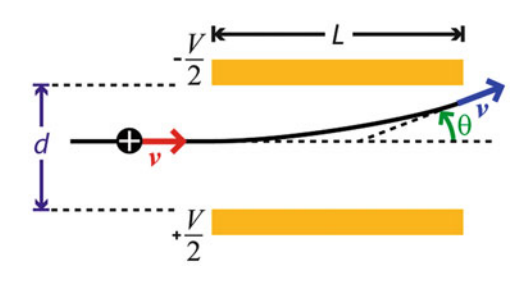


Fig. 1.2 Deflection of an ion using concentric cylindrical plates: $V = \frac{E_{kin}}{q} \frac{2 d}{r}$

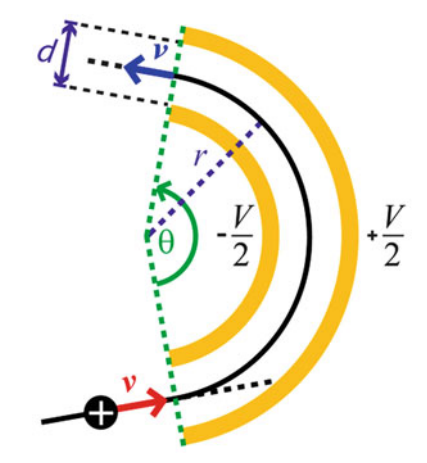
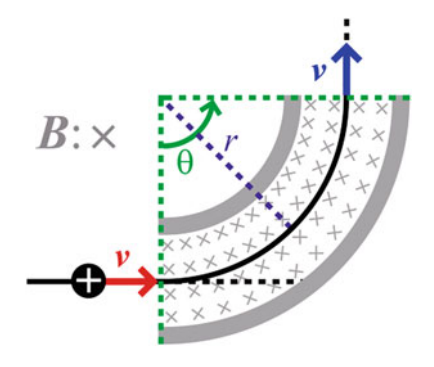


Fig. 1.3 Deflection of an ion using a magnetic field: $B = \frac{m \cdot v}{q} \cdot \frac{1}{r}$



structures, either by intra- or inter-molecular complexation. These complexes are built from stacked G-quartets comprised of four guanines that are hydrogen bonded in a planar motif around a central metal atom (Fig. 1.7).

3

Fig. 1.4 Mononucleotide where the base is adenine. For DNA R represents H, while for RNA it represents OH

Fig. 1.5 Nucleobases. In DNA duplexes, A pairs with T and G with C

The phosphate group is negatively charged, which implies that nucleic acids are multiply charged anions in aqueous solution at neutral pH. Therefore duplex formation requires high salt concentrations to diminish the Coulomb repulsion between the strands. At low pH, both the phosphates and the bases are protonated, which results in positively charged species. Nucleic acids can therefore be produced in the gas phase both as anions and cations dependent on their protonation state.

1.3 Photoactive Amino acids and Peptides, and Their Structures

Aromatic amino acids strongly absorb light in the UV region and are therefore of particular relevance for this volume. They are phenylalanine, tyrosine, and tryptophan (Fig. 1.8). The π -conjugated network of the rings results in highly delocalised

Fig. 1.6 A DNA homopolymer of adenine

molecular orbitals, and these amino acids thus absorb to the red of the other seventeen naturally occurring ones. Excitations in this region are typically $\pi\pi^*$ transitions. Due to these properties, peptides subjected to UV spectroscopic experiments often contain at least one aromatic amino acid.

A dipeptide is made when two amino acids join together, release a water molecule and form an amide bond (see Fig. 1.9). Addition of more amino acids in a similar way results in longer peptides. Proteins are peptides with a biological function, *e.g.*, transport of small molecules or enzymatic activity. A classification of the structural hierarchy was introduced by Linderstrøm-Lang. The sequence of amino acid residues is denoted the primary structure, while the secondary structure

Fig. 1.7 Structure of a G-quartet

Fig. 1.8 Structures of phenylalanine (Phe, F), tyrosine (Tyr, Y), and tryptophan (Trp, W)

Fig. 1.9 Peptide formation from two amino acids. R_1 and R_2 represent the amino-acid side-chains

refers to the different folding motifs of the substructures, e.g., α -helix, β -sheet, and random coil. How the substructures are organised relative to each other in three dimensions is called the tertiary structure. If a protein has more than one polypeptide chain, then the quaternary structure is the arrangement of the polypeptides relative to each other.

In gas phase, peptide basic groups, e.g. amino and guanidine groups, are easily protonated forming positively charged cations, while negatively charged anions are formed by deprotonation of carboxylic acid groups. In mass spectrometry the sequence of a peptide is determined by fragmentation, induced by either collisions after acceleration, electron capture, or photoexcitation, followed by mass spectrometric analysis of the fragment ions. The nomenclature for fragment ions is illustrated for a tetrapeptide in Fig. 1.10.

Fig. 1.10 In the Roepstorff, Fohlman and Biemann fragmentation nomenclature a fragment is labelled according to which bond in the repeating backbone series was broken, and whether it is the amino-terminal (N-terminal) or carboxyl-terminal (C-terminal) part. Cleavage of the C_{α} – C_{β} , C_{β} –N (amide or peptide bond), or N– C_{α} bonds result in a,b, or c fragments, and x,y, or z fragments for the N-terminal and C-terminal sections, respectively. The *subscript* refers to the number of amino-acid side-chains present

1.4 Photophysical Processes

A Jabłoński diagram (Fig. 1.11) is often used to illustrate photophysical processes, with the transitions between the different electronic states and their vibrational levels indicated. Absorption (A) of a photon induces a transition from the initial electronic state (S_0) to a higher-energy one (S_N) , while when a photon is emitted the transition is to a lower state. Such a transition is called fluorescence (F) if there is no change in spin and for phosphorescence (P) if there is a change in spin. Internal conversion (IC) is a radiationless deexcitation process, whereby a molecule relaxes to a lower electronic state with the same spin. IC is faster between S_N and S_{N-1} than S_{N-1} and S_{N-2} since the separation of the levels decreases with increasing N, and thus the nuclear wavefunctions overlap better. This implies that S_1 is populated quickly, and that the IC from S_1 to S_0 is the slowest. Hence most photochemistry occurs from S₁, and emission also normally occurs from there (Kasha's rule). While the energy may initially be localised in one specific vibrational mode, it is redistributed among all modes through a process known as intramolecular vibrational energy redistribution (IVR) that often occurs on sub-ps to ps timescales. (Notice, IC is sometimes also used to denote a transition between different vibrational levels.) In a solution, this excess vibrational energy dissipates to the solvent (i.e., vibrational cooling) on a time scale that depends on the coupling strength between the solute and the solvent molecules. Intersystem crossing (ISC) is a radiationless transition to a state with a different spin. This is possible due to spin-orbit coupling and is particularly important if the S₁ lifetime is long. ISC back to the ground state also requires a spin flip, and as the overlap of the nuclear wavefunctions for T_1 and S_0 is low, it is an even slower process (Fig. 1.12).

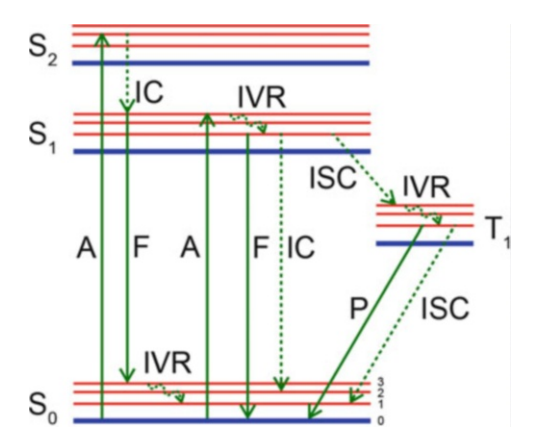


Fig. 1.11 A Jabłoński diagram indicating the electronic ground state (S_0) , the first (S_1) and second (S_2) excited singlet states and the first triplet state (T_1) . According to Hund's rule, T_1 is lower in energy than S_1 . A number of vibrational energy levels are shown for each electronic state; the separation between vibrational levels decreases due to anharmonicity of the potential energy curve. Radiative transitions are depicted with *straight lines*, radiationless transitions with *dashed lines*, and the direction of the transition with an *arrow*. The difference in energy between the absorbed and emitted photons is called the Stokes shift

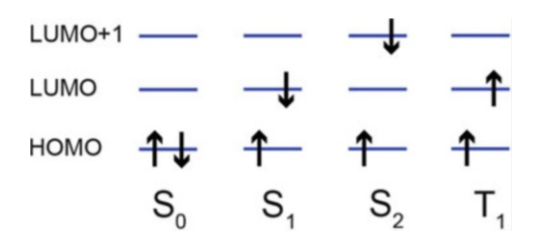


Fig. 1.12 Electronic configurations specified by occupation of orbitals and spin symmetry (each electron "arrow" is associated with a one-electron wavefunction): HOMO Highest Occupied Molecular Orbital; LUMO Lowest Unoccupied Molecular Orbital. The spin multiplicity of a molecule is 2S+1, where S is the total spin quantum number. Singlet (S), doublet (D), and triplet (T) states are states with spin $0, \frac{1}{2}$, and 1, respectively

1.5 σ , π and n Orbitals, and Electronic Transitions

The combination of two atomic s orbitals results in two new molecular orbitals (MOs) that are denoted σ orbitals as when viewed from the side along the atom-atom axis they look like s orbitals (rotational symmetry). This is illustrated for the molecular hydrogen molecule in Fig. 1.13a. Due to the overlap of the atomic orbitals, the energy is different for the plus and minus combinations. The plus combination results in the bonding orbital labelled σ , while the minus combination gives the antibonding orbital labelled σ^* (one nodal plane between the two nuclei). The σ orbital is lower in energy than the original s orbitals while the σ^* orbital is

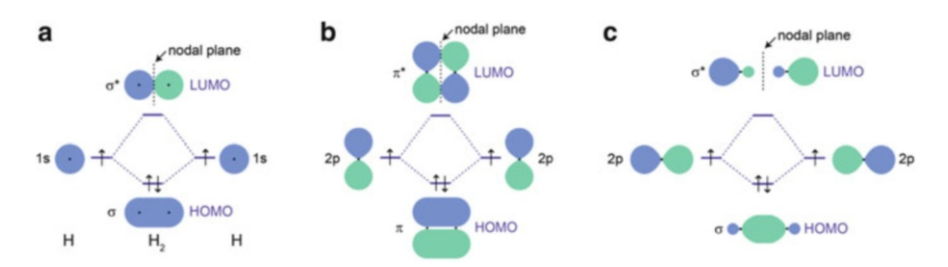


Fig. 1.13 Formation of molecular orbitals from atomic orbitals

higher in energy by more than the σ orbital is lowered. Popularly speaking, "the σ * orbital is more antibonding than the σ is bonding". (This follows from the variational principle and a non-zero orbital overlap integral. Notice that the energy of the H 1s orbital on the figure is not that of an isolated H atom (-13.6 eV) but has been lowered by the favourable interaction between the electron and the other nucleus at the distance where the bond is formed.). In a similar way, the linear combination of N p orbitals leads to N π orbitals; viewed from the side along the axis of the two atoms the two orbitals look like p orbitals, hence the name π orbitals. The simplest case for N=2 is shown in Fig. 1.13b. The more p orbitals that overlap, the more delocalised the state is, and as a result the electronic transition redshifts (Fig. 1.14). It should also be noted that two p orbitals can combine to form σ orbitals (Fig. 1.13c). Atomic orbitals that do not participate in bonding are denoted nonbonding orbitals (n-orbitals) or lone-pair orbitals. As an example see the illustration of the water molecule in Fig. 1.15. All orbitals in a molecule are filled up according to the Aufbau principle (electrons fill the lowest-energy available orbitals first) and Pauli principle (no two electrons can have identical quantum numbers).

A transition from a σ orbital to a σ^* orbital, *i.e.*, $\sigma\sigma^*$ transition, is electronically allowed as the orbitals have different parity. Since the overlap of the two orbitals is large, the oscillator strength is high. Likewise for $\pi\pi^*$ transitions. A charge-transfer transition from say a π orbital of an aromatic ring system to a σ^* orbital of an ammonium group has a low oscillator strength due to the low orbital overlap. $\pi\sigma^*$ states can, however, be populated from long-lived photoactive $\pi\pi^*$ states by internal conversion. The "allowed-ness" of an electronic transition also depends on whether spin is conserved or not and on the overlap of the nuclear wavefunctions between the two states.

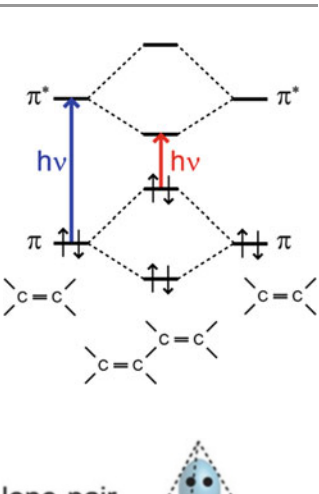
Polar solvents induce shifts in absorption/fluorescence bands relative to those in vacuum. This is because solvent molecules stay still during light-induced electronic transitions, and while they are oriented in the optimal position for a favourable interaction with the initial state orbitals, they may not be in the prime position for the final state orbitals (Figs. 1.16 and 1.17a). A solvent therefore induces a blueshift in absorption for $n\pi^*$ transitions (strong solvent dependence) (Fig. 1.17a). In contrast a redshift in absorption is often seen for $\pi\pi^*$ transitions (Fig. 1.17b) where the dependence on solvent geometry is weak; instead the higher

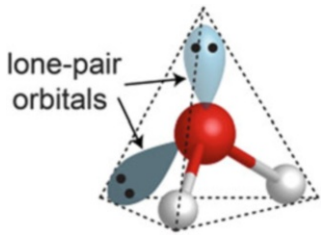
Fig. 1.14 Increased π conjugation causes the absorption to red shift

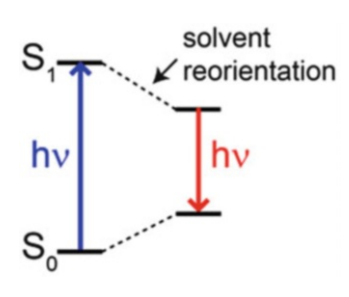
Fig. 1.15 A water molecule has a tetrahedral shape, with lone-pair orbitals occupying two of the vertices

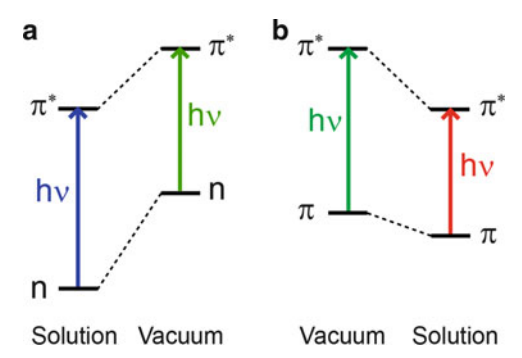
Fig. 1.16 Stokes shift is the difference between the positions of the absorption and emission band maxima

Fig. 1.17 (a) A polar solvent induces a blueshift for $n\pi^*$ transitions. (b) A solvent induces a redshift for $\pi\pi^*$ transitions









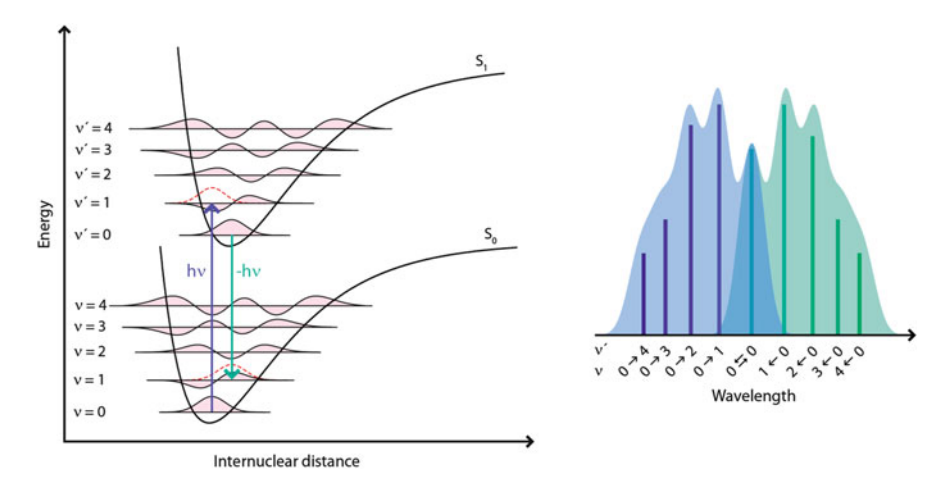


Fig. 1.18 Left: Illustration of the Franck-Condon principle for the electronic excitation/ deexcitation of a diatomic molecule. Vertical transitions have the highest probability as they are associated with large overlap of the nuclear wavefunctions. The wavefunctions include one extra nodal point for each step up in quantum number ν , and become increasingly concentrated at the turning points. The strongest transition will be to the vibrational level whose wavefunction has the largest overlap with the original wavefunction. Red dotted lines are drawn to indicate the initial nuclear wavefunctions. Right: The overall shape of the absorption band is determined by the overlap with each vibrational mode. As fluorescence is likely to occur from $\nu' = 0$ and the structures of S_0 and S_1 are similar, the emission band is often a mirror image of the absorption band (mirror-image rule)

polarisability of the excited state than that of the ground state increases the interaction energy between the chromophore and the solvent molecules.

1.6 The Franck-Condon Principle

According to the Born-Oppenheimer approximation, as nuclei move slowly compared to the far lighter electrons, electrons follow the nuclei instantaneously. Conversely, the nuclei adjust slowly to a change in the electronic state. This implies that in an electronic excitation the wavefunction for the nuclear motion is nearly the same immediately after as before the excitation (Fig. 1.18). The absorption spectrum of the molecule directly reflects this as the pattern is determined by the so-called Franck-Condon (FC) factors. For one particular vibrational level in the electronic excited state, this factor is calculated as the square of the overlap integral of the nuclear wavefunctions in the electronic ground and excited states. In other words, the FC factor is a measure of the relative importance of one vibrational component of an absorption band. The overall intensity of the electronic transition is obtained from the area under the absorption spectrum since the sum of all FC factors adds up to one.

Steen Brøndsted Nielsen

Abstract

This chapter provides a brief introduction to biochromophores encountered in nature, and how their π -conjugated structures determine their excitation energies, *i.e.*, their colour. Perturbations of electronic structure by a microenvironment such as water or charge sites are discussed. These may lead to a colour change (or modulation), depending on the character of the electronic transition. As detailed results for particular chromophores are presented in subsequent chapters, future challenges and new aspects within the research field are instead considered as the author sees them.

2.1 Introduction

Chromophores are ubiquitous in nature: They account for the green colour of leaves, the red colour of blood, the orange colour of carrots, the yellow-green emission from fireflies, and the green or red emission from fluorescent proteins, just to mention a few relevant occurrences. In these examples the chromophore either acts alone, or is one constituent of a complicated network of light absorbers that play together like an orchestra where all have an important role. To qualify as a chromophore, the molecule should be able to absorb visible light. Here, however, we will extend this definition to include also molecules that absorb ultraviolet light.

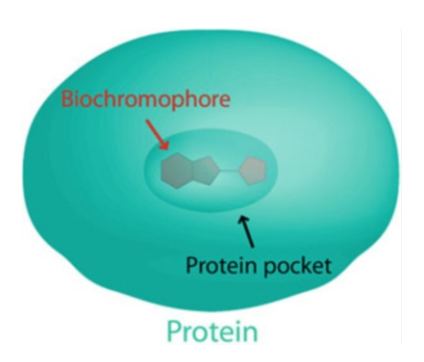
This requirement for absorbing either visible or ultraviolet light implies that the relevant molecules or molecular ions are highly π -conjugated. In other words, the electronic wavefunctions are delocalised over several sp²-hybridised atoms. A physicist will use an argument based on an electron-in-a-box with infinite walls to conclude that the larger the length of the box (the region the photoactive electron can take up), the closer is the separation between the ground-state and first-excited

Department of Physics and Astronomy, Aarhus University, 8000 Aarhus C, Denmark e-mail: sbn@phys.au.dk

S.B. Nielsen (⊠)

12 S.B. Nielsen

Fig. 2.1 Biochromophore buried within a protein pocket



state levels. This simple approach benefits from providing a direct estimate of the excitation energy but it suffers from not considering electron–electron interactions, and also the spacing between the energy levels increases with the quantum number instead of decreasing as they duly should. A chemist will use molecular orbital theory, and from linear combinations of atomic orbitals, the Aufbau principle and the Pauli principle reach the same conclusion regarding the intricate connection between spatial delocalisation and excitation energy based on the number of alternating double and single bonds. Here the qualitative picture is correct but a quick calculation of excitation energy is difficult, if not impossible. Examples of highly π -conjugated biochromophores include the aromatic amino acids (phenylalanine, tyrosine, and tryptophan), the nucleic acid bases (adenine, thymine, guanine, cytosine, and uracil), porphyrins and metalloporphyrins (e.g., chlorophylls and heme), and several protein biochromophores responsible for example for vision, light emission, and signalling. The latter ones absorb in the visible while the former ones (aromatic amino acids and bases) absorb in the UV. Structures of some of the chromophores can be found here, in the other chapters, and in the concepts pages.

Typical ionic chromophores like the anions within the Green Fluorescent Protein (GFP) (the topic of Chap. 5 by Andersen and Bochenkova) and Photoactive Yellow Protein (PYP), the oxyluciferin anion located in the luciferase enzyme and responsible for firefly light emission, and the protonated Schiff base retinal within the rhodopsin vision protein absorb (or emit) in the visible [1]. These are buried within protein pockets or cavities (Fig. 2.1). The low energy separation between the ground and excited states is here ascribed to the fact that the ions can be represented by many resonance forms that do not involve charge separation (see Fig. 2.2 where some of them are drawn; notice the recurring phenolate moiety for the anionic photoactive molecules); all of these should be added together, properly weighted of course, to produce the resonance hybrid (linear combination of basis wave functions). In this sense these chromophores differ significantly from the nucleic acid bases and aromatic amino acids that are all overall neutral at natural pH. These ionic bichromophores, their relatives, and others isolated in vacuo have been exploited in great detail by both experiments and theoretical calculations [2–22], but there are still some disagreements between experiment and theory that need to be settled such as the importance of structural fluctuations potentially causing broad absorption bands.

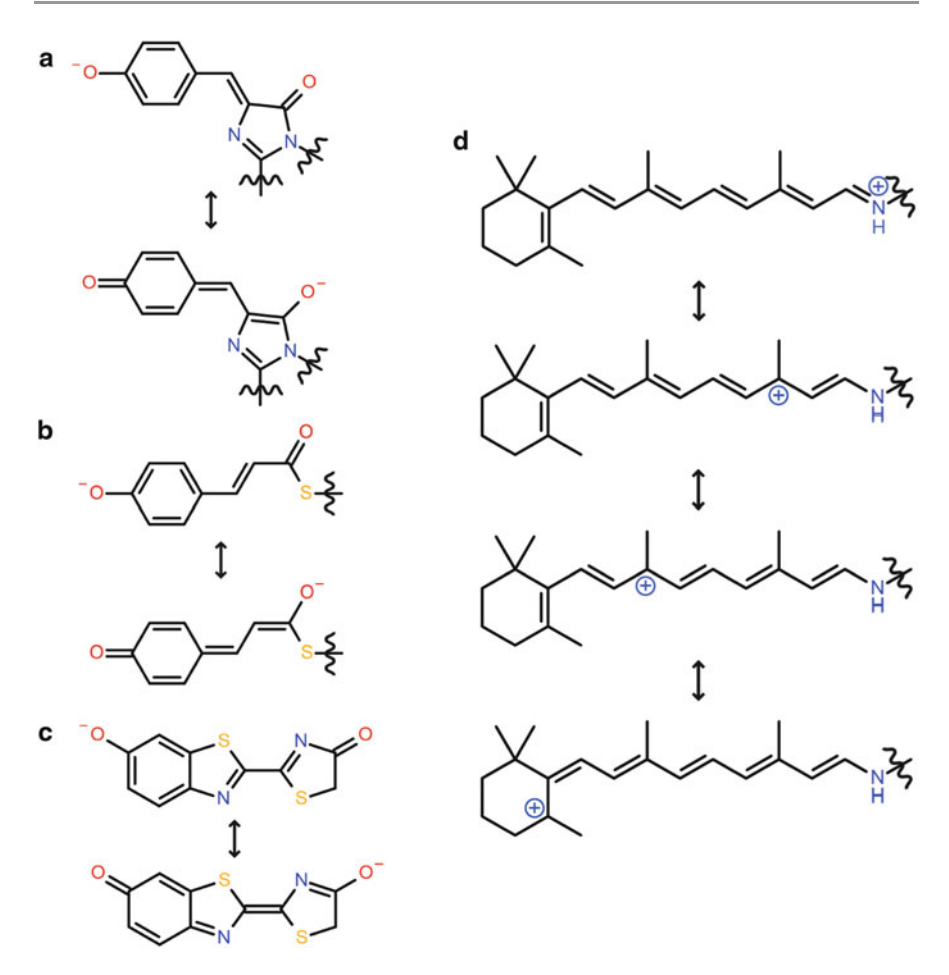


Fig. 2.2 Important resonance structures of ionic biochromophores or luminophores. (a) Green Fluorescent Protein: Derivative of 4-(*p*-hydroxybenzylidene)-5-imidazolinone. (b) Photoactive Yellow Protein (PYP): Thioester derivative of *p*-coumaric acetate. (c) Luciferase: Oxyluciferin anion. (d) Rhodopsin: Protonated Schiff base retinal. A *wavy line* indicates that the structure is joined to a polypeptide chain. The excess electron or the HOMO electron is strongly delocalised, *i.e.*, the "box length" is long

Nearby electric fields set up by an environment will perturb the electronic structure of the chromophore and influence the transition energies, dependent on the character of the electronic transition, and particularly the degree of charge transfer (CT) (Fig. 2.3). Positive or negative charges close to the chromophore can for example originate from acidic or basic amino acid residues (Figs. 2.4 and 2.5). To elucidate electric-field effects and whether an environment is innocent or not, it is useful (or even necessary) to know the intrinsic absorption spectrum of the isolated chromophore!

14 S.B. Nielsen

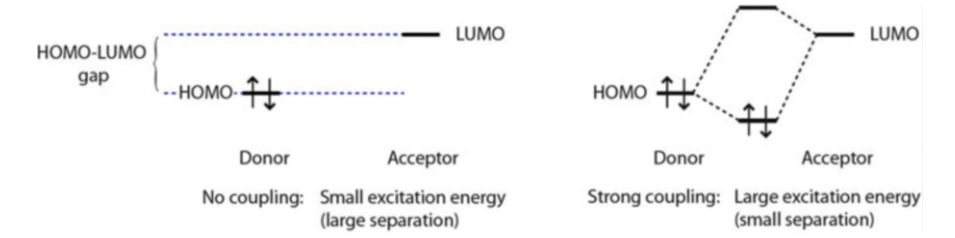


Fig. 2.3 Strong *versus* weak charge transfer. The oscillator strength increases with the degree of coupling

a R b
$$NH_3^+$$
 NH_3^+ NH_3^+ NH_2^+ NH_2^+ NH_2^+

Fig. 2.4 Examples of positive charge sources: (a) N-terminal ammonium group, (b) lysine (Lys) side chain, (c) histidine (His) side chain, (d) arginine (Arg) side chain

Fig. 2.5 Examples of negative charge sources: (a) C-terminal carboxylate group, (b) aspartate (Asp) side chain, (c) glutamate (Glu) side chain

Fig. 2.6 Charge localisation by a single water molecule

Of even larger importance than nearby polar or ionic groups, could be the binding of single water molecules to charge sites (Fig. 2.6) thereby diminishing the electron delocalisation (shorter "box lengths"). However, the actual role of water molecules is not in general easily deduced as charge localisation can imply

that the electronic transition becomes more CT like (decoupling of the overlap between donor and acceptor states); CT transitions are often characterised by low transition energies and low oscillator strengths. In the extreme case of no overlap between the HOMO and LUMO orbitals (Fig. 2.3), the excitation energy is simply the difference between the ionisation energy of the donor and the electron affinity of the acceptor. Intermediate transitions are particularly difficult to account for theoretically. A picture is emerging where the situation *in vacuo* seems much closer to that of the chromophore within the protein pocket than that of the chromophore in bulk aqueous solution, at least when it comes to the chromophore's electronic structure. Still, however, both experimental and theoretical data are needed to explain each individual chromophore case.

2.2 New Aspects and Challenges

Despite the impressive amount of work that has been done in the field, some of it being presented in Chaps. 3–11, it is far from dying out, and more groups worldwide than ever are working on spectroscopy of biomolecular ions. Indeed, there are many interesting new aspects and certainly also challenges to address in the future. Some of them will be discussed in the following.

One frequent complication of the experiments is the presence of multiple isomers in the ion beam that all contribute to the electronic absorption spectrum, to the deexcitation scheme, or even to the dissociation pattern if they do not quickly interconvert. The implementation of an ion mobility device [23] right after the ion source could in many cases solve this issue as this would separate ions with different structures in time due to different drift times through the carrier buffer gas (Fig. 2.7). The combination of mass spectrometry (separation by mass) and ion mobility spectrometry (separation by geometrical structure) indeed seems a very promising and attractive direction for the future. A very recent paper by Bieske and co-workers [24] nicely demonstrates the strength of an ion mobility spectrometer combined with action spectroscopy for the study of the photoisomerisation of molecular ions. Here absorption reveals itself as a geometry change of the molecular ion resulting in a different drift time through the mobility cell! This issue of photoisomerisation is needless to say a highly relevant issue for many protein biochromophores such as the *cis-trans* isomerisation of retinal.

An action spectrum is often taken to represent the gas-phase absorption spectrum. This is in many cases a valid and reasonable assumption (see for example Chap. 3 by Wyer). However, when fluorescence is important, this may not be justified as the fluorescence quantum yield could depend on the excitation wavelength. An ambitious task would be to establish the fluorescence quantum yields for each excitation wavelength to correct for such variations. Likewise, in the photoisomerisation experiment, the isomerisation process may be wavelength dependent, and the absorption spectrum is then modulated by the photoisomerisation probability. Finally, in experiments relying on dissociation, finite time windows for measuring fragmentation can skew the action spectra to either the

16 S.B. Nielsen

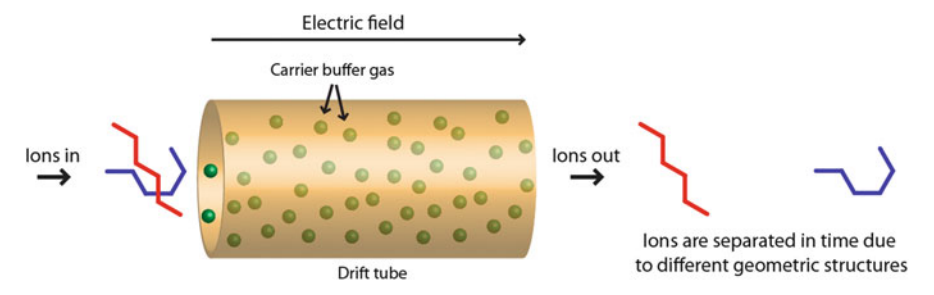


Fig. 2.7 Ion mobility spectrometry

blue or to the red. Only when we can account for the fate of each photoexcited molecule, can we determine the actual absorption spectrum!

Another important issue is the effect of a single solvent molecule or counter ion on the electronic structure of the biochromophore ion as mentioned above. The location of the water could seriously affect the absorption or emission properties of the chromophore/fluorophore. There is a sparse amount of data relating to this, particularly experimental data. The motivation for looking at the effect of single solvent molecules is of course that within hydrophobic protein pockets, there is limited access to water, and often there are only one or two water molecules near to the biochromophore. The advantage of experiments on ions is that such complexes can be made from say ion-molecule reactions between the bare ions and gases or even directly by electrospray ionisation, and they can then subsequently be studied by mass spectroscopic means. Furthermore, water molecules can gradually be added building up the complete solvation shell for comparison with absorption in aqueous solution. Control, selectivity and "in a stepwise manner" are the key words.

Most of the electronic spectroscopy experiments on biomolecular ions have been done at room temperature, and another important direction would therefore be to study cold ions that display much less spectral congestion and provide better benchmarks for theory. Such experiments have successfully been done with regard to vibrational spectroscopy employing 22-pole ion traps (pioneering work by Rizzo, Boyarkin and their co-workers) [25, 26] based on the original trap design by Gerlich [27]. The successful production of cold ions from the combination of electrospray ionisation with cryo-cooled Paul traps by Wang, Johnson and their co-workers [28, 29] has also paved the way for studies of for example H₂-tagged ions [29]; such complexes are easily photodissociated with visible or ultraviolet light, thereby circumpassing one of the inherent problems of action spectroscopy. Likewise, Continetti and co-workers [30] have cryogenically cooled a linear electrostatic ion beam trap for photoelectron-photofragment coincidence spectroscopy. Finally, storage rings cooled down to a few Kelvin or at liquid nitrogen temperatures also provide new interesting avenues along this direction. Such devices are built or under construction in Stockholm, Heidelberg, and Tokyo [31–33]. Spectroscopy of cold ions also provides direct information on the lifetimes of the excited states based on the spectral width (*cf.*, Heisenberg's uncertainty principle), not relying on femtosecond laser experiments. Examples on this exist and are given in Chaps. 7 and 9. The complications of environment and electronic decoupling at higher temperatures can be introduced gradually.

We believe that future work benefitting from cold ion spectroscopy could go beyond the single chromophore to multiple chromophore systems where the electronic coupling between nucleobases changes the electronic properties significantly. Interchromophore coupling is likely of importance in DNA photophysics [34, 35] but is certainly so in photosynthesis where chlorophylls are linked together electronically within light-harvesting proteins [36]. The simplicity of the gas-phase models could provide extremely important results that could be used to test advanced theoretical models such as the Frenkel exciton model. Freezing out structural fluctuations would allow one to be more specific about the actual structure of the ions, and the electronic coupling may increase significantly if π -stacking interactions determine the structures of the dominant isomers.

While fluorescence spectroscopy has been done on a few fluorophore ions *in vacuo* at room temperature (work by Jockusch, Parks, Zenobi and their co-workers [37–39]), similar experiments to those described above on very cold ions are to our knowledge lacking. Indeed, cold ions may have larger fluorescence quantum yields than warm ions as they most likely internally convert slower to the electronic ground state. Again work on multiple chromophore systems would be interesting; for example it would be worth to measure the light emission from long-lived charge-transfer states that are believed to account for long deexcitation times of DNA in aqueous solution [34, 35].

In conclusion, the field of spectroscopy of biomolecular ions isolated *in vacuo* is a relatively new field, but nevertheless the contributions made have been many and significant as is clearly evident from the chapters in this volume. Most importantly, however, the field certainly holds great promise for the future.

References

- Berg, J.M., Tymoczko, J.L., Stryer, L.: Biochemistry, 6th edn. W.H. Freeman, New York (2007)
- Brøndsted Nielsen, S., Lapierre, A., Andersen, J.U., Pedersen, U.V., Tomita, S., Andersen, L.H.:
 Absorption spectrum of the green fluorescent protein chromophore anion in vacuo. Phys.
 Rev. Lett. 87, 228102 (2001)
- Forbes, M.W., Jockusch, R.A.: Deactivation pathways of an isolated green fluorescent protein model chromophore studied by electronic action spectroscopy. J. Am. Chem. Soc. 131, 17038–17039 (2009)
- Chingin, K., Balabin, R.M., Frankevich, V., Barylyuk, K., Nieckarz, R., Sagulenko, P., Zenobi, R.: Absorption of the green fluorescent protein chromophore anion in the gas phase studied by a combination of FTICR mass spectrometry with laser-induced photodissociation spectroscopy. Int. J. Mass Spectrom. 306, 241–245 (2011)
- Zuev, D., Bravaya, K., Makarova, M.V., Krylov, A.I.: Effect of microhydration on the electronic structure of the chromophores of the photoactive yellow and green fluorescent proteins. J. Chem. Phys. 135, 194304 (2011)

18 S.B. Nielsen

 Gromov, E.V., Burghardt, I., Koppel, H., Cederbaum, L.S.: Photoinduced isomerization of the photoactive yellow protein (PYP) chromophore: interplay of two torsions, a HOOP mode and hydrogen bonding. J. Phys. Chem. A 115, 9237–9248 (2011)

- 7. Wanko, M., Garcia-Risueno, P., Rubio, A.: Excited states of the green fluorescent protein chromophore: performance of ab initio and semi-empirical methods. Phys. Status Solidi. B Basic Solid State Phys. **249**, 392–400 (2012)
- Toker, Y., Rahbek, D.B., Klærke, B., Bochenkova, A.V., Andersen, L.H.: Direct and indirect electron emission from the green fluorescent protein chromophore. Phys. Rev. Lett. 109, 128101 (2012)
- Mooney, C.R.S., Sanz, M.E., McKay, A.R., Fitzmaurice, R.J., Aliev, A.E., Caddick, S., Fielding, H.H.: Photodetachment spectra of deprotonated fluorescent protein chromophore anions. J. Phys. Chem. A 116, 7943–7949 (2012)
- Horke, D.A., Verlet, J.R.R.: Photoelectron spectroscopy of the model GFP chromophore anion. Phys. Chem. Chem. Phys. 14, 8511–8515 (2012)
- Nielsen, I.B., Boye-Peronne, S., El Ghazaly, M.O.A., Kristensen, M.B., Brøndsted Nielsen, S., Andersen, L.H.: Absorption spectra of photoactive yellow protein chromophores in vacuum. Biophys. J. 89, 2597–2604 (2005)
- 12. Støchkel, K., Milne, B.F., Brøndsted Nielsen, S.: Absorption spectrum of the firefly luciferin anion isolated in vacuo. J. Phys. Chem. A 115, 2155–2159 (2011)
- Støchkel, K., Hansen, C.N., Houmøller, J., Nielsen, L.M., Anggara, K., Linares, M., Norman, P., Nogueira, F., Maltsev, O.V., Hintermann, L., Brøndsted Nielsen, S., Naumov, P., Milne, B. F.: On the influence of water on the electronic structure of firefly oxyluciferin anions from absorption spectroscopy of bare and monohydrated ions in vacuo. J. Am. Chem. Soc. 135, 6485–6493 (2013)
- Houmøller, J., Wanko, M., Støchkel, K., Rubio, A., Brøndsted Nielsen, S.: On the effect of a single solvent molecule on the charge-transfer band of a donor-acceptor anion. J. Am. Chem. Soc. 135, 6818–6821 (2013)
- Andersen, L.H., Nielsen, I.B., Kristensen, M.B., El Ghazaly, M.O.A., Haacke, S., Brøndsted Nielsen, M., Petersen, M.A.: Absorption of Schiff-base retinal chromophores in vacuo. J. Am. Chem. Soc. 127, 12347–12350 (2005)
- Rajput, J., Rahbek, D.B., Andersen, L.H., Hirshfeld, A., Sheves, M., Altoe, P., Orlandi, G., Garavelli, M.: Probing and modeling the absorption of retinal protein chromophores in vacuo. Angew. Chem. Int. Ed. 49, 1790–1793 (2010)
- Valsson, O., Filippi, C.: Gas-phase retinal spectroscopy: temperature effects are but a mirage.
 J. Phys. Chem. Lett. 3, 908–912 (2012)
- Gozem, S., Krylov, A.I., Olivucci, M.: Conical intersection and potential energy surface features of a model retinal chromophore: comparison of EOM-CC and multireference methods. J. Chem. Theory Comput. 9, 284–292 (2013)
- Virshup, A.M., Punwong, C., Pogorelov, T.V., Lindquist, B.A., Ko, C., Martinez, T.J.: Photodynamics in complex environments: ab initio multiple spawning quantum mechanical/molecular mechanical dynamics. J. Phys. Chem. B 113, 3280–3291 (2009)
- Goto, M., Matsumoto, J., Shiromaru, H., Achiba, Y., Majima, T., Tanuma, H., Azuma, T.: Laser-induced thermal detachment of hot, large molecular ions under multiphoton-absorption conditions. Phys. Rev. A 87, 033406 (2013)
- Saito, M., Tanabe, T., Noda, K., Lintuluoto, M.: Photodissociation of the monoanions of gasphase chlorophylls a and b in an electrostatic storage ring. Phys. Rev. A 87, 033403 (2013)
- Tanabe, T., Saito, M., Noda, K., Starikov, E.B.: Molecular structure conversion of fluorescein monoanions in an electrostatic storage ring. Eur. Phys. J. D 66, 163 (2012)
- Kanu, A.B.., Dwivedi, P., Tam, M., Matz, L., Hill Jr., H.H.: Ion mobility-mass spectrometry.
 J. Mass Spectrom. 43, 1–22 (2008)
- 24. Adamson, B., Coughlan, N., Continetti, R., Bieske, E.: Changing the shape of molecular ions: photoisomerization action spectroscopy in the gas phase. Phys. Chem. Chem. Phys. (2013). doi:10.1039/C3CP51393A

- Boyarkin, O.V., Mercier, S.R., Kamariotis, A., Rizzo, T.R.: Electronic spectroscopy of cold, protonated tryptophan and tyrosine. J. Am. Chem. Soc. 128, 2816–2817 (2006)
- Mercier, S.R., Boyarkin, O.V., Kamariotis, A., Guglielmi, M., Tavernelli, I., Cascella, M., Rothlisberger, U., Rizzo, T.R.: Microsolvation effects on the excited-state dynamics of protonated tryptophan. J. Am. Chem. Soc. 128, 16938 (2006)
- Gerlich, D.: Ion-neutral collisions in a 22-pole trap at very-low energies. Phys. Scr. T59, 256–263 (1995)
- 28. Wang, X.B., Wang, L.S.: Development of a low-temperature photoelectron spectroscopy instrument using an electrospray ion source and a cryogenically controlled ion trap. Rev. Sci. Instrum. **79**, 073108 (2008)
- Kamrath, M.Z., Relph, R.A., Guasco, T.L., Leavitt, C.M., Johnson, M.A.: Vibrational predissociation spectroscopy of the H₂-tagged mono- and dicarboxylate anions of dodecanedioic acid. Int. J. Mass Spectrom. 300, 91–98 (2011)
- Johnson, C.J., Shen, B.B., Poad, B.L.J., Continetti, R.E.: Photoelectron-photofragment coincidence spectroscopy in a cryogenically cooled linear electrostatic ion beam trap. Rev. Sci. Instrum. 82, 105105 (2011)
- 31. Thomas, R.D., Schmidt, H.T., Andler, G., Bjorkhage, M., Blom, M., Brannholm, L., Backstrom, E., Danared, H., Das, S., Haag, N., Hallden, P., Hellberg, F., Holm, A.I.S., Johansson, H.A.B., Kallberg, A., Kallersjo, G., Larsson, M., Leontein, S., Liljeby, L., Lofgren, P., Malm, B., Mannervik, S., Masuda, M., Misra, D., Orban, A., Paal, A., Reinhed, P., Rensfelt, K.-G., Rosen, S., Schmidt, K., Seitz, F., Simonsson, A., Weimer, J., Zettergren, H., Cederquist, H.: The double electrostatic ion ring experiment: a unique cryogenic electrostatic storage ring for merged ion-beams studies. Rev. Sci. Instrum. 82, 065112 (2011)
- 32. von Hahn, R., Berg, F., Blaum, K., Lopez-Urrutia, J.R.C., Fellenberger, F., Froese, M., Grieser, M., Krantz, C., Kuehnel, K.-U., Lange, M., Menk, S., Laux, F., Orlov, D.A., Repnow, R., Schroeter, C.D., Shornikov, A., Sieber, T., Ullrich, J., Wolf, A., Rappaport, M., Zajfman, D.: The electrostatic cryogenic storage ring CSR mechanical concept and realization. Nucl. Instrum. Methods Phys. B 269, 2871–2874 (2011)
- 33. Jinno, S., Takao, T., Omata, Y., Satou, A., Tanuma, H., Azuma, T., Shiromaru, H., Okuno, K., Kobayashi, N., Watanabe, I.: TMU electrostatic ion storage ring designed for operation at liquid nitrogen temperature. Nucl. Instrum. Methods Phys. A 532, 477–482 (2004)
- 34. Middleton, C.T., de La Harpe, K., Su, C., Law, Y.K., Crespo-Hernández, C.E., Kohler, B.: DNA-excited dynamics: from single bases to the double helix. Annu. Rev. Phys. Chem. **60**, 217–239 (2009)
- Vayá, I., Gustavsson, T., Miannay, F.-A., Douki, T., Markovitsi, D.: Fluorescence of natural DNA: from the femtosecond to the nanosecond time scales. J. Am. Chem. Soc. 132, 11834–11835 (2010)
- 36. Cheng, Y.C., Fleming, G.R.: Dynamics of light harvesting in photosynthesis. Annu. Rev. Phys. Chem. **60**, 241–262 (2009)
- Bian, Q.Z., Forbes, M.W., Talbot, F.O., Jockusch, R.A.: Gas-phase fluorescence excitation and emission spectroscopy of mass-selected trapped molecular ions. Phys. Chem. Chem. Phys. 12, 2590–2598 (2010)
- Khoury, J.T., Rodriguez-Cruz, S.E., Parks, J.H.: Pulsed fluorescence measurements of trapped molecular ions with zero background detection. J. Am. Soc. Mass Spectrom. 13, 696–708 (2002)
- Chingin, K., Chen, H.W., Gamez, G., Zenobi, R.: Exploring fluorescence and fragmentation of ions produced by electrospray ionization in ultrahigh vacuum. J. Am. Soc. Mass Spectrom. 20, 1731–1738 (2009)

Experimental Techniques

Jean Ann Wyer

Abstract

Gas-phase ion spectroscopy requires specialised apparatus, both when it comes to measuring photon absorption and light emission (fluorescence). The reason is much lower ion densities compared to solution-phase spectroscopy. In this chapter different setups are described, all based on mass spectrometry and many of them home-built: electrostatic ion storage devices, accelerator mass spectrometers (i.e., sector instruments), reflectron time-of-flight spectrometers, and ion traps. The experimental results presented in this volume were obtained with such instruments. Detection schemes are detailed, both for the identification of neutral products and charged ones. In delayed dissociation experiments, prompt dissociation is a problem as all the fragmentation is then not sampled; an example is photo-induced electron transfer to an ammonium group and subsequent hydrogen loss. A way to circumvent this is discussed based on a chemical approach, namely tagging of ammonium groups by crown ether. Prompt dissociation can sometimes be identified from the total beam depletion differing from that due to statistical dissociation. Special emphasis in this chapter is on the limitations and pitfalls in data interpretation, and the advantages and disadvantages of the different techniques are clarified. New instrumental developments involving cryo-cooled storage rings, which show great promise for the future, are briefly touched upon.

3.1 Action Spectroscopy

In conventional spectroscopy the absorbance of light by a sample is calculated using the intensities of the incident and transmitted light according to the Lambert-Beer law. However, for ionic samples the density of molecules is too low to cause a

Department of Physics and Astronomy, Aarhus University, 8000 Aarhus C, Denmark e-mail: jeanwyer@phys.au.dk

J.A. Wyer (⊠)

22 J.A. Wyer

measurable change in the light intensity. Typically, either electrospray ionisation (ESI) [1] or matrix assisted laser desorption ionisation (MALDI) [2, 3] are used for the production of biomolecular ions, and ion currents may be 0.1 pA. Ions are accumulated in an ion trap for say 0.1 s (experiment with a 10-Hz repetition rate), which results in a total charge of 10^{-14} C corresponding to about 10^5 singly charged ions in a volume of maybe 1 mm³. For comparison, in a solution with the same volume and a sample concentration of 0.1 mM, the number of chromophore ions is 10^{13} , a difference of eight orders of magnitude! Clearly, alternative methods are required to measure the absorbance by thin gas-phase ion targets.

One such method is called action spectroscopy, as the measurement requires an observable "action", *e.g.* dissociation, to determine an absorption spectrum: When gas-phase ions are excited to a higher energy level through photon absorption, several different de-excitation channels are possible; for example, dissociation from the excited-state potential energy surface, internal conversion to a hot ground state and subsequent dissociation, electron detachment (anions) or fluorescence. In action spectroscopy, the daughter products formed after dissociation or electron detachment are monitored at each wavelength, and an action spectrum compiled as the magnitude of photoproducts correlates with the amount of absorption. These spectra are identical to absorption spectra if fluorescence is not a possible pathway or the fluorescence quantum yield is independent of excitation wavelength. In the following, different experimental setups used for action spectroscopy are described.

3.1.1 Electrostatic Ion Storage Rings

Electrostatic storage rings store ions by using a number of electrostatic deflectors such as parallel plates, cylindrical deflectors and quadrupoles to deflect the ions into different straight sections along a closed path. Ions circulate in the ring and can be monitored over time and probed while in straight sections. Numerous different configurations are possible depending on the number of sections required. As an example, in the ELectrostatic Ion Storage ring in Aarhus (ELISA) ions are deflected using two sets of three deflectors each consisting of a set of parallel plates which deflect the ions 10° out of one straight section, a cylindrical deflector which reorients the ions 160° , and a second set of parallel plates which deflect the ions 10° into the other straight section (Fig. 3.1).

In ELISA biomolecule ions are produced using electrospray ionisation, accumulated in a 22-pole ion trap and thermally equilibrated by collisions with a helium buffer gas therein (Fig. 3.2). They are subsequently accelerated as a bunch to kinetic energies of 22 keV, and the desired ions selected using a bending magnet. Following injection into the ring, the lifetimes of ions can be monitored over time by detecting one of the following:

 The production of neutral fragments after dissociation from either vibrationally excited ions or from ions that collide with the residual gas (collision induced dissociation (CID)). After dissociation, ionic fragments will be deflected along an incorrect path and will not be stored in the ring, while neutral products will be

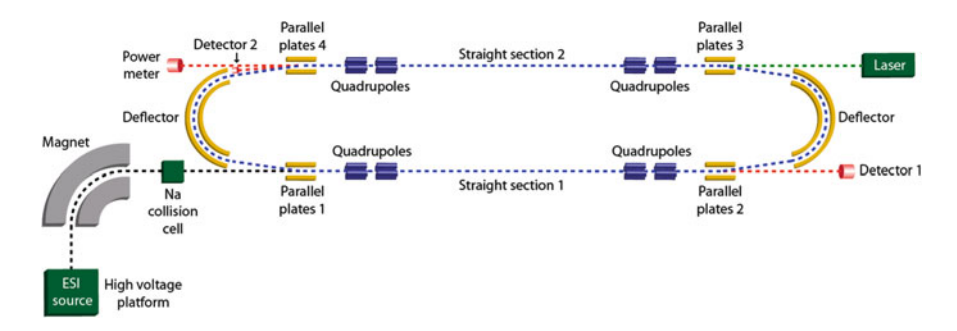


Fig. 3.1 Schematic of ELISA. Deflection within the ring is induced by four parallel-plate deflectors and two cylindrical deflectors. A microchannel plate (MCP) detector (detector 1) is located at the end of straight section 1, while a power meter at the end of straight section 2 is used to measure the laser light intensity. A channeltron detector (detector 2) can measure ionic products with a higher mass-to-charge ratio than that of the parent when positioned on one side of the parent beam (as depicted in the figure), or lower if moved to the other side. Pairs of quadrupoles are used to focus the ion bunch in both horizontal and vertical directions. The pressure in the ring is on the order of 10^{-10} mbar, which sets an upper limit of seconds or hundreds of milliseconds on the storage time

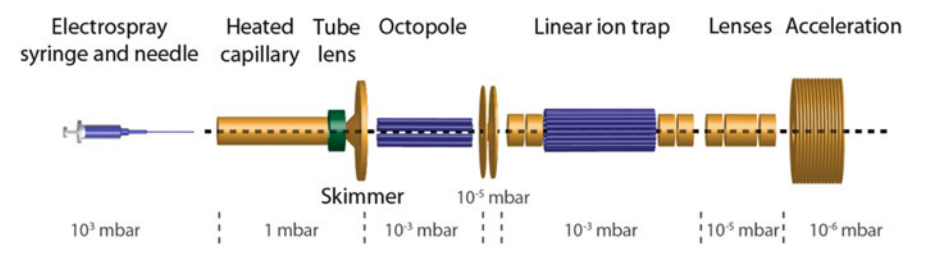


Fig. 3.2 ElectroSpray Ionisation (ESI) source used at ELISA

unaffected by the electrostatic deflectors. Hence neutral fragments produced in straight section 1 will be measured in detector 1 (see Fig. 3.1). An advantage of this detection method is that as all photodissociation channels are measured simultaneously; a change in dissociation channel with excitation wavelength has little or no effect on the experiment. Furthermore, as the dissociation can be monitored over time, kinetic shifts (*vide infra*) can often be corrected for. Ions, however, have to live long enough after photoexcitation to take half a turn in the ring (\sim 50 μ s). The detection efficiency is high as the neutrals travel with high kinetic energies (keV).

2. Neutral products in a Secondary Emission Detector (SED) which can be inserted after straight section 2 (Fig. 3.3). To quantify the production of neutrals, a channeltron detector measures accelerated electrons emitted from a glass plate after neutrals impaction. Laser light, on the other hand, passes through the plate and can be detected in a power meter. The advantage of using this detector is that dissociation from short-lived ions can be identified. However, the wavelength

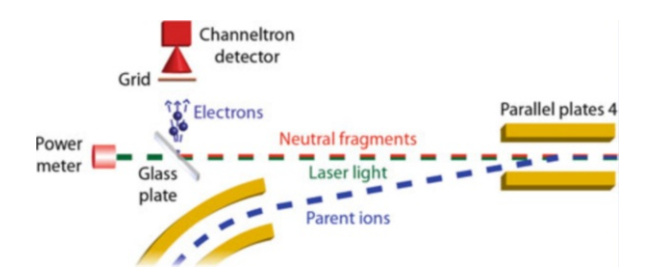


Fig. 3.3 Secondary Emission Detector. Electrons are produced when neutral products hit the glass plate that is biased on a negative voltage. They are subsequently accelerated towards and detected in a channeltron detector. The transmitted laser light can be measured in a power meter

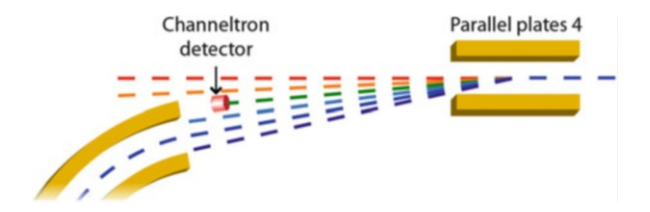


Fig. 3.4 Enlarged view of the channeltron detector region in ELISA showing the paths of the parent ions (*dark blue*), neutral fragments (*red*) and various daughter ions (*orange, green, cyan*, and *violet*). If the electrostatic elements are set to store a parent ion, daughter ions can be measured in the channeltron detector as ions with a higher mass-to-charge ratio than that of the precursor ion are bent less in the 10° deflector (parallel plates 4). The detector can also be placed on the other side of the parent beam to measure fragments with a lower mass-to-charge ratio (*violet path*)

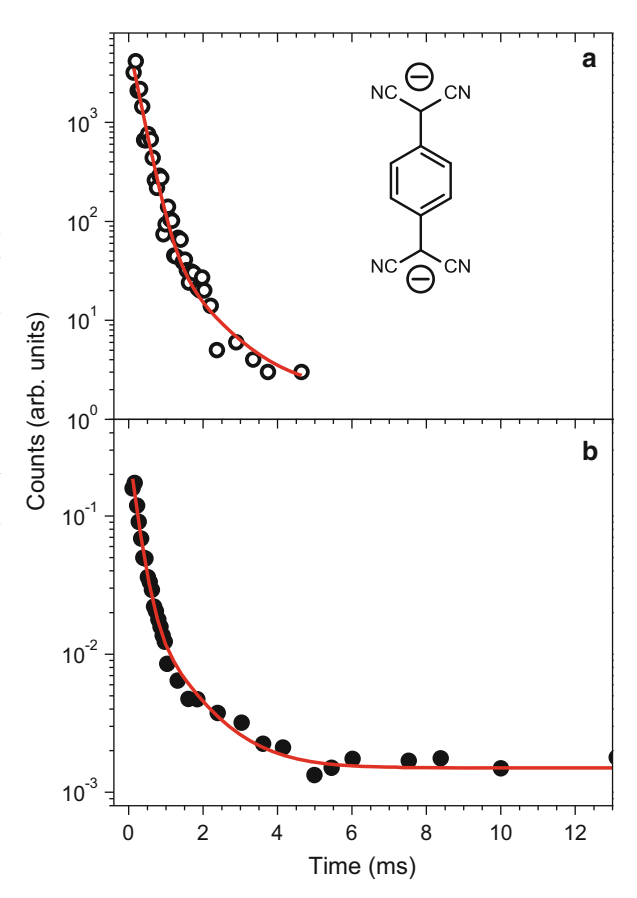
range at which the detector can be operated is limited (>350 nm) as higherenergy photons will damage the coating. More details can be found in Chap. 5 by Andersen and Bochenkova.

- 3. Ionic products (e.g., mono-anions produced from dianions) in a channeltron detector located after one of the 10° deflectors as the detector can be positioned in such a manner that it intersects their path (Fig. 3.4).
- 4. The entire ion bunch at a particular time by turning off one of the 10° deflectors (parallel plates 2) so the ions travel straight into the detector.

That a measurement of product formation is directly correlated to the number of ions in the ring is illustrated in Fig. 3.5. There, the number of 7,7,8,8-tetracyano-p-quinodimethane (TCNQ) dianions in the ring measured by dumping the beam onto the MCP detector after different storage times is compared to the formation of monoanions over time. The same lifetimes and branching ratios describe both sets of data.

Spectroscopy experiments can be performed as the ions can be irradiated by laser light in the ring. After the absorption of a photon, internal conversion results in vibrationally excited ions which will subsequently dissociate. In these experiments ions are stored for several milliseconds to ensure the decay of highly vibrationally excited ions prior to irradiation by a laser-light pulse, and an increased yield of

Fig. 3.5 Lifetimes of TCNQ dianions with respect to electron autodetachment [4]. (a) The formation of TCNO monoanions over time measured in the channeltron detector. (b) The number of dianions in the ring measured by dumping the beam onto the MCP detector after different storage times. Three lifetimes are required to describe the two sets of data (vide infra), with the first two reflecting unstable dianions and the latter one dissociation after collisions with residual gas in the ring. Note that the same lifetimes and branching ratios are used in the fits; 0.2 ms (95 %), 1.0 ms (4 %) and 0.72 s (1 %)



neutrals indicates photon absorption. While the signal can be monitored over time, the first counts are measured after a time delay as the detector is located at the end of straight section 1 while photoexcitation is performed in straight section 2. Hence, ions which dissociate on a fast time scale will not appear to absorb the light (using detector 1 only (*vide infra*)). However, as the dissociation processes are measured over time, it is possible to fit the data if the timescales are long enough, extrapolate back to time zero (defined as the time when the laser was fired) and obtain a number proportional to the total number of excited ions (Fig. 3.6). This is an advantage over other instruments which sample fragmentation over a finite time and thus can introduce kinetic shifts: if the lifetime of fragmentation changes with wavelength, then the fragmentation occurring at each wavelength in a window of time is not linearly representative of the total fragmentation (Fig. 3.7).

Spectroscopy of photo-excited ions can also be done using two lasers [5]. This is discussed in more detail in Chap. 7 by Wyer and Brøndsted Nielsen.

Note Doppler shifts are unimportant in these experiments: Consider an ion with mass 100 and a kinetic energy of 22 keV. The wavelength the ions *see* is

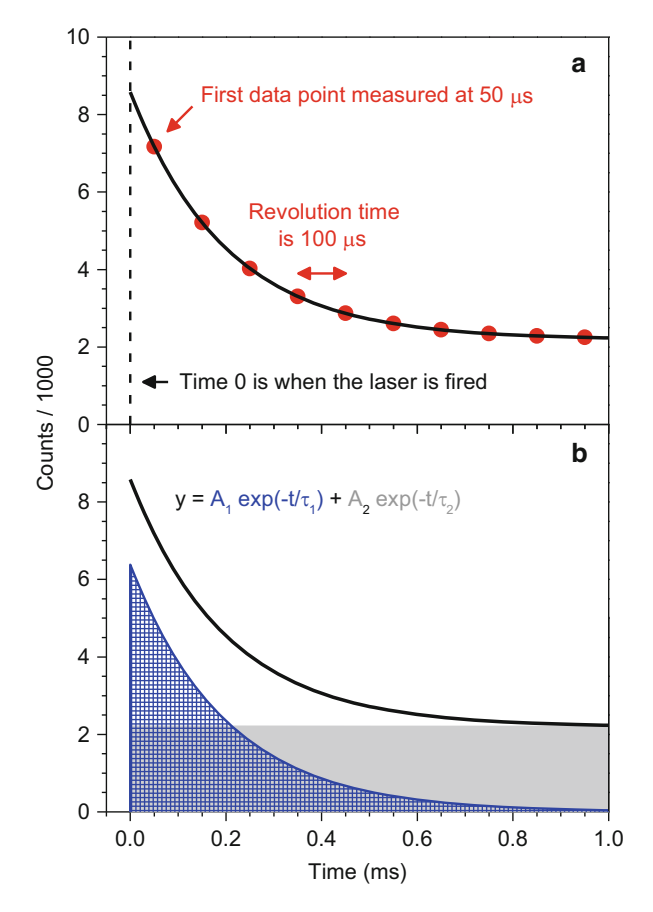


Fig. 3.6 (a) Illustration to show that while the first data point in a time spectrum measured at ELISA is measured after half a revolution in the ring, the data can be fit to determine the total number of photoexcited ions: To describe the data collected at ELISA a set of exponentials are fit to the lifetime data, e.g. for two exponentials; $y = A_1 \exp(-t/\tau_1) + A_2 \exp(-t/\tau_2)$, where the first term relates to the photoexcited ions which decay with a time constant τ_1 and the second term with a time constant τ_2 accounts for CID decay ($\tau_2 \gg \tau_1$). From these fits, it is possible to calculate a number proportional to the total number of photoexcited ions, $N_{lons,1}^* = A_1\tau_1$ and absorption cross sections can be calculated using the following formula: $Abs_1 = A_1\tau_1/(N_{Background}(N_{Photons})^x)$, where $N_{Background}$ is the neutrals signal arising from CID prior to photoexcitation, which is proportional to the number of ions in the beam, and is included to account for variations in the ion-beam intensity; $N_{Photons}$ is the number of photons in the laser pulse; and x is either 1 or 2 for one- or two-photon absorption, respectively. (b) The fit from (a), along with each of the constituent exponentials

 $\lambda_{obs} = \lambda_s \sqrt{\frac{c+\nu}{c-\nu}}$, where λ_s is the wavelength for a stationary observer, c is the speed of light, and v is the speed of the ions. As the ions travel with a speed of 10^5 m/s, which is much less than the speed of light, $\lambda_{obs} \approx \lambda_s$.

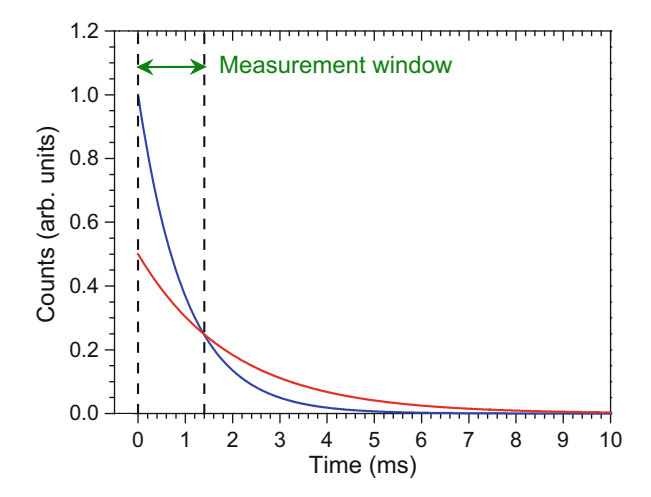


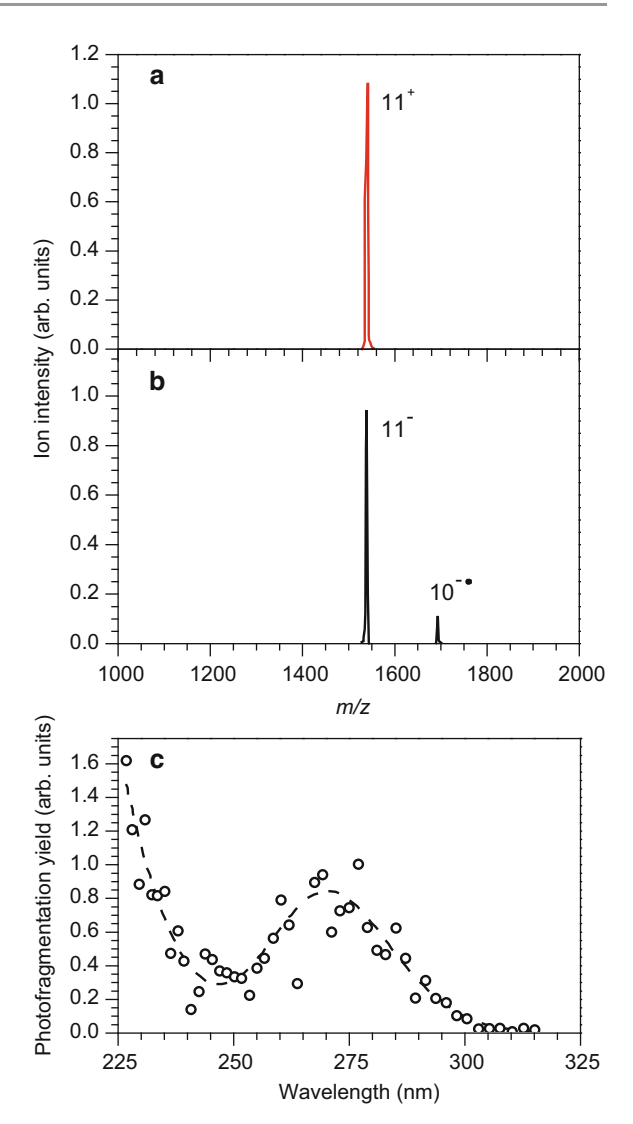
Fig. 3.7 Kinetic shifts occur when the time constant for dissociation changes with wavelength, and the measurement time window is not large enough to measure all fragmentations. Thus, as illustrated here, even though the same number of blue and red photons are absorbed giving the same number of photoexcited ions that all have enough energy to dissociate, the measurement indicates more blue photons were absorbed as more dissociation is measured within the finite time frame of the experiment

In order to fit the data, a number of exponentials are sometimes required with one representing the background decay of the ions due to collision-induced dissociation. The requirement of more than one exponential to describe the decay ascribed to photoexcitation is due to one of the following reasons:

- Ions may have absorbed a different number of photons, with ions which have absorbed more photons decaying over a faster timescale than ions which have absorbed less.
- 2. The width of the internal energy distribution: a time constant for dissociation should be associated with each internal energy of the ions, determined by the activation energy E_0 and pre-exponential factor A for the statistical dissociation process [6]. A simple expression for the rate constant is obtained from Quasi-Equilibrium Theory (QET) [7] and is $k(E) = A (1 E_0/E)^{s-1}$. A is the limit at high internal energy E, and s = 3N 6 (5) is the degrees of freedom of a nonlinear (linear) molecule with N atoms. Note that k is the inverse of the time constant for dissociation. In the extreme, the decay follows a power-law decay, t^{-n} ($n \approx 1$) [6].
- 3. Some photoexcited ions undergo an intersystem crossing to *e.g.* a triplet state: such a crossing would introduce a bottleneck for dissociation as a rate-limiting spin flip is required to reach the electronic ground state [8, 9].

From the pre-exponential factors and time constants a number proportional to the total number of photoexcited ions can be calculated and the absorption-cross sections resulting in dissociation calculated (Fig. 3.6) [10]. These are equal to the real absorption-cross sections (on a relative scale) if luminescence is not a

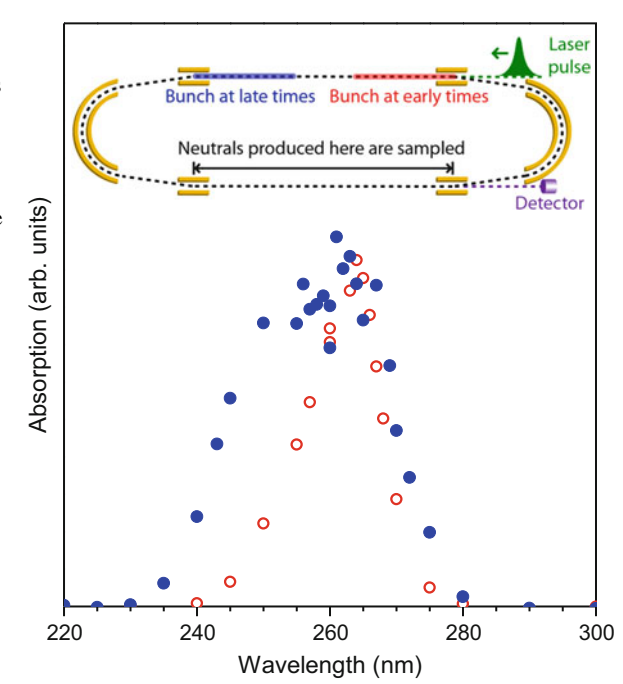
Fig. 3.8 Photodissociation (260 nm) mass spectra of apomyoglobin (a) 11⁺ cations and (b) 11⁻ anions. (c) The action spectrum of the anions obtained by measuring the production of 10⁻¹ anions [11]



relaxation mechanism or the luminescence quantum yield is independent of wavelength, and the ions dissociate on the time scale of the experiment. Another issue to be concerned about is radiative cooling by emission of infrared photons; this occurs on the milliseconds time scale and therefore can be a problem for long dissociation times as some ions may cool down before they dissociate. The experiment will then provide a too low absorption-cross section.

That an ion will not fragment within the time scale of the experiment can be due to its large size (large s). This is illustrated for myoglobin protein cations based on work by Antoine and Dugourd [11] (Fig. 3.8). There, no fragmentation was observed after irradiation by 260 nm as the change in internal energy after

Fig. 3.9 Action spectra of AMP anions recorded after two different excitation times in the ring (see *inset*). When the ions are excited at earlier times, ions which have absorbed higher-energy photons decay too fast for the photoexcited ions to survive to the straight section where dissociation is sampled. Consequently, there is a discrimination against measuring the absorption of higher-energy photons

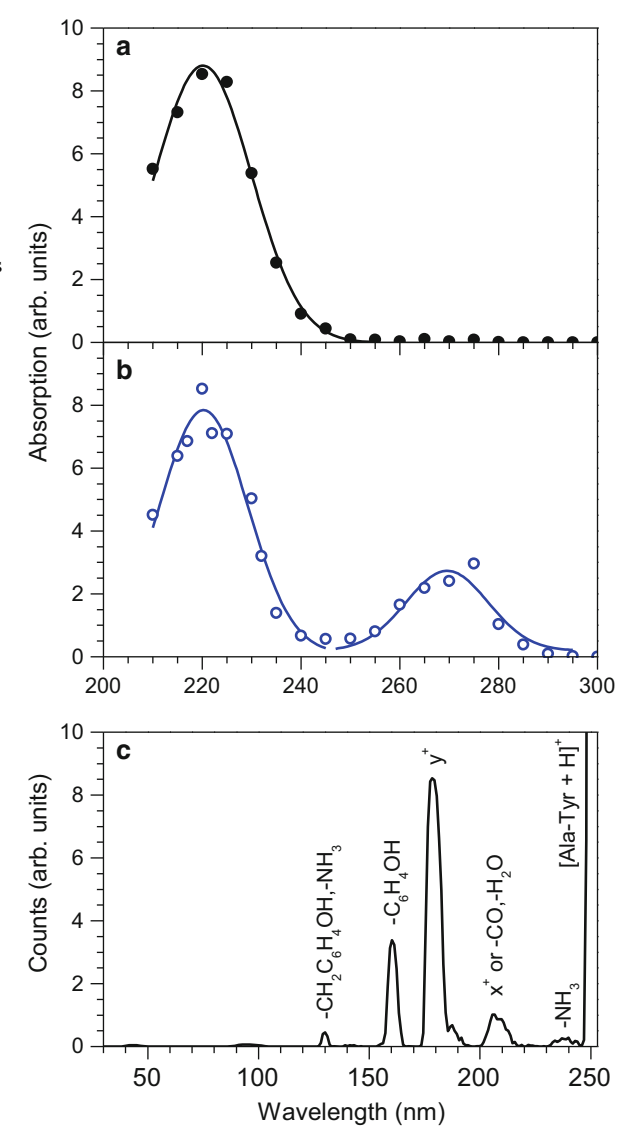


one-photon absorption was too little to cause dissociation on the relevant time scale due to the large number of degrees of freedom. If instead the experiment was done for protein anions, electron detachment was an open channel, and this channel could be used to obtain the action spectrum of the anion. Note: it is not necessarily the photoactive electron that is lost. If not, then a coupling between the photoactive site and the site where the electron loss occurs is present.

As mentioned above, the absorption by ions at all or particular wavelengths may not be identifiable from delayed dissociation experiments due to fast dissociation timescales. Thus, if the lifetime of the ions is on the limit of being detected, one should remember that the spectrum could be skewed towards the red. Such a distortion is due to ions which absorb higher-energy photons decaying too fast to be measurable in detector 1, whilst the decay of colder ions can be detected. As an example in Fig. 3.9 the action spectra of adenosine 5'-monophosphate (AMP) anions recorded after two different excitation times in the ring are shown. When the ions are excited at early times, they have a longer distance to travel before measurements can begin. The resulting spectrum is skewed to the red relative to the spectrum measured when the ions require a shorter time to reach the region where measurements can begin.

Another example of an erroneous measured spectrum due to undesired dissociation is that of the protonated dipeptide cation [Ala-Tyr + H] $^+$ (Ala = alanine and Tyr = tyrosine) (see Fig. 3.10). There, while the absorption of 220-nm light is observed, the absorption of 270-nm light cannot be detected from the delayed

Fig. 3.10 Absorption spectra of (a) $[Ala-Tyr + H]^+$ (m/z 253) and (**b**) [Ala-Tyr + $H_{1}^{+}(CE)$ (m/z 517) in vacuo. Gaussian fits to the data are shown as solid lines. (c) Photodissociation mass spectrum of [Ala-Tyr + H]+ after 270-nm photoexcitation [10]. Absorption at 270 nm is not apparent from delayed dissociation measurements. However, as evidenced from the prompt dissociation mass spectrum, the ions do absorb at this wavelength. Please refer to the Chap. 1 for an explanation of peptide fragmentation nomenclature



production of neutrals, as the main dissociation channel is loss of hydrogen after charge transfer from the photoexcited phenol group to the ammonium group, which occurs on too short a time scale to be measured in the ring (Fig. 3.11) [10]. This is a general issue for protonated aromatic amino acids (see Chap. 9 by Dedonder, Féraud and Jouvet). As the dehydrogenated ions are stored along with the parent due to large acceptance, their subsequent dissociation would be evidence of the initial absorption. (Note, the internal energy distribution of these radical cations is broad as the kinetic energy range of the ejected hydrogen atom is large.) However,

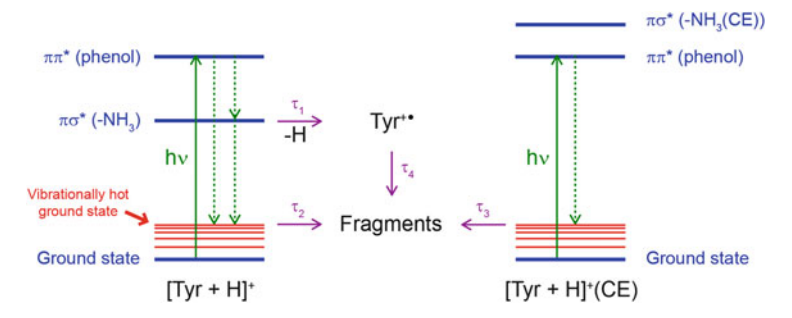
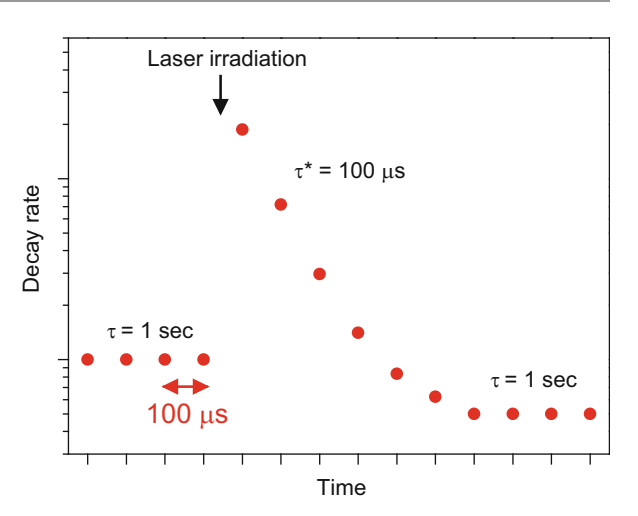


Fig. 3.11 Simplified state level diagrams including some important states for $[Tyr + H]^+$ and $[Tyr + H]^+$ (CE). After photoexcitation of protonated tyrosine $(\pi\pi^*$ transition in the phenol group), internal conversion (IC) occurs either back to the electronic ground state (S_0) or to a CT state located on the ammonium, *cf. dashed arrows*. In the former case a vibrationally excited ion that decays statistically is formed. In the latter case, hydrogen loss is in competition with IC to S_0 . The CT state is not accessible in the supramolecular complex between protonated tyrosine and 18-crown-6 ether, and the pathway is IC back to the S_0 followed by statistical dissociation. The relationship between the time constants is as follows: $\tau_1 \ll \tau_2 \ll \tau_3 < \tau_4$. τ_4 represents a broad range of time constants

the dissociation of these cold radical cations occurs on too long time scales to be measurable in the experiment at 270-nm excitation. In contrast, further dissociation after hydrogen loss following 220-nm photoexcitation is more probable due to the larger amount of energy deposited. To avoid such fast dissociation resulting from the population of charge-transfer (CT) states causing prompt H loss, the excited states of an ion can be manipulated by supramolecular complexation. For example, complexes can be formed between ions and 18-crown-6 ether (CE) as CE targets ammonium groups [12, 13]. Such a complexation can move the dissociative state resulting in hydrogen loss out of the spectral region and instead measurable statistical dissociation occurs on the microsecond to millisecond timescale (Fig. 3.10). Another effect of the CE is to immobilise the proton thereby prohibiting the facile cleavage of the peptide bond [14, 15] and slowing down the decay.

An interesting question is whether delayed dissociation due to statistical processes can account for the total ion beam depletion. The latter is easily calculated from the count rate just before laser irradiation (CID only, n_{before}) and that right after all the photoexcited ions have decayed (CID only, n_{after}). If the time constant (τ) associated with CID is much longer than that for photodissociation (τ^*) (see Fig. 3.12), then the total beam depletion is simply $1 - \frac{n_{\text{offer}}}{n_{\text{hefore}}}$. For exponential decays, the decay rate before photoexcitation is given as $\frac{N_0}{\tau} \exp\left(-\frac{t}{\tau}\right)$ and that for photoexcitation is $\frac{N_0^*}{\tau^*} \exp\left(-\frac{t}{\tau^*}\right)$, where N_0 is the total number of ions before photoexcitation, and N_0^* is the total number of photoexcited ions. The depletion due to statistical dissociation is then $\frac{N_0^*}{N_0} = \frac{n^*(t) \ \tau^*}{n_{\text{hefore}} \tau} \exp\left(\frac{t}{\tau^*}\right)$, for $\tau \gg \tau^*$, where $n^*(t)$ is the decay rate at time t after photoexcitation. This procedure has been used in the case of AMP anions and cations [16], see Chap. 10 by Weber, Marcum, and Brøndsted Nielsen.

Fig. 3.12 Photoexcitation of ions in a ring leads to a higher decay rate, and an ion beam depletion is evident after some time (lower count rate than before photoexcitation). The time constant for dissociation before photoexcitation and after some time is in this example 1 s while that due to photodissociation is 100 μs. The decay rate is measured with Detector 1 (*cf.*, Fig. 3.1)



Daughter ion mass spectrometry is an alternative method for detecting dissociation and can be relevant in cases where dissociation is fast or where statistical dissociation *versus* non-statistical is to be compared. Daughter ions can be measured by changing, at a particular time, the voltages on the electrostatic elements so that the parent ions are no longer stored but instead ions with a different kinetic energy (proportional to their mass-to-charge ratio) are. Then after some time the 10° deflector (parallel plates 2) can be switched off, and if any ions with this mass-to-charge ratio were produced, a signal will be detected (Fig. 3.13). By repeating this process for different potential daughter ions a mass spectrum can be obtained (Figs. 3.10c and 3.14).

Daughter ion mass spectrometry is possible as ELISA has been equipped with pulsed power supplies with microsecond response times [17–19]. A disadvantage with using a storage ring to perform mass spectrometry is that as the ring is designed to maximise the storage of ions, even ions with imperfect trajectories are stored. Furthermore, in contrast to other instruments where ions are differentiated based on their mass-to-charge ratio and not kinetic energies or velocities, e.g. an FT-ICR (vide infra), ions are stored based on their kinetic energies. Thus, the resolution of daughter ion mass spectra is poor (~100). However, in most cases this resolution is enough to determine the dissociation channels and their time dependence. If the electrostatic elements are switched concurrently with photoexcitation, prompt dissociation can be measured. With the detection of ionic fragments produced at short times, it is possible to measure absorption which cannot be measured from the production of neutrals due to short dissociation timescales (Fig. 3.10c). It should be noted, however, that the resulting mass spectrum will be inaccurate if a daughter ion is unstable and dissociates prior to when the bunch is dumped on the detector. The elements can be switched at later times to investigate if and how the dissociation channels vary over time (Fig. 3.14c).

In other experiments, the excitation of ions by electron capture from an alkali metal, e.g., Na is facilitated in a collision cell prior to the ring. The decay of dianions or charge-reduced cations in the ring can then be followed in time.

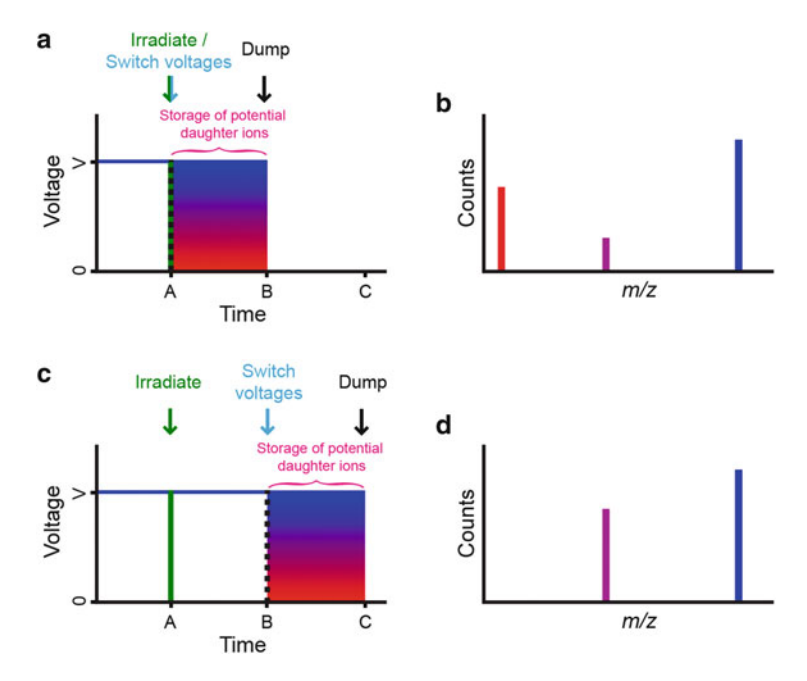
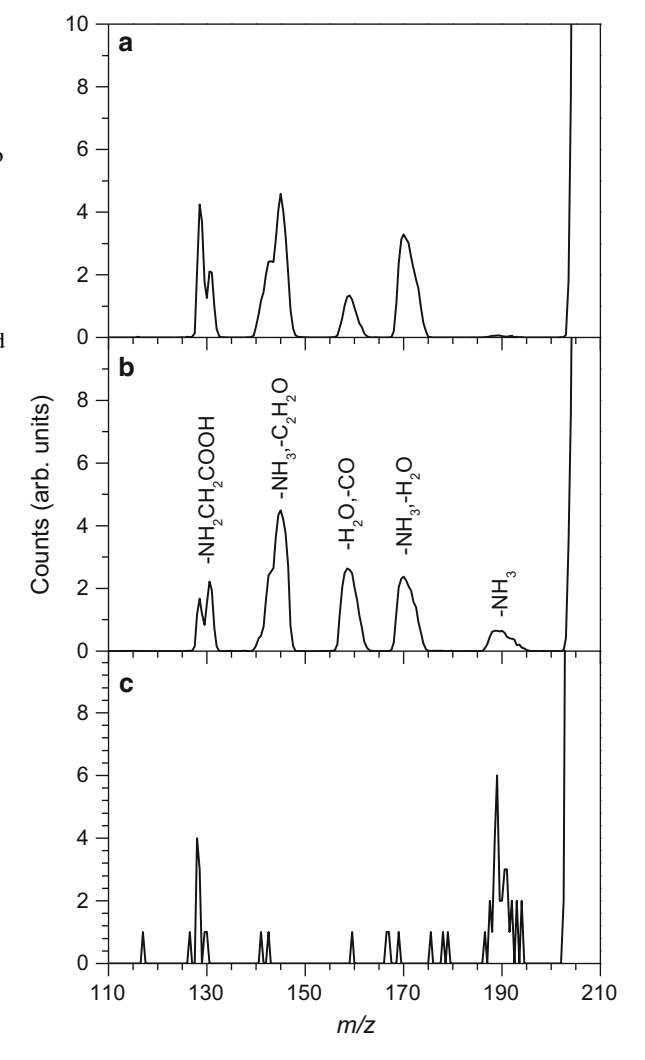


Fig. 3.13 Fragmentation can be measured at ELISA by switching the voltages at a particular time to store a potential daughter ion with a different kinetic energy, and subsequently dumping any stored ions on the detector [17–19]. Mass spectra are obtained by repeating this process for different potential daughter ions. (a) Voltages are switched at the same time as laser irradiation to measure prompt decay. (b) Prompt mass spectrum. (c) The parent ions continue to be stored after laser irradiation, and voltages are only switched at a later time to measure delayed dissociation. (d) Delayed mass spectrum. The delayed and prompt mass spectra may be different from one another, *e.g.*, hot ions (two-photon absorption) dissociate faster than colder ions (one-photon absorption)

3.1.2 Accelerator Mass Spectrometer

Ions which dissociate on fast timescales can be studied at a single-pass instrument such as an accelerator mass spectrometer (also known as a sector instrument as magnetic and electrostatic sectors follow each other in space) (Fig. 3.15). In the illustrated instrument ions are produced by electrospray, and passed through a heated capillary and tube-lens/skimmer region into an octopole which can be operated as a trap by proper pulsing of the lens directly following it. When the octopole is used in trapping mode, ion-molecule reactions can occur between the ions and an injected gas to form complexes of interest. The following linear ion trap can be used to bunch and thermalise the ions when the octopole is used as an ion guide, to thermalise the ion bunch formed in the octopole through collisions with helium buffer gas, or simply as an ion guide. Ions are then accelerated to kinetic energies of 50 keV times charge state, and those of interest selected by an electromagnet and subsequently irradiated with laser light. Irradiation can be done in

Fig. 3.14 Photodissociation mass spectra of [Trp + H]⁺ (m/z 205) after (**a**) 220-nm, and (**b**, **c**) 266-nm photoexcitation: Fragment ions were formed (**a**, **b**) up to 15 μs and (**c**) between 57 μs and 72 μs after photoexcitation [20]. In the latter spectrum, dissociation is of the Trp⁺ radical cation while in the two former spectra it is of [Trp + H]⁺ and Trp⁺. Trp Tryptophan



either a merged-beam or crossed-beam configuration. In the former, a large number of ions are excited, while in the latter few are excited, but the window for dissociation is the same for all excited ions. Fragment ions are then identified by scanning an electrostatic analyser (ESA) and monitoring yields. Action spectra can be obtained from measurements of photo-induced fragment ion production as a function of wavelength. It is possible to probe the aftermath of interactions between the ions and a gas and/or an electron captured from an alkali metal. As with all single-pass experiments, fragmentation within a limited window is sampled. Thus the setup requires fast dissociation on the µs time scale (useful for weakly bond complexes). Spectra from such an instrument could be skewed to the blue, as ions

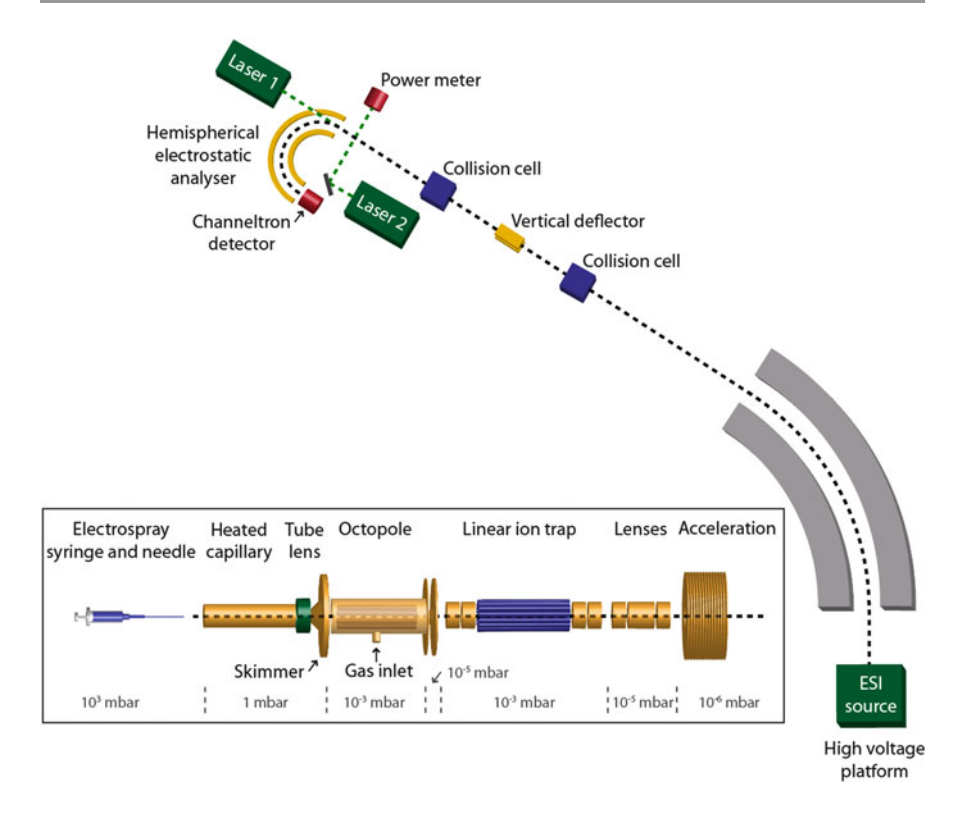


Fig. 3.15 Schematic of the accelerator mass spectrometer in Aarhus [21–23]. Ions can interact with a gas of for example argon, molecular oxygen, or an alkali metal in the collision cells. Photoexcitation can be conducted in either a merged-beam or crossed-beam configuration. The vertical deflector is used for neutral reionisation experiments not discussed here

which have absorbed lower wavelengths are more likely to dissociate within the measurement time window, see Fig. 3.7.

3.1.3 Reflectron Time-of-Flight Mass Spectrometer

Another single pass instrument that can be used to study photofragmentation is a reflectron time-of-flight (R-TOF) mass spectrometer (Fig. 3.16) [24]. In the depicted instrument, ions are produced using electrospray, desolvated in a heated capillary, and accumulated in a hexapole ion trap. They are subsequently extracted, focused and injected into the acceleration region of a TOF mass spectrometer. There ions are accelerated perpendicularly into a flight tube, and those of interest irradiated using a nanosecond-pulsed tuneable laser. A two-stage reflectron is then used to separate ions according to their mass-to-charge ratio, and the ions are detected on a microchannel plate detector. A conversion dynode and channeltron located next to the TOF acceleration region can be used for ion beam diagnostics.

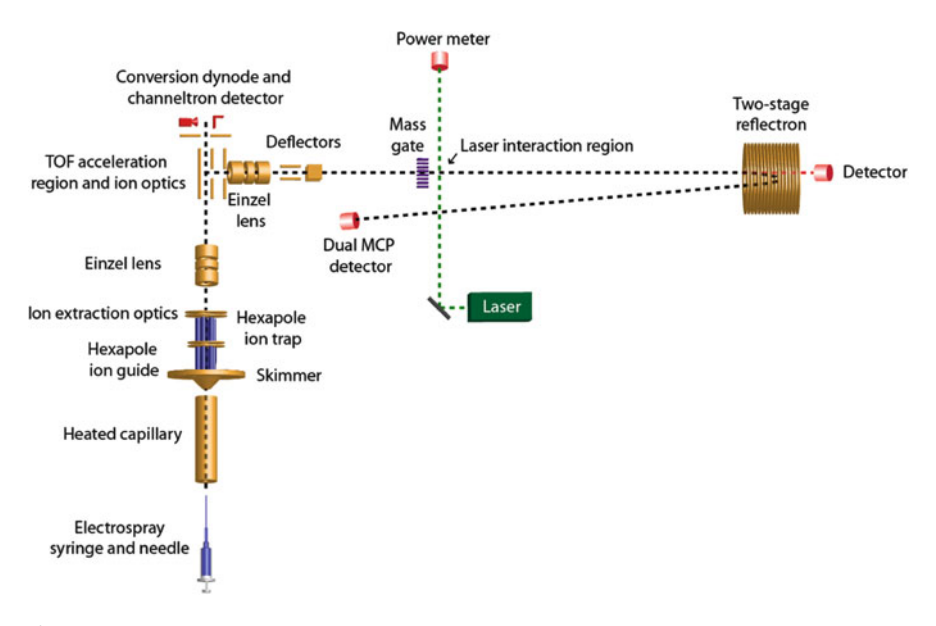


Fig. 3.16 Schematic of the reflectron time-of-flight mass spectrometer coupled to an electrospray ionisation source and laser at Boulder [25]

3.1.4 Dissociation in an Electric Field

Ionic dissociation can be studied in an electric field (Fig. 3.17). In the illustrated apparatus, ions are produced, bunched and accelerated, after which they are deflected along a new trajectory in order to remove any generated neutrals. The bunch is subsequently trapped in a Zaifman trap (see below), extracted and accelerated from a potential of V_0 . Neutral products are unaffected by the following 45° electrostatic parallel-plate analyser and detected on a position sensitive detector (PSD), while ions are deflected and identified on another PSD. Photoexcitation is performed in either the ion trap or the following interaction region, depending on the fragmentation time scale of interest. This interaction region is set at a higher potential than V_0 , in order to differentiate the fast fragmentation which occurs inside the region from that which occurs outside. Neutral fragments resulting from CID can be excluded as their arrival times will depend on the parent ion velocities during fragmentation. Experiments monitor single fragmentation events in order to determine the number of fragmentation steps involved and are repeated with different settings as only fragment ions within a narrow mass window $(\Delta m \approx 10 \text{ amu})$ can be detected for each setting.

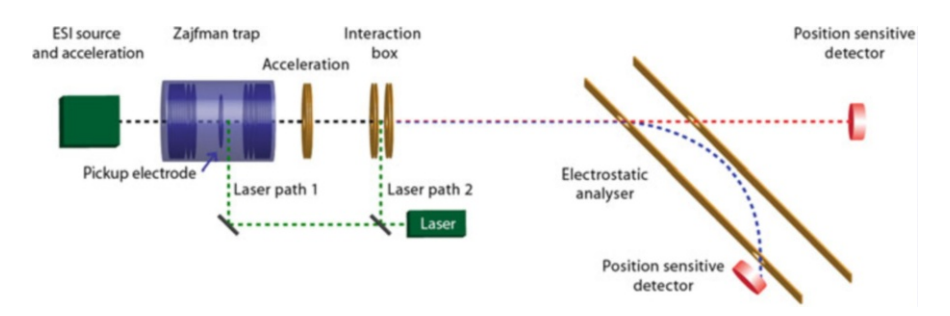


Fig. 3.17 Schematic of the apparatus at Orsay used to study dissociation in an electric field [26]

3.1.5 The Zajfman Trap

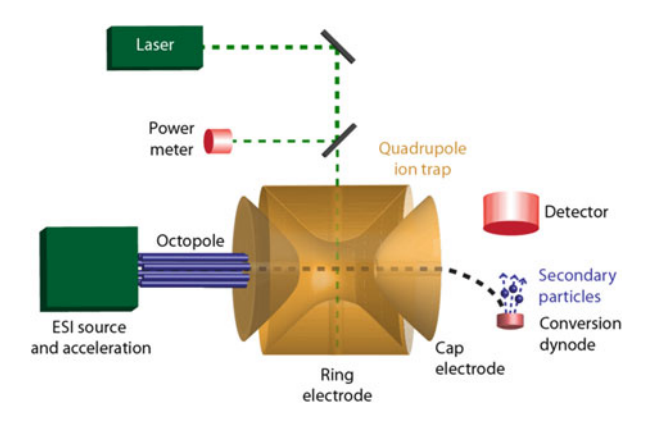
The Zajfman trap [27] depicted in Fig. 3.17 consists of two identical cylindrically symmetric electrostatic mirrors comprised of eight electrodes, which trap ions along the longitudinal direction and focus them transversally. Ions are allowed to enter the trap when the entrance mirror voltages are switched off. The electrode potentials then force them to oscillate resonantly within the trap where they can be monitored by measuring the image charge induced on a ring "pickup" electrode located in the field-free region between the two cylindrical electrodes. The resulting signal can be analysed with a Fourier transform in order to determine the ion masses. In photofragmentation experiments, the produced neutrals can be detected on a detector located after the trap each time the ion bunch moves in a forward direction. By monitoring this signal over time, the fragmentation lifetimes can be determined.

3.1.6 Quadrupole Ion Trap

Another experimental apparatus where spectroscopic experiments can be performed is a quadrupole ion trap (Fig. 3.18). For information on standard ion traps please see [29, 30]. In the portrayed setup, ions are generated by electrospray, mass selected using an octopole and injected into the trap. There, ions are cooled due to the presence of a buffer gas and stored by applying alternating frequencies on the ring electrode and end caps. The ions of interest are then isolated by ejecting all other ions from the trap (resonant excitation). Holes through the ring electrode allow the trapped ions to be irradiated by a tuneable laser, after which all ions are ejected from the trap and analysed.

As the trap is normally filled with helium buffer gas, dissociation has to occur before the ions are cooled down internally in collisions with helium atoms. This implies that for long dissociation times (tens of microseconds) that multiple absorption steps are needed for dissociation even though the energy of a single photon is above the dissociation barrier, which complicates the analysis.

Fig. 3.18 Schematic of the Quadrupole ion trap at the University of Lyon [28]



3.2 Fluorescence Measurements

In the previous section, apparatus used to obtain action spectra were discussed, and it was mentioned that these action spectra are often taken to be equivalent to absorption spectra. However, as fluorescence is a possible relaxation pathway for some excited molecules, and its quantum yield may be wavelength dependent, fluorescent measurements are necessary to acquire a true absorption spectrum. Fluorescence experiments are superior to action spectroscopy ones as only one photon need be absorbed, and there are no kinetic shifts to be concerned about as dissociation is not sampled. However, a true measurement should detect all emitted photons, and in reality only a limited emission angle is sampled due to physical constraints. Furthermore, extremely sensitive photon detectors are required due to the low number of emitting ions, and scattered light and ambient light consequently become a problem. Different experimental apparatus used for fluorescence measurements are discussed in the following.

3.2.1 Fluorescence Measurements in a Quadrupole Ion Trap

One instrument that can be used to conduct fluorescence experiments is a quadrupole ion trap (Fig. 3.19). In the depicted instrument, ions are generated by electrospray, and injected into the trap (*vide supra*) which has a stretched configuration. There, ions of interest are isolated, heated/cooled to the desired temperature (90–650 K) in the presence of a buffer gas (He, Ne or Ar *ca.* 10⁻³ mbar), and excited by a continuous wave (CW) laser synchronised with the experiment. During irradiation the buffer-gas pressure is increased (0.02–0.2 mbar) to ensure that any residual energy deposited into the ions by consecutive absorption and fluorescence cycles can be transferred to the buffer gas via collisions. To diminish scattered light a Brewster window and set of baffle stacks are located on both sides of the trap. Fluorescent light is collected by an infinity-corrected microscope objective and

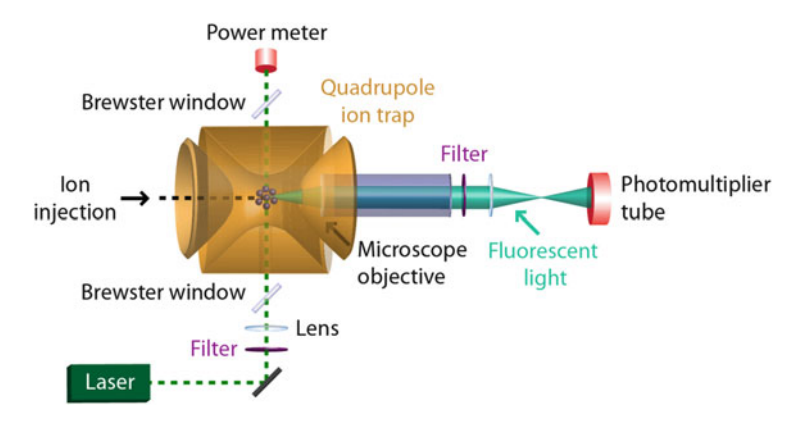


Fig. 3.19 Fluorescence measurements can be conducted in a quadrupole ion trap coupled to a fluorescence microscope, such as the instrument in Karlsruhe, Germany [31]

passed through a filter to remove scattered light before detection. After irradiation, the buffer gas is pumped away, and the ions in the trap are ejected and analysed using a dynode/channeltron assembly (not shown).

Note, the use of a CW laser limits the wavelengths which can be studied. Furthermore, the energy of the ion is not strictly defined as ions can absorb and fluoresce multiple times. Absorption by daughter ions also affects the results.

3.2.2 Fluorescence Measurements in an FT-ICR

Another instrument in which fluorescence experiments can be performed is a Fourier-Transform Ion Cyclotron Resonance (FT-ICR) instrument [32]. At the FT-ICR instrument in Zurich (Fig. 3.20) [33], ions are produced by electrospray ionisation, mass selected using hexapole filters, and stored in an ICR cell which is enclosed in a 4.7-T superconducting magnet (Penning trap). Fluorescent light emitted by the ions after irradiation by a CW laser is detected and the photoproducts determined: The ICR cell is comprised of two excitation elements, two detection elements, and two trapping plates for axial trapping. The uniform magnetic field, **B**, provided by the superconducting magnet induces ions to move along circular paths in a perpendicular plane (radial trapping). The frequency of this motion is known as the cyclotron frequency, ω_c , and depends on the mass-to-charge ratio of the ion: $\omega_c = (q/m) B (q = z e)$. Ions of a specific m/q are excited to a higher orbit by applying a uniform electric field oscillating at ω_c on the excitation elements, and can be detected by measuring the image charge induced on the detection plates over time. Excitation of all the ions can be effected almost simultaneously (by scanning the excitation voltages), and as the frequency of oscillation is proportional to mass, by applying a Fourier transform to the data, a mass spectrum of the ions can be found. Such spectra obtained from FT-ICR instruments have a very high mass resolution as kinetic energies are not measured. It should be noted that the actual

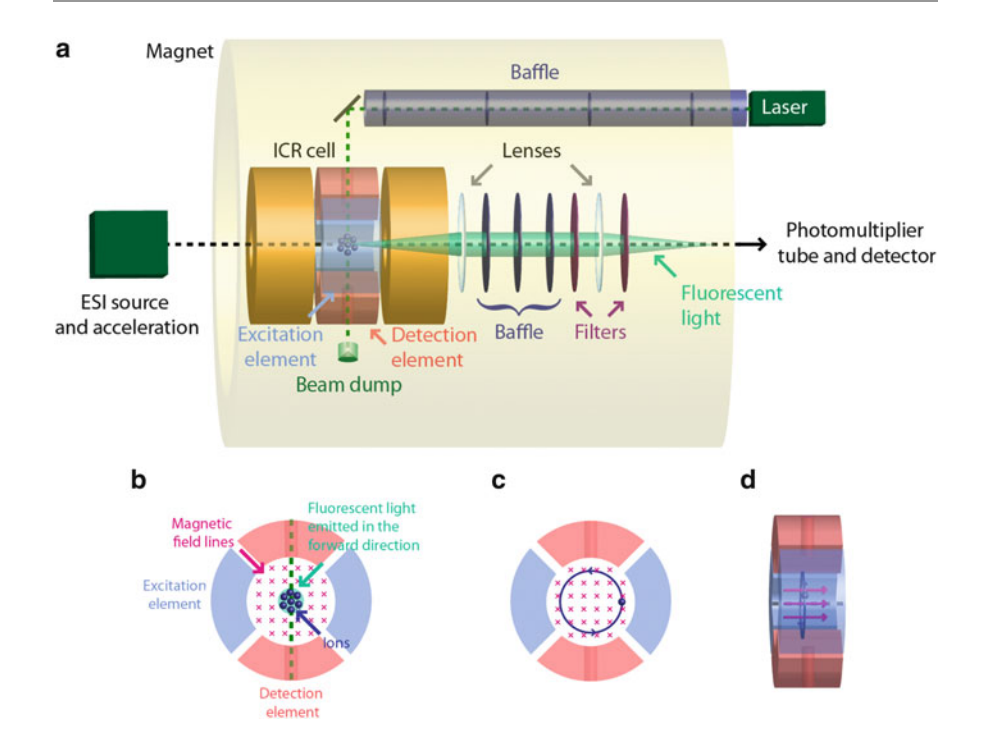


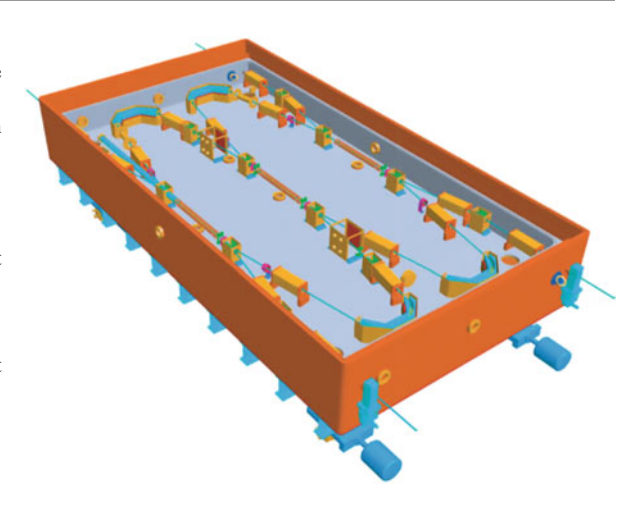
Fig. 3.20 (a) Schematic of the FT-ICR instrument at ETH Zurich configured for fluorescence experiments [33]. As fluorescence experiments are extremely sensitive to light, scattered light is prevented from reaching the detector by the use of several baffle systems, filters and a conical beam dump. Ions are irradiated while in the trap, and induced fluorescent light emitted in the forward direction detected. (b) Enlarged view of the ICR cell (front view). (c) Enlarged view of the ICR cell (front view) indicating that in order to obtain a mass spectrum ions (here positive) are excited to larger orbits where they can be detected as they revolve in the trap. (d) Side view of (c)

motion of an ion within the trap is more complicated than described above due to the axial trapping in the electric field which introduces a second radial motion called magnetron motion that occurs at another frequency.

3.3 Cryogenically Cooled Instruments

Spectroscopy experiments on biomolecular ions have primarily been performed at room temperature. However, vibrational fine structure is often hidden in absorption spectra for room-temperature ions, and instead broad bands are seen. Hence, spectra from cold ions which display less spectral congestion would provide better benchmarks for theory. Such spectra also probe the lifetimes of the excited states, with broad bands indicating a short excited-state lifetime (*cf.*, Heisenberg's uncertainty principle). This is a direction which is currently being pursued, with instruments under construction in Heidelberg [34], Stockholm (Fig. 3.21) [19],

Fig. 3.21 The double electrostatic ion beam storage ring (DESIREE) in Stockholm [35]. An ion beam of one charge is injected into one ring, while one of opposite charge is injected into the other. The beams merge in the common straight central section and their interaction studied. The inner vacuum chamber and electrostatic elements are kept at cryogenic temperature. Figure kindly provided by Henrik Cederquist (Stockholm University)



and Tokyo [36]. The black-body radiation is significantly reduced at a few Kelvin, and the ions will ascertain the trap temperature by radiative cooling after some time.

3.4 Summary

It is important to remember that different instruments are ideal for studying certain molecular ions and processes. Storage rings for example are beneficial when dissociation occurs on the tens of microseconds to tens of milliseconds time scale while for faster dissociation, single-pass instruments like accelerator mass spectrometers and reflectron time-of-flight instruments are sufficient. Hence spectroscopy of weakly bound complexes, *e.g.*, microsolvated ions, is most easily done with the latter-type instruments. In general, experiments on high-keV ions have the advantage that the fragments have high kinetic energies, and both ions and neutrals can easily be detected.

If high mass resolution is required, ion traps where the measurements do not rely on ion velocity, such as Penning traps, are superior. However, time-resolved experiments cannot easily be done on the tens of microseconds time scale with an FT-ICR instrument as cyclotron frequencies are too small for enough cycles in the time window to do a proper Fourier transform of the time spectrum to a frequency spectrum (mass-to-charge spectrum). This time scale is therefore best investigated with storage-ring instruments or the Zajfman trap.

In general dissociation on a long time scale (tens of milliseconds) is problematic as radiative cooling can quench the dissociation. Multiple photon absorption can therefore be required to observe dissociation within the sampling time. Furthermore, when the dissociation time scale is long, it is particularly important to be aware of kinetic shifts as the identification of low-energy photon absorption is disfavoured when the dissociation is sampled in a finite time window. In ion traps

where helium buffer gas is present another issue to consider is cooling by collisions which can result in complicated power dependencies.

While action spectroscopy of positive ions requires dissociation, electron loss can be the action channel for negative ions. This circumvents the problem associated with spectroscopy of large biomolecular ions where one photon hardly changes the internal energy per degree of freedom. Prompt dissociation of large molecular ions occurring on the excited-state potential energy surface can be another way to identify that photon absorption has occurred, but this is of course very much limited to certain ions and is a less general approach. These fast dissociation processes can be explored by photoexcitation of ions in an electric field as fragment ions formed in the field region will have different kinetic energies than those formed outside. Ion-beam depletion experiments with storage rings also shed light on the importance of such fast dissociation processes.

When it comes to fluorescence experiments, ion traps are the instruments of choice. The difficulty is to detect enough emitted light but recent developments have shown that this is indeed possible.

Finally, electronic spectroscopy of cold biomolecular ions is in its infancy but is likely to be an intense research field within the next years, particularly due to the construction of new state-of-the-art instruments.

References

- Fenn, J.B., Mann, M., Meng, C.K., Wong, S.F., Whitehouse, C.M.: Electrospray ionization for mass-spectrometry of large biomolecules. Science 246, 64–71 (1989)
- Karas, M., Bachmann, D., Hillenkamp, F.: Influence of the wavelength in high-irradiance ultraviolet-laser desorption mass-spectrometry of organic-molecules. Anal. Chem. 57, 2935–2939 (1985)
- 3. Tanaka, K., Waki, H., Ido, Y., Akita, S., Yoshida, Y., Yoshida, T., Matsuo, T.: Protein and polymer analyses up to m/z 100 000 by laser ionization time-of-flight mass spectrometry. Rapid Commun. Mass Spectrom. 2, 151–153 (1988)
- 4. Panja, S., Kadhane, U., Andersen, J.U., Holm, A.I.S., Hvelplund, P., Kirketerp, M.B.S., Brøndsted Nielsen, S., Støchkel, K., Compton, R.N., Forster, J.S., Kilsa, K., Nielsen, M.B.: Dianions of 7,7,8,8-tetracyano-p-quinodimethane and perfluorinated tetracyanoquino-dimethane: Information on excited states from lifetime measurements in an electrostatic storage ring and optical absorption spectroscopy. J. Chem. Phys. 127, 124301 (2007)
- Støchkel, K., Wyer, J.A., Kirketerp, M.B.S., Brøndsted Nielsen, S.: Laser pump-probe experiments on microsecond to millisecond timescales at an electrostatic ion storage ring: triplet-triplet absorption by protoporphyrin-IX anions. J. Am. Soc. Mass Spectrom. 21, 1884–1888 (2010)
- Andersen, J.U., Cederquist, H., Forster, J.S., Huber, B.A., Hvelplund, P., Jensen, J., Liu, B., Manil, B., Maunoury, L., Brøndsted Nielsen, S., Pedersen, U.V., Schmidt, H.T., Tomita, S., Zettergren, H.: Power-law decay of collisionally excited amino acids and quenching by radiative cooling. Eur. Phys. J. D 25, 139–148 (2003)
- Rosenstock, H.M., Wallenstein, M.B., Wahrhaftig, A.L., Eyring, H.: Absolute rate theory for isolated systems and the mass spectra of polyatomic molecules. Proc. Natl. Acad. Sci. USA. 38, 667–678 (1952)

- Lykkegaard, M.K., Zettergren, H., Kirketerp, M.-B.S., Ehlerding, A., Wyer, J.A., Kadhane, U., Brøndsted Nielsen, S.: Photodissociation of isolated ferric heme and heme-His cations in an electrostatic ion storage ring. J. Phys. Chem. A 113, 1440–1444 (2009)
- Calvo, M.R., Andersen, J.U., Hvelplund, P., Brøndsted Nielsen, S., Pedersen, U.V., Rangama, J., Tomita, S., Forster, J.S.: Photophysics of protoporphyrin ions in vacuo: triplet-state lifetimes and quantum yields. J. Chem. Phys. 120, 5067–5072 (2004)
- Wyer, J.A., Ehlerding, A., Zettergren, H., Kirketerp, M.-B.S., Brøndsted Nielsen, S.: Tagging of protonated Ala-Tyr and Tyr-Ala by crown ether prevents direct hydrogen loss and proton mobility after photoexcitation: importance for gas-phase absorption spectra, dissociation lifetimes, and channels, J. Phys. Chem. A 113, 9277–9285 (2009)
- Antoine, R., Dugourd, P.: Visible and ultraviolet spectroscopy of gas phase protein ions. Phys. Chem. Chem. Phys. 13, 16494–16509 (2011)
- Raevsky, O.A., Solovev, V.P., Solotnov, A.F., Schneider, H.J., Rudiger, V.: Conformation of 18-crown-5 and its influence on complexation with alkali and ammonium cations: Why 18crown-5 binds more than 1000 times weaker than 18C6. J. Org. Chem. 61, 8113–8116 (1996)
- Julian, R.R., Beauchamp, J.L.: Site specific sequestering and stabilization of charge in peptides by supramolecular adduct formation with 18-crown-6 ether by way of electrospray ionization. Int. J. Mass Spectrom. 210, 613–623 (2001)
- Wysocki, V.H., Tsaprailis, G., Smith, L.L., Breci, L.A.: Special feature: Commentary Mobile and localized protons: a framework for understanding peptide dissociation. J. Mass Spectrom. 35, 1399–1406 (2000)
- Wysocki, V.H., Resing, K.A., Zhang, Q.F., Cheng, G.L.: Mass spectrometry of peptides and proteins. Methods 35, 211–222 (2005)
- Brøndsted Nielsen, S., Andersen, J.U., Forster, J.S., Hvelplund, P., Liu, B., Pedersen, U.V., Tomita, S.: Photodestruction of adenosine 5'-monophosphate (AMP) nucleotide ions in vacuo: Statistical versus nonstatistical processes. Phys. Rev. Lett. 91, 048302 (2003)
- Møller, S.P.: ELISA, and electrostatic storage ring for atomic physics. Nucl. Instrum. Methods Phys. Res. A 394, 281–286 (1997)
- Andersen, J.U., Hvelplund, P., Brøndsted Nielsen, S., Tomita, S., Wahlgreen, H., Møller, S.P., Pedersen, U.V., Forster, J.S., Jørgensen, T.J.D.: The combination of an electrospray ion source and an electrostatic storage ring for lifetime and spectroscopy experiments on biomolecules. Rev. Sci. Instrum. 73, 1284–1287 (2002)
- Støchkel, K., Kadhane, U., Andersen, J.U., Holm, A.I.S., Hvelplund, P., Kirketerp, M.B.S., Larsen, M.K., Lykkegaard, M.K., Brøndsted Nielsen, S., Panja, S., Zettergren, H.: A new technique for time-resolved daughter ion mass spectrometry on the microsecond to millisecond time scale using an electrostatic ion storage ring. Rev. Sci. Instrum. 79, 023107 (2008)
- Kadhane, U., Andersen, J.U., Ehlerding, A., Hvelplund, P., Kirketerp, M.B.S., Lykkegaard, M. K., Brøndsted Nielsen, S., Panja, S., Wyer, J.A., Zettergren, H.: Photodissociation of protonated tryptophan and alteration of dissociation pathways by complexation with crown ether. J. Chem. Phys. 129, 184304 (2008)
- Kirketerp, M.B.S., Ryhding, T., Støchkel, K., Nielsen, M.B., Brøndsted Nielsen, S.: Role of nearby charges on the electronic structure of pi-conjugated molecules: symmetric versus asymmetric charge distributions in Oligo(p-phenyleneethynylene). J. Phys. Chem. A 115, 1222–1227 (2011)
- Stochkel, K., Milne, B.F., Nielsen, S.B.: Absorption spectrum of the firefly luciferin anion isolated in vacuo. J. Phys. Chem. A 115, 2155–2159 (2011)
- Wyer, J.A., Nielsen, S.B.: Absorption by isolated ferric heme nitrosyl cations in vacuo. Angew. Chem. Int. Ed. 51, 10256–10260 (2012)
- Johnson, M.A., Lineberger, W. C. p. 591. In: Farrar, J. M., Saunders, W. (eds.) Techniques for the Study of Gas-Phase Ion Molecule Reactions. Wiley, New York. (1988)
- Marcum, J.C., Halevi, A., Weber, J.M.: Photodamage to isolated mononucleotidesphotodissociation spectra and fragment channels. Phys. Chem. Chem. Phys. 11, 1740–1751 (2009)

Lepere, V., Lucas, B., Barat, M., Fayeton, J.A., Picard, V.J., Jouvet, C., Carcabal, P., Nielsen, I., Dedonder-Lardeux, C., Gregoire, G., Fujii, A.: Comprehensive characterization of the photodissociation pathways of protonated tryptophan. J. Chem. Phys. 127, 134313 (2007)

- Dahan, M., Fishman, R., Heber, O., Rappaport, M., Altstein, N., Zajfman, D., van der Zande, W.J.: New type of electrostatic ion trap for storage of fast ion beams. Rev. Sci. Instrum. 69, 76–83 (1998)
- 28. Talbot, F.O., Tabarin, T., Antoine, R., Broyer, M., Dugourd, P.: Photodissociation spectroscopy of trapped protonated tryptophan. J. Chem. Phys. 122, 074310 (2005)
- March, R.E.: An introduction to quadrupole ion trap mass spectrometry. J. Mass Spectrom. 32, 351–369 (1997)
- Douglas, D.J., Frank, A.J., Mao, D.M.: Linear ion traps in mass spectrometry. Mass Spectrom. Rev. 24, 1–29 (2005)
- Kordel, M., Schooss, D., Neiss, C., Walter, L., Kappes, M.M.: Laser-induced fluorescence of Rhodamine 6G cations in the gas phase: a lower bound to the lifetime of the first triplet state. J. Phys. Chem. A 114, 5509–5514 (2010)
- Comisarow, M.B., Marshall, A.G.: Fourier-transform ion-cyclotron resonance spectroscopy. Chem. Phys. Lett. 25, 282–283 (1974)
- Chingin, K., Chen, H.W., Gamez, G., Zenobi, R.: Exploring fluorescence and fragmentation of ions produced by electrospray ionization in ultrahigh vacuum. J. Am. Soc. Mass Spectrom. 20, 1731–1738 (2009)
- 34. von Hahn, R., Berg, F., Blaum, K., Lopez-Urrutia, J.R.C., Fellenberger, F., Froese, M., Grieser, M., Krantz, C., Kuhnel, K.U., Lange, M., Menk, S., Laux, F., Orlov, D.A., Repnow, R., Schroter, C.D., Shornikov, A., Sieber, T., Ullrich, J., Wolf, A., Rappaport, M., Zajfman, D.: The electrostatic cryogenic storage ring CSR mechanical concept and realization. Nucl. Instrum. Methods Phys. B 269, 2871–2874 (2011)
- 35. Schmidt, H.T., Johansson, H.A.B., Thomas, R.D., Geppert, W.D., Haag, N., Reinhed, P., Rosen, S., Larsson, M., Danared, H., Rensfelt, K.G., Liljeby, L., Bagge, L., Bjorkhage, M., Blom, M., Lofgren, P., Kallberg, A., Simonsson, A., Paal, A., Zettergren, H., Cederquist, H.: DESIREE as a new tool for interstellar ion chemistry. Int. J. Astrobiol. 7, 205–208 (2008)
- 36. Jinno, S., Takao, T., Omata, Y., Satou, A., Tanuma, H., Azuma, T., Shiromaru, H., Okuno, K., Kobayashi, N., Watanabe, I.: TMU electrostatic ion storage ring designed for operation at liquid nitrogen temperature. Nucl. Instrum. Methods A 532, 477–482 (2004)

Marius Wanko and Angel Rubio

Abstract

The description of the electronic structure of molecules in the excited state is usually more involved than the calculation of ground-state properties. The development of approaches to calculate optical properties of chromophores, including their specific interactions with a complex environment is a very active field of research. This chapter gives an overview of quantum mechanical methods and schemes to integrate them into a multi-scale description of extended systems that contain an optically active center. Special attention is paid to the problems and limitations of quantum methods that are commonly used to describe excited-state properties of biological chromophores.

4.1 Introduction

There are two main goals in computational modelling of biochromophores and their characterisation in terms of theoretical spectroscopy. The first is to propose atomistic structural models where structural information from experiments is limited. Often it is difficult to produce 3D crystals of the active state of proteins, in particular of mutants that prohibit oligomerisation. Short-lived intermediates that cannot be trapped thermally can be identified from time-resolved spectroscopy, but structural information from these experiments is limited and the interpretation ambiguous. Lacking hydrogen atoms and mobile waters, x-ray crystallographic structures often lack information about the protonation state of titratable amino acid residues and their role in hydrogen-bonded networks (HBN) and electrostatic interactions. All these issues are readily addressed by computational approaches

Nano-Bio Spectroscopy Group and ETSF Scientific Development Centre, Departamento de Física de Materiales, Centro de Física de Materiales CSIC-UPV/EHU-MPC and DIPC, Universidad del País Vasco, Av. Tolosa 72, 20018 San Sebastián, Spain

e-mail: marius.wanko@gmail.com; angel.rubio@ehu.es

M. Wanko (⋈) • A. Rubio

46 M. Wanko and A. Rubio

once a convincing structural model is obtained and validated. The latter can be achieved by simulating any spectroscopic features, such as UV-Vis, IR, or NMR, for which experimental data is available. Care must be taken not to overrate the agreement between experimental and theoretical data, which can be due to error cancellation or due to correlation between observables. The retinal chromophore of rhodopsin (Rh) provides an example of a strong correlation between the C=C stretching frequency of a charged conjugated chain and its UV-Vis absorption maximum [1]. Therefore, both properties show the same response to electrostatic perturbation of the chromophore, they essentially probe the potential difference between the two ends of the conjugated system and yield redundant information [2]. Further assessment can be achieved by direct comparison between xray and theoretical structure. The validation power of these tests can be amplified by combining them with site-directed mutation experiments or extended molecular dynamics (MD) simulations (see Sect. 4.4).

The second benefit of theoretical approaches is to provide a physical explanation for the observed spectral features. They can be related to individual structural features or to electrostatic or steric interactions between the chromophore and its molecular environment. Quantum chemical calculations can reveal the individual contributions of geometric changes, electrostatic interactions with charged, polar, or polarisable groups, the effect of dispersive interactions or charge transfer and delocalisation. These aspects will be discussed in Sect. 4.3.

The great challenge for computational approaches is to capture the essential physics involved in the observed features of the chromophore and to correctly describe their response to perturbations from the environment. As the electronically excited state is involved, this remains one of the critical points in theoretical predictions and it is important to consider the influence of the employed quantum mechanical (QM) methods on the results. In particular, it is essential to know whether or not error cancellation can be assumed for a specific property, which is often necessary to predict small effects, like frequency shifts due to mutation or structural changes. This topic will be addressed for individual classes of quantum chemical methods in Sect. 4.2.

4.2 OM Methods

The demands to be met by the QM method include the qualitative correct response of the calculated property (e.g., spectroscopic features) to any kind of external perturbation that may affect this property. These can be grouped as follows: (1) geometric distortions (in particular bonds lengths, rotation of single and double bonds), (2) electrostatic polarisation (by H-bonds, counter ions, charged and close-by polar groups), (3) exchange of charge density (mainly across H-bonds), and (4) dispersion redshift in presence of vicinal highly polarisable groups. (1)–(4) imply different demands on the employed QM methods and it is essential knowledge to which extend commonly used approaches meet them, or show systematic errors. The low-lying electronic valence states of ionic chromophores typically involve

considerable charge transfer upon excitation, as they include groups that have different electron affinities (EA) and ionisation energies (IE) in the gas phase and are coupled via conjugated parts. In so-called charge-transfer (CT) systems, an electron donating group may transfer electron density to an acceptor group upon excitation. The charge localisation in the ground state and the excitation-induced charge transfer can considerably depend on the geometry and the employed QM method. This can be rationalised for a given system in terms of the involved resonance structures. The contribution of these resonances to the ground and excited state determines both charge localisation and bond length alternation of the minimum energy structure in the respective electronic state. The balance between different valence bond structures often strongly depends on the description of electron correlation by the QM method, and, in the case of time-dependent density functional theory (TDDFT), on the employed density functional. In the following, we will discuss the advantages and typical shortcomings of the most commonly used QM methods and the resulting performance in the description of perturbations of the kind (1)-(4). Moreover, the description of photochemical properties requires an analysis of the excited-state potential energy surface (PES). Already the qualitatively correct description of the excited-state PES, i.e., its topology in terms of minima, conical intersections and transition states, represents a major challenge for state-of-the-art quantum chemical methods. This will be discussed in Sects. 4.2 and 4.4.

4.2.1 TDDFT

The extension of density functional theory (DFT) to the time domain [3] provides access to excited-state properties. If the ground state is perturbed by an external field of the form $v_{\rm ext}(t) = x\delta(t-t_0)$ (small instantaneous kick), the perturbed density can be propagated in time following the time-dependent Kohn-Sham equations. The absorption spectrum can then be obtained from the Fourier transformed dipole moment. This approach is useful to calculate the spectrum within a large energy window, e.g., beyond the ionisation threshold, and for large systems (high density of states), where linear scaling of cpu time vs. system size can easily be achieved [4]. The more common approach is to solve analytically the linear-response problem in a basis of molecular orbitals to obtain a limited number of excited states [5]. This leads to the solution of a pseudo-eigenvalue problem for the excitation energies ω_l which are associated with the poles of the dynamic polarisability of the Kohn–Sham model system:

$$\Omega \mathbf{F}_I = \omega_I^2 \mathbf{F}_I,\tag{4.1}$$

where Ω is the response matrix, which for closed-shell systems (indices i, j and a, b refer to occupied and virtual orbitals, respectively) is

$$\mathbf{\Omega}_{ia,jb} = \delta_{ij}\delta_{ab}\mathbf{\omega}_{jb}^2 + 2\sqrt{(n_i - n_a)\mathbf{\omega}_{ia}}\mathbf{K}_{ia,jb}\sqrt{(n_j - n_b)\mathbf{\omega}_{jb}}.$$
 (4.2)

The first term contains the Kohn–Sham eigenvalue differences $\omega_{ia} = \varepsilon_a - \varepsilon_i$. The second term contains the coupling matrix K, which gives a correction to the diagonal terms that causes a singlet–triplet splitting and off-diagonal elements that are responsible for the mixing of the single-particle transitions. For the singlet case it reads

$$K_{ia,jb} = \int \int \phi_i(r)\phi_a(r) \left(\frac{1}{|r-r'|} + \frac{\delta^2 E_{xc}}{\delta \rho(r)\delta \rho(r')}\right) \phi_j(r')\phi_b(r') dr dr'$$
(4.3)

The approach also grants access to transition properties, analytical derivatives of the excitation energy, the excited-state density matrix, and derived observables, like the excited-state charge distribution and dipole moment [6, 7]. Although time-dependent DFT (TDDFT), is an exact method in principle, the unknown exchange-correlation (XC) potential, a unique functional of the density, must be approximated in practice, which determines the accuracy of the method. Approximate functionals can be grouped into classes that use similar analytical forms and behave in a similar way when applied to situations where large errors are expected. Functionals that employ the local density approximation (LDA), generalised gradient approximation (GGA), or higher-order gradient corrections to LDA (meta GGA), are usually applied to TDDFT using the adiabatic approximation, i.e., approximating the XC potential by a local functional in time $v_{xc}^{adia}(t) - v_{xc}^{LDA}[\rho(t)]$, i.e., simply evaluate the analytical density functional with the time-dependent density $\rho(t)$. This approximation has well known shortcomings, which must be kept in mind when applying this method. They shall be discussed in the following.

DFT with local density functionals (LDA, GGA, meta-GGA) breaks down if the ground state involves strong static correlation, i.e., when wave-function-based methods describe the ground-state as multi-configurational, with significant contributions from excited configurations [8–11]. This case is associated with the triplet instability [9, 12, 13], i.e., the total energy can be lowered by breaking spin symmetry. In regions of the nuclear configuration space close to triplet instabilities or in the vicinity of conical intersections between ground and excited state, the lowest excitation energy can be drastically underestimated by TDLDA. Moreover, the shape of the PES close to conical intersections between the ground and first excited state can be qualitatively wrong. Within the two-dimensional branching space, which is created by the nonadiabatic coupling vector and the gradient difference vector, the latter is often described artificially large or reaches zero, in which case the dimensionality of the branching space appears to be reduced to one [14].

Another problem is the general underestimation of the ionisation energy, which originates from the wrong asymptotic shape of the XC potential of LDA, which decays exponentially, whereas the exact Kohn–Sham potential decays like -1/r

[15, 16]. Also GGA potentials decay too fast in the asymptotic region, e.g., like $-c/r^2$ [9]. As a consequence, artificial Rydberg states appear in the spectrum of finite (LCAO) basis set calculations and are unbound in the basis set limit. Asymptotic correction schemes have been proposed that recover the Rydberg series without changing the spectrum of valence excitations, but they require an experimental or estimated values for the IE as input [16–18].

A more challenging problem for the adiabatic approximations to TDDFT are charge-transfer (CT) excitations, in which an electron is promoted from a donor to an acceptor orbital that is located in a different region of the system. Excitations with partial CT character are most common in organic dyes, biological chromophores and of particular interest for applications in dye-sensitised solar cells. In these systems, the donor and acceptor states are coupled and their wave functions overlap to create a large transition dipole moment. Depending on the spatial separation of donor and acceptor states, adiabatic approximations drastically underestimate such transitions. The problem is best understood for the case of non-overlapping donor/acceptor orbitals that are located on two separate molecules [19]. In this case, the product $\phi_i(r)\phi_n(r)$ vanishes in Eq. (4.3) and the excitation energy of the CT transition reduces to the difference of the Kohn–Sham energy levels, e.g., $\varepsilon_{\text{LUMO}}^{\text{acceptor}} - \varepsilon_{\text{HOMO}}^{\text{donor}}$. The exact excitation energy, for infinite distance R between the molecules, would be the difference between the IE of the donor and the EA of the acceptor site. If asymptotically corrected potentials are used, $-\varepsilon_{\rm HOMO}^{\rm donor}$ indeedapproximates the exact IE, but $\varepsilon_{\rm LUMO}^{\rm acceptor}$ does not approximate the EA of the acceptor, unlike in Hartree–Fock (HF) theory, because of the missing XC part of the derivative discontinuity of the energy with respect to the particle number [20]. This leads to a drastic underestimation of CT excitations by common density functionals. At finite separation R between the molecules, the energy of the CT excited state is lowered by the Coulomb attraction between the hole created on the donor and the excess electron on the acceptor, and additional higher-order polarisation terms. In time-dependent HF, or configuration interaction singles (CIS), which is the same for CT states, the particle-hole term is included in the response calculation due to the non-local exchange operator. In TDDFT, the exact XC kernel diverges with vanishing overlap of the donor/acceptor orbitals [21], which is not described by common density functionals. Therefore, the latter lack the correct 1/R asymptotic behavior of CT transitions.

The underestimation of CT excitations by local density functionals within the adiabatic approximation to TDDFT has two important implications. (1) When the QM system is extended to include parts of the environment (solvent, protein, or a surface), the spectrum of valence excitations on the chromophore can be messed up by a multitude of artificially low CT excitations that appear in the same energy region. Although these are expected to couple weakly with the long-range CT excitations, they tend to mix strongly with the latter when the energy difference is small [22, 23]. (2) In general, the amount of CT character depends on the geometry and can vary substantially along certain reaction coordinates. Therefore, the excited-state PES can be distorted such that reaction pathways towards structures that enhance the CT character are energetically favoured [24].

The problems with CT excitations are alleviated but not solved by partially substituting the DFT exchange by nonlocal HF exchange. Using such hybrid functionals, the dependency of excitation energies on the amount of HF exchange represents a good test for the validity of the results. An *a priori* criterion has been proposed by Peach et al. [25]. To completely eliminate the problem, range-separated hybrid methods have been proposed [26], which evaluate exchange integrals using the short-range part of a local density functional and combine it with the long-range part of HF exchange. Known as Coulomb-attenuation method (CAM) [27] or long-range corrected (LC) functionals [28], this approach has been shown to produce accurate results for CT, Rydberg, and local excitations [29–31].

4.2.2 Single-Reference Methods

Single-reference methods use the HF wave function as a starting point to describe electron correlation. Although variational methods based on truncated configuration interaction (CI) expansions are in principal more robust than many-body perturbation theory (MBPT), they are not size-extensive, i.e., total energies are not size consistent. For example, the energy of two separated molecules is not the sum of the monomer energies. Coupled-cluster methods pursue the goal to be both size-extensive and achieve a faster convergence towards the full-CI limit. Excitation energies are obtained from linear-response or equation-of-motion (EOM) theory. In analogy to the CI series, including singles, doubles, triples, etc. excitations (CIS, CISD, CISDT, ...), they build a hierarchy towards full-CI: CCS, CC2, CCSD, CC3, CCSDT, ... [32]. Their scaling with system size N is to the power of 4, 5, 6, 7, 8, respectively. For most applications to larger molecules, CC2 and CCSD are the methods of choice nowadays, while CC3 is feasible for smaller dyes. The accuracy of excitation energies depends on the character of the excited state. For excited states that are dominated by single excitations, CC2 gives energies that are correct to second order and competes well with CCSD [33]. For states with strong contributions of double excitations, CCSD is the lowest level of theory that is applicable. Efficient parallelised implementations of CC2 make this method attractive as an alternative to TDDFT [34]. The performance is usually superior for local valence excitations and describes CT and Rydberg excitations reasonably well [33, 35, 36]. In close vicinity to state crossings, EOM-CC methods produce artifacts in the PES due to their non-Hermiticity, which may cause problems in the optimisation of conical intersection seams [37].

4.2.3 Multi-Reference Methods

The idea of multi-reference methods is to substitute the HF reference wave function in single-reference methods by a (small) multiconfigurational one to achieve a qualitative description of ground and excited states. The remaining part of the correlation, referred to as dynamic correlation, is described by extending the

interacting space using truncated CI (MRCI), coupled-cluster theory (MRCC), or perturbation theory (MRPT). The latter requires the reference to already include all important configurations such that the perturbations are small. The most prominent version is the CASPT2 method, which employs a complete active space self-consistent field (CASSCF) reference. The CASSCF wave function uses a full-CI expansion for a limited set of "active" orbitals, the "inactive" orbitals are doubly occupied or unoccupied. The energy is minimised with respect to both orbital rotations and CI coefficients. If several states are calculated, the orbitals are often optimised for the average of the selected CI root energies (SA-CASSCF), to avoid root-flipping problems. In principle, the CASSCF wave function can provide a robust description of nearly degenerate states (static correlation), but the number of active orbitals is limited due to the factorial scaling of the full-CI problem. Therefore, the description of electron correlation is incomplete and the missing part of the correlation energy, usually referred to as dynamic correlation, must be calculated to obtain quantitative results.

The most widely used way to do this is via second-order perturbation theory, in terms of the CASPT2 method. CASPT2 can be considered size-consistent if the active orbital space increases naturally with the system, e.g., comprises all orbitals of an irreducible representation. Truncated MRCI and MRMP2 methods are generally not size-consistent and empirical correction schemes, e.g., the Davidson correction [38] are applied to alleviate the problem. If the CASSCF states form a good reference for the perturbative treatment, CASPT2 is comparable in accuracy with CC3 [33]. Dynamic correlation can strongly contribute to excitation energies and alter the order of excited states. In some cases, states that are well separated in energy in the exact solution can be nearly degenerate and strongly mix in the CASSCF solution. In these cases, the CASSCF states do not represent a good reference for perturbation theory and the error of CASPT2 can be considerably larger than 0.1 eV. This situation typically arises close to (avoided) crossings between states of different character, e.g., valence and Rydberg states. The multistate CASPT2 method (MS-CASPT2) solves this problem by calculating perturbatively an effective Hamiltonian in the space of the reference wave functions from a SA-CASSCF calculation [39]. A recent example where a MS-CASPT2 treatment is required is the spectrum of the HBDI chromophore of the greenfluorescent protein (GFP) [40]. The same article also reports a large influence of the zeroth-order Hamiltonian, for which several modifications have been suggested to improve the convergence behavior of the perturbation series. Recently, the IPEA ansatz [41] has been proposed, which eliminates a systematic underestimation of excitation energies of the previously common G1 and G3 Hamiltonians [42], but introduces an empirical parameter.

The spectroscopy-oriented CI (SORCI) method [43, 44] combines the concepts of MRCI and MRPT. More flexible than CASPT2, arbitrary molecular orbitals and reference wave functions can be used. Instead of multiconfigurational SCF orbitals, approximate natural orbitals are used by default, which are obtained in a preliminary MRCI calculation by diagonalizing the state-averaged density matrix. After a first MRMP2 calculation, the first-order interacting space (FOIS) is divided into

52 M. Wanko and A. Rubio

subspaces of weakly and strongly perturbing configurations, corresponding to their contribution to the MRMP2 energy. The reference and the strongly perturbing configurations build the interacting space for the final MRCI calculation, which gives the variational part of the correlation energy. The contribution of the weakly perturbing configurations is then determined from a second, relaxed, MRMP2 calculation, which uses the same FOIS as the first one. Due to the variational treatment of strongly perturbing configurations, excitation energies from SORCI are much less sensitive to the size of the reference than those of CASPT2. For a 2-root calculation, e.g., good results can be obtained with less than 100 configurations. The latter are selected by their weights in a preliminary CAS or RAS calculation. In the MRCI calculations, certain types of excitations are excluded that have little influence on excitation energies, following the concept of difference-dedicated CI (DDCI). In the final DDCI3 calculation, e.g., double excitations involving only inactive orbitals that are not part of the reference space are excluded. The Davidson correction is applied to the MRCI part and G3 zerothorder Hamiltonian in the MRMP2 part.

4.2.4 Semiempirical Methods

Due to the advancement of computational power and implementation of efficient (linear scaling, resolution-of-identity approximation), parallelised single-reference methods like TDDFT and CC2, semiempirical methods have lost their dominance in excited-state calculations of large molecules. In view of the hype for "ab initio" methods and the limitations addressed above, semiempirical methods should be redeemed as a valuable tool for excited-state applications. Their low computational cost allows for excited-state dynamics on the ps to ns time scale, configurational sampling of the excitation spectrum to obtain inhomogeneous line broadening and applications to extended systems, like light-harvesting complexes or molecules absorbed on a solid-state surface. They can also give satisfying results where TDDFT is not applicable, e.g., for CT excitations or systems involving static correlation. In general, the accuracy of excitation energies from semi-empirical Hamiltonians parameterised for the ground state, like AM1 or PM3, is not great. They are commonly used in combination with small CI expansions (usually CIS) to calculate excitation energies, because in the full-CI limit they underestimate excitation energies considerably [45]. This error can be fixed by a special parametrization for CIS excitation energies (ZINDO/S [46]), or by adding orthogonalisation corrections to the matrix elements (OM1 [47], OM2 [45], OM3 [48]). The latter approach is very appealing as it fixes another error of NDDO-type Hamiltonians, the underestimation of torsional barriers, in particular around double bonds [48–52]. As a by-product, the underestimation of excitation energies in the full-CI limit is removed, without the need for a special parametrisation for excited states. The use of the OMx Hamiltonians for MRCI calculations makes sense because of the fast convergence of excitation energies with respect to the size of the CI expansion. Compared with ab initio MRCI, very small reference wave functions and active orbital spaces are sufficient to obtain results close to the

full-CI limit. This is a direct consequence of the implicit incorporation of dynamic electron correlation in the parameterization and the resulting smaller two-electron integrals [53, 54]. OM2/MRCI hence recovers both dynamic and static correlation in a balanced way and performs well in the calculation of $\pi - \pi^*$ excitations with partial CT character. It has been applied, e.g., to the retinal chromophore and the related colour tuning of rhodopsins as well as to calculations on the green fluorescent protein (GFP), where it outperforms TDDFT with GGA and conventional hybrid functionals and correctly describes excitation-induced CT, response to electrostatic and steric interactions and excited-state geometries [23, 55, 56]. For nonadiabatic excited-state dynamics simulations, the electronic time-propagation and the surface-hopping algorithm have been implemented and applied to many systems (see Sect. 4.4).

4.3 QM/MM and Beyond

To understand the photophysical properties of organic chromophores, it is inevitable to study their intrinsic properties in vacuo. For practical applications, however, the influence of the environment on these properties is at least as important. This applies in particular to biological chromophores inside proteins, whose optical properties are regulated by the specific steric and electrostatic interactions with the protein. Approaches to account for these and further interactions (static polarisation, dispersion, charge exchange) will be discussed in this section. The main idea is to combine different levels of theory for the optically active part of the system and the environment. The most prominent scheme employs a QM method for the description of the active part and a classical molecular dynamics (MM) force field for the description of the environment (QM/MM) [57]. The MM force field can be extended to describe polarisation effects and coupled to a continuum-electrostatic model to describe the long-range effect of bulk solvation.

4.3.1 Schemes

Traditionally, additive (QM/MM [57]) and subtractive (ONIOM [58]) schemes are distinguished. The latter is conceptually clear and applicable in a general context. It requires three calculations of energy and its gradient. The energy of the entire system is calculated with a lower-level method ($E_{\rm low}^{\rm all}$) and a subsystem is calculated with both the lower- and higher-level methods, yielding $E_{\rm low}^{\rm subsystem}$ and $E_{\rm high}^{\rm subsystem}$. The total energy is then defined as

$$E_{\rm tot} = E_{\rm low}^{\rm all} + E_{\rm high}^{\rm subsystem} - E_{\rm low}^{\rm subsystem} \tag{4.4}$$

In case of an MM force field as the lower-level method, the additive scheme is equivalent but the energy is written in the form

$$E_{\text{tot}} = E_{\text{OM}} + E_{\text{OMMM}} + E_{\text{MM}} \tag{4.5}$$

Where $E_{\rm QM}=E_{\rm high}^{\rm subsystem}$ and $E_{\rm QMMM}$ gathers all interaction terms between the subsystem and the rest of the system that are not included in $E_{\rm QM}$. $E_{\rm MM}$ thus contains only interactions that do not involve QM atoms.

In both schemes, mechanical and electrostatic embedding are used. The first treats all interactions between the subsystem and the remaining atoms at the lower level. This is insufficient for excited-state calculations of ionic chromophores as the electrostatic interactions between QM and MM parts are strong (hydrogen bonds, counter ions) and the charge distribution in the QM region depends on the electronic state and the level of theory. In the electrostatic embedding, the polarisation of the subsystem by the environment is included in the (higher level) QM Hamiltonian. A fully self-consistent polarisation between QM and MM region with a polarisable force field is more involved and will be addressed in Sect. 4.3.3.

The choice of an appropriate splitting between the subsystem, in the following called OM region, and the rest of the system, for sake of simplicity referred to as the MM region, will be discussed in the next paragraph. Often it is necessary to cut covalent bonds, in which case the QM-MM boundary needs to be cured to avoid artifacts. The most common approach is to satisfy dangling bonds with hydrogen link atoms, which are invisible to the MM region and are constrained to the axis between the QM and MM frontier atoms. In order to avoid over-polarization of the link atom, the charge of the MM frontier atom is deleted and, in the divided frontier charge (DIV) scheme, redistributed among neighbor MM atoms. In the charge shift scheme, a dipole is introduced to compensate for the charge redistribution. For a comparison of different link atom approaches see [59–64]. For proteins, the linkatom approach works well and is most widely used, although many alternatives have been suggested, such as the local self-consistent field (LSCF) method [65, 66], the generalised hybrid-orbital (GHO) [67, 68], the frozen orbital [69], frozen-core orbital (FCO) [70], the pseudobond [71, 72], quantum-capping potential (QCP) [72, 73], effective group potential (EGP) [74, 75], optimised effective Hamiltonian [76], and the semiempirical connection-atom (CA) [77] approach. For a comprehensive overview of QM/MM schemes and frontier treatments see [78, 79].

4.3.2 Charge Transfer and the Proper Size of the QM Region

If the QM/MM frontier is cutting covalent bonds, the ideal situation is to choose non-polar single bonds, such that the charge density of the QM region integrates to an integer in an extended calculation. This is nearly satisfied when cutting through the $C_{\alpha} - C_{\beta}$ bond in a protein, because inter-residual charge transfer via the peptide backbone is negligible. It has been shown, however that inter-molecular or interresidual charge exchange across hydrogen bonds can be significant and affects excitation energies. In the case of the retinal chromophore in rhodopsins, for example, blue shifts of the excitation energy of 0.2–0.5 eV have been obtained when extending the QM region from the cationic chromophore to the counter ion [80, 81], which is essentially due to charge exchange [56]. The QM region should

therefore be chosen sufficiently large to ensure that the total charge on the optically active moiety is converged. This can be tested with little computational effort by extending the QM region stepwise and calculating NPA charges [82] from the HF ground-state density [54]. Note, that DFT (in particular LDA, GGA) strongly overestimates inter-residual charge exchange [54]. Directly considering the excitation energy as criterion for the appropriate extend of the QM region is problematic. Apart from size-consistency issues, the successive substitution of MM point charges by a QM density causes fluctuations in the electrostatic potential and excitation energies that converge very slowly with the size of the QM region and cannot be achieved efficiently. It is therefore more practical to focus on a converged charge exchange and improve the electrostatic description of the surrounding protein or solvent environment by other means, e.g., by using a polarisable force field.

4.3.3 Environment polarisation

The development of polarisable force fields is a very active field of research and has grown considerably in the last 10 years. Apart from geometry-dependent terms, the explicit treatment of polarisation is regarded as the key ingredient to improve the accuracy of conventional force fields. Excited-state QM/MM studies can take profit from this development as polarisation also improves the electrostatic representation of the solvent/protein environment and allows a self-consistent mutual polarisation between OM and polarisable MM regions. The calculation of vertical excitation energies based on the ground-state adopted polarisable MM region already reduces the error in the electrostatic potential when compared to different fixed point charge models from various force fields [83, 84]. If the polarisable environment is allowed to respond to the excitation-induced charge re-distribution in the QM region, the problem arises that the wave functions of the fully self-consistent solution for the different electronic states are not orthogonal anymore [85, 86]. A simple solution consists in taking the vertical excitation energy of the ground-state adapted system as a lower bound and that of the excited-state adapted one as an upper bound. In the next step, the polarisable region is allowed to respond to the new QM charge distribution, but the QM calculation is not iterated, hence preserving orthogonality. This reduces the difference between the upper and lower bound. The average of the two results can then be considered as the best approximation [84, 86, 87].

A straight-forward approach to explicit polarisation is to introduce another (QM2) layer around the optically active region (QM1). As the computational demand for calculating a ground-state charge distribution is lower than that for the accurate calculation of excitation energies, a lower-level method and further approximations to obtain a linear-scaling can be used [88, 89]. The X-POL method [90], e.g., uses iterative AM1 fragment calculations to obtain a self-consistent charge distribution. The effect of protein polarisation is rather long-range. It is therefore not sufficient to apply the polarisation method only within a layer of a few Å in thickness around the QM1 region [83]. Therefore, further approximations are

desirable that do not require MO theory, which leads to approaches generally referred to as polarisation models or polarisable force fields.

Two types of polarisation models are used in MM force fields. The first is based on chemical potential equilibration (CPE), sometimes called fluctuating charge models. These introduce atomic parameters for electronegativity χ and chemical hardness η and use an energy expression of the form

$$E(\mathbf{Q}) = E_0 + \sum_{i} X_i Q_i + \frac{1}{2} \sum_{i} \sum_{j} S(r_{ij}, \eta_i, \eta_j) Q_i Q_j$$
 (4.6)

The analytical function S describes the Coulomb interaction between atomic charges Q_i in the long range limit $r_{ii} \to \infty$ and converges to a finite value for $r_{ij} = 0$, which depends on the chemical hardness parameters for atoms i and j. The atomic charges Q_i can describe either the total atomic net charges or the difference to a reference charge for the specific atom type without an external field. In order to describe out-of-plane and out-of-axis polarisation, the model must be augmented by atomic dipoles, like in the ABEEM $\sigma\pi$ [91] or CPE model of Chelli et al. [92]. The second type of polarisable force fields uses an atomic induced dipole model [57]. It was shown by Thole et al. [93] that molecular polarizability tensors can be described very well with just one set of atomic polarizability parameters for each element if the model includes (1) the interaction between the induced dipoles and (b) a proper short-range damping term for the charge-dipole and dipole-dipole interaction. These parameters were shown to be transferable to amino acids [83] and yield side chain polarizabilities that agree within 3 % with ab initio results. A variant of the induced atomic dipole model is the Drude oscillator model [94, 95], in which the induced dipole is represented by fixed charge q (drude particle) that is attached to the host atom by a spring (force constant k) according to the atomic polarizability $\alpha = q^2/k$. Table 4.1 gives an overview of existing polarisable force fields for proteins.

4.4 Molecular Dynamics

The time-propagation of the nuclear equation of motion, referred to as molecular dynamics (MD), is the most common approach to explore the configuration space of the nuclear coordinates of large biosystems (see [110] for a recent review of MD and alternative techniques). Ground-state MD at variable temperature T can be used to find the global energy minimum structure, which is required to simulate spectroscopy at cryogenic temperatures (see [111] for an example of microsolvated dianions). In simulated annealing, T is slowly reduced to zero. In metadynamics [112], different trajectories at different T are calculated in parallel and combined to overcome barriers and efficiently sample the low-energy regions of the configuration space.

Name	References	Permanent charge	Polarisable model
ff02 (AMBER)	[96, 97]	Point charges ^a	Interactive, undamped ind. dipoles, atom-type-based α , no groups
AMOEBAPRO (TINKER)	[98–100]	DMA	Interactive, damped (Thole) ind. dipoles, element-based α from [93], groups
CPE	[92]	_	CPE and dipoles (s-/p-type Gaussians), atom- type-based η_s , η_p , and χ
DRF90	[101–103]	Point charges	Interactive, damped (Thole) ind. dipoles, element-based α , molecular groups
ENZYMIX	[57]	Point charges	Ind. dipoles, element-/row-based α
FQ (CHARMM)	[104, 105]	Point charges	CPE, atom-type-based η and χ
PFF	[106, 107]	Point charges, ^a dipoles	Interactive, undamped, ^b ind. dipoles, atom-based α, no groups
SIBFA	[108, 109]	DMA	Distributed, anisotropic, damped ind. multipoles, molecular groups

Table 4.1 Polarisable force fields for proteins

Model parameters: α : polarizability, χ : electronegativity, η : chemical hardness

4.4.1 Configurational Sampling

MD at fixed temperature, volume, and particle number (NVT) is the most common way to obtain a canonical ensemble, the structures (configurations) of which can be used to obtain a statistical average of a property in the thermodynamic equilibrium at a given temperature. The MD simulation must be sufficiently long to explore the relevant regions of the configurational space, i.e., provide ergodicity. It is an open problem to predict a priory when this condition is satisfied. The property, e.g., absorption spectrum is then calculated for a set of randomly chosen MD snapshots. Configurational sampling removes the problem that a single point calculation only considers the structure of an arbitrary local minimum that may or may not well represent the average structure at room temperature. Furthermore, it provides an estimate for the line broadening and the effect of superposition of different conformations that are occupied in the thermodynamic equilibrium. Examples can be found for the calculation of solvent shifts of acrolein in water [113–115], the opsin shift of the absorption maximum of the retinal chromophore in different rhodopsin proteins [116–118], the calculation of NMR chemical shifts [119], and the calculation of vertical detachment energies for microsolvated ions [120].

Another powerful application of configurational sampling is to analyze the correlation between a calculated property and structural parameters. For retinal chromophore, e.g., a strong correlation can be found between the bond-length alternation of the chromophore and the absorption maximum [116].

^aIncluding lone pair sites

^bExcluding 1–2, 1–3 interactions

4.4.2 Non-adiabatic Excited-State Dynamics

MD in the electronically excited state is the basis for simulating time-resolved spectroscopy, fluorescence quenching, excited-state electron or proton transfer, and resonant energy transfer. Topological analysis of the excited-state PES in terms of minima, transition states, and conical intersections provides a rigorous understanding of the photochemistry that supports the interpretation of time-resolved experimental data. This is, however, the most challenging area of theoretical spectroscopy (see [121] for a recent review). The description of excited-state PES reveals many limitations of the quantum chemical methods described in Sect. 4.2 that can be widely ignored in ground-state simulations close to the equilibrium. The QM method must deal with open-shell and multi-configurational wave functions, with variable amount of CT. It must provide a balanced description of both dynamic and static correlation, because these often have contrary effects on observables. Error bars of a few kcal/mol, as desired for quantitative predictions of reaction rates for competing pathways, are difficult to achieve for excited states. Therefore, benchmarks and error discussions are much more important for excited-state applications than for standard ground-state simulations, where established methods like B3LYP, MP2, CCSD(T) have well-known error bars and can be used in a black-box manner.

To describe the decay of the excited-state population due to the nonadiabatic coupling between the electronic and vibronic degrees of freedom, the Tully surface hopping (SH) approach [122, 123] is most widely used for larger molecules. It is efficient and easy to implement due to the stochastic treatment of the nuclear degrees of freedom and the separate time-propagation of electrons and nuclei on different timescales. Approximate variants omit the electronic time-propagation and simply use the nonadiabatic coupling vector (or even more simple criteria) to calculate the electronic transition probability on-the-fly. Other approaches, like multiple-spawning [124] or the variational multi-configuration Gaussian wavepacket method (vMCG) [125] include interference effects by expressing the nuclear wavepacket in a Gaussian basis.

Many successful simulations of nonadiabatic excited-state dynamics employed CASSCF/CASPT2, ab initio [126] or semi-empirical MRCI [127, 128]. Illustrative examples can be found for the photoisomerisation of the retinal chromophore [129, 130], the solvated chromophore of the green fluorescent protein [131], photoswitching of a fluorescent protein [132], DNA bases [133–135] and other systems [124, 136, 137].

References

- 1. Kochendoerfer, G., Wang, Z., Oprian, D.D., Mathies, R.A.: Examination of the wavelength regulation mechanism in human visual pigments. Biochemistry **36**, 6577–6587 (1997)
- Frähmcke, J.S., Wanko, M., Phatak, P., Mroginski, M.A., Elstner, M.: The protonation state
 of Glu181 in rhodopsin revisited: interpretation of experimental data on the basis of QM/MM
 calculations. J. Phys. Chem. B 114, 11338–11352 (2010)

3. Runge, E., Gross, E.: Density-functional theory for time-dependent systems. Phys. Rev. Lett. **52**, 997 (1984)

59

- Castro, A., Appel, H., Oliveira, M., Rozzi, C., Andrade, X., Lorenzen, F., Marques, M., Gross, E., Rubio, A.: Octopus: a tool for the application of time-dependent density functional theory. Physica Status Solidi B 243, 2465–2488 (2006)
- Casida, M.E.: Time-dependent density functional response theories of molecules. In: Chong, D.P. (ed.) Recent Advances in Density Functional Methods, Part 1. Recent Advances in Computational Chemistry, vol. 1. World Scientific, Singapore (1995)
- Furche, F.: On the density matrix based approach to time-dependent density functional response theory. J. Chem. Phys. 114(14), 5982–5992 (2001)
- 7. Furche, F., Ahlrichs, R.: Adiabatic time-dependent density functional methods for excited state properties. J. Chem. Phys. **117**(16), 7433–7447 (2002)
- Baerends, E.J.: Exact exchange-correlation treatment of dissociated H₂ in density functional theory. Phys. Rev. Lett. 87(13), 133004 (2001)
- 9. Gritsenko, O.V., van Gisbergen, S.J.A., Görling, A., Baerends, E.J.: Excitation energies of dissociating H₂: a problematic case for the adiabatic approximation of time-dependent density functional theory. J. Chem. Phys. **113**(19), 8478–8489 (2000)
- Grüning, M., Gritsenko, O.V., Baerends, E.J.: Exchange-correlation energy and potential as approximate functionals of occupied and virtual Kohn-Sham orbitals: application to dissociating H2. J. Chem. Phys. 118(16), 7183–7192 (2003)
- 11. Grüning, M., Gritsenko, O.V., van Gisbergen, S.J.A., Baerends, E.J.: The failure of generalized gradient approximations (GGAs) and meta-GGAs for the two-center three-electron bonds in He⁺₂, (H₂O)⁺₂, and (NH₃)⁺₂. J. Phys. Chem. A **105**(40), 9211–9218 (2001)
- Cizek, J., Paldus, J.: Stability conditions for solutions of Hartree-Fock equations for atomic and molecular systems. Application to pi-electron model of cyclic polyenes. J. Chem. Phys. 47(10), 3976–3985 (1967)
- Cordova, F., Doriol, L.J., Ipatov, A., Casida, M.E., Filippi, C., Vela, A.: Troubleshooting time-dependent density-functional theory for photochemical applications: oxirane. J. Chem. Phys. 127(16), 164111 (2007). doi:10.1063/1.2786997
- Levine, B.G., Ko, C., Quenneville, J., Martinez, T.J.: Conical intersections and double excitations in time-dependent density functional theory. Mol. Phys. 104(5–7), 1039–1051 (2006)
- Casida, M.E., Jamorski, C., Casida, K.C., Salahub, D.R.: Molecular excitation energies to high-lying bound states from time dependent density-functional response theory: characterization and correction of the time-dependent local density approximation ionization threshold. J. Chem. Phys. 108(11), 4439–4449 (1998)
- Tozer, D., Handy, N.C.: Improving virtual Kohn-Sham orbitals and eigenvalues: application to excitation energies and static polarizabilities. J. Chem. Phys. 109(23), 10180 (1998)
- 17. Grüning, M., Gritsenko, O.V., van Gisbergen, S.J.A., Baerends, E.J.: Shape corrections to exchange-correlation potentials by gradient-regulated seamless connection of model potentials for inner and outer region. J. Chem. Phys. **114**(2), 652–660 (2001)
- van Leeuwen, R., Baerends, E.J.: Exchange-correlation potential with correct asymptotic behavior. Phys. Rev. A 49, 2421–2431 (1994)
- Dreuw, A., Head-Gordon, M.: Failure of time-dependent density functional theory for longrange charge-transfer excited states: the zincbacteriochlorin-bacteriochlorin and bacteriochlorophyll-spheroidene complexes. J. Am. Chem. Soc. 126, 4007–4016 (2004)
- Tozer, D.J.: Relationship between long-range charge-transfer excitation energy error and integer discontinuity in Kohn-Sham theory. J. Chem. Phys. 119(24), 12697–12699 (2003)
- Hellgren, M., Gross, E.K.U.: Discontinuities of the exchange-correlation kernel and chargetransfer excitations in time-dependent density-functional theory. Phys. Rev. A 85(2), 022514 (2012)

- Lange, A., Herbert, J.M.: Simple methods to reduce charge-transfer contamination in timedependent density-functional calculations of clusters and liquids. J. Chem. Theory Comput. 3 (5), 1680–1690 (2007)
- Wanko, M., García-Risueño, P., Rubio, A.: Excited states of the green fluorescent protein chromophore: performance of ab initio and semi-empirical methods. Phys. Status Solidi B 249(2), 392–400 (2012)
- 24. Wiggins, P., Williams, J.A.G., Tozer, D.J.: Excited state surfaces in density functional theory: a new twist on an old problem. J. Chem. Phys. **131**(9), 091101–091104 (2009)
- Peach, M.J.G., Sueur, C.R.L., Ruud, K., Guillaume, M., Tozer, D.J.: TDDFT diagnostic testing and functional assessment for triazene chromophores. Phys. Chem. Chem. Phys. 11 (22), 4465–4470 (2009)
- Leininger, T., Stoll, H., Werner, H.J., Savin, A.: Combining long-range configuration interaction with short-range density functionals. Chem. Phys. Lett. 275(3–4), 151–160 (1997)
- Yanai, T., Tew, D.P., Handy, N.C.: A new hybrid exchange-correlation functional using the Coulomb-attenuating method (CAM-B3LYP). Chem. Phys. Lett. 393, 51–57 (2004)
- Tawada, Y., Tsuneda, T., Yanagisawa, S., Yanai, T., Hirao, K.: A long-range-corrected timedependent density functional theory. J. Chem. Phys. 120(18), 8425–8433 (2004)
- Jacquemin, D., Perpete, E.A., Scalmani, G., Frisch, M.J., Kobayashi, R., Adamo, C.: Assessment of the efficiency of long-range corrected functionals for some properties of large compounds. J. Chem. Phys. 126(14), 144105 (2007)
- Peverati, R., Truhlar, D.G.: Performance of the M11 and M11-L density functionals for calculations of electronic excitation energies by adiabatic time-dependent density functional theory. Phys. Chem. Chem. Phys. 14(32), 11363–11370 (2012)
- 31. Tsai, C.W., Su, Y.C., Li, G.D., Chai, J.D.: Assessment of density functional methods with correct asymptotic behavior. Phys. Chem. Chem. Phys. **15**(21), 8352–8361 (2013)
- 32. Christiansen, O., Koch, H., Jorgensen, P.: The 2nd-order approximate coupled-cluster singles and doubles model CC2. Chem. Phys. Lett. **243**(5–6), 409–418 (1995)
- Schreiber, M., Silva-Junior, M.R., Sauer, S.P.A., Thiel, W.: Benchmarks for electronically excited states: CASPT2, CC2, CCSD, and CC3. J. Chem. Phys. 128(13), 134110 (2008)
- 34. Hättig, C., Kohn, A.: Transition moments and excited-state first-order properties in the coupled-cluster model CC2 using the resolution-of-the-identity approximation. J. Chem. Phys. **117**(15), 6939–6951 (2002)
- Szalay, P.G., Watson, T., Perera, A., Lotrich, V.F., Bartlett, R.J.: Benchmark studies on the building blocks of DNA. I. Superiority of coupled cluster methods in describing the excited states of nucleobases in the Franck-Condon region. J. Phys. Chem. A 116(25), 6702–6710 (2012)
- 36. Winter, N.O.C., Graf, N.K., Leutwyler, S., Hattig, C.: Benchmarks for 0-0 transitions of aromatic organic molecules: DFT/B3LYP, ADC(2), CC2, SOS-CC2 and SCS-CC2 compared to high-resolution gas-phase data. Phys. Chem. Phys. 15(18), 6623–6630 (2013)
- 37. Köhn, A.: Can coupled-cluster theory treat conical intersections? J. Chem. Phys. 127(4), 044105 (2007)
- 38. Langhoff, S.R., Davidson, E.R.: Configuration interaction calculations on the nitrogen molecule. Int. J. Quantum Chem. **8**(1), 61–72 (1974)
- 39. Finley, J., Malmqvist, P.A., Roos, B.O., Serrano-Andres, L.: The multi-state CASPT2 method. Chem. Phys. Lett. 288(2–4), 299–306 (1998)
- Filippi, C., Zaccheddu, M., Buda, F.: Absorption spectrum of the green fluorescent protein chromophore: a difficult case for ab initio methods? J. Chem. Theory Comput. 5(8), 2074–2087 (2009)
- Ghigo, G., Roos, B.O., Malmqvist, P.A.: A modified definition of the zeroth-order hamiltonian in multiconfigurational perturbation theory (caspt2). Chem. Phys. Lett. 396(1–3), 142–149 (2004)

42. Andersson, K.: Different forms of the 0th-order hamiltonian in 2nd-order perturbation-theory with a complete active space self-consistent-field reference function. Theor. Chim. Acta **91** (1–2), 31–46 (1995)

61

- Neese, F.: A spectroscopy oriented configuration interaction procedure. J. Chem. Phys. 119, 9428–9443 (2003)
- 44. Neese, F., Petrenko, T., Ganyushin, D., Olbrich, G.: Advanced aspects of ab initio theoretical optical spectroscopy of transition metal complexes: multiplets, spin-orbit coupling and resonance Raman intensities. Coord. Chem. Rev. 251(3–4), 288–327 (2007)
- 45. Weber, W.: Ein neues semiempirisches NDDO-verfahren mit orthogonalisierungskorrekturen. Ph.D. thesis, Universität Zürich (1996)
- 46. Zerner, M.C., Ridley, J.: An intermediate neglect of differential overlap technique for spectroscopy; pyrrole and the azines. Theor. Chim. Acta 32, 111 (1973)
- 47. Kolb, M.: Ein neues semiempirisches Verfahren auf Grundlage der NDDO Näherung. Ph.D. thesis, Universität Wuppertal (1991)
- 48. Tuttle, T., Thiel, W.: OMx-D: semiempirical methods with orthogonalization and dispersion corrections. Implementation and biochemical application. Phys. Chem. Chem. Phys. **10**(16), 2159–2166 (2008)
- Paizs, B., Tajkhorshid, E., Suhai, S.: Electronic effects on the ground-state rotational barrier of polyene Schiff bases: a molecular orbital study. J. Phys. Chem. B 103, 5388–5395 (1999)
- 50. Weber, W., Thiel, W.: Orthogonalisation corrections for semiempirical methods. Theor. Chem. Acc. **103**, 495–506 (2000)
- Winget, P., Selcuki, C., Horn, A.H.C., Martin, B., Clark, T.: Towards a "next generation" neglect of diatomic differential overlap based semiempirical molecular orbital technique. Theor. Chem. Acc. 110(4), 254–266 (2003)
- Zhou, H., Tajkhorshid, E., Frauenheim, T., Suhai, S., Elstner, M.: Performance of the AM1, PM3, and SCC-DFTB methods in the study of conjugated Schiff base molecules. Chem. Phys. 277, 91–103 (2002)
- Silva-Junior, M.R., Thiel, W.: Benchmark of electronically excited states for semiempirical methods: MNDO, AM1, PM3, OM1, OM2, OM3, INDO/S, and INDO/S2. J. Chem. Theory Comput. 6(5), 1546–1564 (2010)
- 54. Wanko, M.: Optical excitations in biological systems: multiscale-simulation strategies and applications to rhodopsins. Ph.D. dissertation, TU Braunschweig (2009). http://www.digibib.tu-bs.de/?docid=00030605
- 55. Keal, T., Wanko, M., Thiel, W.: Assessment of semiempirical methods for the photoisomerisation of a protonated Schiff base. Theor. Chem. Acc. 123(1), 145–156 (2009)
- Wanko, M., Hoffmann, M., Strodel, P., Koslowski, A., Thiel, W., Neese, F., Frauenheim, T., Elstner, M.: Calculating absorption shifts for retinal proteins: computational challenges. J. Phys. Chem. B 109, 3606–3615 (2005)
- Warshel, A., Levitt, M.: Theoretical studies of enzymic reactions: dielectric, electrostatic and steric stabilization of the carbonium ion in the reaction of lysozyme. J. Mol. Biol. 103(2), 227–249 (1976)
- 58. Vreven, T., Morokuma, K.: The ONIOM (our own N-layered integrated molecular orbital + molecular mechanics) method for the first singlet excited (S1) state photoisomerization path of a retinal protonated Schiff base. J. Chem. Phys. 113, 2969 (2000)
- Ferre, N., Olivucci, M.: The amide bond: pitfalls and drawbacks of the link atom scheme.
 J. Mol. Struct. (Theochem) 632(71–82) (2003)
- Jung, G., Werner, M., Schneider, M.: Efficient photoconversion distorts the fluorescence lifetime of GFP in confocal microscopy: a model kinetic study on mutant Thr203Val. ChemPhysChem 9(13), 1867–1874 (2008)
- König, P., Hoffmann, M., Frauenheim, T., Cui, Q.: A critical evaluation of different QM/MM frontier treatments using SCC-DFTB as the QM method. J. Phys. Chem. B 109, 9082 (2005)

- Lin, H., Truhlar, D.G.: Redistributed charge and dipole schemes for combined quantum mechanical and molecular mechanical calculations. J. Phys. Chem. A 109(17), 3991–4004 (2005)
- Reuter, N., Dejaegere, A., Maigret, B., Karplus, M.: Frontier bonds in QM/MM methods: a comparison of different approaches. J. Phys. Chem. A 104(8), 1720–1735 (2000)
- 64. Riccardi, D., Schaefer, P., Cui, Q.: pK(a) calculations in solution and proteins with QM/MM free energy perturbation simulations: a quantitative test of QM/MM protocols. J. Phys. Chem. B **109**(37), 17715–17733 (2005)
- 65. Ferre, N., Assfeld, X., Rivail, J.L.: Specific force field parameters determination for the hybrid ab initio QM/MM LSCF method. J. Comput. Chem. **23**(6), 610–624 (2002)
- Thery, V., Rinaldi, D., Rivail, J.L., Maigret, B., Ferenczy, G.G.: Quantum-mechanical computations on very large molecular-systems - the local self-consistent-field method. J. Comput. Chem. 15(3), 269–282 (1994)
- Gao, J., Amara, P., Alhambra, C., Field, M.J.: A generalized hybrid orbital (GHO) method for the treatment of boundary atoms in combined QM/MM calculations. J. Phys. Chem. A 102 (24), 4714–4721 (1998)
- Rodriguez, A., Oliva, C., Gonzalez, M., van der Kamp, M., Mulholland, A.J.: Comparison of different quantum mechanical/molecular mechanics boundary treatments in the reaction of the hepatitis C virus NS3 protease with the NS5A/5B substrate. J. Phys. Chem. B 111(44), 12909–12915 (2007)
- 69. Philipp, D.M., Friesner, R.A.: Mixed ab initio QM/MM modeling using frozen orbitals and tests with alanine dipeptide and tetrapeptide. J. Comput. Chem. **20**, 1468–1494 (1999)
- Fornili, A., Loos, P.F., Sironi, M., Assfeld, X.: Frozen core orbitals as an alternative to specific frontier bond potential in hybrid quantum mechanics/molecular mechanics methods. Chem. Phys. Lett. 427(1–3), 236–240 (2006)
- 71. Zhang, Y.K.: Pseudobond ab initio QM/MM approach and its applications to enzyme reactions. Theor. Chem. Acc. **116**(1–3), 43–50 (2006)
- 72. Zhang, Y.K., Lee, T.S., Yang, W.T.: A pseudobond approach to combining quantum mechanical and molecular mechanical methods. J. Chem. Phys. **110**(1), 46–54 (1999)
- DiLabio, G.A., Hurley, M.M., Christiansen, P.A.: Simple one-electron quantum capping potentials for use in hybrid QM/MM studies of biological molecules. J. Chem. Phys. 116, 9578–9584 (2002)
- Bessac, F., Alary, F., Carissan, Y., Heully, J.L., Daudey, J.P., Poteau, R.: Effective group potentials: a powerful tool for hybrid QM/MM methods? THEOCHEM 632, 43–59 (2003)
- Poteau, R., Ortega, I., Alary, F., Solis, A.R., Barthelat, J.C., Daudey, J.P.: Effective group potentials. I. Method. J. Phys. Chem. A 105(1), 198–205 (2001)
- Yasuda, K., Yamaki, D.: Simple minimum principle to derive a quantum-mechanical/ molecular-mechanical method. J. Chem. Phys. 121(9), 3964–3972 (2004)
- 77. Antes, I., Thiel, W.: Adjusted connection atoms for combined quantum mechanical and molecular mechanical methods. J. Phys. Chem. A **103**, 9290–9295 (1999)
- 78. Lin, H., Truhlar, D.G.: QM/MM: what have we learned, where are we, and where do we go from here? Theor. Chem. Acc. 117(2), 185–199 (2007)
- Senn, H.M., Thiel, W.: QM/MM methods for biological systems. Top. Curr. Chem. 268, 173290 (2007)
- Hayashi, S., Ohmine, I.: Proton transfer in bacteriorhodopsin: structure, excitation, IR spectra, and potential energy surface analyses by an ab initio QM/MM method. J. Phys. Chem. B 104, 10678–10691 (2000)
- 81. Schreiber, M., Buß, V., Sugihara, M.: Exploring the opsin shift with ab initio methods: geometry and counterion effects on the electronic spectrum of retinal. J. Chem. Phys. 119 (23), 12045–12048 (2003)
- 82. Reed, A.E., Weinstock, R.B., Weinhold, F.: Natural population analysis. J. Chem. Phys. 83 (2), 735–746 (1985)

4 Theoretical Methods 63

83. Wanko, M., Hoffmann, M., Frähmcke, J., Frauenheim, T., Elstner, M.: Effect of polarization on the opsin shift in rhodopsins. 2. Empirical polarization models for proteins. J. Phys. Chem. B **112**(11), 11468–11478 (2008)

- 84. Wanko, M., Hoffmann, M., Frauenheim, T., Elstner, M.: Effect of polarization on the opsin shift in rhodopsins. I. A combined QM/QM/MM model for bacteriorhodopsin and pharaonis sensory rhodopsin II. J. Phys. Chem. B 112, 11462–11467 (2008)
- 85. Luzhkov, V., Warshel, A.: Microscopic calculations of solvent effects on absorption spectra of conjugated molecules. J. Am. Chem. Soc. **113**, 4491–4499 (1991)
- 86. Thompson, M.A., Schenter, G.K.: Excited states of the bacteriochlorophyll b dimer of rhodopseudomonas viridis: a QM/MM study of the photosynthetic reaction center that includes MM polarization. J. Phys. Chem. **99**, 6374–6386 (1995)
- 87. Gao, J., Alhambra, C.: Solvent effects on the bond length alternation and absorption energy of conjugated compounds. J. Am. Chem. Soc. 119, 2962–2963 (1997)
- 88. Cui, Q., Guo, H., Karplus, M.: Combining ab initio and density functional theories with semiempirical methods. J. Chem. Phys. 117, 5617–5631 (2002)
- 89. Hratchian, H.P., Parandekar, P.V., Raghavachari, K., Frisch, M.J., Vreven, T.: Qm:qm electronic embedding using mulliken atomic charges: energies and analytic gradients in an oniom framework. J. Chem. Phys. 128, 034,107 (2008)
- 90. Xie, W., Gao, J.: Design of a next generation force field: the X-POL potential. J. Chem. Theory Comput. 3(6), 1890–1900 (2007)
- 91. Zhao, D.X., Liu, C., Wang, F.F., Yu, C.Y., Gong, L.D., Liu, S.B., Yang, Z.Z.: Development of a polarizable force field using multiple fluctuating charges per atom. J. Chem. Theory Comput. **6**(3), 795–804 (2010)
- Chelli, R., Procacci, P.: A transferable polarizable electrostatic force field for molecular mechanics based on the chemical potential equalization principle. J. Chem. Phys. 117(20), 9175–9189 (2002)
- 93. Thole, B.: Molecular polarizabilities calculated with a modified dipole interaction. Chem. Phys. **59**, 341–350 (1981)
- 94. Anisimov, V.M., Lamoureux, G., Vorobyov, I.V., Huang, N., Roux, B., MacKerell, A.D.: Determination of electrostatic parameters for a polarizable force field based on the classical Drude oscillator. J. Chem. Theory Comput. 1(1), 153–168 (2005)
- 95. Drude, P.: The Theory of Optics. Dover, New York (1959)
- Applequist, J., Carl, J.R., Fung, K.K.: An atom dipole interaction model for molecular polarizability. Application to polyatomic molecules and determination of atom polarizabilities. J. Am. Chem. Soc. 94(9), 2952–2960 (1972)
- 97. Cieplak, P., Caldwell, J., Kollman, P.: Molecular mechanical models for organic and biological systems going beyond the atom centered two body additive approximation: aqueous solution free energies of methanol and n-methyl acetamide, nucleic acid base, and amide hydrogen bonding and chloroform/water partition coefficients of the nucleic acid bases. J. Comput. Chem. 22(10), 1048–1057 (2001)
- 98. Ponder, J.W., Case, D.A.: Force fields for protein simulations. Adv. Protein Chem. **66**, 27–85 (2003)
- Ren, P., Ponder, J.W.: Polarizable atomic multipole water model for molecular mechanics simulation. J. Phys. Chem. B 107, 5933–5947 (2003)
- 100. Ren, P.Y., Ponder, J.W.: Consistent treatment of inter- and intramolecular polarization in molecular mechanics calculations. J. Comput. Chem. 23(16), 1497–1506 (2002)
- Swart, M., van Duijnen, P.T.: Drf90: a polarizable force field. Mol. Simul. 32(6), 471–484 (2006)
- 102. Swart, M., Snijders, J.G., van Duinen, P.T.: Polarizabilities of amino acid residues. J. Comput. Methods Sci. Eng. 4(1–2), 419–425 (2004)
- 103. Swart, M., Van Duijnen, P.T., Snijders, J.G.: A charge analysis derived from an atomic multipole expansion. J. Comput. Chem. 22(1), 79–88 (2001)

- 104. Patel, S., Brooks, C.L.: CHARMM fluctuating charge force field for proteins: I Parameterization and application to bulk organic liquid simulations. J. Comput. Chem. 25(1), 1–15 (2004)
- 105. Patel, S., MacKerell, A.D., Brooks, C.L.: CHARMM fluctuating charge force field for proteins: II Protein/solvent properties from molecular dynamics simulations using a nonadditive electrostatic model. J. Comput. Chem. 25(12), 1504–1514 (2004)
- 106. Kaminski, G.A., Stern, H.A., Berne, B.J., Friesner, R.A.: Development of an accurate and robust polarizable molecular mechanics force field from ab initio quantum chemistry. J. Phys. Chem. A 108(4), 621–627 (2004)
- 107. Kaminski, G.A., Stern, H.A., Berne, B.J., Friesner, R.A., Cao, Y.X.X., Murphy, R.B., Zhou, R.H., Halgren, T.A.: Development of a polarizable force field for proteins via ab initio quantum chemistry: first generation model and gas phase tests. J. Comput. Chem. 23(16), 1515–1531 (2002)
- 108. Gresh, N., Claverie, P., Pullman, A.: Theoretical studies of molecular conformation. Derivation of an additive procedure for the computation of intramolecular interaction energies. Comparison with ab initio scf computations. Theor. Chim. Acta **66**(1), 1–20 (1984)
- 109. Guo, H., Gresh, N., Roques, B.P., Salahub, D.R.: Many-body effects in systems of peptide hydrogen-bonded networks and their contributions to ligand binding: a comparison of the performances of DFT and polarizable molecular mechanics. J. Phys. Chem. B 104(41), 9746–9754 (2000)
- 110. Adcock, S.A., McCammon, J.A.: Molecular dynamics: survey of methods for simulating the activity of proteins. Chem. Rev. **106**(5), 1589–1615 (2006)
- 111. Wende, T., Wanko, M., Jiang, L., Meijer, G., Asmis, K.R., Rubio, A.: Spectroscopic characterization of solvent-mediated folding in dicarboxylate dianions. Angew. Chem. Int. Ed. **50**, 3807–3810 (2011)
- 112. Laio, A., Parrinello, M.: Escaping free-energy minima. PNAS 99(20), 12562-12566 (2002)
- 113. Brancato, G., Barone, V., Rega, N.: Theoretical modeling of spectroscopic properties of molecules in solution: toward an effective dynamical discrete/continuum approach. Theor. Chem. Acc. 117(5–6), 1001–1015 (2007)
- 114. Brancato, G., Rega, N., Barone, V.: A quantum mechanical/molecular dynamics/mean field study of acrolein in aqueous solution: analysis of h bonding and bulk effects on spectroscopic properties. J. Chem. Phys. 125(16), 164,515 (2006)
- 115. Georg, H.C., Coutinho, K., Canuto, S.: A sequential monte carlo quantum mechanics study of the hydrogen-bond interaction and the solvatochromic shift of the n-pi(*) transition of acrolein in water. J. Chem. Phys. 123, 124307 (2005)
- 116. Hoffmann, M., Wanko, M., Strodel, P., König, P., Frauenheim, T., Schulten, K., Thiel, W., Tajkhorshid, E., Elstner, M.: Color tuning in rhodopsins: the mechanism for the spectral shift between bacteriorhodopsin and sensory rhodopsin II. J. Am. Chem. Soc. 128, 10808–10818 (2006)
- 117. Rajamani, R., Gao, J.: Combined QM/MM study of the opsin shift in bacteriorhodopsin. J. Comput. Chem. 23(1), 96–105 (2002)
- 118. Warshel, A., Chu, Z.T.: Nature of the surface crossing process in bacteriorhodopsin: computer simulations of the quantum dynamics of the primary photochemical event. J. Phys. Chem. B **105**, 9857–9871 (2001)
- 119. Röhrig, U.F., Sebastiani, D.: Nmr chemical shifts of the rhodopsin chromophore in the dark state and in bathorhodopsin: a hybrid qm/mm molecular dynamics study. J. Phys. Chem. B **112**, 1267–1274 (2008)
- 120. Yang, X., Fu, Y.J., Wang, X.B., Slavicek, P., Mucha, M., Jungwirth, P., Wang, L.S.: Solvent-mediated folding of a doubly charged anion. J. Am. Chem. Soc. 126(3), 876–883 (2004)
- 121. Plasser, F., Barbatti, M., Aquino, A., Lischka, H.: Electronically excited states and photodynamics: a continuing challenge. Theor. Chem. Acc. 131(1), 1–14 (2012)
- 122. Tully, J.C.: Perspective: Nonadiabatic dynamics theory. J. Chem. Phys. 137(22), 22A301 (2012)

4 Theoretical Methods 65

123. Tully, J.C., Preston, R.K.: Trajectory surface hopping approach to nonadiabatic molecular collisions - reaction of h+ with d2. J. Chem. Phys. **55**(2), 562 (1971)

- 124. Martinez, T.J.: Insights for light-driven molecular devices from ab initio multiple spawning excited-state dynamics of organic and biological chromophores. Acc. Chem. Res. **39**(2), 119–126 (2006)
- 125. Lasorne, B., Robb, M.A., Worth, G.A.: Direct quantum dynamics using variational multi-configuration gaussian wavepackets. Implementation details and test case. Phys. Chem. Chem. Phys. **9**(25), 3210–3227 (2007)
- Ruckenbauer, M., Barbatti, M., Mueller, T., Lischka, H.: Nonadiabatic photodynamics of a retinal model in polar and nonpolar environment. J. Phys. Chem. A 117(13), 2790–2799 (2013)
- 127. Fabiano, E., Groenhof, G., Thiel, W.: Approximate switching algorithms for trajectory surface hopping. Chem. Phys. **351**(1–3), 111–116 (2008)
- 128. Fabiano, E., Keal, T.W., Thiel, W.: Implementation of surface hopping molecular dynamics using semiempirical methods. Chem. Phys. **349**, 334–347 (2008). doi:10.1016/j.chemphys. 2008.01.044
- 129. Warshel, A., Chu, Z.T., Hwang, J.K.: The dynamics of the primary event in rhodopsin revisited. Chem. Phys. **158**, 303–314 (1991)
- 130. Weingart, O., Schapiro, I., Buss, V.: Photochemistry of visual pigment chromophore models by ab initio molecular dynamics. J. Phys. Chem. B **111**(14), 3782–3788 (2007)
- 131. Toniolo, A., Olsen, S., Manohar, L., Martinez, T.J.: Conical intersection dynamics in solution: the chromophore of green fluorescent protein. Faraday Discuss. **127**, 149–163 (2004)
- Schäfer, L.V., Groenhof, G., Boggio-Pasqua, M., Robb, M.A., Grubmüller, H.: Chromophore protonation state controls photoswitching of the fluoroprotein asfp595. PLoS Comput. Biol. 4 (3), e1000034 (2008)
- 133. Barbatti, M., Lan, Z.G., Crespo-Otero, R., Szymczak, J.J., Lischka, H., Thiel, W.: Critical appraisal of excited state nonadiabatic dynamics simulations of 9h-adenine. J. Chem. Phys. 137(22), 22A503 (2012)
- 134. Lan, Z.G., Fabiano, E., Thiel, W.: Photoinduced nonadiabatic dynamics of 9h-guanine. ChemPhysChem 10(8), 1225–1229 (2009)
- 135. Lan, Z.G., Fabiano, E., Thiel, W.: Photoinduced nonadiabatic dynamics of pyrimidine nucleobases: on-the-fly surface-hopping study with semiempirical methods. J. Phys. Chem. B 113(11), 3548–3555 (2009)
- 136. Virshup, A.M., Punwong, C., Pogorelov, T.V., Lindquist, B.A., Ko, C., Martinez, T.J.: Photodynamics in complex environments: ab initio multiple spawning quantum mechanical/molecular mechanical dynamics. J. Phys. Chem. B **113**(11), 3280–3291 (2009)
- Levine, B.G., Martinez, T.J.: Isomerization through conical intersections. Annu. Rev. Phys. Chem. 58, 585–612 (2007)

5

Photo-initiated Dynamics and Spectroscopy of the Deprotonated Green Fluorescent Protein Chromophore

Anastasia V. Bochenkova and Lars H. Andersen

Abstract

This chapter combines recent advances in understanding the photophysics of the chromophore anion of the Green Fluorescent Protein (GFP) from the jellyfish Aequorea Victoria. GFP and its homologues are widely used for in vivo labeling in biology through their remarkable fluorescent properties. Besides longtimescale light emission, the GFP proteins also show an unusual diversity in terms of their non-radiative excited-state decay channels, including ultrafast conical intersection dynamics and light-driven electron transfer, where GFP acts as an electron donor in photochemical reactions. Knowledge of intrinsic properties of the GFP photoabsorbing molecular unit is a prerequisite in understanding the atomic-scale interactions that play a key role for the diverse functioning of these proteins. Here, we show how recent developments in action and photoelectron spectroscopy combined with state-of-the-art electronic structure theory provide valuable insights into photo-initiated quantum dynamics and enable to disclose mechanisms of multiple intrinsic excited-state decay channels in the bare GFP chromophore anion. When taken out of the protein, the deprotonated chromophore exhibits the ultrafast excited state dynamics, where non-radiative decay occurs on a (sub)picosecond timescale. Deactivation includes resonant electron emission and fast internal conversion followed by slow statistical decay in the vibrationally hot ground state. Remarkably, both electronic and nuclear excited-state decay channels may here efficiently compete with each other in spite of their inherently different intrinsic timescales. The reason behind this is an efficient coupling between the nuclear and electronic motion in the photo-initiated dynamics, where the energy may be transferred from nuclei to electrons and from electrons to nuclei mediated by specific vibrational modes. Prompt photodetachment occurs indirectly through vibrational autodetachment out of the first excited state within the energy range

A.V. Bochenkova (⋈) • L.H. Andersen

Department of Physics and Astronomy, Aarhus University, 8000 Aarhus C, Denmark e-mail: bochenkova@phys.au.dk

of the corresponding absorption band. Time-resolved transient photoelectron spectroscopy confirms the ultrafast decay of the excited-state population through internal conversion, which here proceeds through a conical intersection seam. We discuss the ways, by which the GFP proteins may use such efficient electron-to-nuclei coupling revealed in the intrinsic excited-state decay of their chromophore, to guide the photochemistry and photophysics upon which their functioning is based.

5.1 Introduction

Light-induced processes are ubiquitous in nature. Interaction of molecules with light is central to vital activity of living organisms and human beings. Photosynthesis, vision in vertebrates, solar energy harvesting and conversion, and light sensing are remarkably efficient processes, and much focus has been on elucidating the role played by the protein environment in their primary events which occur on a timescale down to sub-picoseconds. Photoactive proteins attract immense attention not only because of their crucial role for the functioning of living organisms, but they also provide a stage for studying some very elementary processes in nature, such as photoinduced isomerisation, light-driven electron transfer, and charge separation. These fundamental events, initiated as a primary response to light absorption, are ultrafast and, at the same time, are rate-determining inside the proteins. In this respect, the intrinsic photoresponse of light-absorbing molecular units of these proteins, and the characteristic timescales of their photo-initiated dynamics are of utmost importance as they provide a well-defined reference to the functioning of the proteins.

The wild-type GFP is a 27 kDa protein composed of 238 amino acids. The protein has an 11-stranded β -barrel structure with a single α -helix running through the center [1]. The heart of the protein is the chromophore which is formed at the central helix, well shielded by the hydrophobic core of the protein (see Fig. 5.1). The GFP chromophore is a 4-(p-hydroxybenzylidene)-5-imidazolinone (pHBI) derivative formed by autocatalytic cyclisation of the Ser65-Tyr66-Gly67 tripeptide [2, 3]. One important role of the protein environment is to dictate the balance between a neutral chromophore and a deprotonated phenolate ion. Numerous wildtype and mutant GFP-like proteins contain solely the anionic chromophore and are therefore characterised by a single-peak excitation, as seen in one of the most popular GFPs, enhanced eGFP [4]. In wild-type GFP, the ratio between the two forms is six to one in the electronic ground state [1]. Therefore, the absorption spectrum has two major peaks in the visible range, around 390 nm (neutral form) and 480 nm (anion). Figure 5.2 shows structures of the two chromophores' binding pockets of the wild-type GFP protein and of the S65T-GFP mutant. The mutation of serine to threonine, which is introduced in eGFP, favors the anionic form due to rearrangement of a hydrogen-bonding network in the vicinity of the chromophore.

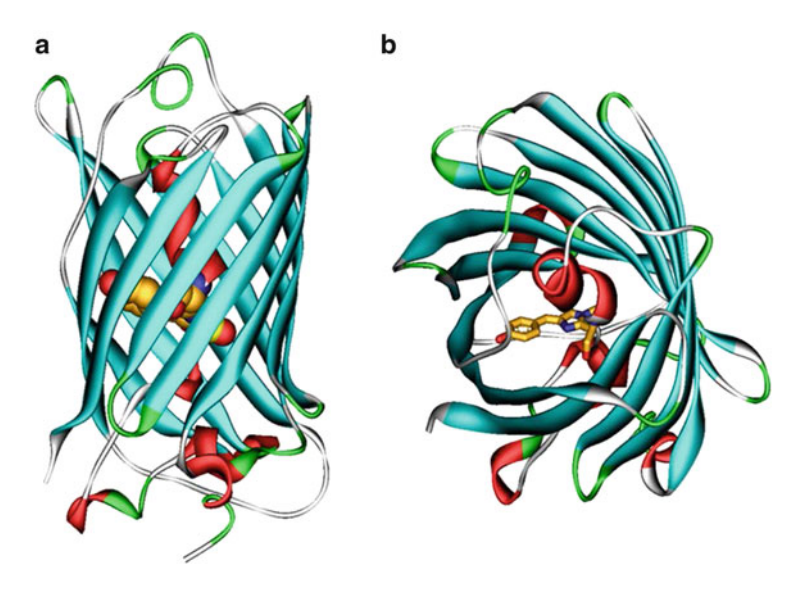


Fig. 5.1 X-ray structure of the wild-type GFP protein (PBD entry code 1GFL): *side view* (**a**) and *top view* (**b**). The β -barrel is represented by the *cyan ribbons* and the α -helix is shown in *red*. The chromophore is shown as *spheres* (**a**) and *sticks* (**b**). The colour code corresponds to the C, O, and N atoms depicted in *orange*, *red* and *blue*, respectively

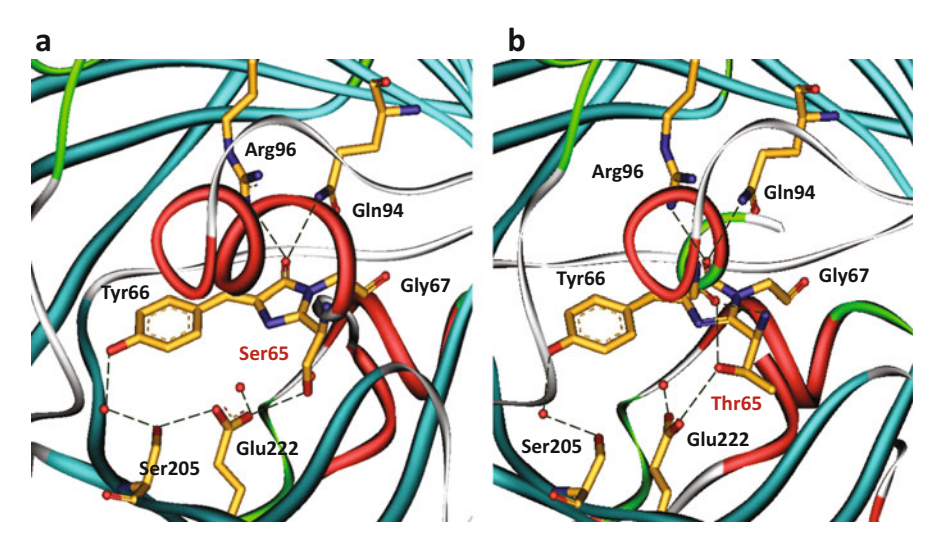


Fig. 5.2 Hydrogen-bonding network in the chromophore's binding pocket of the wild-type GFP [PBD entry code 1GFL, (a)] and of the S65T-GFP mutant [PBD entry code 1EMA, (b)]. Shown are only heavy atoms according to the corresponding X-ray structures. The wild-type GFP favours the neutral form of the chromophore, whereas the Ser65Thr mutation stabilises the anion and the Glu222 residue becomes protonated and neutral

The neutral chromophore exhibits increased acidity in the excited state [5]. An excited-state proton transfer occurring on the sub-picosecond timescale is well known to result in a remarkable blue-to-green light conversion in absorption/emission of the wild-type GFP protein [6, 7]. Out of the 238 amino acids, Gly67 is essential for the formation of the chromophore, but others form by substitution the basic principles behind the development of the many GFP colour variants that are so widely used as *in vivo* fluorescent tags [4]. For this purpose numerous studies have been aimed at fine-tuning the photophysical properties of fluorescent proteins, in particular to work in the far-red spectral regions to enable a mammalian deep tissue imaging [8, 9].

The GFP is strongly fluorescent because the conjugated system of the chromophore with the two rings exists in a nearly co-planar orientation in the *cis*-configuration in the protein. The planarity is maintained by a network of hydrogen bonds which prevents the rings from twisting after the chromophore is photo-excited. In the gas-phase, as well as in solutions, nothing, however, prevents the chromophore in the excited state from returning to the ground state by internal conversion without emission of fluorescent light, and indeed the search for gas-phase fluorescence has been unsuccessful [10]. The twisting in the central methine bridge is thought to induce a non-adiabatic coupling between the two surfaces. This results in a very fast excited-state decay via a conical intersection [11–13].

The (sub)picosecond non-radiative deactivation, which leads to efficient fluorescence quenching outside the protein environment, has extensively been studied in various solvents by time-resolved spectroscopy [14–16]. The effect of conformational freedom on the rapid internal conversion has also been studied through structural modifications of the chromophore and through adjustments of supramolecular systems [5]. All these studies strongly support the idea that internal conversion occurs through the conical intersection(s) induced by twisting in the methine bridge.

Since many GFP-like proteins are fluorescent, much focus has been on elucidating the role of the protein in suppressing the competing non-radiative channel. However, there are certain GFP homologues which are non-fluorescent, but they may reversibly be photo-activated [17, 18]. Photoinduced isomerisation is thought to be responsible for the photo-switching of these kindling fluorescent proteins. Most recent results suggest that diverse GFPs, containing anionic tyrosine-based chromophores, may also be involved in biological photoinduced electron transfer reactions [19]. Therefore, GFP-like proteins show a remarkable diversity in terms of their excited-state decay channels, thus enabling a wide range of their possible applications as fluorescent markers in bioimaging, as photoswitches in super-resolution optical microscopy and ultimately as redox sensors in living cells. Such a diversity has to be closely related to the intrinsic excited-stated decay channels of the deprotonated GFP chromophore.

Until a few years ago charged molecular systems were not amenable to experiments in their bare form due to the lack of experimental techniques. This obstacle was removed by developing new highly efficient ion-storage techniques pioneered by the Aarhus group. Since then action spectroscopy of isolated

Fig. 5.3 Chemical structure of the GFP chromophore anion, pHBDI—a dimethyl derivative of 4-(p-hydroxybenzylidene)-5-imidazolinone. The two mesomeric structures exist in a nearly perfect resonance

biological chromophores has become a common tool to gain new insights in their intrinsic photophysical properties and the atomic-scale interactions that play a key role for their functioning.

About 10 years ago, the first gas-phase absorption measurement of a deprotonated GFP-model chromophore (a dimethyl derivative of pHBI, called pHBDI, see Fig. 5.3) was performed [20]. It was found that it absorbs at about the same wavelength in vacuum and in the protein, implying that the sum of perturbations in the wild-type GFP environment has very little effect on the absorption wavelength, which to a large extent is determined by the intrinsic properties of the chromophore. To reveal a general tendency in the structureproperties relationship in this subclass of fluorescent proteins a number of isolated GFP-related model chromophores have been studied. In particular, we have examined an impact of the length of the conjugation [21] and the charge state, namely anionic [20], cationic [22] as well as a series of model neutral forms [23–25], on photoabsorption. The absorption of the GFP mutant chromophores has also been measured [26]. It is well established today that the spectral diversity (colour tuning) of fluorescent proteins is first and foremost a consequence of chemical modifications of their chromophore itself [4, 8, 27], and fine tunings are primarily achieved by non-covalent interactions with the surrounding amino acids through mutagenesis.

In a bottom-up approach we wish to understand the naked chromophore and then add perturbations like those encountered in the protein and see the photophysical consequences thereof. Fine tunings from H-bonding and Br-substitution have been investigated [28]. The effect of a spectator positive charge on the photoabsorption maximum of the neutral chromophore has also been studied [24]. It has been shown that large red shifts can be imposed by partial charge transfer to the conjugated system mediated by the presence of strong hydrogen bonds, which change considerably the local shape of the ground-state potential energy surface. The data serve to understand the effects of perturbations in proteins, but importantly, they also serve to guide and test quantum chemistry calculations on large molecular systems that are challenging to theory. As the confident level of theory increases, calculations certainly provide an important tool for understanding gas and liquid-phase measurements as well as whole proteins.

Since the first measurements, action spectroscopy has extensively been used to study the absorption of biologically relevant chromophores and, in particular, the GFP chromophore anion in the gas phase. Various ion storage techniques, including electrostatic storage rings [29, 30], quadrupole ion traps [10, 31] and ion cyclotron resonance cells [32], along with detection of both ionic [10, 31] and neutral fragments [29, 30], as well as parent ions loss [10, 31, 32] after photoexcitation have been used. However, several precautions should apply when using a photoresponse of these chromophores for retrieving their absorption profiles. In particular, a multiple photon absorption and an electron autodetachment channel in the case of anions have to be taken into account. Measurements by the Toronto group [10, 31] showed loss of stored chromophore ions after photoexcitation that could not be accounted for by the recorded ionic fragments. This loss was suggested to be due to electron detachment which would produce undetectable neutral chromophores that are lost from the ion trap. Moreover, structures in the ion-loss signal was observed, the origin of which might be related to the influence of vibrations. Recent photoelectron spectroscopy studies have directly confirmed that electron emission is one of the deactivation channels in the bare anion [33–35]. Experiments carried out by the Zurich group [32] also bring up a discussion of the effect of multiple photon absorption and suggest that an intrinsic absorption maximum is blue-shifted compared to earlier results, even though such a conclusion was drawn in the case of ions trapped up to 200 s with an unknown impact of IR radiative cooling on the observed absorption profiles.

A persistent interest in the action spectroscopy of the pHBDI anion underscores an enriched intrinsic photo-induced dynamics of the chromophore as well as difficulties in correct interpretation of the results reported hitherto. The reliability of action spectroscopy in revealing the absorption profiles of the bare GFP chromophore anion is one of the most important issues. We highlight a recent progress in studying the intrinsic photoresponse of the chromophore by introducing *time-resolved* measurements based on the new experimental detection techniques, where one is able to record action spectra according to the timescale at which the action takes place. Thus, neutral products belonging to prompt electron emission as well as delayed ones are now detected separately. When combined with theoretical account of observed action spectra, this new time-domain approach based on direct detection, in which spectral properties of the two different channels are simultaneously, but separately recorded, enables to disclose mechanisms of intrinsic excited-state decay channels in the GFP chromophore anion.

5.2 Time-Resolved Action Spectroscopy

5.2.1 Prompt and Delayed Action at ELISA

We wish to be able to register the event of a photon being absorbed by a molecule. The technique that has been developing for this over the years involves registration of some form of 'action'; hence the name is action spectroscopy. The action is typically a break-up of the molecule (fragmentation), or in the case of an anion, it may be the emission of an electron. In action spectroscopy, molecular fragments, or

electrons, are much easier to detect than the change in photon flux through a thin gas-phase sample. Naturally, the actual decay/action depends on the molecule and the absorbed energy from a single photon or any given number of photons. The detectable action may happen on electronically excited states or after the return to the electronic ground state. The advantage of using the ion-storage ring technique is that it allows us to track decay processes over a long time span, unlike in a single-pass setup, where distances and ion velocities typically define a fixed and rather narrow time window.

Action spectroscopy may be used to obtain information about the location of electronically excited states, as it has indeed been a prime goal for quite some time. Of particular importance in relation to molecular action is also the fact that timescales, at which action takes place, branching ratios in decay channels, their wavelength dependence, etc. bring important information about the photo-initiated molecular dynamics and enable disclosure of intra-molecular mechanisms, like internal conversion and non-adiabatic energy-sharing mechanisms between electronic and nuclear degrees of freedom [36].

To facilitate detection of instantaneous action as well as delayed action on the ms-timescale, different detectors are being applied at the electrostatic ion-storage ring ELISA. Most recently, a new Secondary Emission Detector (SED) was installed at ELISA [37]. By this detector, a glass plate is placed into the path of the laser light and the neutral particles [38]. The glass is transparent for the laser light used here, but particles create secondary electrons which are accelerated towards and registered by a channeltron detector. To avoid charging of the glass and to be able to accelerate the secondary electrons, the plate has a conductive coating (In_2O_3 :Sn). The detector arrangement not only increases the time resolution of photofragmentation studies at ELISA, but most importantly it also allows for a dead-time free detection of fragments produced immediately after photoabsorption. A multi-channel plate detector (MCP) is located after the first straight section in ELISA (see Fig. 5.4) to count neutral dissociation fragments leaving the ring. This detector only registers fragmentation events that happen later than about a quarter of a revolution time.

A given experimental setup based on a molecular 'action' has a characteristic time window, where the action may be monitored. In the present experiment, we detect prompt action with no time delay by the SED arrangement, and at the same time with the MCP detector we detect action at times down to about a quarter of a revolution time (here $\sim 15~\mu s$) and up to tens of ms after laser excitation (limited by the time, where radiative cooling sets in and inhibits the action, *i.e.*, the creation of neutral particles).

The many milliseconds of storage in vacuum prior to photoexcitation ensure that we start with a molecule occupying the electronic ground state S_0 . In the case of the GFP chromophore anion at room temperature, the total vibrational energy is about 0.3 eV (see Fig. 5.5) distributed over the 75 vibrational modes [29], so the average energy per mode is about 30 cm⁻¹, leaving many medium and high-energy oscillators in the vibrational ground state. At the same time, low-frequency soft modes may be excited (see Fig. 5.6). Inspection of Fig. 5.5 reveals that a reduction

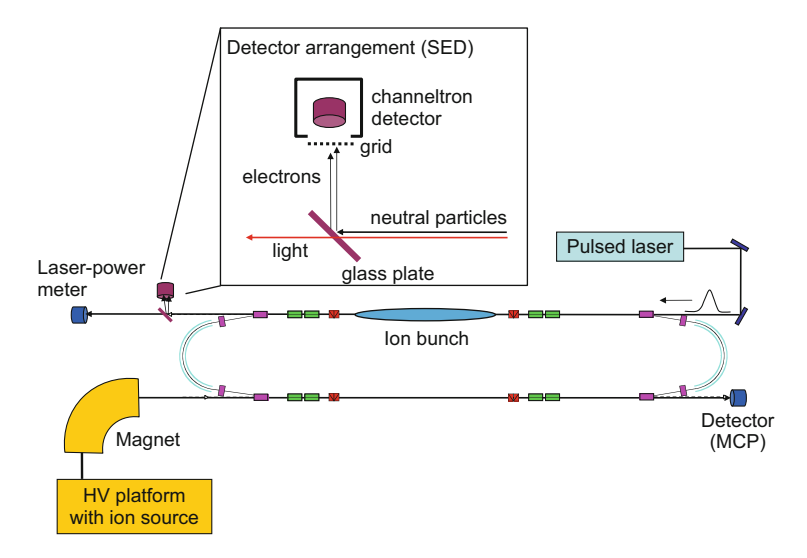


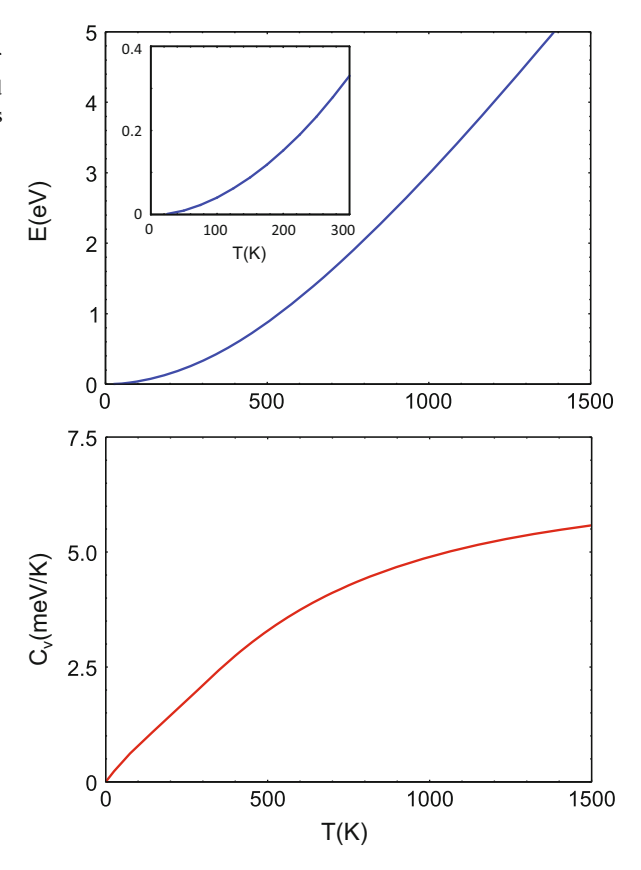
Fig. 5.4 Schematic of the Electrostatic Ion Storage ring (ELISA). An electrospray-ion source is used to generate chromophore ions in the gas phase. Two detectors are used to monitor the photoresponse (neutral fragments): (1) a 'delayed' multi-channel plate (MCP) detector after the first straight section and (2) a 'prompt' detector based on secondary-electron emission (SED) located in front of the laser-power meter in the section of ELISA, where the laser interaction takes place

of the ion-trap temperature (in the ion source) from 300 K to 100 K reduces the internal energy from 0.3 eV to about 0.03 eV. Inhomogeneous broadening due to structural variations around a minimum on the ground state potential energy surface may play a significant role for the width and shape of action-absorption profiles, in particular, if the ground-state potential has a rather shallow minimum. Cooling of the chromophore prior to injection into the storage ring may help in eliminating this effect. However, the absorption profiles for electronic transitions of relatively large biological chromophores are often quite broad because there may be a reasonable Franck-Condon overlap to a rather dense band of vibrationally excited levels of many degrees of freedom in the electronically excited state. Such broadening will occur even with initially cold chromophore molecules.

5.2.2 Decay Channels

Before proceeding with more experimental details we discuss possible ways the chromophore anion may respond to excitation in the present wavelength region. The situation is illustrated in Fig. 5.7. A vibrationally hot ground state anion (S_0) may be formed by fast internal conversion (IC) from the electronically excited singlet state. Being transferred to the ground state, the anion with high internal energy undergoes a fast intra-molecular internal energy redistribution (IVR) on the

Fig. 5.5 Internal energy and heat capacity as a function of temperature, calculated based on the vibrational frequencies of the GFP chromophore anion. The *inset* shows the internal energy as a function of the temperature below room temperature



timescale of picoseconds, so that anything that happens after has a statistical nature. The reason behind that is a very high vibrational level density of the anion in the S_0 state after 'heating' by one-photon absorption. The hot ground state may then proceed and decay by Arrhenius-type statistical fragmentation (SF) or by thermionic electron emission (Tem), a delayed vibrationally mediated electron ejection process [39, 40], with a relative strength that depends on the respective activation energies [41]. The Beyer-Swinehart algorithm together with calculated vibrational frequencies of the deprotonated GFP chromophore were used to calculate the vibrational level density of the anion in the S_0 state as a function of excitation energy. The density is indeed very high ($\sim 10^{27}/\text{cm}^{-1}$) at the excitation energy of 2.9 eV, corresponding to excitation at 480 nm plus 0.3 eV internal energy at room temperature (Fig. 5.5), thus creating a vibrational quasi-continuum at this energy.

We have identified negatively charged dissociation products, which by itself does not exclude the co-existence of the emission of an electron from the hot ground state. From the opening of the prompt channel at about 500 nm, one can judge that the electron affinity is about 2.5 eV. As will be discussed later, the experimental vertical detachment energy is 2.68 eV [35] and is located very close to the adiabatic

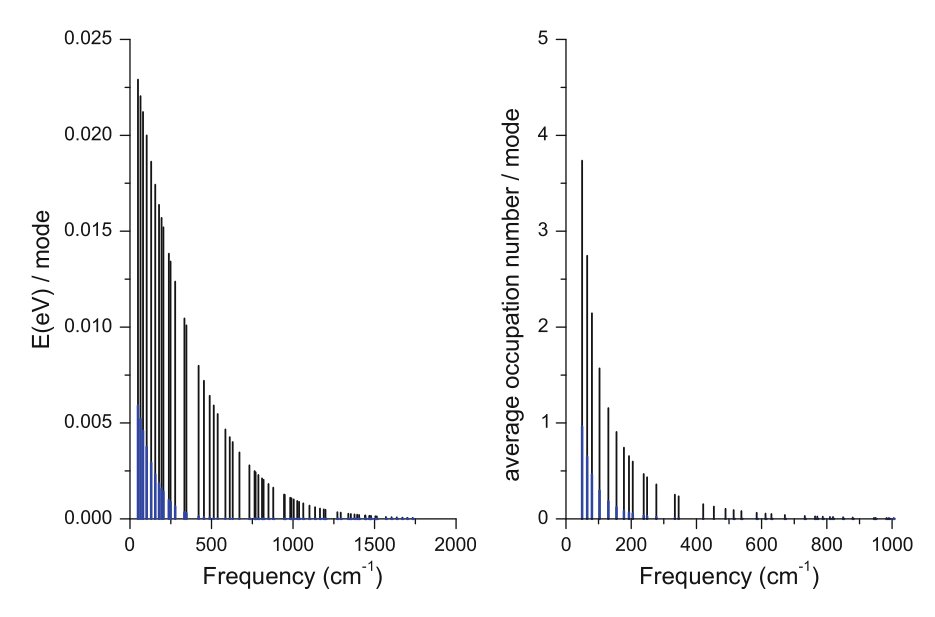


Fig. 5.6 Distribution of the internal energy over the vibrational modes (*left*) and average excitation level for each mode (*right*) of the GFP chromophore anion at 300 K (*black*) and 100 K (*blue*)

transition. It may well be that the activation energy for fragmentation is of the same order, but likely lower [29]. A B3LYP/6-311++G(d,p) calculation yields ~2.1 eV, when corrected for differences in zero-point energies. Therefore, statistical fragmentation is expected to dominate over delayed electron emission in the decay of the hot ground state. Importantly, both statistical channels, which facilitate either thermionic emission or bond fragmentation, should appear in the delayed channel, and branching ratios in the $S_{\rm 1}$ state are not affected by possible multiple pathways in the hot $S_{\rm 0}$ state.

Photodetachment may proceed *directly* into the electronic continuum, non-resonantly, or *indirectly*, resonantly via autodetachment from the S₁ excited state of the anion (here together termed photodetachment, PD). Such electronic resonances embedded in the continuum was initially treated by Fano, who showed that one might expect effects of the continuum on the line shape as well as on the resonance position [42]. The resonant PD channel may also be open for an electronically bound excited state, when a molecular anion has a particularly small electron affinity in this state. In such a case, PD may occur through vibrational resonances embedded in the electronic continuum. Distorted Fano profiles have indeed been observed for excited vibrational levels, which are strongly coupled to the electronic continuum for negatively charged small water clusters in the gas phase [40, 43]. In the case of the GFP chromophore anion, recent photoelectron spectroscopy studies strongly suggest that S₁ has indeed a bound character in the Franck-Condon region [33–35]. Therefore, photo-electron emission below the vertical detachment energy, which is observed indirectly via the prompt channel

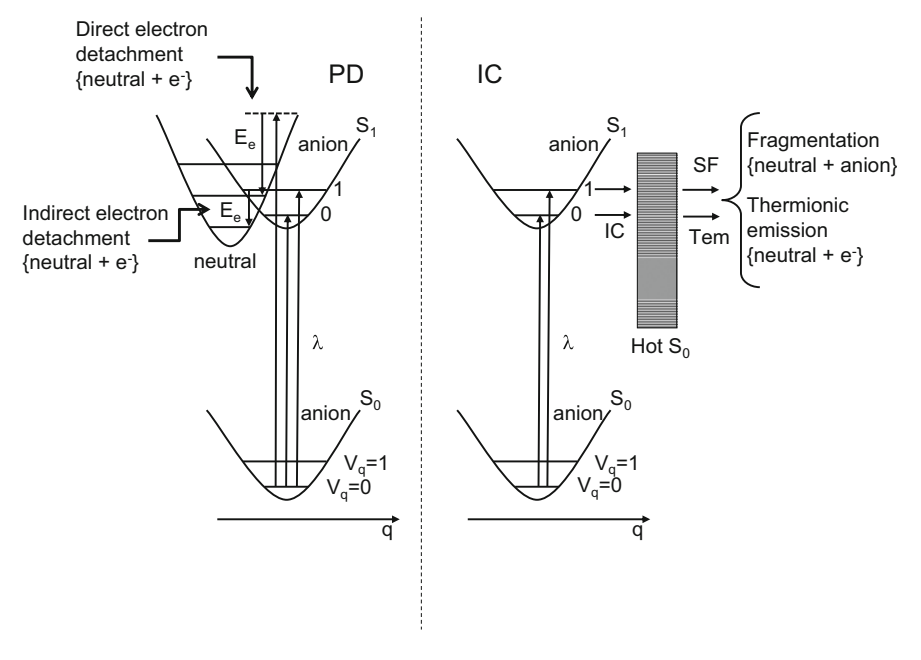


Fig. 5.7 Photoresponse after excitation in the S_1 spectral region. *Left:* photodetachment (PD) via resonant excitation to S_1 as well as non-resonant detachment directly into the continuum. *Right:* internal conversion (IC) into a vibrationally hot anion in the electronic ground state S_0 . From the hot S_0 state statistical fragmentation (SF) or thermionic electron emission (Tem) may occur. V_q denotes a vibrational mode

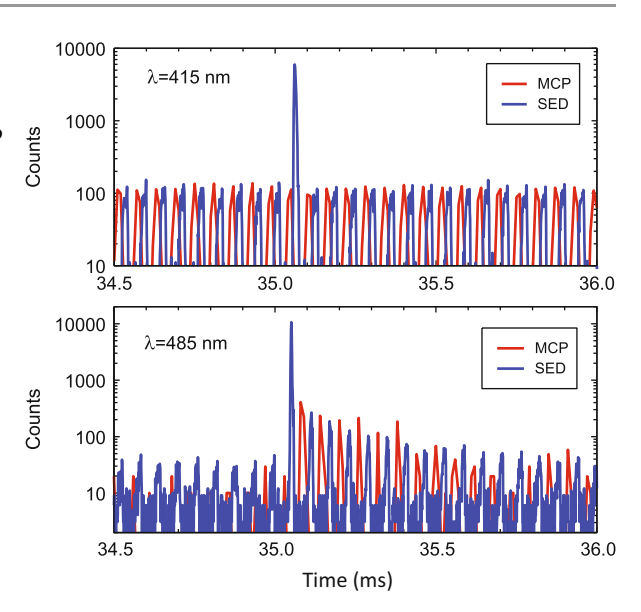
at ELISA, as well as by direct detection in a separate laboratory [35], results from prompt vibrational autodetachment (VAD) out of the first excited state of the GFP chromophore anion [36]. VAD is enabled through a non-adiabatic energy-sharing mechanism between the electronic and nuclear dynamics.

As discussed, at ELISA we are able to detect the prompt neutral chromophores from PD as well as neutral fragments created in statistical processes from the hot S_0 electronic ground state after IC. The timing information of the present experiment is unique and is used to separate the PD *versus* IC decay modes. The ratio between the two channels is related to the preference of the molecular chromophore to respond by transferring energy into the electronic degrees of freedom or into the nuclear motion.

5.2.3 Signal Detection

It is evident from Fig. 5.8 that the SED was recording a very significant prompt signal at 485 nm (close to the S_1 action absorption maximum previously registered at 479 nm (2.59 eV) [20]). A delayed signal is seen in both detectors at 485 nm, but not on any of the detectors at 415 nm, for example, where only the prompt

Fig. 5.8 Counts (arbitrary normalisation) for the GFP chromophore anion as a function of time from the two detectors in ELISA, zoomed in at the time of laser excitation, here about 35 ms after injection into ELISA. Notice the log scale on the y-axis, the significant prompt contribution in the SED detector only, and the similar delayed decay observed on both detectors



contribution persisted. There was no sign of an excess prompt contribution in the MCP at any wavelength, showing that the prompt contribution is associated with a decay time significantly shorter than a quarter of a revolution time. It was established at our single-pass setup (separate laboratory) [37] that the prompt signal was associated with a decay time shorter than 100 ns.

5.2.4 Power Dependence

It has earlier been proposed that photodetachment is operative upon absorption of a single photon by the GFP chromophore anion [10, 31]. Recently three independent groups [33–35] have reported on the photoelectron spectrum of the bare chromophore and have directly confirmed this decay mode in de-excitation of the molecular anion, which has to be registered as a prompt signal. Sequential absorption of several photons during the ns-wide laser pulse in connection with internal conversion may, however, also produce a very fast response and contribute to the prompt signal at ELISA. To establish the very nature of the prompt signal (single versus multiple-photon absorption), we measured the yield of the prompt and delayed contribution as a function of laser-pulse energy. The prompt SED yield was at low pulse energy a linear function of the laser-pulse energy (Fig. 5.9), ensuring that at low pulse energies we were to a good approximation having single-photon absorption conditions for the fast channel. The delayed channel also showed an approximate linear growth with the laser pulse energy. A fit to a Poisson distribution (n = 2), however, confirmed our earlier findings [20] that it was indeed due to a two-photon process, as it was also reported by the Toronto group [10].

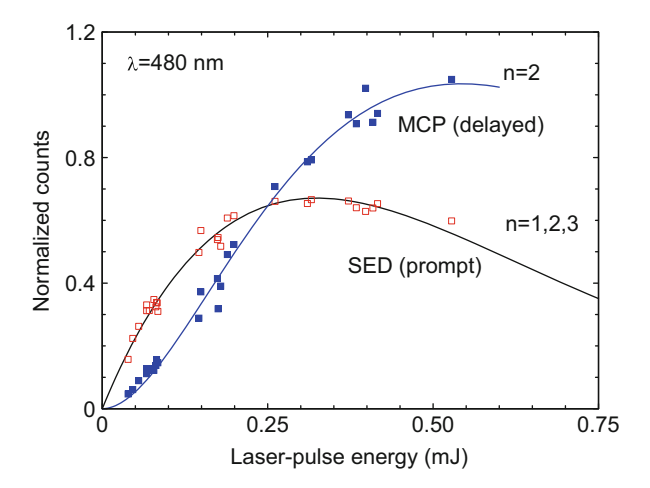


Fig. 5.9 Counts normalised to the number of stored ions in ELISA (arbitrary scale) as a function of laser-pulse energy for the GFP chromophore anion. Shown are data from the SED (prompt contribution) and the MCP detector (delayed contribution). The *solid curves* are fits with the Poisson distribution with n=1,2,3 in the prompt case and n=2 in the delayed case. Note, that the two-photon yield appears approximately linear with laser-pulse energy up to about 0.5 mJ/pulse

We assume that photons are absorbed independently of previous absorptions and use Poisson statistics:

$$P(n) = (\nu)^n / n! \times exp(-\nu). \tag{5.1}$$

Here, v is the average number of photons absorbed during the laser pulse, which is given by (cross section times flux):

$$\nu = \sigma \frac{E_{laser} \lambda}{Ahc},\tag{5.2}$$

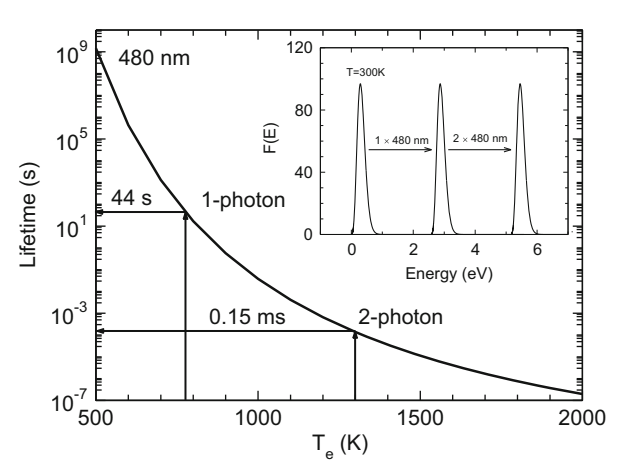
where E_{laser} is the laser-pulse energy, A is the overlap area, h is Planck's constant, and c is the speed of light.

The power dependence of the yield of neutral photo-fragments is presented in Fig. 5.9. From fits we obtain $\nu = (3.3 \pm 0.3) \times E_{laser}$ [mJ]. With an estimated effective beam-overlap area $A = 70 \times 10^{-3} \ cm^2$ (0.3 cm laser-beam diameter), we obtain an absorption cross section of $1.0 \times 10^{-16} \ cm^2$ and the relation:

$$\nu = 7.1 \times 10^{-3} \times E_{laser}[mJ]\lambda[nm]. \tag{5.3}$$

It is readily seen from this equation, as well as from Fig. 5.9, that multiple photon-absorption plays a role already at pulse energies as low as 0.1 mJ. To analyze the situation, consider the data at 485 nm, displayed in Fig. 5.8. The observed delayed action in the two detectors only results from n = 2 fragmentation

Fig. 5.10 Statistical dissociation lifetimes as a function of emission temperature (T_e). The *inset* shows the energy distribution at room temperature, and after one and two-photon absorption. Listed are the micro-canonical temperatures as well as the emission temperatures (after a first order finite heat-bath correction) at the peaks of the distributions after one and two-photon absorption



processes, since the n=1 fragmentation contribution is too slow (see Fig. 5.10), and the n=3 contribution is decaying so fast that it contributes to the prompt signal only. Hence, for the fast prompt channel, $n=1,2,3,\ldots$ processes all contribute, where n=1 is ascribed only to PD, and several factors, therefore, make the prompt action dominate over the delayed action (see Fig. 5.8).

5.2.5 Lifetimes and Action

To understand the different nature of the prompt and delayed channels we here discuss the situation, where photons are absorbed near the $S_0 \rightarrow S_1$ transition. Consider first the canonical internal energy distribution at room temperature in the ion source. It is approximately Gaussian, peaking at 0.3 eV with a width of 0.3 eV (FWHM). After the ions are sent into ELISA they travel in ultra-high vacuum and each molecule conserves its energy. The absorption of n photons increases the energy by nhv and shifts the energy profile F(E) accordingly, as illustrated in Fig. 5.10. From the vibrational frequencies we calculate the micro-canonical temperatures (T_m) equal to 995 K (n = 1) and 1,490 K (n = 2). To account for the temperature change due to energy loss upon dissociation, a first order finite heat-bath correction is applied [44], and the emission temperatures (T_e) become 776 K (n = 1) and 1,298 K (n = 2).

The Arrhenius rate constant $k=A \times e^{-E_a/k_BT_e}$ may be used to estimate the statistical dissociation lifetimes [29]. Here, the statistical fragmentation results in methyl loss from the imidazolinone ring of the chromophore. To assign the observed action to a particular time window, we use the calculated activation energy of 2.1 eV [29] and a pre-exponential factor $A=10^{12} \, \mathrm{s}^{-1}$. We then assign the sub-ms lifetime decay observed at excitation energies near the $S_0 \to S_1$ transition shown in Fig. 5.8 to a two-photon absorption process. This is in full accord with the observed power-dependence presented in Fig. 5.9. The calculated

rate constant reproduces the observed decay time of the SF channel. It also explains why no delayed *one-photon* signal is observed. The associated lifetime is much too long and there is basically no decays in the time-interval of observation. This illustrates very well that the order of absorption, single *versus* multiple-photon, is largely dictated by the time-window of observation in the experiment. By studying sub-ms action one basically avoids problems with radiative cooling of the hot intermediate molecules. With an instrument, where tens-of-seconds components are monitored (for example, for n = 1 absorption), one would have to consider the loss of action (dissociation) due to infrared cooling.

5.3 Time-Resolved Action and Photoelectron Spectra

In the following, the experimental spectroscopic data for the isolated GFP chromophore anion will be discussed. We first consider the spectral region near the first electronically excited state (S_1) , where both prompt and delayed action are observed. Then, additional information is obtained by also considering our photoelectron measurements at a variety of different wavelengths within and beyond the S_1 spectral region [35].

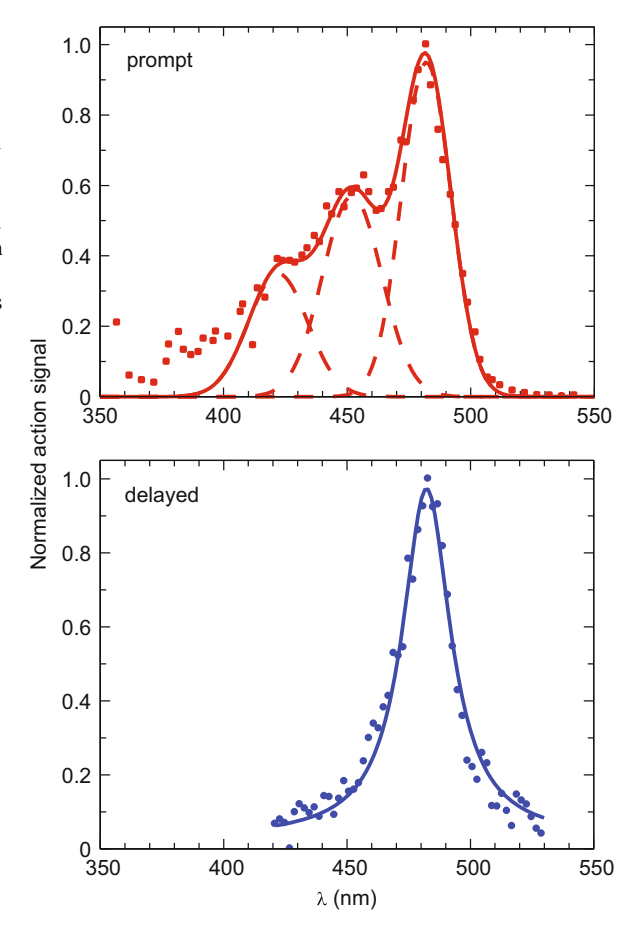
5.3.1 Action Spectra Near the S₁ State

The action spectra of absorption for the deprotonated GFP chromophore near the S_1 state are shown in Fig. 5.11. The lower graph shows the spectrum for the delayed signal of the MCP (see Fig. 5.8). The maximum of absorption (482 nm) is in good agreement with earlier measurements at ELISA (479 nm) [29] and the recent measurement in a quadrupole-ion trap (482.5 nm) [10].

The upper graph shows the prompt spectrum of the SED (Fig. 5.8). It is seen that the data (prompt and delayed) have a maximum at the same wavelength (482 nm). The prompt spectrum has major adjacent shoulders to the blue side of the main peak at 452 nm and 422 nm and a weak one at 472 nm. Similar features were observed at the quadrupole ion trap [10, 31] with almost the same wavelength assignments (470, 450 and 425 nm). The identical peak position in the prompt and delayed channels at 482 nm strongly indicates that we are addressing the same S_1 state through two different decay channels.

It is important to note that there is a substantial contribution from a multiplephoton absorption to the main peak of the prompt spectrum. By comparing the red side of the prompt and delayed spectra, it is realised that heating by one or two (multiple) photons does not alter much the absorption near threshold energies for this chromophore. This can easily be rationalised in terms of sequential *resonant* absorptions. The absorption of the second photon at a given wavelength can only be possible if the first photon is absorbed. Thus, the probability of sequential absorptions is defined as a product of independent probabilities. If we assume vanishing spectral overlap of individual absorptions before and after heating by

Fig. 5.11 Upper graph: the action absorption spectrum associated with the prompt channel. The maximum is at 482 nm. Shoulders at 452 nm and 422 nm are indicated. Lower graph: the action absorption spectrum obtained with the delayed detector with a maximum at 482 nm (a similar delayed spectrum was obtained from the SED data)



the first photon, the final two-photon cross-section would be close to zero. In fact, the first absorption maximum strongly suggests that the 0–0 transition is close to 482 nm, provided that changes in equilibrium structures in the S_0 and S_1 excited states enable a sufficient Franck-Condon overlap of zero vibrational levels. This is indeed the case as shown recently [45]. Therefore, the red-sided spectral feature at 482 nm, which appears in both action spectra, is closely connected to that of a true one-photon absorption.

The delayed channel essentially vanishes at wavelengths below 450 nm. The comparison of the blue parts of the spectra strongly supports the idea that the PD mechanism changes above a certain energy, so that electron emission becomes a dominating channel with a higher rate that prevents internal conversion and, as a result, further sequential photon absorptions and statistical fragmentation. In this case, a true one-photon absorption profile is directly revealed in the blue-part of the prompt action spectra. What has to be specifically noted, however, is that due to the multiple-photon nature of the main peak in the prompt spectrum, its relative height

might be somewhat altered compared to that of a 'true' one-photon absorption spectrum. An invaluable support to the experimental results is provided by theoretical simulations of the one-photon absorption profile, as will be discussed below. However, state-of-the-art action spectroscopy is, beyond no doubt, a highly reliable tool for unraveling a substantial information about main transitions in one-photon absorption profiles.

5.3.2 Photo-electron Spectra

The prompt action absorption spectrum obtained at ELISA only indirectly shows that electron detachment is operative. To investigate this in greater detail we measured photo-electron spectra of the deprotonated GFP chromophore at several wavelengths within and beyond the first photo-absorption band. These measurements give the vertical detachment energy (VDE), and, importantly, they also reveal a competition between direct and indirect electron emission, which are alternative 'action' routes to internal conversion (see Fig. 5.7). The direct and indirect electron emission channels have different signatures in the photo-electron spectra, which make their relative importance evident.

The photoelectron data presented here have been obtained at the SEP-II laboratory [46] at the Department of Physics and Astronomy, Aarhus University. A nano-second laser is used to create photoelectrons from the deprotonated HBDI chromophore. The electrons are accelerated under velocity-map imaging conditions towards a Multi-Channel Plate (MCP) detector (labeled E-MCP in Fig. 5.12), where their position and time-of-flight are recorded. The main ion beam and neutral fragments pass through a hole in the center of the E-MCP detector. A deflector is used to steer away the main ion beam after the electron spectrometer, while the neutral fragments are counted by a second MCP detector. Thus, the position of electrons and the time-of flight of both the electrons and neutral molecules are measured. Photodetachment results in very low energy electrons, which under normal operating conditions continue co-linearly with the ion beam and exit the spectrometer region undetectable through the hole in the center of the detector. Therefore, a small magnetic field has been introduced, which causes the electrons to be slightly deflected from the central ion-beam axis and hit the detector.

A Monte-Carlo algorithm is used to produce the electron-energy distribution (Fig. 5.13) from the measured radial distribution [35]. At low photon energy, the data consists of a low-energy peak, whose shape essentially does not change with wavelength. This fact clearly indicates that PD here occurs resonantly through vibrational autodetachment out of the S_1 state of the molecular anion:

$$\hbar\omega + S_0(v) \to S_1(v') \to D_0(v'') + e^-,$$
(5.4)

which we denote as 'indirect' electron emission. The low-energy group has a tail extending up to ~ 0.3 eV corresponding to the average thermal energy of the chromophore molecules.

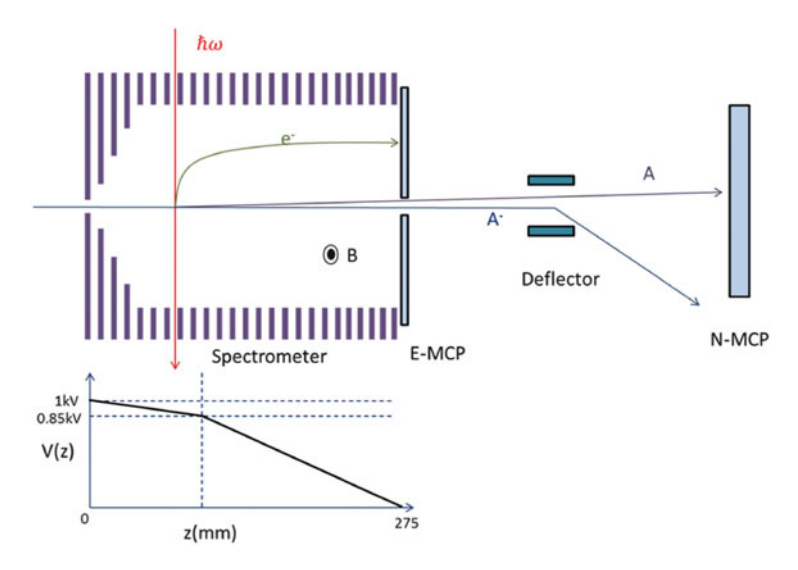


Fig. 5.12 Schematic illustration of the interaction region and the positions of detectors in the experiment

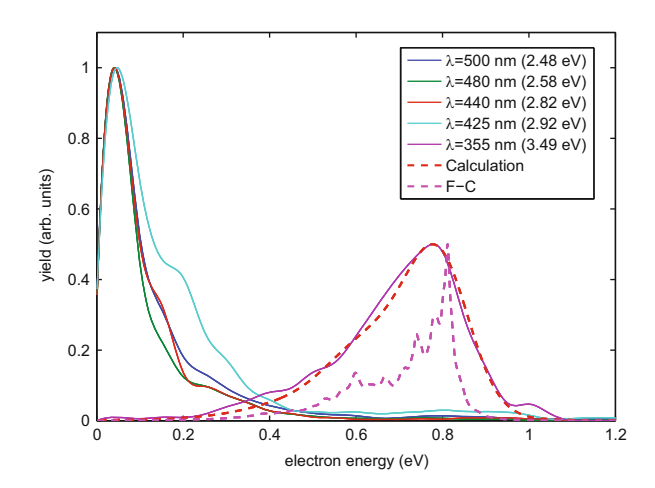


Fig. 5.13 Photoelectron energy distribution for the GFP chromophore anion as a function of excitation wavelength. The simulated spectra for the non-resonant PD channel are shown as the *dashed lines*: the S_0/D_0 profile at room temperature (*purple*) and the one convoluted according to the experimental resolution (*red*). Reproduced from Ref. [35]

Alternatively, the low energy electrons could result from thermionic emission after internal conversion, where electrons are emitted from the hot ground state [33]. In thermionic emission, the energy distribution of the emitted electrons should alter with changing wave-length, which has not been observed. The timescale for thermionic emission is long—tens of microseconds or longer [20, 47]. The fact that

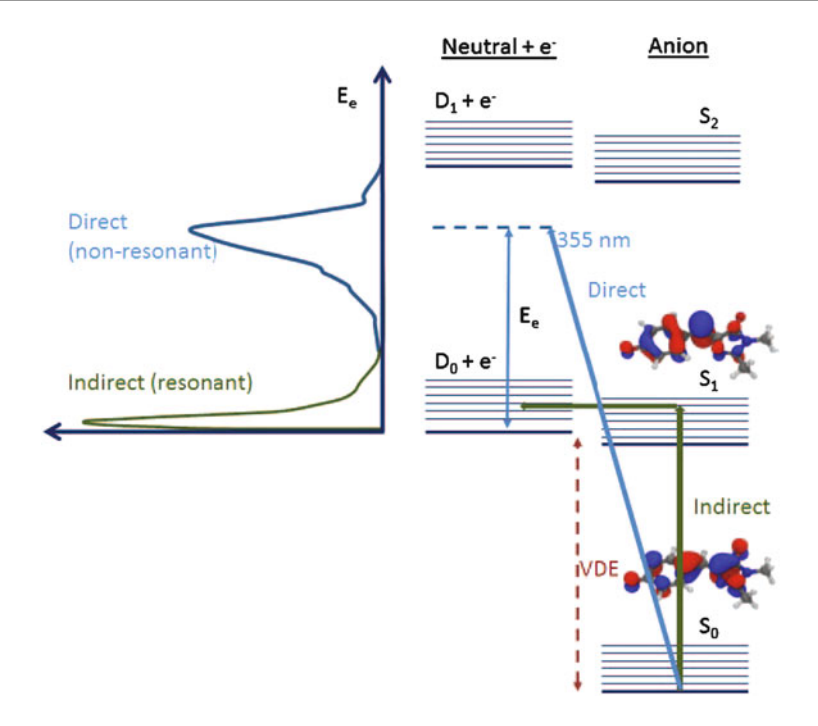


Fig. 5.14 Direct and indirect electron emission shown schematically. S_0 is the electronic ground state, and S_1 is the first electronically excited state of the anion. D_0 is the ground state of the neutral chromophore. Reproduced from Ref. 35

no sign of thermionic emission is observed here may be a consequence of our instrument configuration, where the keV ions will pass through the focus of the electron spectrometer on the sub μ s timescale, and delayed emission of electrons will hence not be registered (at least, not giving a meaningful radial distribution on the detector).

With increasing photon energy an additional high-energy peak appears, the position of which shifts with photon energy. It corresponds to direct electron emission, which completely dominates at higher photon energy (355 nm) beyond the $S_0 \to S_1$ absorption band:

$$\hbar\omega + S_0(v) \to D_0(v') + e^-. \tag{5.5}$$

At 355 nm indirect electron emission is no longer seen, since the excitation is not resonant with any electronically excited anion states (Fig. 5.14).

The width of the non-resonant peak in the photoelectron spectrum is determined by the vibrational structure of the $S_0 \rightarrow D_0 + \mathrm{e}^-$ electronic transition. The Frank-Condon envelope takes into account the initial vibrational levels of the anions which are populated at room temperature as well as the many accessible vibrational levels of the neutral. The Frank-Condon envelope of the S_0 to D_0 transition was

calculated using a time-domain formalism based on Fourier transforms of the Lax's autocorrelation function within the double harmonic parallel-mode approximation [48]. Geometry parameters and vibrational frequencies in the ground electronic states of the anion and neutral radical were found using the PBE0/(aug)-cc-pVDZ functional in the frame of the Firefly quantum chemistry package [49]. As the Frank-Condon envelope only determines the shape of the electron energy distribution and not the absolute position in energy, the calculated curve was shifted to match the experimental data. Indeed, good correspondence between experiment and theory can be made. The resulting VDE is determined to be 2.68 ± 0.1 eV, 0.04 eV lower than obtained from the peak position of the experimental data in Fig. 5.13. This value is slightly lower than the recently reported value of 2.85 ± 0.1 eV [34] and 2.8 ± 0.1 eV [33], but within the combined error bars.

Combining the information from the time-resolved action spectra and the photoelectron spectra, we conclude that the S_1 anionic state is a bound excited state with a binding energy of only ~0.1 eV. Photodetachment in the spectral region of this state proceeds by indirect (resonant) excitation to S_1 followed by vibrational autodetachment into the continuum of the neutral D_0 ground state. Internal energy residing in the chromophore makes electron emission possible even below the vertical detachment energy, as evident from the action spectra at long wavelengths. In regions without excited anion states, detachment proceeds directly into the electronic continuum. At the wavelength of maximum action (482 nm) we estimate that the branching ratio for internal conversion is about an order of magnitude higher than that for electron emission. At first sight this might seem surprising as electronic dynamics normally proceeds faster than nuclear dynamics. The reason for the 'slow' electron emission is that it requires a non-adiabatic coupling with the nuclear motion. In the next sections we will look into the nature of the nuclear electron dynamics, which is operative in the GFP chromophore anion.

5.4 Theoretical Account of Photo-initiated Dynamics

5.4.1 Coupling to the Electronic Continuum

Negative ions hold a special position in atomic and molecular physics, where electron correlation plays a crucial role for their stability. This gives this class of objects special properties like low electronic binding energies. Provided that the first excited state of the GFP chromophore anion is very close to the electronic continuum, it is of particular interest to access the nature of the coupling between them. The $S_0 \to S_1$ transition has a well-established $\pi - \pi^*$ character. The nature of the first excited state with respect to the corresponding detachment threshold is of utmost importance, since it predefines the fate and the lifetimes of the chromophore upon photoexcitation, and until recently it has been largely debated [33–35, 50]. To address this problem theoretically, highly accurate and highly-correlated quantum chemistry methods along with extended basis sets are required.

In general, two cases may be considered. The first excited state of the anion can be referred to as either a metastable state embedded in the electronic continuum or an electronically stable state with a particularly low electron affinity in the Franck-Condon (FC) region, as was discussed earlier. The former refers to resonances of a shape-type [51], where an electron is temporarily trapped inside the potential with a minimum embedded in the spectral continuum. The penetration through the barrier proceeds via tunneling which is solely a quantum effect. Such resonances, or quasibound states, embedded in the electronic continuum have been studied in atomic and molecular cases, where both line shape and resonance position are affected by the continuum [42, 51, 52]. The interference of a discrete autoionizing state with a continuum results in its diluting throughout the band of actual stationary states (at time equal to zero), whose profile has a width proportional to the square of the interaction strength. Special complex techniques are required for proper describing the electronic interaction of these quasi-bound states with the continuum, which should allow line widths of the resonances to be computed and not only their spectral locations [53]. In the case of the deprotonated GFP chromophore, we might expect that each vibronic transition is affected by its own continuum related to vibrational states of its neutral core. Therefore, individual resonant profiles are hidden in smooth and mostly structureless shapes of photoabsorption bands, which consist of trillions of individual transitions in the case of large isolated molecules. The true experimental shape thus constitutes a challenge for theory, as opposed to cases of atoms and simple molecules.

One way to proceed is to address a time-dependent approach and to experimentally estimate a lifetime of the autoionizing state, the inverse of which gives a line width of the resonance. We have shown that the lifetime of the GFP chromophore anion in the S_1 state is remarkably long compared to the characteristic timescales for the electronic dynamics in the emission channel, which also enables internal conversion followed by fragmentation in the ground state to occur near the threshold energies. Thus, a relatively weak coupling of the quasi-bound state to the electronic continuum is envisaged. It is worth noting that shape resonances usually have a rather short lifetime. For example, the resonance state of HCl⁻ that correlates with the bound anionic ground state [53] has a lifetime of 20 fs, as shown in the experiments, where the neutral molecule is vibrationally excited by low-energy electrons [54]. In this case, the line width is equal to 0.2 eV $(1,613 \text{ cm}^{-1})$. The lifetime of the metastable ground state of H_2^- is further reduced and is of the order of 1 fs, giving rise to a significant spectral broadening [55].

Alternatively, an electronically stable anion in the FC region with a very low electron affinity can fully support the experimental finding of the substantial lifetime in the S_1 state. Our calculated vertical detachment energy is 2.62 eV, and that places the D_0 state vertically above the S_1 state by 0.1 eV [36]. The VDE value has been calculated at the XMCQDPT2/CASSCF(14,14) level of theory within the (p-type d-aug)-cc-pVTZ basis set. Oxygen atoms, which almost equally share the negative charge due to the almost perfect resonance interaction in the pHBDI anion (see Fig. 5.3), are treated with the entire aug-spdf diffuse shells. The electron density is redistributed in a way that the bridge middle carbon atom (C_{θ}) acquires

an additional negative charge upon the $S_0 \to S_1$ excitation. Since the most weakly bound electron in the S_1 state populates this particular orbital, the basis set is augmented with an additional diffuse function of the p-type centered at C_β with a particularly small exponent equal to -10. The π^* orbital of this highly diffuse shell is included in the active space spanned by almost all valence-type π and π^* orbitals (14,13) and is used to mimic an electron ejection. Importantly, electronic ground and detached states are treated in a balanced way within a state-averaging procedure in the frame of a single calculation.

The calculated vertical detachment and excitation energies, as well as origin shifts (minimum displacements) between the S_0 and S_1 electronic states of the anion and between the anion S₁ state and the ground neutral D₀ state may be used for a pictorial representation of vibrational resonances embedded in the electronic continuum for the GFP chromophore anion in S₁. Figure 5.15 shows quadratically approximated potential energy surfaces for the three states as a function of the two emission-active mode coordinates. They refer to the totally symmetric in-plane medium and high-frequency stretching modes. If not being coupled to the nuclear motion, electron detachment would never occur, since the S₁ state is electronically bound in the FC region. These are vibrational resonances that enable electron autodetachment (VAD). The crossing point of the S_1 and D_0 surfaces is importantly located outside the FC region; hence even at energies where this crossing occurs (~2.7 eV), vibrations are required to reach this point (autodetachment through vibrational Feshbach resonances, VFRAD). At the crossing point, the states are electronically degenerate, and this can be distinguished from VAD that occurs even below the crossing point. In VAD, the energy has to be transferred from the nuclei to the electrons through their (non-adiabatic) coupling. Such a mechanism enables electron emission in the cases, where the state of a molecular anion and its neutral counterpart do not cross at all [56].

The mode-specificity in VAD comes from the calculated S_1/D_0 origin shifts. The larger the shift is, the more active is a particular mode in the electron emission. It serves as a reaction coordinate, since electron ejection has to be accompanied by the nuclear rearrangements along this particular mode. Furthermore, the non-adiabatic couplings in VAD should depend on vibrational overlap between the final vibrational wavefunction and the derivative of the initial vibrational wavefunction with respect to the corresponding nuclear coordinates. At low excitation energies, the final state refers to the ground vibrational level, and such overlap is larger if the two surfaces are displaced farther along the corresponding normal modes.

Remarkably, the PD-active modes are those that are excited upon the $S_0 \rightarrow S_1$ transition. This means that the S_1 surface is shifted in the same direction with respect to both the S_0 and D_0 surfaces. This is easily recognised by comparing the corresponding equilibrium geometry parameters in S_0 , S_1 and D_0 (see Fig. 5.15). Upon excitation of the PD-active modes in the blue part of the spectrum, electron ejection becomes a dominating channel.

A special consideration is needed for the lowest-energy PD pathway at excitation energies in the red part of the $S_0 \rightarrow S_1$ absorption band. One can superficially come to the striking conclusion that PD occurs even below VDE. However,

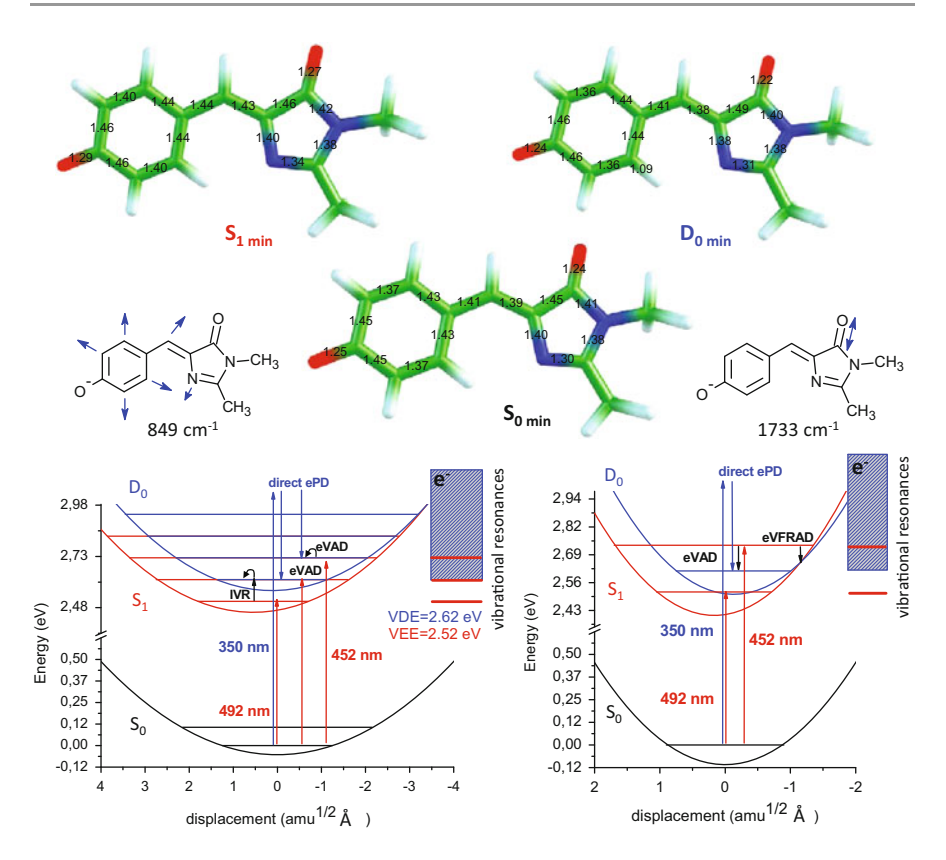


Fig. 5.15 Equilibrium geometry parameters of the GFP chromophore anion in S_1 , D_0 and S_0 . Three one-dimensional quadratic surfaces of these states shifted according to the calculated minimum displacements along the totally symmetric stretching coordinates and according to the calculated vertical detachment and excitation energies. Note, that PD occurs through vibrational resonances out of S_1 within the S_0 – S_1 absorption band down to ~350 nm. The ground-state parameters of the anion and the neutral have been optimised within PBE0/(aug)-cc-pVDZ functional. The excited-state equilibrium structure has been found at the XMCQDPT2/CASSCF (14,13)/(aug)-cc-pVDZ level of theory. All distances are given in Å. Reproduced from Ref. [36] with permission from The Royal Society of Chemistry

Fig. 5.15 shows two one-dimensional representations, whereas low-frequency bath modes of the anion (see Fig. 5.6) bear vibrational energy in excess to the electron binding energy when combined with the photon energy. The internal energy of \sim 0.3 eV at room temperature is enough to cover the gap of \sim 0.1 eV between vertical detachment and excitation energies upon absorption of a single photon. Here, vibrational energy redistribution (IVR) through anharmonic couplings between the modes play an essential role in determining a characteristic timescale for VAD. A statistical RRKM/QET theory may be used to estimate the corresponding rate constant for energy gathering on the emission-active mode, which corresponds to its $0 \rightarrow 1$ vibrational excitation, as discussed below.

It is worth noting that a valence-type anion is formed initially upon photoexcitation. However, a large dipole moment of the neutral core, which is greater than the critical value, 2.5 D [56], may also support the so-called dipole-bound states, which are governed solely by the long-range electrostatic interactions. A remarkable feature of the GFP chromophore is that its radical neutral core has a very large dipole moment. Our estimates based on the extended multiconfigurational quasidegenerate perturbation theory [57] give a value of 7 D. Therefore, such bound states might also occur in the case of the GFP chromophore anion. Being close to the detachment threshold, the dipole-bound states reside in the same energy domain as the S₁ state. Experimentally, a direct population of these states is unlikely due to a negligible oscillator strength for such transitions compared to that of the bright $S_0 \rightarrow S_1$ transition. However, these states may serve as doorways into the PD channel by bridging the valence-type bound S_1 state to the neutral D_0 plus an unbound electron state. Importantly, the ion-dipole interaction also has a crucial impact on the threshold behavior of PD cross-sections. One might remember that even the leading term of the threshold function alters from the well-known form of a Wigner law [58], which presumes that final-state forces are of a finite range vanishing faster than r^{-2} . Therefore, the dipole potential has to be taken into account while describing and simulating VAD spectral profiles [59].

5.4.2 Internal Conversion

In photochemistry of polyatomic molecules, nuclear relaxation through conical intersections plays a crucial role in their fast electronic de-excitation [60, 61]. Upon such non-adiabatic transitions, the particular nuclear motion induces a coupling between two adiabatic surfaces that eventually cross. The intersecting hypersurfaces constitute a dynamical funnel for the most efficient electron-to-nuclei energy transfer in radiationless decays. In light-sensitive proteins, such a coupling makes the primary step in vision the fastest known biological process in nature, where nuclear rearrangements along the reaction pathway occur within 200 fs [62].

In the case of the GFP chromophore anion, femtosecond time-resolved photoelectron spectroscopy has been used to study the excited-state dynamics following excitation of the S_1 state at 500 nm (2.48 eV) and probing it with 800 nm (1.55 eV) [63]. The excited-state population is found to decay bi-exponentially, with the characteristic lifetimes of (sub)picoseconds. Such an ultrafast decay, attributed to internal conversion that is a dominant channel at low excitation energies [36], indicates that conical intersection(s) might be involved in radiationless de-excitation.

Indeed, high-level *ab initio* calculations within the XMCQDPT2 multistate multi-reference perturbation theory [57] reveals two non-equivalent pathways in IC, where the S_1 and S_0 surfaces approach each other upon twisting in the central bridge moiety of the chromophore. Remarkably, only one of them directly leads to a conical intersection seam, energetically lying below the planar minimum in S_1 . It is mediated by twisting about the bond adjacent to the heterocyclic ring and formally

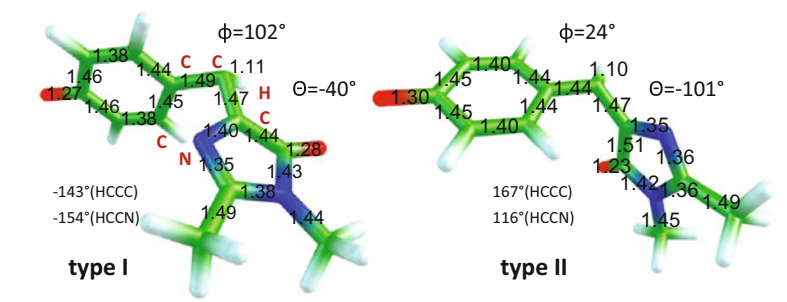


Fig. 5.16 Geometry parameters of the type I S_1/S_0 MECI (*left*) and the type II S_1/S_0 MECI (*right*). The type I exhibits a hula-twist geometry for the bare anion. Note, this type of the S_1/S_0 conical intersections lies higher in energy than the transition state, which leads out of the fluorescent state in S_1 . The type II is the lowest-energy MECI, which lies 0.2 eV below the planar minimum in S_1 . For this type, small variations of the angle ϕ belong to the conical intersection seam. Due to symmetry consideration, two MECI structures of each type exist. All distances and angles are depicted in Å and degrees, respectively. Reproduced from Ref. [36] with permission from The Royal Society of Chemistry

refers to the *cis/trans* isomerisation coordinate (θ angle). The other branch, which corresponds to rotation about the bond adjacent to the phenol-ring (ϕ angle), requires an additional decoupling in the electronic structure of the chromophore to enable a degeneracy of the two electronic states [36]. The corresponding conical intersection exhibits a hula-twist geometry and lies higher in energy compared to that of the unrelaxed FC point in S₁, as it has also been shown previously [12]. The two types of the minimum-energy conical intersections (MECI) are shown in Fig. 5.16.

Both branches in internal conversion proceed via distinct twisted intra-molecular charge-transfer pathways. The different electronic structure of these branches results in their different efficiency in inducing the non-adiabatic couplings between the two states of the anion. However, the barrier heights for twisting along the two alternative coordinates are expected to be remarkably small. The two bridge bonds are simultaneously elongated upon excitation (see Fig. 5.15), as it also follows from the simple Hückel theory. This inevitably leads to a splitting of the excited-state population into two alternative branches in S_1 , leading out of the planar fluorescent state. The less efficient route results in the short-lived transient intermediate in S_1 , and this subpopulation may be reflected back to the fluorescent state. This causes a bi-exponential decay with the second component characterised by an increased excited-state lifetime of a few picoseconds [63].

The planar minimum of the anion does exist in S_1 , as it follows from the unconstrained geometry optimisation procedure. However, as it is expected, the S_1 potential energy surface is very flat in the vicinity of the fluorescent state. By performing a series of constrained geometry searches along the two alternative twisting coordinates, the corresponding transition states have been located. The barrier heights are similar and equal to ~ 0.05 eV.

Since internal conversion is a dominant excited-state decay channel in the gas phase at low excitation energies, as well as in solutions, one might be interested in comparing the IC lifetimes in both environments. Remarkably, the experimental results in various solvents also reveal an ultrafast bi-exponential fluorescence decay with a sub-picosecond predominant component, indicating a nearly barrierless radiationless conversion, and a weak dependence on solvent viscosity [15, 18]. This striking agreement in the excited-state decay of the chromophore anion in the gas phase and in solution clearly indicates that internal conversion is indeed a very efficient nearly barrierless decay channel with a very steep potential, leading to the lowest-lying conical intersection [36].

5.4.3 Branching Ratio in Excited-State Decay Channels

After excitation to the S_1 state there is at a given wavelength a branching ratio for prompt electron detachment (PD) versus internal conversion (IC), where the latter results in delayed action. The following discussion pertains to the spectral region of low excitation energies close to the maximum at 482 nm observed in both prompt and delayed action spectra.

The PD and IC rate constants, their branching ratio and the associated excited-state lifetimes may be estimated using the RRKM/QET quasi-equilibrium theory [36], provided that both excited-state decay channels are IVR-mediated and have a statistical nature at low excitation energies. The average excited-state lifetime equals the inverse of the effective rate constant, which is a sum of the PD and IC microcanonical unimolecular rate constants.

The IC lifetime is determined by crossing a barrier along the two branches that lead out of the planar fluorescent state. Here, we provide an estimation of the IC lifetime based on a somewhat simplified scheme, disregarding a re-population of the fluorescent state from the transient twisted intermediate in S_1 , as discussed above. Such a timescale should provide an estimation that lies in between the two lifetime components found experimentally [63], as shown below.

According to the generalised scheme, the decay of the fluorescent state occurs along the two branches, where one of them directly leads to the S_1/S_0 conical intersection and the other leads to a short-lived transient intermediate in S_1 that may re-populate the fluorescent state in time. The decay via two parallel branches, where one of them is reversible, has an analytical solution:

$$I_{fl}(t) \sim [FS] = \frac{k_{-1} - \gamma_1}{\gamma_2 - \gamma_1} e^{-\gamma_1 t} + \frac{k_{-1} - \gamma_2}{\gamma_1 - \gamma_2} e^{-\gamma_2 t}, \tag{5.6}$$

where FS denotes the fluorescent state, k_{-1} is the rate constant for re-populating the fluorescent state along one of the two alternative branches. γ_1 and γ_2 are the effective rate constants, which define the two lifetimes components:

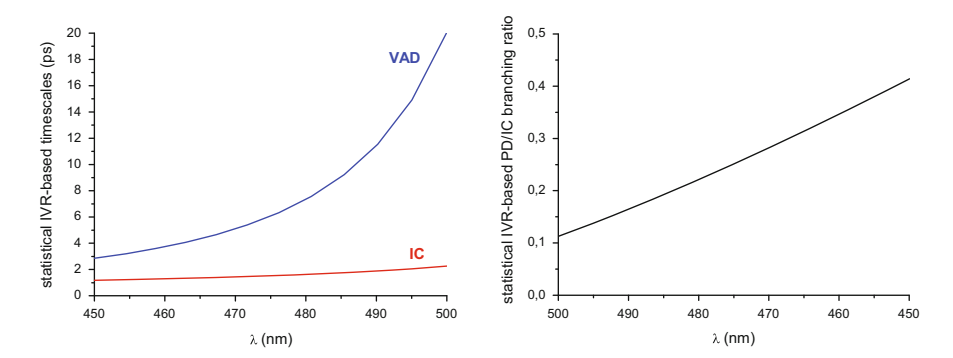


Fig. 5.17 The calculated statistical VAD and IC lifetimes (*left*) and their branching ratio (*right*) as a function of excitation wavelength. Reproduced from Ref. [36] with permission from The Royal Society of Chemistry

$$\gamma_{1,2} = \frac{1}{2}(k_1 + k_{-1} + k_2) \mp \frac{1}{2}\sqrt{(k_1 + k_{-1} + k_2)^2 + 4k_1k_2}$$

$$\approx \frac{2k_1 + k_{-1}}{2} \mp \frac{\sqrt{k_{-1}^2 + 4k_1^2}}{2}$$
(5.7)

where k_1 and k_2 are the rate constants along the two alternative branches. Provided that k_1 is almost equal to k_2 , the Eq. (5.7) boils down to the right-hand side expression. The analysis of this expression shows that the IC lifetime estimated as inverse of $2k_1$ lies in between the corresponding values defined as inverse of γ_1 and γ_2 .

At low excitation energies, the VAD rate is determined by the energy transfer to the lowest-frequency emission-active mode of 849 cm⁻¹ (0.105 eV). The amount of energy that is required for VAD corresponds to the 0–1 excitation energy for this mode. This enables a nearly perfect resonance between the S_1 ($\nu=1$) and D_0 ($\nu=0$) states (see Fig. 5.15). The rate constant for the energy transfer may then statistically be estimated. It is proportional to the total number of vibrational states, where the emission-active mode is excited at least to the first level. And it is reciprocally proportional to the density of all states at the energy E. Note, that the VAD activation energy is two times higher than that of IC. The estimated IC and VAD lifetimes as well as their branching ratio as functions of excitation wavelength are shown in Fig. 5.17.

IC is indeed a predominant excited-state decay channel at low excitation energies, as follows from our theoretical estimations. It occurs on the picosecond timescale, whereas electron emission out of S_1 is one order of magnitude slower. Our predictions are very close to those found experimentally, in time-resolved pump-probe [63] as well as in time-resolved action spectroscopy.

What should specifically be stressed here is that the timescales are very sensitive to the excitation wavelength, since the PD mechanism changes upon increase in photon energy [36]. The timescales discussed above are relevant only at low

energies, when both processes are IVR-mediated in the vicinity of the planar minimum in S_1 (governed by crossing a transition state or a pseudo-transition state). At higher energies, the emission active modes are directly excited, and the electron-emission dynamics may occur within a timescale of vibrational decoherence. Support to this comes from the experiment [10], where the IC channel essentially vanishes at energies higher than 2.75 eV (450 nm). To completely surpass IC, PD should be ultrafast and non-statistical.

5.4.4 Spectral Shape and Excited-State Nuclear Dynamics

Both absorption spectra and excited-state decay are determined by photo-initiated dynamics, usually occurring, however, on different timescales and influenced by different factors. However, a lifetime broadening may influence spectral shapes, as, for example, in the cases of auto-detaching resonance excited-states embedded in the electronic continuum or dissociative states that directly lead to molecular fragmentation. In the case of the GFP chromophore anion, two characteristic timescales may be outlined: a timescale of a hundred of femtoseconds, when the early-time adiabatic nuclear dynamics in S₁ defines the spectral shape of photoabsorption, and a picosecond timescale of the non-adiabatic dynamics in the excited-state decay channels at low excitation energies. As discussed earlier, the excited-state decay of the isolated anion is mostly governed by crossing barriers upon twisting in internal conversion. The corresponding barrier heights are remarkably small both in the gas phase and in solution, giving rise to the similar excitedstate lifetime components found experimentally [15, 63]. Upon fixing a planarity of the chromophore, e.g., in the protein, internal conversion becomes largely prohibited, and other decay channels, like fluorescence, play an essential role in electronic de-excitation. The question then arises how similar the early-time nuclear dynamics of the GFP chromophore anion in vacuo and inside the protein is. We discuss below a remarkable similarity between the early-time dynamics in these environments and outline possible implications of the intrinsic photophysical properties of the light-absorbing molecular unit to the photoresponse of the GFP proteins as a whole.

The simulated spectra of the GFP chromophore anion in the gas phase and inside the protein have been obtained using a time-domain formalism within the Born-Oppenheimer approximation for separating the nuclear and electronic motion. According to this formalism, the spectra are formulated in terms of Fourier transforms of appropriate autocorrelation functions [64]. An explicit formula for the overlap of the thermally-averaged initial ground-state vibrational wave function evolving in S_1 at time t with those at t=0 can be derived in the double harmonic parallel-mode approximation [65]. The latter assumes a simplified picture of multidimensional ground and excited-state harmonic potential energy surfaces displaced relative to each other along each normal mode. Neither frequency change nor Duschinsky rotation is assumed to occur upon electronic transition. The details of this approach can be found elsewhere [48]. The protein simulations are described

in [36]. The total propagation time in simulating absorption profiles is set to 500 fs based on the characteristic timescale of ~100 fs in the early-time decay of the autocorrelation function at room temperature, which defines a spectral resolution. The time-independent approach based on explicit calculation of the Franck-Condon factors has also been applied to supplement results on the early-time excited-state nuclear dynamics with detailed insights into the origin of observed spectral features. Both formalisms produce exactly the same final spectral shapes under the above-mentioned approximations.

Although approximations made for treating a nuclear problem in calculating absorption profiles may be thought of as an oversimplified approach, it is important to underline that a highly reliable prediction of the ground-to-excited state minimum displacements (origin shifts) play the most crucial role in simulating major spectral features. Here, we use a highly correlated multistate multi-reference perturbation theory in its invariant XMCQDPT2 version, formulated recently [57]. One way to validate an electronic structure method used for calculating an excited-state gradient is to compare the final overall widths in the experimental and simulated spectra. By the time-energy uncertainty principle the broadest feature of the spectrum, its width, is determined by the shortest feature in time. This feature refers to the initial dynamics of vibrational wave packet moving downhill along the path of steepest descent, which is anti-parallel to the gradient at the initial FC point on the upper electronic potential energy surface. The steeper the upper surface in the FC region is, the faster is the decay and the broader is the shape of the absorption profile. As a result, the initial S₁ gradient essentially determines the major spectral feature of the spectrum, its total width.

As seen in Fig. 5.18, the simulated vibrational profile of the isolated GFP chromophore anion is rather broad and do not give precise spectroscopic information. The broadening is caused by the large manifold of contributing vibrational levels. Active low-frequency modes, which are also excited in the ground electronic state at room temperature, completely wash out all fine structures upon temperature increase (compare the blue and red lines in Fig. 5.18). Importantly, spectral profiles of relatively large isolated biological chromophores are inherently smooth and mostly structureless. For resolved structures to appear in the spectrum, there should be a nice recurrence in the autocorrelation function in the time domain [64]. In other words, all nuclei should simultaneously come close to the initial FC point. The larger the molecule is, the larger is the number of active vibrational modes excited upon absorption; hence, larger displacements in the multidimensional phase space and a poor recurrence in the time domain are expected.

The calculated shape of the isolated anion at room temperature is well consistent with the prompt action spectrum (see Fig. 5.11), provided that the first peak in the action spectrum at 482 nm is corrected for the multiple-photon contribution. Structures at 482, 469, 452, and 421 nm practically coincide with those found experimentally (482, 472, 452, and 422 nm). Importantly, the major spectral feature, its total width, is fully accounted for. As a result, by comparing the experimental and theoretical shapes directly, we show that a nuclear dynamic broadening is responsible for the observed absorption profile in the gas phase.

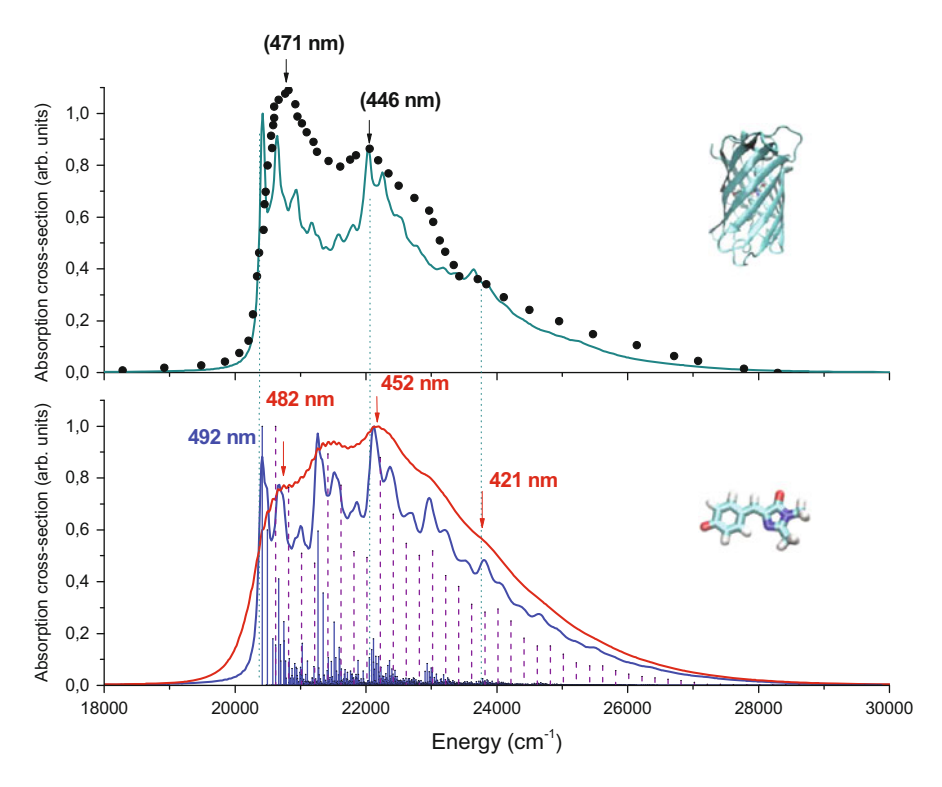


Fig. 5.18 Calculated S₀–S₁ absorption profiles of the deprotonated GFP chromophore. *Lower panel*: the *solid blue* and *red lines* refer to the calculated spectra of the isolated anion at 0 K and 300 K, respectively. The *blue vertical lines* illustrate the relative strength of the Franck-Condon factors. The high density of states of active modes in the blue part of the spectrum is visualised by *purple dashed vertical lines*, which represent the total intensity per 200 cm⁻¹ energy bin. *Upper panel*: the *solid cyan line* corresponds to the calculated spectrum of the S65T-GFP protein at 0 K. The experimental low-temperature excitation spectrum of the emission, attributed to the anionic form of the chromophore in the wild-type GFP, is shown as the *black circles* (adapted from [66]). The calculated spectra are shifted such that the experimental and theoretical structures coincide at 452 nm (gas phase) and 446 nm (protein). The protein spectra are further shifted by 484 cm⁻¹ such that the 0–0 transition with the largest FC relative strength coincides with that in the gas phase. Note the similar spectral widths in the gas phase and inside the protein. Adapted from Ref. [36] with permission from The Royal Society of Chemistry

This supports our findings for a relatively long lifetime of the anion in the S_1 state, which is consistent with a bound character of the first excited state with respect to electron emission.

Remarkably, the maximum of the true one-photon absorption is blue-shifted up to 452 nm compared to those in both prompt and delayed action spectra, which peak at 482 nm. Such a blue shift in the action spectrum maximum has previously been indicated in [32]. Importantly, the experimental one-photon action spectrum spectrum may appear to be blue-shifted also by another reason. Experimentally, it is challenging to reconstruct the true absorption profile, since there is a branching ratio in the excited-state decay channels that depends on excitation wavelength.

Moreover, the characteristic timescales of action vary from the tens of seconds up to the tens of femtoseconds upon one-photon absorption throughout the $S_0 \rightarrow S_1$ spectral range. One has to bear in mind, that IC is a dominant channel at low excitation energies, which is one order of magnitude faster than electron emission out of S_1 , whereas prompt PD completely surpasses IC at higher energies. The problem arises in the red part of the spectrum, since only a small fraction of the signal, which comes from the prompt PD, might have been registered [32], whereas a larger fraction coming from IC has to be registered in the delayed channel, corresponding to the decay of the anion in the hot ground state. Upon one-photon absorption, the delayed action occurs on a timescale of seconds (see Fig. 5.10), when IR radiative cooling sets in and inhibits the action.

Precautions should apply, however, when trying to interpret the blue shift of the maximum in the one-photon absorption profile compared to those in the action spectra. The peak at 482 nm, registered in the action spectra, may erroneously be attributed solely to the multiple-photon absorption [32]. As discussed above, this cannot be the case, when photons are absorbed sequentially. Moreover, the calculated FC factors reveal that the 0–0 transition has the largest relative strength, and it is located at 492 nm close to the maximum in the action spectra at 482 nm (see Fig. 5.18). It must be stressed that the single-photon cross section does not necessarily peak at the wavelength of the main transition with the largest FC strength. This is well-known, but it is often overlooked, since such shifts are usually small $(\sim 300-500 \text{ cm}^{-1})$ [45] and originate from a set of transitions to the states, where low-frequency active modes are excited in addition to the main transition. Even though the relative strengths of such transitions are smaller, but their density is obviously higher. However, the shift disclosed here is much larger than that predicted in [45]. The maximum rather refers to the transitions, where the highfrequency modes are excited. This is usually not expected, since each subsequent higher-energy transition, also accompanied by the same low-frequency satellites as the main transition, has a smaller relative strength according to the corresponding FC progression. The non-trivial aspect here is that there is an accidental degeneracy of two sets of active modes, breathing at 849 cm⁻¹ and stretches at 1,600-1,700 cm⁻¹. The former breathing mode has a long FC progression, such that its 0–2 excitation coincides in energy and in the corresponding strengths with those of the 0-1 excitation for the high-frequency modes. This causes a peak in the density of states of the active modes and a maximum in the absorption at 452 nm. The sequential two-photon contribution in the delayed peak, as well as the multiplephoton contribution to the prompt peak at 482 nm, on the other hand, are indeed relevant, as they peak in the region of the vertical excitation that is close to the adiabatic transition in this case.

The experimental low-temperature excitation spectrum of the emission [66], which is solely attributed to the anionic form of the chromophore in the wild-type GFP, also perfectly matches the calculated spectrum (see Fig. 5.18). The shoulder at 446 nm in the low-temperature spectrum refers to the excitation of high-frequency stretching modes that can unambiguously be correlated with those excited in the gas phase (see Fig. 5.18).

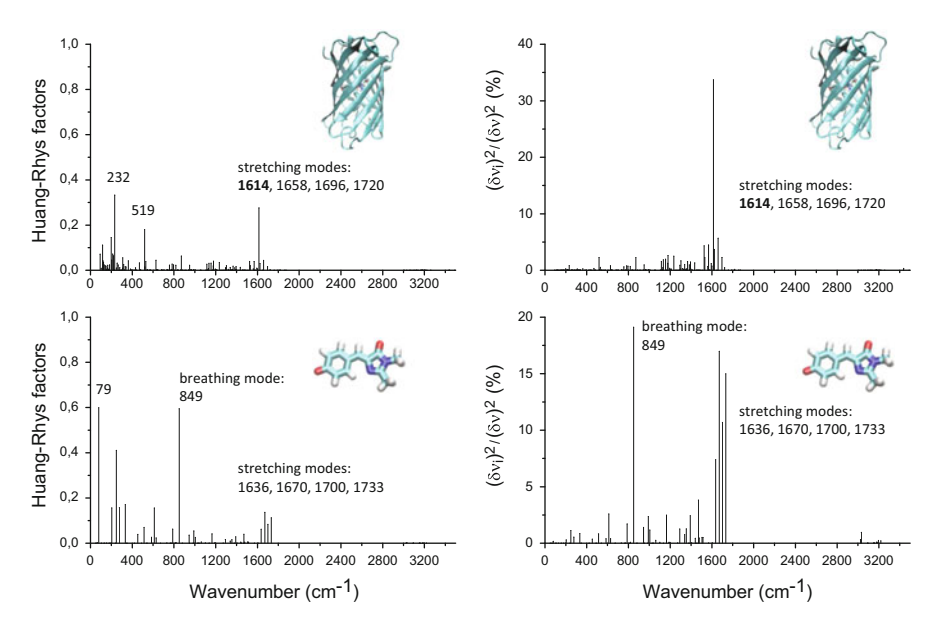


Fig. 5.19 Active Franck-Condon modes for the $S_0 \rightarrow S_1$ transition in the bare deprotonated GFP chromophore (*lower panel*) and in the S65T-GFP protein (*upper panel*). Shown are the Huang-Rhys factors and the contributions of each normal mode to the spectral width. Reproduced from Ref. [36] with permission from The Royal Society of Chemistry

The active Franck-Condon modes of the deprotonated chromophore in the gas phase and in the protein are shown in Fig. 5.19. To the left, the graphs represent the so-called Huang-Rhys factors [65], which are defined as squares of origin shifts in the dimensionless normal coordinates divided by a factor of two. To the right, the graphs show the contributions from each normal mode to the overall band width. It is worth noting, that the major contribution to the width comes from the high-frequency modes, while those with low frequencies promote a spectral blurring. The most active FC modes refer to in-plane vibrations of the conjugated part of the chromophore both in the gas phase and in the protein. In the latter case, there are also certain modes with non-zero ground-to-excited state minimum displacements that are attributed to changes in the protein as a response to perturbation within the chromophore. Two groups of modes contribute to the environmental rearrangements: low-frequency modes and deformation vibrations with frequencies below 1,600 cm⁻¹ of the –OH and –NH groups that are involved in the hydrogen bonding network in the binding pocket of the chromophore.

Remarkably, the high-frequency stretching modes play the same role in the early-time excited-state nuclear dynamics that determines the corresponding spectral shapes in the gas phase as well as in the protein (see Fig. 5.19). These modes define the spectral width, while the large-amplitude lower-frequency bending and breathing modes are, to a large extent, arrested in the protein due to the steric constraints imposed by the environment. The calculated vertical excitation energy is red-shifted by only 0.1 eV in the S65T GFP protein compared to the gas phase,

and this is fully consistent with the experimental findings and earlier theoretical predictions [67]. Note, that there are small deviations in the absorption maxima of various GFP variants. In particular, the maximum of the wild-type GFP (471 nm at 77 K and 477 nm at 300 K) [66] is blue-shifted compared to those of the S65T structure (489 nm) [68, 69] and of the enhanced S65T/F64L GFP mutant (492 nm) [70] at 300 K.

Importantly, the PD-active modes are those that are excited upon the $S_0 \rightarrow S_1$ transition. Upon excitation of the totally symmetric stretching modes in the blue part of the spectrum, electron ejection becomes a dominating channel (see Fig. 5.15). On the other hand, out-of-pane twisting induces a non-adiabatic coupling between the S_1 and S_0 states in internal conversion. Such a mode-specificity in the intrinsic photoresponse of the chromophore should have a direct implication to the diverse functioning of the GFP proteins.

5.5 Concluding Remarks

Here, we have discussed how recent developments in action and photoelectron spectroscopy combined with state-of-the-art electronic structure theory give the detailed insights into photo-initiated quantum dynamics of the isolated GFP chromophore anion. It is worth noting, that this anionic chromophore exhibits a remarkable efficiency in the non-adiabatic couplings between the electronic and nuclear motion in the excited-state decay channels. This results in a dual energy transfer from the electrons to the nuclei in internal conversion occurring through the S_1/S_0 conical intersection and from the nuclei to the electrons in vibrational autodetachment out of the S_1 state, which has a bound character in the Franck-Condon region.

The mode-specificity revealed in the excited-state decay channels [36] might have possible implications to the functioning of the GFP proteins. The well-established paradigm in the functioning of the fluorescent proteins is the IC suppression by the protein environment. However, a new emerging scenario [19] is based on the active role of the GFP proteins containing tyrosine-based chromophores in photochemical reactions. Remarkably, the modes that are excited upon photoabsorption should also be most active in the possible electron transfer reactions, involving the GFP oxidation, since the S_1/D_0 minimum displacements are large along these high-frequency stretching modes, similar to the gas phase [36]. The electron transfer through a resonant tunneling, involving GFPs as electron donors, should then be accompanied by nuclear rearrangements along these particular modes.

The biological function is closely connected to the ways, by which the protein environment tunes the intrinsic photoresponse of their chromophores and guides their excited-state evolution. Many GFP proteins prohibit internal conversion of their chromophores, thus possibly directing the decay towards the fast electron transfer governed by the most Franck-Condon active stretching modes.

Remarkably, the long-timescale fluorescence may then be regarded as a side channel [19, 71] only enabled in the absence of relevant electron acceptors.

References

- 1. Tsien, R.Y.: The green fluorescent protein. Annu. Rev. Biochem. 67, 509-544 (1998)
- 2. Ormö, M., Cubitt, A.B.., Kallio, K., Gross, L.A., Tsien, R.Y., Remington, S.J.: Crystal structure of the *Aequorea victoria* green fluorescent protein. Science 273, 1392–1395 (1996)
- 3. Yang, F., Moss, L.G., Phillips, G.N.: The molecular structure of green fluorescent protein. Nat. Biotechnol. 14, 1246–1251 (1996)
- Chudakov, D., Matz, M., Lukyanov, S., Lukyanov, K.: Fluorescent proteins and their applications in imaging living cells and tissues. Physiol. Rev. 90, 1103–1163 (2010)
- Tolbert, L.M., Baldridge, A., Kowalik, J., Solntsev, K.M.: Collapse and recovery of green fluorescent protein chromophore emission through topological effects. Acc. Chem. Res. 45, 171–181 (2012)
- Chattoraj, M., King, B., Bublitz, G., Boxer, S.: Ultra-fast excited state dynamics in green fluorescent protein: multiple states and proton transfer. Proc. Natl Acad. Sci. USA 93, 8362–8367 (1996)
- 7. Fang, C., Frontiera, R.R., Tran, R., Mathies, R.A.: Mapping GFP structure evolution during proton transfer with femtosecond Raman spectroscopy. Nature **462**, 200–204 (2009)
- 8. Sample, V., Newman, R.H., Zhang, J.: The structure and function of fluorescent proteins. Chem. Soc. Rev. 38, 2852–2864 (2009)
- Shcherbo, D., Shemiakina, I., Ryabova, A., Luker, K., Schmidt, B., Souslova, E., Gorodnicheva, T., Strukova, L., Shidlovskiy, K., Britanova, O., Zaraisky, A., Lukyanov, K., Loschenov, V., Luker, G., Chudakov, D.: Near-infrared fluorescent proteins. Nat. Methods 7, 827–829 (2010)
- Forbes, M.W., Jockusch, R.A.: Deactivation pathways of an isolated green fluorescent protein model chromophore studied by electronic action spectroscopy. J. Am. Chem. Soc. 131, 17038–17039 (2009)
- 11. Toniolo, A., Olsen, S., Manoha, L., Martinez, T.J.: Conical intersection dynamics in solution: the chromophore of green fluorescent protein. Faraday Discuss. 127, 149–163 (2004)
- Martin, M.E., Negri, F., Olivucci, M.: Origin, nature, and fate of the fluorescent state of the green fluorescent protein chromophore at the CASPT2//CASSCF resolution. J. Am. Chem. Soc. 126, 5452–5464 (2004)
- Polyakov, I.V., Grigorenko, B.L., Epifanovsky, E.M., Krylov, A.I., Nemukhin, A.V.: Potential energy landscape of the electronic states of the GFP chromophore in different protonation forms: electronic transition energies and conical intersections. J. Chem. Theory Comput. 6, 2377–2387 (2010)
- Kummer, A., Kompa, C., Niwa, H., Hirano, T., Kojima, S., Michel-Beyerle, M.: Viscosity dependent fluorescence decay of the GFP chromophore in solution due to fast internal conversion. J. Phys. Chem. B 106, 7554–7559 (2002)
- Mandal, D., Tahara, T., Meech, S.: Excited-state dynamics in the green fluorescent protein chromophore. J. Phys. Chem. B 108, 1102–1108 (2004)
- Gepshtein, R., Huppert, D., Agmon, N.: Deactivation mechanism of the green fluorescent chromophore. J. Phys. Chem. B 110, 4434–4442 (2006)
- Lukyanov, K.A., Chudakov, D.M., Lukyanov, S., Verkhusha, V.V.: Photoactivatable fluorescent proteins. Nat. Rev. Mol. Cell Biol. 6, 885–890 (2005)
- 18. Meech, S.R.: Excited state reactions in fluorescent proteins. Chem. Soc. Rev. **38**, 2922–2934 (2009)

- Bogdanov, A.M., Mishin, A.S., Yampolsky, I.V., Belousov, V.V., Chudakov, D.M., Subach, F. V., Verkhusha, V.V., Lukyanov, S., Lukyanov, K.A.: Green fluorescent proteins are light-induced electron donors. Nat. Chem. Biol. 5, 459

 –461 (2009)
- Nielsen, S.B., Lapierre, A., Andersen, J.U., Pedersen, U.V., Tomita, S., Andersen, L.H.: Absorption spectrum of the green fluorescent protein chromophore anion in vacuo. Phys. Rev. Lett. 87, 228102 (2001)
- Boyé, S., Nielsen, S.B., Krogh, H., Nielsen, I.B., Pedersen, U.V., Bell, A.F., He, X., Tonge, P. J., Andersen, L.H.: Gas-phase absorption properties of DsRed model chromophores. Phys. Chem. Chem. Phys. 5, 3021–3026 (2003)
- Andersen, L.H., Lapierre, A., Nielsen, S.B., Nielsen, I.B., Pedersen, S.U., Pedersen, U.V., Tomita, S.: Chromophores of the green fluorescent protein studied in the gas phase. Eur. Phys. J. D 20, 597–600 (2002)
- 23. Lammich, L., Petersen, M.Å., Nielsen, M.B., Andersen, L.H.: The gas-phase absorption spectrum of a neutral GFP model chromophore. Biophys. J. **92**, 201–207 (2007)
- 24. Rajput, J., Rahbek, D.B., Andersen, L.H., Rocha-Rinza, T., Christiansen, O., Bravaya, K.B., Erokhin, A.V., Bochenkova, A.V., Solntsev, K.M., Dong, J., Kowalik, J., Tolbert, L.M., Petersen, M.Å., Nielsen, M.B.: Photoabsorption studies of neutral green fluorescent protein model chromophores in vacuo. Phys. Chem. Chem. Phys. 11, 9996–10002 (2009)
- Petersen, M.A., Riber, P., Andersen, L.H., Nielsen, M.B.: Synthesis and characterization of model compounds for the neutral green fluorescent protein chromophore. Synthesis 23, 3635–3638 (2007)
- Boyé, S., Nielsen, I.B., Nielsen, S.B., Krogh, H., Lapierre, A., Pedersen, H.B., Pedersen, S.U., Pedersen, U.V., Andersen, L.H.: Gas-phase absorption properties of a green fluorescent protein–mutant chromophore: the w7 clone. J. Chem. Phys. 119, 338–345 (2003)
- Pakhomov, A.A., Martynov, V.I.: GFP family: structural insights into spectral tuning. Chem. Biol. 15, 755–764 (2008)
- Lincke, K., Solling, T., Andersen, L.H., Klaerke, B., Rahbek, D.B., Rajput, J., Oehlenschlaeger, C.B., Petersen, M.A., Nielsen, M.B.: On the absorption of the phenolate chromophore in the green fluorescent protein – role of individual interactions. Chem. Commun. 46, 734–736 (2010)
- Andersen, L.H., Bluhme, H., Boye, S., Jørgensen, T.J.D., Krogh, H., Nielsen, I.B., Nielsen, S. B., Svendsen, A.: Experimental studies of the photophysics of gas-phase fluorescent protein chromophores. Phys. Chem. Chem. Phys. 6, 2617–2627 (2004)
- Tanabe, T., Saito, M., Noda, K.: Relaxation of green fluorescent protein chromophore anion observed by photodissociation in an electrostatic storage ring. Eur. Phys. J. D 62, 191–195 (2011)
- 31. Forbes, M.W., Nagy, A.M., Jockusch, R.A.: Photofragmentation of and electron photodetachment from a GFP model chromophore in a quadrupole ion trap. Int. J. Mass Spectrom 308, 155–166 (2011)
- 32. Chingin, K., Balabin, R.M., Frankevich, V., Barylyuk, K., Nieckarz, R., Sagulenko, P., Zenobi, R.: Absorption of the green fluorescent protein chromophore anion in the gas phase studied by a combination of FTICR mass spectrometry with laser-induced photodissociation spectroscopy. Int. J. Mass Spectrom. 306, 241–245 (2011)
- 33. Horke, D.A., Verlet, J.R.R.: Photoelectron spectroscopy of the model GFP chromophore anion. Phys. Chem. Chem. Phys. 14, 8511–8515 (2012)
- Mooney, C.R.S., Sanz, M.E., McKay, A.R., Fitzmaurice, R.J., Aliev, A.E., Caddick, S., Fielding, H.H.: Photodetachment spectra of deprotonated fluorescent protein chromophore anions. J. Phys. Chem. A 116, 7943–7949 (2012)
- 35. Toker, Y., Rahbek, D.B., Klærke, B., Bochenkova, A.V., Andersen, L.H.: Direct and indirect electron emission from the green fluorescent protein chromophore. Phys. Rev. Lett. **109**, 128101 (2012)

- Bochenkova, A.V., Andersen, L.H.: Ultrafast dual photoresponse of isolated biological chromophores: link to the photoinduced mode-specific non-adiabatic dynamics in proteins. Faraday Discuss. 163, 297–319 (2013)
- 37. Lammich, L., Rajput, J., Andersen, L.H.: Photodissociation pathways of gas-phase photoactive yellow protein chromophores. Phys. Rev. E 78, 051916 (2008)
- 38. Hanstorp, D.: A secondary emission detector capable of preventing detection of the photoelectric effect induced by pulsed lasers. Meas. Sci. Technol. 3, 523–527 (1992)
- Ding, D., Huang, J., Compton, R.N., Klots, C.E., Haufler, R.E.: CW laser ionization of C₆₀ and C₇₀. Phys. Rev. Lett. **73**, 1084–1087 (1994)
- Elliott, B.M., McCunn, L.R., Johnson, M.A.: Photoelectron imaging study of vibrationally mediated electron autodetachment in the type I isomer of the water hexamer anion. Chem. Phys. Lett. 467, 32–36 (2008)
- 41. Arnold, S.T., Morris, R.A., Viggiano, A.A.: Competition between electron detachment and monomer evaporation in the thermal destruction of hydrated electron clusters. J. Chem. Phys. **103**, 9242–9248 (1995)
- 42. Fano, U.: Effects of configuration interaction on intensities and phase shifts. Phys. Rev. **124**, 1866–1878 (1961)
- 43. Hammer, N.I., Shin, J.-W., Headrick, J.M., Diken, E.G., Roscioli, J.R., Weddle, G.H., Johnson, M.A.: How do small water clusters bind an excess electron? Science **306**, 675–679 (2004)
- 44. Andersen, J.U., Bonderup, E., Hansen, K.: On the concept of temperature for a small isolated system. J. Chem. Phys. **114**, 6518–6525 (2001)
- 45. Kamarchik, E., Krylov, A.I.: Non-Condon effects in the one- and two-photon absorption spectra of the green fluorescent protein. J. Phys. Chem. Lett. 2, 488–492 (2011)
- Pedersen, H.B., Jensen, M.J., Safvan, C.P., Urbain, X., Andersen, L.H.: Fast beam photofragment apparatus for studies of electronic and nuclear dynamics. Rev. Sci. Instrum. 70, 3289–3298 (1999)
- Andersen, J.U., Bonderup, E., Hansen, K.: Thermionic emission from clusters. J. Phys. B 35, R1–R30 (2002)
- Yurenev, P.V., Kretov, M.K., Scherbinin, A.V., Stepanov, N.F.: Environmental broadening of the CTTS bands: the hexaammineruthenium(II) complex in aqueous solution. J. Phys. Chem. A 114, 12804–12812 (2010)
- 49. Granovsky, A.A.: Firefly. http://classic.chem.msu.sugran/firefly/index.html
- Bravaya, K.B., Grigorenko, B.L., Nemukhin, A.V., Krylov, A.I.: Quantum chemistry behind bioimaging: insights from ab initio studies of fluorescent proteins and their chromophores. Acc. Chem. Res. 45, 265–275 (2012)
- 51. Moiseyev, N.: Quantum theory of resonances: calculating energies, widths and cross-sections by complex scaling. Phys. Rep. **302**, 212–293 (1998)
- 52. Reinhardt, W.P.: Complex coordinates in the theory of atomic and molecular structure and dynamics. Annu. Rev. Phys. Chem. **33**, 223–255 (1982)
- 53. Honigmann, M., Liebermann, H.-P., Buenker, R.J.: Use of complex configuration interaction calculations and the stationary principle for the description of metastable electronic states of HCl⁻. J. Chem. Phys. **133**, 044305 (2010)
- 54. Rohr, K., Linder, F.: Vibrational excitation of polar molecules by electron impact. I. Threshold resonance in HF and HCl. J. Phys. B 9, 2521–2537 (1976)
- 55. Eliezer, I., Taylor, H.S., Williams, J.K.: Resonant states of H_2^- . J. Chem. Phys. **47**, 2165–2177 (1967)
- 56. Simons, J.: Molecular anions. J. Phys. Chem. A 112, 6401-6511 (2008)
- Granovsky, A.A.: Extended multi-configuration quasi-degenerate perturbation theory: the new approach to multi-state multi-reference perturbation theory. J. Chem. Phys. 134, 214113 (2011)
- 58. O'Malley, T.F.: Effect of long-range final-state forces on the negative-ion photodetachment cross-section near threshold. Phys. Rev. **137**, A1668–A1672 (1965)

- Adams, C.L., Schneider, H., Weber, J.M.: Vibrational autodetachment intramolecular vibrational relaxation translated into electronic motion. J. Phys. Chem. A 114, 4017–4030 (2010)
- 60. Martinez, T.J.: Physical chemistry: seaming is believing. Nature 467, 412–413 (2010)
- Domcke, W., Yarkony, D.R., Köppel, H. (eds.): Conical Intersections: Theory, Computation and Experiment. Advanced Series in Physical Chemistry, vol. 17. World Scientific, Singapore (2011)
- 62. Polli, D., Altoe, P., Weingart, O., Spillane, K.M., Manzoni, C., Brida, D., Tomasello, G., Orlandi, G., Kukura, P., Mathies, R.A., Garavelli, M., Cerullo, G.: Conical intersection dynamics of the primary photoisomerization event in vision. Nature 467, 440–443 (2010)
- 63. Mooney, C.R.S., Horke, D.A., Chatterley, A.S., Simperler, A., Fielding, H.H., Verlet, J.R.R.: Taking the green fluorescence out of the protein: dynamics of the isolated GFP chromophore anion. Chem. Sci. **4**, 921–927 (2013)
- 64. Heller, E.J.: The semiclassical way to molecular spectroscopy. Acc. Chem. Res. 14, 368–375 (1981)
- Lax, M.: The Franck-Condon principle and its application to crystals. J. Chem. Phys. 20, 1752–1760 (1952)
- 66. Lossau, H., Kummer, A., Heinecke, R., Pöllinger-Dammer, F., Kompa, C., Bieser, G., Jonsson, T., Silva, C., Yang, M., Youvan, D., Michel-Beyerle, M.: Time-resolved spectroscopy of wild-type and mutant green fluorescent proteins reveals excited state deprotonation consistent with fluorophore-protein interactions. Chem. Phys. 213, 1–16 (1996)
- 67. Bravaya, K.B., Khrenova, M.G., Grigorenko, B.L., Nemukhin, A.V., Krylov, A.I.: Effect of protein environment on electronically excited and ionized states of the green fluorescent protein chromophore. J. Phys. Chem. B 115, 8296–8303 (2011)
- 68. Heim, R., Cubitt, A., Tsien, R.: Improved green fluorescence. Nature 373, 663-664 (1995)
- Brejc, K., Sixma, T., Kitts, P., Kain, S., Tsien, R., Ormö, M., Remington, S.: Structural basis for dual excitation and photoisomerization of the Aequorea victoria green fluorescent protein. Proc. Natl. Acad. Sci. USA 94, 2306–2311 (1997)
- 70. Hosoi, H., Yamaguchi, S., Mizuno, H., Miyawaki, A., Tahara, T.: Hidden electronic excited state of enhanced green fluorescent protein. J. Phys. Chem. B 112, 2761–2763 (2008)
- 71. Lukyanov, K.A., Serebrovskaya, E.O., Lukyanov, S., Chudakov, D.M.: Fluorescent proteins as light-inducible photochemical partners. Photochem. Photobiol. Sci. 9, 1301–1306 (2010)

Fluorescence from Gas-Phase Biomolecular Ions

Steen Brøndsted Nielsen

Abstract

This chapter deals with measurements of fluorescence from electronically excited biomolecular ions where there are no interactions with an external environment. Biomolecules with no natural fluorophores are labelled with a dye for such experiments. First, some of the advantages, but also difficulties, of fluorescence spectroscopy compared to absorption spectroscopy are discussed. Extensive work has been done on the isolated dyes in characterising them with respect to their dispersed fluorescence spectra, excited-state lifetimes, and gas-phase Stokes shifts. After a brief introduction, results from experiments on dye-derivatised biomolecular ions that provide important information on folding/unfolding processes and local structural changes are presented. Examples included here are a model DNA duplex, the Trp-cage protein, polyproline peptides, and the cytochrome c heme protein. The chapter ends with a discussion on the oxyluciferin anion, the molecule responsible for light emission from fireflies where the electronic transition has charge-transfer character.

6.1 Introduction

While action spectroscopy provides highly relevant information on the level separation between the electronic ground and excited states of an isolated biochromophore ion, similar information can be obtained from light-emission experiments. If the excited state lives long enough, the ion may undergo a geometry change on the excited state potential energy surface. The energy of the emitted photon will then reflect the energy separation between the ground and excited states but with the optimum geometry for the latter. In an environment where mobile

S.B. Nielsen (⊠)

Department of Physics and Astronomy, Aarhus University, 8000 Aarhus C, Denmark e-mail: sbn@phys.au.dk

106 S.B. Nielsen

water molecules may orient themselves to optimise their interactions with the luminophore, there can be a significant shift in the maxima for light absorption and light emission (Stokes shift). Indeed, a dye molecule is a good reporter on the microenvironment [1]. In the gas phase where the ions are isolated, the Stokes shift is expectedly smaller than in solution phase, which is also seen experimentally [2].

Measuring the spectrum of light emitted (i.e., dispersed fluorescence) from isolated ions has one important benefit compared to measuring the action spectrum: The experiment does not rely on the absorption of more than one photon, and kinetic shifts do not need to be considered as ionic dissociation is not sampled. Of particular relevance, spectroscopy of large protein ions can be done; action spectroscopy is limited to multiply charged anions where it is possible to sample electron detachment (see Chap. 8 by Antoine and Dugourd). The difficulty, of course, is to detect enough photons that are emitted in all directions from a low number of ions (see instrumental setup description in Chap. 3 by Wyer) [3]. Experiments are normally done on mass-selected trapped ions, either in linear quadrupole, Paul or Penning ion traps [4–7]. The collection angle is often low due to poor accessibility to the trapped ions, and sensitive light detectors must be used. Scattered light from the laser or ambient light reduces the signal-to-noise ratio. Detection efficiencies of a few percent have been reported, which are enough in some cases to produce beautiful fluorescence spectra, and even time-resolved light emission has been followed on the nanosecond time scale [4, 8–10]. Fluorescence lifetimes seem to be longer for gaseous ions than for solvated ones [10]. Spectra have been recorded for several biomolecular ions, e.g., xanthene-based rhodamine dyes [2, 3, 6, 10], fluorescein and derivatives [11, 12], and non-covalent host-guest complexes [8].

It should be mentioned that light emission or direct internal conversion to the electronic ground state are not the only pathways after photoexcitation. Indeed, Kappes and co-workers [13] showed that continuous photoexcitation of rhodamine 6G cations led to the disappearance of fluorescence due to trapping of all the ions in long-lived (seconds), dark triplet states. They found that the ground-state ions could be recovered from quenching the triplet state in interactions with molecular oxygen (triplet-state molecule), turning fluorescence back on when these were photoexcited.

Finally, information on the emitted photon can also be obtained indirectly: Williams and co-workers [14] used mass spectrometry to "weigh" the photon that is emitted after UV photoexcitation of hydrated protonated proflavine ions. Fewer water molecules evaporate on average if an ion has emitted light compared to the number that is lost following non-radiative population of the electronic ground state (either directly by internal conversion or via a triplet state by intersystem crossing). In other words, the energy of the emitted photon is not available for water loss. Simply from the difference in the number of evaporated water molecules and the known water binding energies, the energy of the emitted photon can be estimated! The branching ratio provides the fluorescence quantum yield. Furthermore, as the authors pointed out: "A key advantage of this indirect detection method is that all dissociation products resulting from emission are observed, irrespective of the direction of which the photon is emitted." The collection efficiency is 100 %.

6.2 Fluorescence as a Probe of Structural Changes of Biomolecular Ions

Maybe the largest potential of gas-phase emission spectroscopy is to use it to probe DNA and protein conformations and dynamics based on Förster Resonance Energy Transfer (FRET) [1] or photoinduced electron transfer where the biomolecule is labelled with one or more fluorescent probes. Indeed, changes in fluorescence intensity can be correlated with changes in the average conformation of the molecule as the rate of energy transfer between a donor-acceptor pair strongly depends on their separation, to the inverse power of six. The absorption band of the donor is normally to the blue of that of the acceptor and likewise for the emission bands, but such that the donor emission band overlaps with the acceptor absorption band. The photo-excited donor transfers its excitation energy to the acceptor as a result of long-range dipole-dipole interactions; no photon emission and photon absorption is involved in the RET process! As the FRET method is distancesensitive, it can be used as a "molecular ruler". The distance between the donor and acceptor at which the energy transfer efficiency is half of its maximum is denoted the Förster distance, R_0 , and is typically 20–60 Å, which renders this method optimum for the study of biomolecular structures. In summary, if the donor is selectively photoexcited (possible as the absorption spectra of the donor and acceptor are different) and the acceptor is far away, the emission will be solely from the donor. If the acceptor is close to the photo-excited donor, RET will take place to a certain extent, and there will be both donor and acceptor emission. At optimum distance between the two, the donor is fully quenched, and only acceptor emission is seen (100 % RET efficiency).

Pioneering work on gas-phase biomolecular ions relating to FRET has been done by Parks, Zenobi, Jockusch and their co-workers [15–17]. Some of their work will be summarised in the following.

Danell and Parks [15] monitored the separation of double-stranded oligonucleotide anions (i.e., duplex melting) based on FRET using two dyes (the BODIPY-TMR donor and the BODIPY-TR acceptor), one on each single strand and attached to the ends so that they are in close proximity for the intact duplex. The model duplex was composed of two complementary 14-mer strands that formed seven AT Watson-Crick base pairs at one end and seven GC base pairs at the other end (A =adenine, T = thymine, G = guanine, C = cytosine). The dyes were attached to the AT end as melting expectedly occurs here; cf, only two hydrogen bonds between A and T versus three between G and C. The donor fluorescence as well as dissociation was followed as a function of temperature. If the donor separates from the acceptor, its fluorescence increases as it does not transfer its excitation energy to the acceptor; in contrast acceptor fluorescence will go down (this light was, however, not detected in the experiment). The results showed clear evidence for an intermediate state (partly "unzipped" duplex at the AT end) preceding dissociation (Fig. 6.1). While dissociation was easily established by mass spectrometry, the intermediate state has the same m/z as the initial duplex, and its formation could not be inferred 108 S.B. Nielsen

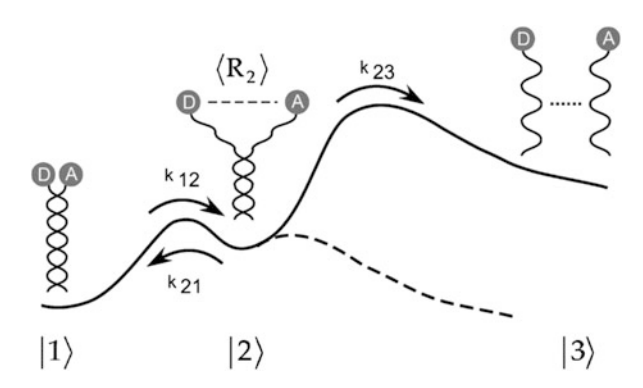


Fig. 6.1 Simplified potential energy diagram for the melting of a duplex, 11>, to two single strands, 13>. It involves an intermediate state, 12>, that is partially "unzipped". Rate constants for the different conversions are indicated. The *dashed curve* is for a "two-state" transition. One strand is labelled with a donor fluorophore and the other with an acceptor fluorophore. Reprinted from [15], with permission from Elsevier

from mass spectrometry, which demonstrates the strength of FRET for following structural changes of DNA.

The BODIPY-TMR dye was also used by Parks and co-workers [18–20] to monitor conformational changes in the small unsolvated Trp-cage protein upon heating. This protein only contains 20 amino-acid residues with a Trp residue "caged" by three proline residues in a hydrophobic core. Here the Trp quenches dye fluorescence when it is released from its cage. The quenching results from intramolecular collisions between the excited dye and the Trp, resulting in electron transfer from Trp to the half-filled orbital of the dye from where an electron was photoexcited to a higher-lying orbital, followed by back transfer of the electron in the excited-state orbital of the dye to Trp+• [21]. This work showed that 3+ charge state proteins more readily unfold than 2+ charge state proteins (see Fig. 6.2), partly due to the greater Coulomb repulsion.

Conformational changes in dye-derivatised polyproline peptides, a β-hairpin peptide, and vancomycin-peptide noncovalent complexes were studied in the same way [20–22]. For polyproline peptides it was found that interactions between the attached dye and charged residues led to variations in the fluorescence intensity due to perturbation of the electronic levels of the dye (Stark effects). Furthermore, as revealed from later work [23], the charge-transfer state between the dye and Trp, D⁻T⁺, is lowered in energy in the vicinity of the electric field of a positively charged arginine amino-acid residue (Fig. 6.3), explaining the fluorescence quenching by charged residues. Hence the local environment of the dye-Trp pair determines the fluorescence intensity. Clearly, a careful positioning of the dye, the Trp, and charged residues allows one to associate a fluorescence change with a specific structural change, and this technique therefore holds great promise in the future for increasing our knowledge at a detailed level on the dynamics of protein folding. Finally, Parks and co-workers [21] found from comparisons to solution-phase

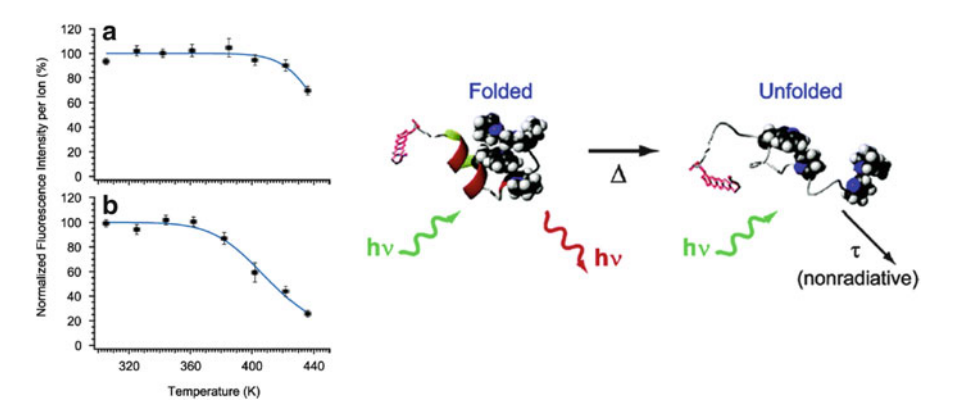


Fig. 6.2 Normalised fluorescence intensity per ion *versus* temperature for (a) doubly and (b) triply protonated Trp-cage protein ions labelled with a dye. The decrease in fluorescence sets in earlier for the 3+ ion than for the 2+ ion. Reprinted with permission from [18]. Copyright (2005) American Chemical Society

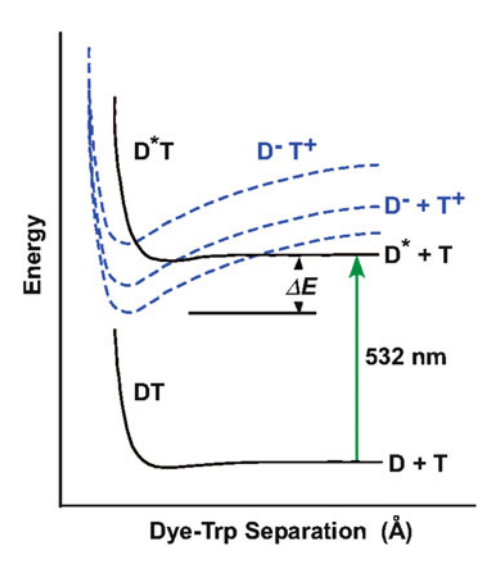


Fig. 6.3 Potential-energy curves for ground state DT, photoexcited DT (the dye is the absorber), and D^-T^+ charge-transfer states. The energy of the charge-transfer state depends on the local electric field: The higher the field, the lower the energy. D dye (and not donor), T Trp. Reprinted with permission from [23]. Copyright (2008) American Chemical Society

experiments that in solution the kinetics is also governed by the shielding of charges by solvent molecules and limited by diffusion.

Conformations of polyproline peptides with different lengths and charge states were explored by Jockusch and co-workers [17] based on FRET. Two rhodamine dyes were used as a FRET pair. The action and emission spectra of the donor (D) and acceptor (A) are shown in Fig. 6.4. It is evident that the emission spectrum

110 S.B. Nielsen

Fig. 6.4 Absorption and emission spectra of two rhodamine dyes used for FRET. The *green curves* are for the donor dye and the *red* ones for the acceptor dye. The *shaded area* is the overlap between the donor emission and the acceptor absorption (their spectral overlap). Reprinted with permission from [17]. Copyright (2010) American Chemical Society

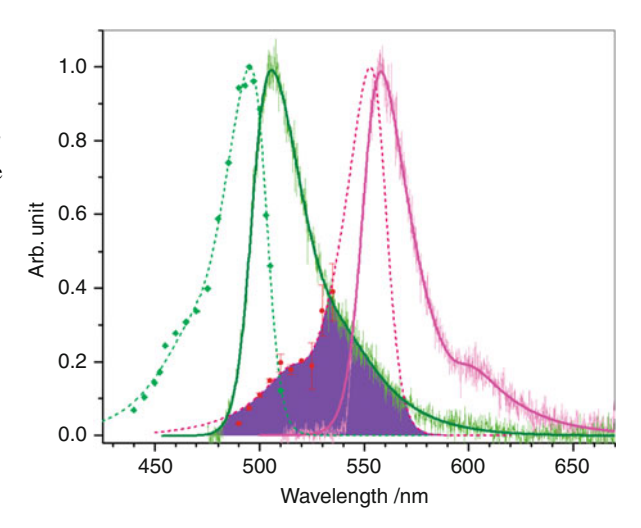
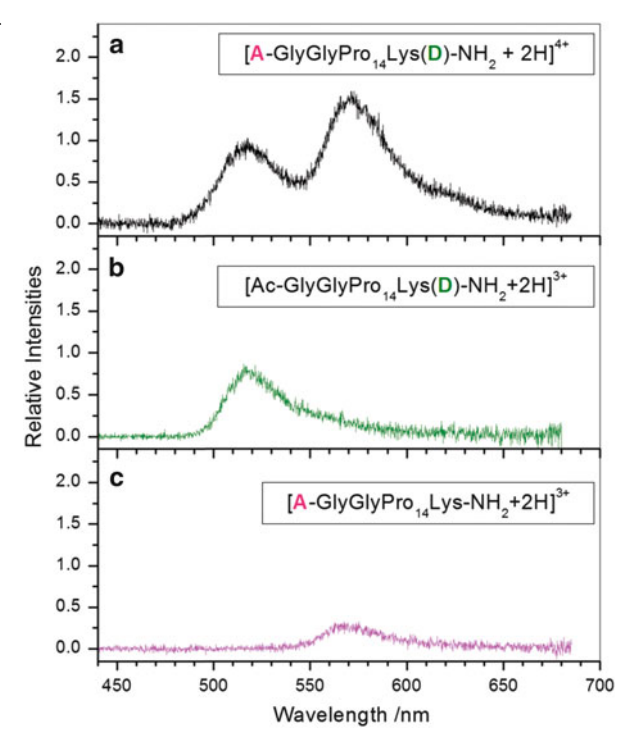


Fig. 6.5 Emission spectra of Pro₁₄-based peptides with (a) both donor and acceptor (photoexcitation of donor), (b) donor only (photoexcitation of donor), and (c) only acceptor (photoexcitation of acceptor). Reprinted with permission from [17]. Copyright (2010) American Chemical Society



almost mirrors the absorption spectrum (mirror image rule), which indicates little change between the ground-state and excited-state structures. The general formula of the labelled peptides are A-Gly-Gly-Pro $_n$ -Lys(D)-NH $_2$ where the number of proline repeats is 8, 14, and 20. Emission spectra of n=14 peptides with donor only, acceptor only, and both donor and acceptor are shown in Fig. 6.5. Peptides that

contain only a donor or an acceptor display emission spectra similar to those for the isolated dyes except for small redshifts (compare with Fig. 6.4). However, importantly, photoexcitation of the donor in the DA peptide leads to emission from both donor and acceptor, which implies that RET has occurred. In line with this, fluorescence lifetimes are longer for D-only peptides and A in DA peptides (photoexcitation of A) than those for D in DA peptides (photoexcitation of D, here the fluorescence lifetime refers to the lifetime of the electronically excited state of D) (see Fig. 6.6), again demonstrating that quenching of the photoexcited donor takes place in the presence of an acceptor. There are two lifetimes for the DA peptides, which were associated with two distinct conformational families of the peptide. The authors found that the n = 8 peptide, where the distance between the two dyes is shortest, showed almost no fluorescence from the donor independent of the charge state being 2+ or 3+. Hence energy transfer is nearly complete. For n = 14 the FRET efficiency was found to decrease with an increase in charge state, which is in agreement with the peptides adopting more extended structures due to the higher Coulomb repulsion. Surprisingly, the n=20 peptides with 4+ charge state displayed similar extents of RET as the n = 14 peptides, which indicates similar dve-dve distances. For the 5+ charge state peptide virtually complete energy transfer occurred suggesting a hair-pin structure in which the two ends are close together. This work again very nicely shows the usefulness of FRET to study conformations of biomolecular ions in vacuo.

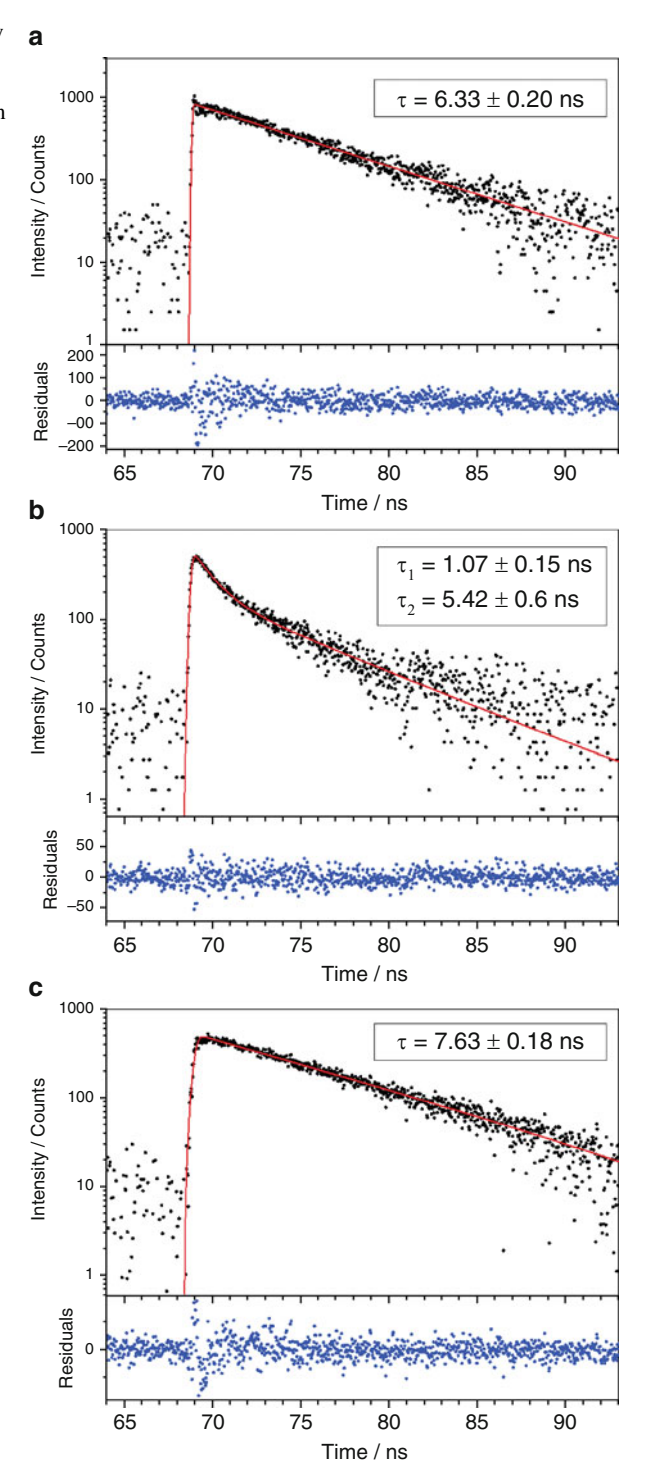
An interesting question up for much debate is whether macromolecular ions preserve their solution-phase structures when transferred to the gas phase no matter how gently this is done. To address this, Parks and co-workers [24] measured the fluorescence from cytochrome c protein ions within electrospray droplets, that is, non-isolated ions. There a Trp residue is the light emitter and heme the quencher via resonance energy transfer at close proximity between the two. High fluorescence is associated with protein unfolding or refolding of the protein at large alcohol concentrations. The work revealed significant differences between the protein conformation in the plume and in a similar solution with various methanol-to-water ratios. Care must therefore be taken in establishing the gas-phase structures.

6.3 Light Emission from Fireflies: Emission from the Bare Oxyluciferin Anion?

In fireflies the oxyluciferin anion is formed in an electronically excited state within the luciferase enzyme [25]. The precursor is D-luciferin and the chemical reactions catalysed by the enzyme involve the energy-rich adenosine triphosphate (ATP), Mg²⁺, and molecular oxygen. The anion can return to the ground state by light emission (bioluminescence), which occurs with a high efficiency [26]. Interestingly, different species emit light with different wavelengths despite the fact that they all possess the same luminophore. One explanation is based on various microenvironments of the oxyluciferin within the protein pocket [27], *e.g.*, single water molecules or charged amino acid residues. To disentangle the intrinsic

112 S.B. Nielsen

Fig. 6.6 Fluorescence decay spectra for (a) the donor in [Ac-Gly-Gly-Pro₁₄-Lys(D)-NH₂ + 2H]³⁺, (b) the donor in [A-Gly-Gly-Pro₁₄-Lys(D)-NH₂ + 2H]⁴⁺, and (c) the acceptor in [A-Gly-Gly-Pro₁₄-Lys(D)-NH₂ + 2H]⁴⁺. Lifetime fits are included. Reprinted with permission from [17]. Copyright (2010) American Chemical Society



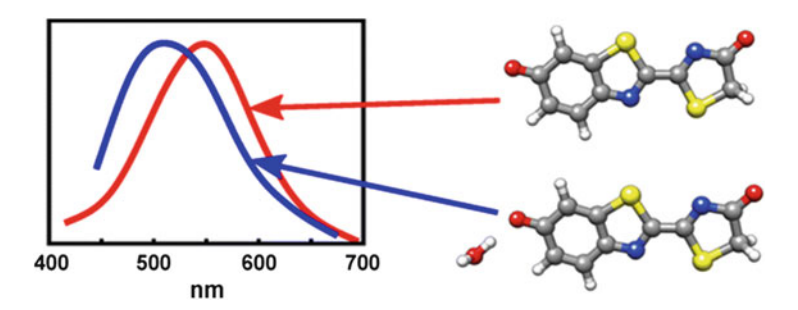


Fig. 6.7 Action spectra of bare oxyluciferin anions and monohydrated ions *in vacuo*. Carbon is *grey*, oxygen *red*, nitrogen *blue*, sulfur *yellow*, and hydrogen *white*. Reprinted with permission from [28]. Copyright (2013) American Chemical Society



Fig. 6.8 *meta*-Nitrophenolate and its HOMO and LUMO. Reprinted with permission from [17]. Copyright (2013) American Chemical Society

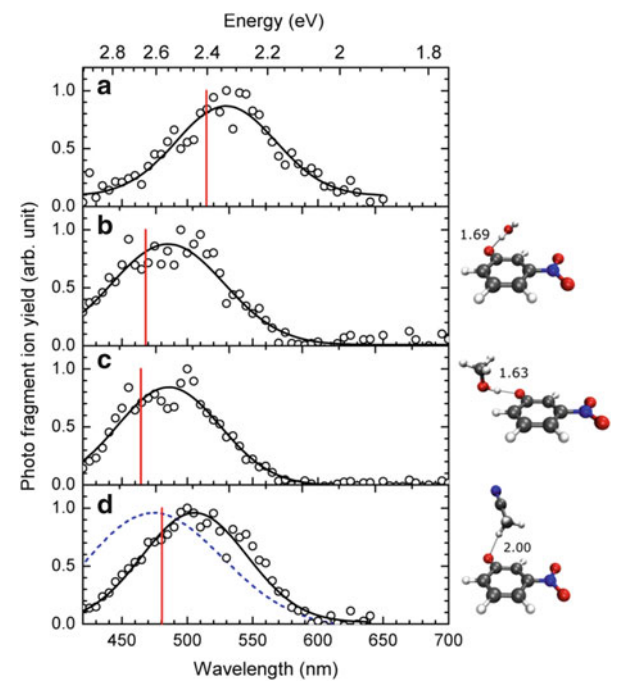
photophysical properties of the oxyluciferin anion from environmental perturbations, work on isolated ions is needed.

Recently, the gas-phase absorption spectra of bare oxyluciferin anions and their complexes with a single water molecule were reported (Fig. 6.7) [28]. The absorption band of the bare ion has a maximum at 548 ± 10 nm, which blueshifts by about 50 nm (0.2 eV) upon addition of the water molecule. In the experiment the water is located in a favourable position for the ground-state ion, and clearly this geometry may not be the same within the protein pocket where the electronically excited oxyluciferin is formed biochemically. In any case, the water molecule significantly perturbs the electronic structure, which is indicative of the transition having charge-transfer character.

A similar shift was measured for the *meta*-nitrophenolate anion that represents an excellent example of ions undergoing charge-transfer transitions [29]. In the *meta* ion (Fig. 6.8) there is limited coupling between the donor (phenolate oxygen) and the acceptor (nitro group) as there are no resonance forms where the excess electron can be moved to the nitro group (in contrast to the *ortho* and *para* family members). When a solvent molecule is attached to the bare ion, the absorption band maximum blueshifts by 0.22 eV, 0.22 eV, and 0.12 eV for water, methanol, and acetonitrile, respectively (uncertainty of 0.05 eV) (see Fig. 6.9 where predicted coupled-cluster excitation energies are also included).

While these data have provided information on excitation energies going from the ground state to an excited state, it would be useful to study the light-emission 114 S.B. Nielsen

Fig. 6.9 Action spectra of (a) bare *meta*-nitrophenolate anion, (b) anion with one water attached, (c) anion with one methanol attached, and (d) anion with one acetonitrile attached. The red sticks are CC2-calculated values. The blue dashed curve in (d) is the spectrum obtained in bulk acetonitrile solution. Distances [in Å] from hydrogen to the phenolate oxygen are given on the structures to the right. Carbon is grev, oxygen red, nitrogen blue, and hydrogen white. Reprinted with permission from [29]. Copyright (2013) American Chemical Society



process that is the relevant transition in fireflies. Future work recording the light emitted from electronically excited oxyluciferin anions isolated *in vacuo* would therefore be highly illuminating. Also the quantum yield for light emission when there is no protein environment would be relevant to measure, and whether one single water molecule plays a biological role or not.

References

- Lakowicz, J.R.: Principles of Fluorescence Spectroscopy, 2nd edn. Kluwer Academic/Plenum, New York (1999)
- Forbes, M.W., Jockusch, R.A.: Gas-phase fluorescence excitation and emission spectroscopy of three xanthene dyes (Rhodamine 575, Rhodamine 590 and Rhodamine 6G) in a quadrupole ion trap mass spectrometer. J. Am. Soc. Mass Spectrom. 22, 93–109 (2011)
- Bian, Q., Forbes, M.W., Talbot, F.O., Jockusch, R.A.: Gas-phase fluorescence excitation and emission spectroscopy of mass-selected trapped molecular ions. Phys. Chem. Chem. Phys. 12, 2590–2598 (2010)
- Friedrich, J., Fu, J., Hendricksson, C.L., Marshall, A.G., Wang, Y.-S.: Time resolved laserinduced fluorescence of electrosprayed ions confined in a linear quadrupole trap. Rev. Sci. Instrum. 75, 4511–4515 (2004)
- Khoury, J.T., Rodriguez-Cruz, S.E., Parks, J.H.: Pulsed fluorescence measurements of trapped molecular ions with zero background detection. J. Am. Soc. Mass Spectrom. 13, 696–708 (2002)

- Chingin, K., Balabin, R.M., Frankevich, V., Chen, H., Barylyuk, K., Nieckarz, R., Fedorov, A., Zenobi, R.: Optical properties of protonated Rhodamine 19 isomers in solution and in the gas phase. Phys. Chem. Chem. Phys. 12, 14121–14127 (2010)
- Chingin, K., Chen, H., Gamez, G., Zenobi, R.: Exploring fluorescence and fragmentation of ions produced by electrospray ionization in ultrahigh vacuum. J. Am. Soc. Mass Spectrom. 20, 1731–1738 (2009)
- Czar, M.F., Jockusch, R.A.: Understanding photophysical effects of cucurbituril encapsulation: a model study with acridine orange in the gas phase. ChemPhysChem 14, 1138–1148 (2013)
- Nagy, A.M., Talbot, F.O., Czar, M.F., Jockusch, R.A.: Fluorescence lifetimes of rhodamine dyes in vacuo. J. Photochem. Photobiol. A Chem. 244, 47–53 (2012)
- Sagoo, S.K., Jockusch, R.A.: The fluorescence properties of cationic rhodamine B in the gas phase. J. Photochem. Photobiol. A Chem. 220, 173–178 (2011)
- McQueen, P.D., Sagoo, S., Yao, H., Jockusch, R.A.: On the intrinsic photophysics of fluorescein. Angew. Chem. Int. Ed. 49, 9193–9196 (2010)
- 12. Yao, H., Jockusch, R.A.: Fluorescence and electronic action spectroscopy of mass-selected gas-phase fluorescein 2',7'-dichlorofluorescein, and 2',7'-difluorofluorescein ions. J. Phys. Chem. A 117, 1351–1359 (2013)
- Kordel, M., Schooss, D., Neiss, C., Walter, L., Kappes, M.M.: Laser-induced fluorescence of Rhodamine 6G cations in the gas phase: a lower bound to the lifetime of the first triplet state. J. Phys. Chem. A 114, 5509–5514 (2010)
- Donald, W.A., Leib, R.D., Demireva, M., Negru, B., Neumark, D.M., Williams, E.R.: "Weighing" photon energies with mass spectrometry: effects of water on ion fluorescence. J. Am. Chem. Soc. 132, 6904–6905 (2010)
- Danell, A.S., Parks, J.H.: FRET measurements of trapped oligonucleotide duplexes. Int. J. Mass Spectrom. 229, 35–45 (2003)
- Dashtiev, M., Azoz, V., Frankevich, V., Scharfenberg, L., Zenobi, R.: Clear evidence of fluorescence resonance energy transfer in gas-phase ions. J. Am. Soc. Mass Spectrom. 16, 1481–1487 (2005)
- Talbot, F.O., Rullo, A., Yao, H., Jockusch, R.A.: Fluorescence resonance energy transfer in gaseous, mass-selected polyproline peptides. J. Am. Chem. Soc. 132, 16156–16164 (2010)
- Iavarone, A.T., Parks, J.H.: Conformational change in unsolvated Trp-cage protein probed by fluorescence. J. Am. Chem. Soc. 127, 8606–8607 (2005)
- Iavarone, A.T., Patriksson, A., van der Spoel, D., Parks, J.H.: Fluorescence probe of Trp-cage protein conformation in solution and in gas phase. J. Am. Chem. Soc. 129, 6726–6735 (2007)
- Iavarone, A.T., Duft, D., Parks, J.H.: Shedding light on biomolecule conformational dynamics using fluorescence measurements of trapped ions. J. Phys. Chem. A 110, 12714–12727 (2006)
- Iavarone, A.T., Meinen, J., Schulze, S., Parks, J.H.: Fluorescence probe of polypeptide conformational dynamics in gas phase and in solution. Int. J. Mass Spectrom. 253, 172–180 (2006)
- Shi, X., Parks, J.H.: Fluorescence lifetime probe of biomolecular conformations. J. Am. Soc. Mass Spectrom. 21, 707–718 (2010)
- 23. Shi, X., Duft, D., Parks, J.H.: Fluorescence quenching induced by conformational fluctuations in unsolvated polypeptides. J. Phys. Chem. B 112, 12801–12815 (2008)
- 24. Rodriguez-Cruz, S.E., Khoury, J.T., Parks, J.H.: Protein fluorescence measurements within electrospray droplets. J. Am. Soc. Mass Spectrom. 12, 716–725 (2001)
- Shimomura, O.: Bioluminescence: Chemical Principles and Methods. World Scientific, Hackensack, NJ (2006)
- Ando, Y., Niwa, K., Yamada, N., Enomoto, T., Irie, T., Kubota, H., Ohmiya, Y., Akiyama, H.: Firefly bioluminescence quantum yield and colour change by pH-sensitive green emission. Nat. Photon. 2, 44–47 (2008)
- Hosseinkhani, S.: Molecular enigma of multicolor bioluminescence of firefly luciferase. Cell. Mol. Life Sci. 68, 1167–1182 (2011)

116 S.B. Nielsen

28. Støchkel, K., Hansen, C.N., Houmøller, J., Nielsen, L.M., Anggara, K., Linares, M., Norman, P., Nogueira, F., Maltsev, O.V., Hintermann, L., Brøndsted Nielsen, S., Naumov, P., Milne, B. F.: On the influence of water on the electronic structure of firefly oxyluciferin anions from absorption spectroscopy of bare and monohydrated ions in vacuo. J. Am. Chem. Soc. 135, 6485–6493 (2013)

29. Houmøller, J., Wanko, M., Støchkel, K., Rubio, A., Brøndsted Nielsen, S.: On the effect of a single solvent molecule on the charge-transfer band of a donor-acceptor anion. J. Am. Chem. Soc. 135, 6818–6821 (2013)

Spectroscopy of Ferric Heme and Protoporphyrin IX Ions *In Vacuo*

Jean Ann Wyer and Steen Brøndsted Nielsen

Abstract

This chapter deals with gas-phase spectroscopy of protoporphyrin IX and heme ions, two important biochromophores in nature. These ions strongly absorb blue and green light, which accounts for e.g. the red colour of blood. We present absorption spectra of four-coordinate ferric heme cations at room temperature and in cold helium droplets, obtained in both cases from light-driven dissociation processes. These spectra serve as references for protein biospectroscopy and provide a natural testing ground for advanced quantum chemical modelling. The role of axial ligands bound to the iron centre, i.e., amino acids and nitric oxide, on the electronic structure of the porphyrin ring is discussed, and gas-phase spectra are compared to relevant protein ones. Spectroscopy on intact multiply charged protein anions with the heme prosthetic group is possible by monitoring the detachment of electrons triggered by light absorption. Similar experiments on protein cations rely on the absorption of too many photons for dissociation to be of practical use. This is illustrated from results on cytochrome c in vacuo. Time constants for dissociation and the corresponding dissociation channels obtained from storage-ring experiments are presented and discussed in the context of vibrational cooling within a heme protein cavity. Finally, we show the time spectrum for dissociation of photoexcited protoporphyrin IX anions, from which it is concluded that intersystem crossing to triplet states is in competition with internal conversion to the ground state. This is somewhat supported by spectroscopic characterisation of the long-lived states based on pump-probe experiments. Hence from one time spectrum (a one-laser experiment), triplet quantum yields can easily be estimated.

Department of Physics and Astronomy, Aarhus University, 8000 Aarhus C, Denmark e-mail: jeanwyer@phys.au.dk; sbn@phys.au.dk

J.A. Wyer (⋈) • S.B. Nielsen

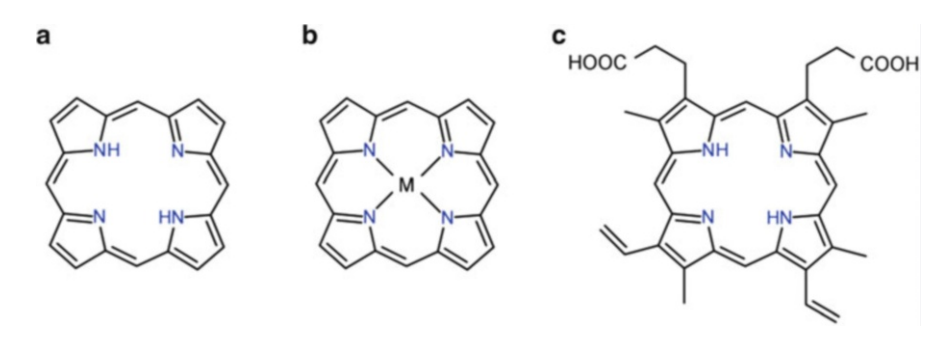


Fig. 7.1 Schematic drawings of (a) porphin, (b) metalloporphin, where M represents a metal atom, and (c) protoporphyrin IX (PP)

7.1 Introduction

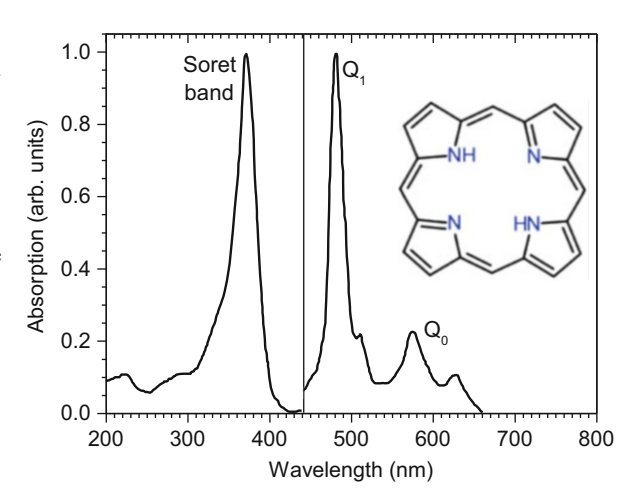
Porphyrin-molecules are ubiquitous in nature and are engaged in many essential biological processes, e.g., photosynthesis, dioxygen transport and storage, signalling and sensing [1–3]. They belong to a class of highly symmetric heterocyclic π -conjugated systems composed of the parent unit porphin with various peripheral substituents (see Fig. 7.1). Metalloporphyrins are formed when a metal atom is substituted for the two central protons and bound to the four central nitrogens.

In general metalloporphyrins have an intense absorption band called the Soret band between 380 nm and 450 nm and two visible bands separated by ~1,250 cm⁻¹ between 500 nm and 600 nm denoted the Q-bands [4]. However, the exact band positions depend on the particular porphyrin molecule and its environment. The Soret band is ascribed to a $\pi\pi^*$ transition to the second excited singlet state, while the Q-bands are due to a $\pi\pi^*$ transition to the first excited singlet state (lower-energy band) and a vibronic transition (higher-energy band) [4]. For porphyrins there is a further splitting of the bands in the visible region due to the breaking of the D_{4h} symmetry of the porphyrin ring by the central proton axis (D_{2h} symmetry), see Fig. 7.2 [4].

One molecule of particular interest is protoporphyrin IX (PP) (Fig. 7.1) as when iron is substituted for the two central protons, heme is formed. Ferrous and ferric heme refers to iron being in oxidation state +2 (Fe(II)) or +3 (Fe(III)), respectively. Heme is often located in hydrophobic protein pockets or crevices with minimal access to water and other molecules. Well-known proteins in which it is found are myoglobin (Mb) and hemoglobin (Hb) where it is responsible for the storage and transport of dioxygen, respectively.

The central iron in heme has six coordination positions, four of which are occupied by the porphyrin ring nitrogens. The remaining two are perpendicular to the plane of the heme molecule. In many heme proteins a proximal histidine (His) amino acid residue axially ligates to the iron [1], which causes the iron atom to displace slightly from the porphyrin ring. If molecular oxygen binds to Fe(II) in the remaining coordination position, the iron atom moves back into the plane of the

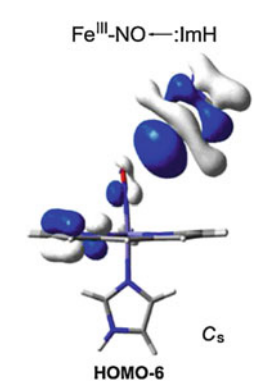
Fig. 7.2 Vapour-phase absorption spectra of porphin. Data are taken from [5]. As the intensity of absorption in the Q-band region is less intense than that in the Soretband region, the data have been expanded for clarity. The *vertical line* separates the different expansion regions. A schematic drawing of porphin is included. Adapted from [5], 1971, with permission from Elsevier



ring, pulling the histidine, which causes a strain that induces conformational changes in the protein. O_2 and CO only bind to ferrous heme, while the NO radical can coordinate to both ferrous and ferric heme. These diatomic molecules activate or inhibit key biological processes by binding to heme, but the processes strongly depend on the surrounding protein environment that modulates the electronic properties of the adduct. Both electrostatic interactions and hydrogen-bonding effects associated with sidechains distal to the bound molecule can play a role. Furthermore, the axial ligand trans to the diatomic molecule is important, often being either histidine (cf., Mb and Hb) or cysteine. The strength of its binding influences the bond between iron and the diatomic molecule.

Heme-NO proteins play a key role in many physiological functions including blood clotting, blood pressure regulation, immune response, nerve signal transduction, and vasodilation upon the bite of blood-sucking insects [6–8]. Even though ferric heme can bind NO, the affinity for NO is lower for Fe(III) than Fe(II), a fact that is exploited in the liberation of NO after transportation [9]. Furthermore, the Fe (II)-NO and Fe(III)-NO moieties are different, with the former adopting a bent conformation and the latter a linear one when the proximal ligand is histidine [9–12]. As this linearity is caused by electron transfer from NO to Fe(III) through the σ orbital a more proper description of the unit is Fe(II)–NO⁺ [9–12]. According to TD-DFT and CASSCF calculations this is a singlet state [11, 13]. The absorption in the Q band region in measured ferric nitrosyl proteins ranges from 549 nm to 574 nm in the Q_0 band and 518 nm to 538 nm in the Q_1 band (see Table in [14]). If, on the other hand, the proximal ligand is an electron-rich ligand such as cysteinate, then the electron donation is retarded and back-donation from the iron to NO is facilitated. This results in a slightly bent and tilted coordination [10, 11], and the absorption in the Q-band region is redshifted to 571-585 nm (Q_0) and 533-549 nm (Q1). For both ferric heme nitrosyl complexes, the Enemark-Feltham notation is {Fe(NO)}⁶ where 6 refers to the number of Fe d electrons plus the unpaired electron of NO.

Fig. 7.3 The lone pair of a distal imidazole (ImH) group that is near to an Fe(II)–NO $^+$ heme adduct interacts with the HOMO-6 of the latter. This orbital interaction leads to electron density being pushed out of the NO π^* orbital and onto the porphyrin. Reprinted from [17], with permission from Elsevier



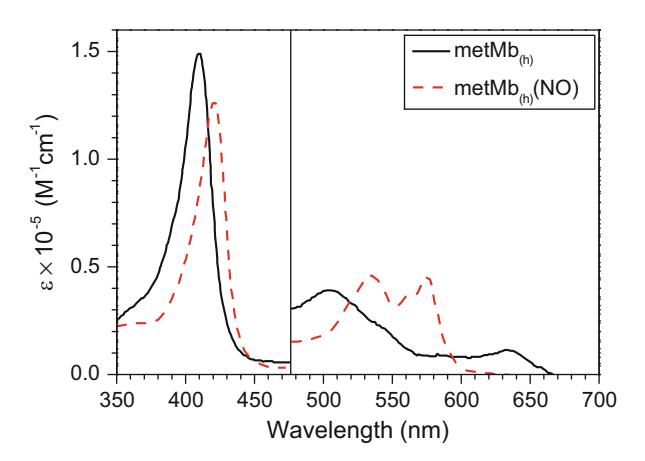
Interestingly, the positive charge on NO when it coordinates to ferric heme implies stronger interactions with the environment than those for the isoelectronic Fe(II)–CO adduct. Thus, DFT modelling has revealed that the lone pair of a nearby imidazole would be directed toward the NO with an interaction energy of 0.05 eV [15]. Indeed, when the distal histidine in Mb is replaced by apolar residues, the Fe (III)–NO dissociation rate has experimentally been found to increase seven to tenfold [16]. The lone pair actually pushes electron density out of the NO π^* orbital and onto the porphyrin (Fig. 7.3) [17]. A structured water in the protein cavity can display a similar effect. These electronic perturbations are likely to show up in the electronic absorption spectrum, in the Soret and/or Q-band regions.

It is a great advantage and highly exploited fact that the absorption by heme proteins strongly depends on the microenvironment of the heme, with spectral features depending on the iron oxidation state, peripheral substituents, axial ligands, coordination state, spin state, and nearby amino acid residues. Sample absorption spectra are shown in Fig. 7.4 for metMb with and without NO bound to the prosthetic ferric heme group. The spectral features change upon NO binding, and both the Soret and Q bands redshift. The band between 600 nm and 650 nm seen for metMb is ascribed to porphyrin π -iron(III) charge transfer transitions. It disappears when NO is bound because the electron donation from NO to iron reduces the formal oxidation state of the iron to +2. Thus, with appropriate reference spectra, spectroscopy can provide important information on the environment of the heme. While some of the required reference spectra are easily obtainable, others are not as will be discussed next.

7.2 Spectroscopy of 4c Ferric Heme, Complexes with Amino Acids and NO, and Proteins *In Vacuo*

Under certain conditions it has been speculated that 5-coordinated (5c) ferric heme proteins undergo histidine deligation. Two possible pathways for lowering the coordination state to four are acid-induced rupture of the iron–histidine bond due to histidine protonation [19], or local heating after multiple photon absorption.

Fig. 7.4 Electronic absorption spectra of equine heart metmyoglobin metMb_(h) (solid black line) and its complex with nitric oxide (dotted red line) in 50 mM pH 7.4 phosphate buffer solution. Data to the right of the vertical line has been expanded for clarity (×5). Adapted with permission from [18]. Copyright (2001) American Chemical Society



Spectroscopic characterisation of 4c ferric heme in order to obtain a reference spectrum (or finger-print spectrum) is by conventional methods, however, hampered by the strong affinity of Fe(III) for water and anions. A change in protein absorption at low pH is therefore difficult to interpret since it may be due to a different heme microenvironment caused by conformational changes and denaturation, and not necessarily to the formation of 4c Fe(III)—heme. Two very different approaches were taken to circumvent these obstacles and are described in the following.

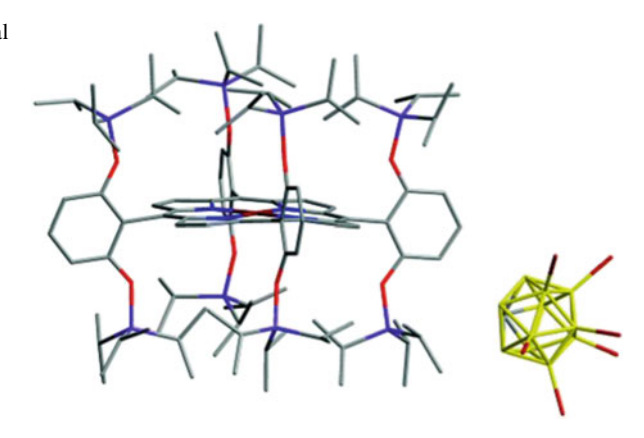
The first measurement of a 4c Fe(III)–porphyrin cation was performed by Fang et al. [20], who used an elegant synthesis approach to sterically hinder ligation and produce the 4c $[Fe(III)-(TipsiPP)]^+[CB_{11}H_6Br_6]^-(5,10,15,20-tetrakis(2',6'-bis (triisopropylsiloxy)-phenyl) porphyrinatoiron (III) hexabromocarborane) (see Fig. 7.5). Maximal absorption in the Soret-band region is at 400 nm, while in the Q band there is a single band at 505 nm (Fig. 7.6).$

An alternative way of recording the absorption spectra of such 4c Fe(III)—porphyrin ions involves using electrospray ionisation to bring the bare ions gently and intact into the gas phase. Then isolated ions can be investigated *in vacuo* where there are with certainty no external perturbations. This method can also be used to study more complex ions as axial ligands can be added in a controlled way. However, a disadvantage with studying ions in the gas phase is that the number of ions produced is too low to cause a measurable change in the number of photons in the transmitted light, and conventional absorption spectroscopy cannot be used. This is true even when a trap is used to create a bunch of ions. Absorption measurements instead rely on the detection of fragmentation or electron detachment (*i.e.* action spectroscopy). We note that for iron porphyrins luminescence does not need to be considered as all transitions after photoexcitation are radiationless; the reason for this is that low-lying d–d excited states of the iron atom rapidly depopulate the excited state (Fig. 7.7) [24].

The first measurements on the absorption by bare Fe(III)—heme⁺ ions (Fig. 7.8) were performed *in vacuo* at the ELISA storage ring (see Fig. 7.6b) [21, 22]. There

Fig. 7.5 X-ray single-crystal structure of [Fe (III)–(TipsiPP)]

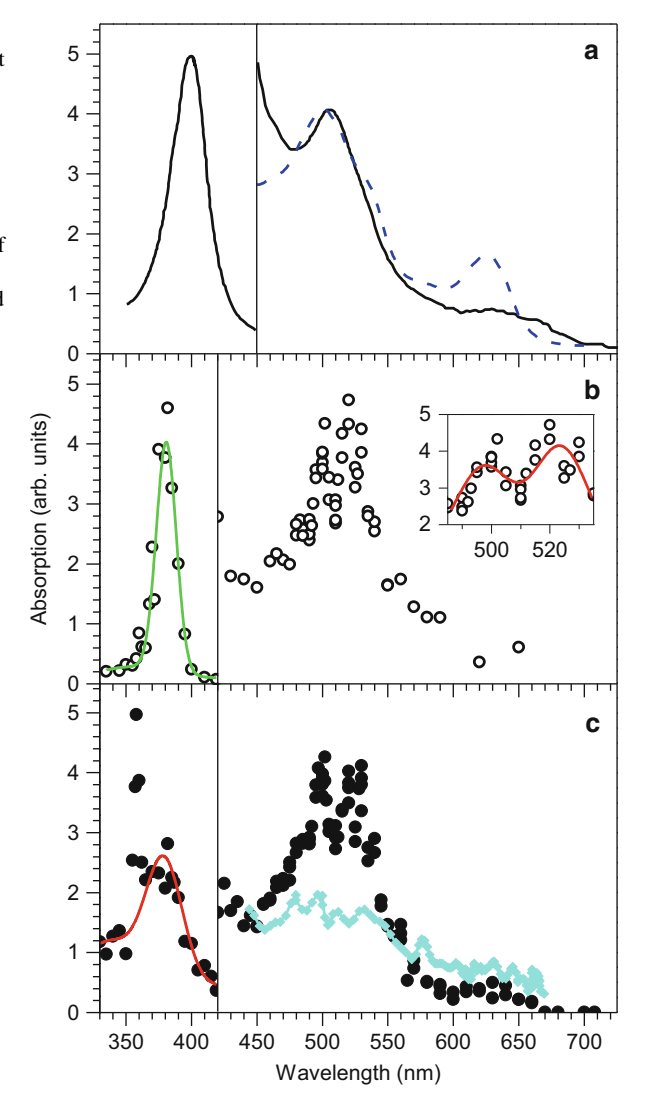
⁺[CB₁₁H₆Br₆] [20]. The Fe (III)–porphyrin is located within a cage that prevents water and anions from binding to the central iron atom. Carbon is *grey*, nitrogen *blue*, oxygen *red*, boron *yellow*, and bromine *dark red*. Reprinted with permission from [20]. Copyright (2008) American Chemical Society



the maximal absorption in the Soret band was found to be at 380 nm which is 20 nm to the blue of that measured for the bis-pocket siloxyl porphyrin. This suggests that the cage around the porphyrin is not completely innocent, and that it actually does perturb the $\pi\pi^*$ transition. It should also be mentioned that the peripheral substituents are different. In the O-band region increased absorption at ~532 nm was due to a change in the laser beam profile which resulted in increased overlap with the ion beam at the second harmonic of the pump laser used to create the output light. A fit to the data after exclusion of these erroneous points found maxima at 497 nm and 524 nm for the gaseous ion. This corresponds to an energy difference of 1,020 cm⁻¹. The absorption spectrum of heme⁺ in solution where both axial positions of the heme are taken up by ligands (solvent molecules or anions) is shown as a dashed blue line in Fig. 7.6a. It displays a broad band between 450 nm and 550 nm which appears to be formed from two individual band maxima at 500 nm and 539 nm. It is evident that the position of the Q band for isolated 4c ferric heme, solvated ferric heme, and the cage complex is similar (Fig. 7.6), showing that in this region the environment does not have a strong effect on the absorption. The ligand-to-metal transition at high wavelengths is, however, more pronounced in solution phase revealing a clear band at 626 nm.

In a recent, beautiful experiment, von Helden and co-workers [25] produced Fe(III)—heme⁺ ions in cold helium droplets (16 K). Spectroscopic measurements on those found the Soret-band position and width to be similar to that measured for the room-temperature ions, although a slight blue shift (\sim 2 nm) and slight narrowing of the band (full width half maximum of \sim 11 nm vs. \sim 16 nm) at the low-energy side were seen, in accordance with less hot-band transitions (Fig. 7.9). While a wide band is expected for room-temperature ions, the still rather broad and unstructured band for the cold ions was attributed to an ultra-short lifetime in the excited state (cf., Heisenberg's uncertainty principle). Indeed, coupling to the S₁ state and d–d excited states provides an efficient deexcitation route.

Fig. 7.6 (a) Absorption spectra of hindered bis-pocket siloxyl porphyrin ([Fe (III)-(TipsiPP)]+ [CB₁₁H₆Br₆]⁻) (solid black line) [20], and hemin (heme chloride salt) in a methanol solution (dashed blue curve) [21]. (b) Gas-phase spectra of 4c Fe(III)-heme+ (open circles) [21, 22]. An enlarged view of the Q band is shown in the inset. (c) Gas-phase spectra of 5c Fe (III)-heme+(His) (closed circles) [21, 22], and Fe (III)-heme+(DMSO) (DMSO dimethylsulfoxide) (cyan line) [23]. Curves are shown to guide the eye, green and red representing heme+ and heme⁺(His), respectively



In addition to measuring the absorption by 4c ferric heme, the spectrum for the 5c ferric heme with a histidine ligand (Fe(III)-heme⁺(His)) (Fig. 7.8c) was also recorded at ELISA (see Fig. 7.6c). In the Q-band region the spectrum for the adduct is almost identical to that of the 4c Fe(III)-heme⁺. This again shows that the environment does not perturb the absorption much in this region. In the Soretband region, there is a sharp peak at ~358 nm that is due to anomalies in the laser beam profile (the third harmonic of the pump laser used to create the output light is 355 nm). Indeed close investigation of the Fe(III)-heme⁺ spectrum also reveals increased absorption at this wavelength, albeit with far less intensity due to the

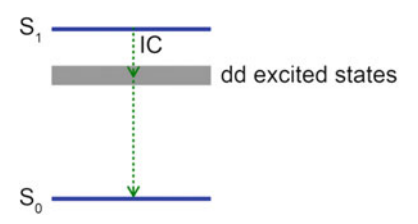


Fig. 7.7 dd excited states act as doorway states, quickly bringing the heme back to its electronic ground state. Note vibrational levels are not included for clarity

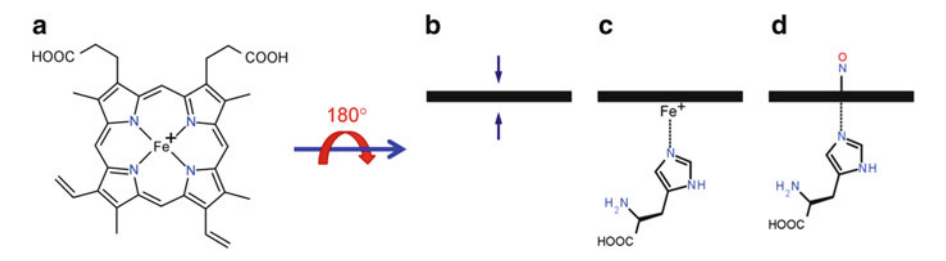


Fig. 7.8 Schematic drawings of (a) Fe(III)—heme⁺, (b) Fe(III)—heme⁺ (side-view), (c) Fe(III)—heme⁺(His), and (d) Fe(III)—heme⁺(His)(NO). The *two arrows* in (b) indicate the central iron atoms fifth- and sixth-coordination positions which are perpendicular to the plane of the heme molecule (*black bar*). As indicated in (c), when histidine is bound to iron at the fifth coordination position, the central iron is pulled out of the plane of the porphyrin ring. If the sixth coordination position is occupied, the iron moves back into the plane (d). It should be noted that the propionic acid side chains are ionised in the protein in contrast to the gas-phase species

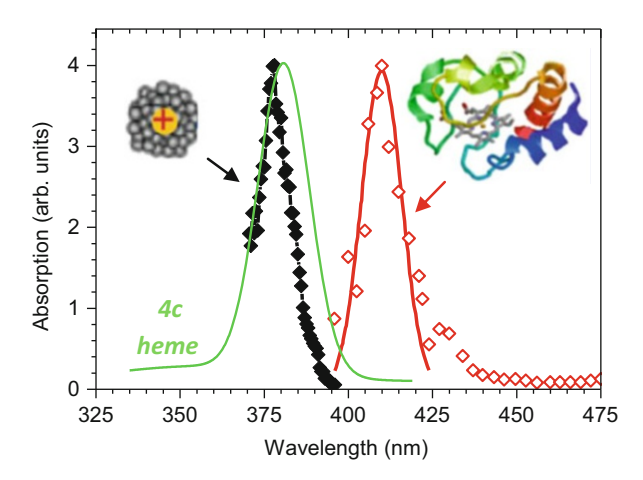


Fig. 7.9 Absorption spectra of cold Fe(III)–heme⁺ in helium droplets (*black diamonds*) [25], and ferri-cytochrome c⁶⁻ *in vacuo* (*red open diamonds*) [26]. The fit to the gas-phase Fe(III)–heme⁺ data displayed in Fig. 7.6b is shown here for comparative purposes (*green line*)

lower absorption of light by Fe(III)–heme⁺ here. A similar anomaly was seen at the second harmonic (532 nm) of the pump laser (*vide supra*). If this anomalous peak is ignored, it can be seen that the complex displays a broad absorption band with a maximum at 379 nm and a pronounced shoulder on the high energy side. This shoulder is likely due to charge-transfer transitions. In relation to the bare Fe(III)–heme⁺ ion, the maximum of the Soret band for Fe(III)–heme⁺(His) is at approximately the same position but the band has broadened considerably and displays the aforementioned high-energy shoulder. The broadening is likely due to the different electronic structures of the porphyrin in the two molecules: In heme the iron occupies the central hole of the porphyrin ring (planar heme), while in Fe(III)–heme⁺(His) it is displaced out of the plane by 0.28 Å to maximise chemical bonding with the histidine (Fig. 7.8c) [27].

The spectrum of the adduct is similar in shape to that of 5c high-spin Fe(III)—heme in metmyoglobin variants in which the distal histidine is replaced by a nonpolar residue. The latter prevents water from taking up the available sixth coordinate site [27, 28]. However, such protein variants display maximum absorption at about 395 nm, which is a redshift of 16 nm compared to the isolated complex. Likewise, the adduct between 1,2-dimethyl-imidazole and ferric heme embedded in SDS (sodium dodecyl sulfate) micelles has a maximum at 400 nm, which is again significantly redshifted compared to the isolated Fe(III)—heme⁺(His) [29]. The environment within the micelle mimics the hydrophobic cavity of heme proteins.

In other work, Nonose et al. [23] measured the absorption by the adduct between Fe(III)—heme⁺ and DMSO (dimethylsulfoxide) in the visible light region and found a broad absorption band at ~500 nm (Fig. 7.6c). While the position of the band is similar to that of Fe(III)—heme(His)⁺, the relative intensities of absorption in the Q band to that at higher wavelengths are different.

Excitations at wavelengths higher than in the Q-band region are, as mentioned previously, ascribed to porphyrin π -iron charge-transfer transitions, likely transitions to the iron $e_g(d_{xy},d_{yz})$ orbitals [4, 24]. For Fe(III) there are three possible spin states; 1/2, 3/2 and 5/2. A comparison of the gas-phase Fe(III)—heme⁺ and Fe(III)—heme⁺ (His) data to spectra for myoglobin indicates that the iron is not high spin [30]. The similarities between the two spectra indicate that isolated 4c and 5c ferric heme ions are in the same spin state. This is consistent with quantum-chemical modelling which find that the electronic ground states of both Fe(III)—heme⁺ and Fe(III)—heme⁺(His) are quartet states [31–34].

In a recent study Dugourd and co-workers [26] produced the entire ferricytochrome c protein in the gas phase and recorded its absorption spectrum in the Soret-band region by monitoring the electron photodetachment yield of cytochrome c⁶⁻ from measurements of the production of cytochrome c⁵⁻ (Fig. 7.9). Maximal absorption was found to be at 410 nm, which is similar to the position of the band for the native cytochrome c in solution. Thus, the protein pocket induced a shift of 30 nm from that of the bare Fe(III)—heme⁺ *in vacuo*. As one histidine residue broadened the absorption spectrum but did not induce a significant shift, the authors conclude that the entire protein pocket is important in restoring the optical properties of the heme protein. Furthermore, their results suggest that the protein environments of the heme group are similar in both solution and gas phase, and that

the chromophore is protected from water molecules by the polypeptide chain. More details can be found in Chap. 8 by Antoine and Dugourd.

It should be mentioned that spectroscopy of protein cations *in vacuo* is nontrivial as one photon is seldom enough to cause dissociation. The many degrees of freedom act, so to speak, as an internal heat bath rendering it unlikely that a sufficient amount of energy accumulates in the dissociation mode. As a demonstration of this, Fig. 7.10 shows the time spectrum of [cytochrome c + 17H]¹⁷⁺ stored in ELISA [35]. The protein was irradiated with intense 532-nm light after 2.27 ms of storage time in the ring; the light was the second harmonic output from an Nd: YAG laser. Absorption is seen based on the increased yield of fragment ions measured by the detector but at least five photons were required. Most likely the output from an OPO would not be intense enough to cause dissociation, and wavelength scans are therefore not easily done.

Next we consider NO binding to 4c ferric heme. Such complexes were first made by Fornarini and co-workers [36] from ion-molecule reactions between heme ions and NO gas. Interestingly, the stabilisation of the associative complexes was afforded by radiative emission and not ternary collisions. This gas-phase synthesis approach nicely eliminates the problems of reductive nitrosylation processes in solution phase which lead to reduced iron species [36–38]. The complexes and other Fe^{III}–NO model complexes were characterised based on infrared multiphoton photodissociation [13, 39]. Their work agreed with the formulation of the ground state as Fe^{II}– NO⁺ and ruled out the Fe(η^1 -ON) linkage isomer. The η^2 -NO isomer is more than 1 eV higher in energy than the η^1 -NO isomer [13].

In recent experiments, we did spectroscopy of Fe(III)-heme⁺(NO) [14]. These ions are weakly bound requiring only about 1 eV for dissociation, which implies that the time scale for their dissociation is short after absorption of a visible photon (>2 eV). An accelerator mass spectrometer was therefore used instead of the storage ring to sample dissociation from the yield of ionic fragments produced at each wavelength. Unlike in the storage ring where all fragmentation channels that result in at least one neutral fragment can be measured simultaneously, each fragmentation channel has to be measured independently at this setup. Fortunately, however, the only photoinduced fragment of Fe(III)-heme⁺(NO) at low photon fluxes was heme⁺ (vide infra).

The action spectrum of Fe(III)–heme $^+$ (NO) in the Q-band region is shown in Fig. 7.11 [14]. There, a prominent band with a maximum at 561 ± 4 nm and corresponding to the Q_0 band is seen. A shoulder at ~523 nm is also evident and absorption extends up to 700 nm. For the bare Fe(III)–heme $^+$ ion the Q_0 band has a maximum at 524 nm (*vide supra*); thus NO ligation redshifts the absorption by 37 nm. As mentioned above, the position of the Q_0 band for ferric heme(NO) proteins with a proximal His residue was measured to lie between 549 nm and 574 nm. However, the position for most of the measured proteins lies in the range between 560 nm and 572 nm, which is very close to that observed for the gas-phase Fe(III)–heme $^+$ (NO) ion (561 nm). This again shows that the effect of the His is limited, and thus variations at the distal site likely account for any small differences. For example a distal histidine or water molecule in the hydrophobic protein pocket may orient an electron lone pair towards the NO $^+$ ligand with a concomitant

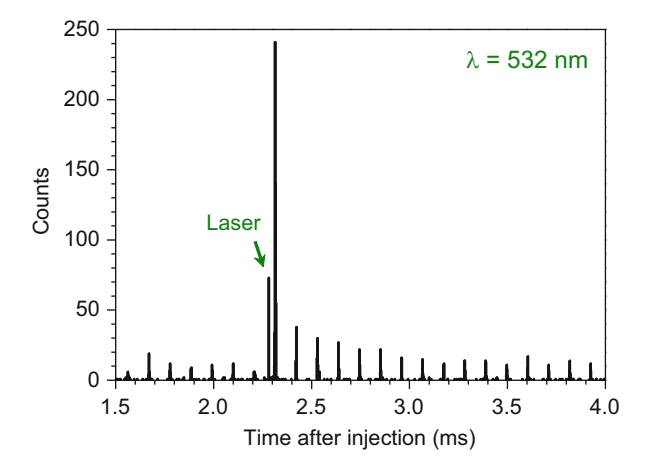


Fig. 7.10 Decay of [cytochrome $c + 17H]^{17+}$ ions circulating in ELISA. Fragment ions were measured by a channeltron detector (see Chap. 3), and the spacing between the peaks is the ion revolution time in the ring. After 2.27 ms of storage the ions were irradiated by 532-nm light on the same side as where the detector was located. A small amount of the laser light hit the detector giving rise to a detector signal (labelled 'Laser'). Fragment ions are formed as a result of either collisions with residual gas in the ring or photon absorption. Reprinted with permission from [35]. Copyright [2002], American Institute of Physics

disturbance of the electronic structure of the porphyrin macrocycle (cf., Fig. 7.3). As some of the protein spectra are slightly redshifted (by up to about 13 nm) relative to that of the naked complex, it seems that such a perturbation lowers the energy difference between the S_0 and S_1 states.

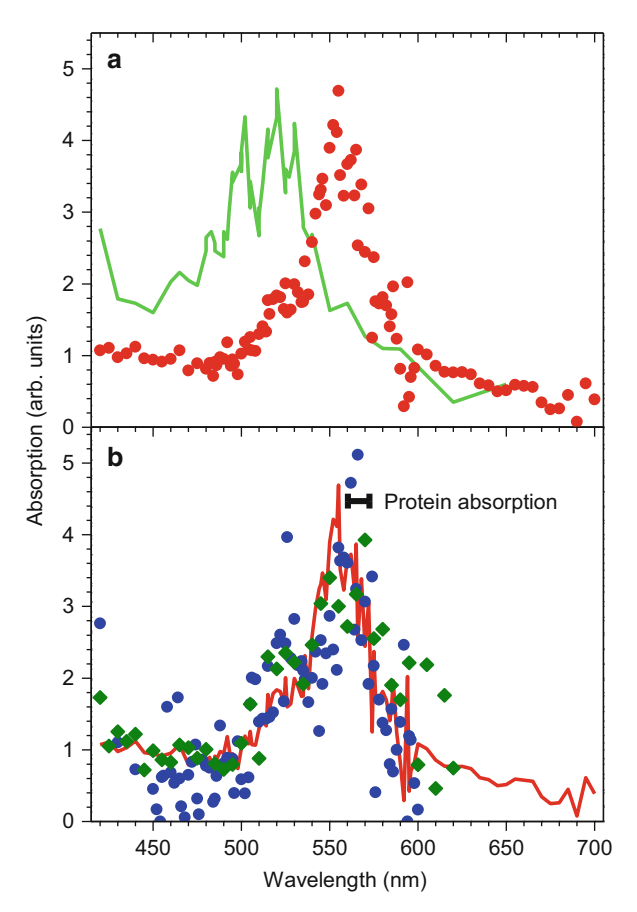
When methionine (Met) is bound to Fe(III)–heme $^+$ (NO), the absorption spectrum displays two transitions; the Q_0 band at 563 ± 5 nm and the Q_1 band at 524 ± 5 nm (Fig. 7.11) [14]. Thus the lowest-energy transition is not perturbed much by the axial coordination of Met, but coupling to vibrational modes is enhanced. This is in agreement with the fact that in general, two bands of similar magnitude are seen for ferric heme nitrosyl proteins (6c heme), see for example Fig. 7.4.

A similar absorption spectrum is obtained when cysteine (Cys) is bound to Fe(III)-heme⁺(NO), although the band is to some extent broadened at lower energies. Based on protein data, a spectral redshift is expected if Cys binds as a thiolate to the iron (and the amino group is protonated to account for the overall +1 charge in our experiments) (see Fig. 7.12). Hence two dominant isomers may be present in the ion bunch, one of which has an iron thiolate ammonium ion structure with the other adopting a binding mode similar to that in Fe(III)-heme⁺(Met)(NO).

Overall, the similarity between the above-mentioned gas-phase Q-band absorption maxima of 6c ferric heme nitrosyl cations and the band maxima of many proteins indicates that the microenvironment of these protein cavities is almost innocent in perturbing the electronic structure of the macrocycle, though redshifts are observed for some proteins. Or more precisely, the difference between S_0 and S_1 does not depend much on the environment.

The spectroscopic data presented have been collected in Table 7.1.

Fig. 7.11 (a) Action spectra of 4c Fe(III)-heme⁺ (green line) [22], and Fe (III)-heme+(NO) (red solid *circles*) [14]. (**b**) Action spectra of Fe (III)-heme+(Met)(NO) (blue circles) and Fe (III)-heme⁺(Cys)(NO) (green diamonds) [14]. The action spectrum of Fe (III)-heme⁺(NO) (red line) and the range most measured proteins absorb in (560-572 nm, proximal histidine ligand) are also included in (b) for comparative purposes



7.3 Time Constants and Channels for Photo-induced Dissociation

Dissociation of photoexcited Fe(III)–heme⁺ and Fe(III)–heme⁺(His) ions occurs on the microsecond to millisecond time scale with the main channels being ascribed to loss of either one or two CH₂COOH groups through β -cleavage, and loss of histidine, respectively (see Figs. 7.13 and 7.14) [31]. The former reaction is associated with a reaction energy of about 2 eV while histidine loss costs less energy, only about 1.4 eV. In agreement with this, the dissociation of Fe(III)–heme⁺ was found to result from the absorption of either one or two photons, somewhat dependent on the excitation wavelength, while that of Fe(III)–heme⁺(His) could be accounted for purely by one-photon absorption. In this regard, the formation of the m/z-498 fragment ion from heme⁺ (loss of two CH₂COOH groups) right after photoexcitation is clear evidence of two-photon absorption as one visible photon is not enough to cause loss of both CH₂COOH groups (Fig. 7.14c).

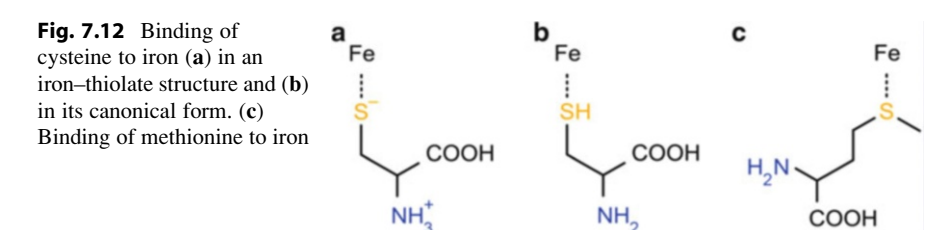


Table 7.1 Band maxima for Fe(III)–porphyrin, ferric heme ions and complexes

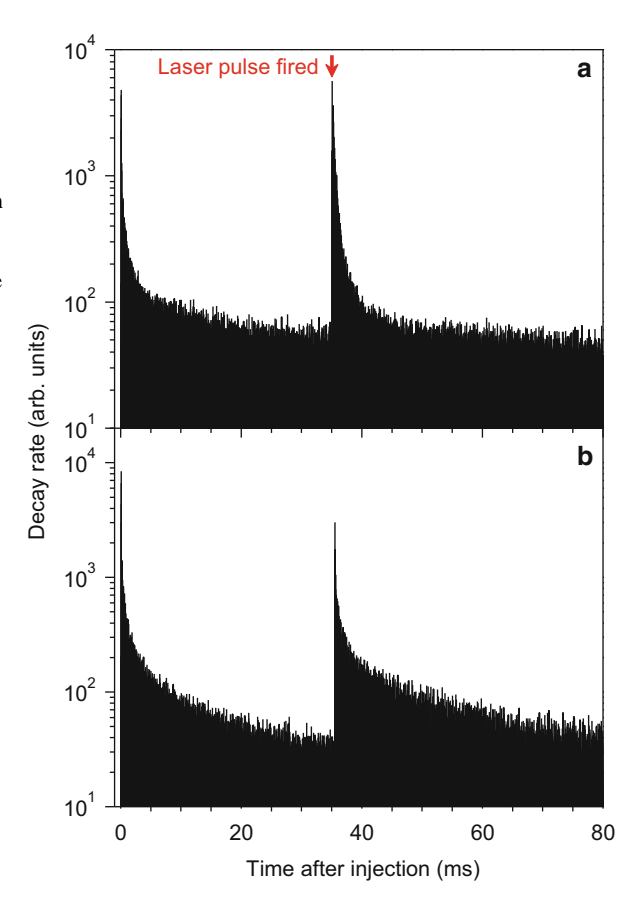
	Soret band (nm)	Q ₁ band (nm)	Q ₀ band (nm)	Reference
4c				
$\overline{(\text{TipsiPP})]^{+}[\text{CB}_{11}\text{H}_{6}\text{Br}_{6}]^{-}}$	400	505		[20]
heme ⁺ (room temp)	380	497	524	[21, 22]
heme ⁺ (16 K)	378	_		[25]
5c				
heme ⁺ (His)	379	497	524	[21, 22]
hemin ⁺ (DMSO)	_	500		[23]
cytochrome c	410	_		[26]
heme ⁺ (NO)	_	523	561	[14]
6c				
heme ⁺ (Met)(NO)	_	524	563	[14]

A relevant question is whether dissociation can compete with heat dissipation when the heme is located within a protein cavity. In the case of horse heart cytochrome c, Negrerie et al. [40] reported the time constant for vibrational cooling to be *ca*. 4 ps based on time-resolved spectroscopy. Furthermore, no photodissociation of axial ligands took place in agreement with the long timescale for breakup of the gas-phase Fe(III)—heme⁺(His) complex. Thus, from a heme protein point of view, the heme is highly photostable.

Finally, the photodissociation mass spectrum of Fe(III)–heme $^+$ (NO) recorded at an accelerator mass spectrum is shown in Fig. 7.15. The by far dominant reaction channel was loss of NO in agreement with a 1 eV breakup energy of the complex, and there was no indication of the formation of NO $^+$. That NO $^+$ was not observed is in accordance with a crossing after excitation from the Fe(II)–NO $^+$ electronic ground state to the nearby Fe(III)–NO (radical) state that is dissociative along the Fe–NO coordinate, which accounts for the weak binding of NO to ferric heme [9, 41]. From a spectroscopic point of view it appears as if NO is bound strongly to the iron (strong σ bond between Fe³⁺ and N), while in reality it is thermodynamically weakly bound!

In very recent work, Park et al. [42] showed based on time-resolved vibrational spectroscopy of ferric Mb(NO) that the majority of proteins (86 %) undergoes NO deligation immediately after photoexcitation in the Q band. This can proceed faster than 100 fs [42, 43]. The remaining 14 % of the population returns to the ground state and thermally relaxes without NO deligation [43]. For the gas-phase complex

Fig. 7.13 Decay spectra of
(a) Fe(III)—heme⁺ and (b) Fe
(III)—heme⁺(His) recorded at
ELISA [31]. A laser pulse of
390-nm photons was fired
after 35 ms. This gave rise to
a higher yield of neutrals than
that just before excitation
where the signal was due to
the dissociation of metastable
ions and ions that collided
with residual gas in the ring.
Reprinted with permission
from [31]. Copyright 2009
American Chemical Society



described above, the vibrational energy dissipation pathway is of course not accessible since there is no protein environment to interact with, and instead vibrationally hot complexes are destined to dissociate. The assumption of complete dissociation within the microsecond-time scale of the experiment seems to be a good one.

7.3.1 Photoexcitation of Porphyrin Anions In Vacuo

The protoporphyrin IX anion (structure in Fig. 7.1c with one deprotonated carboxylic acid group) was also subjected to gas-phase spectroscopy experiments [44, 45]. In Fig. 7.16a the decay spectrum of PP anions after 430-nm photon excitation is shown. The ions dissociated by loss of CO_2 , which only requires about half an eV. Two exponential functions were needed to describe the decay of photoexcited ions, with associated time constants of 67 μ s and 0.87 ms. From power-dependence measurements it was concluded that the whole decay was mainly due to the

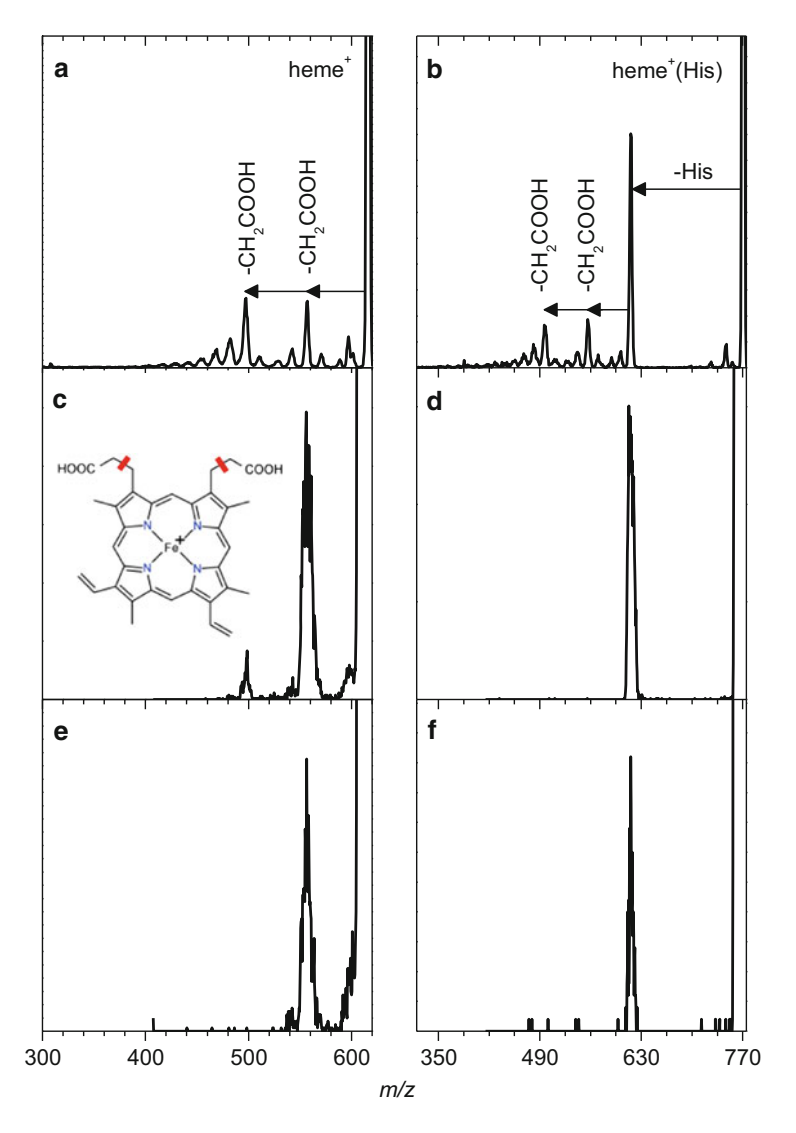
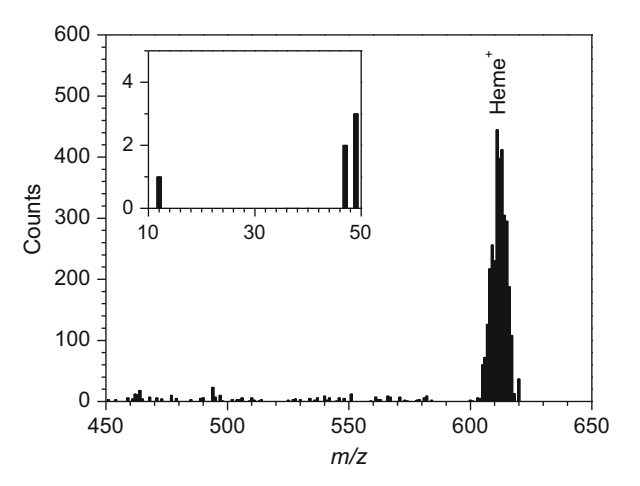


Fig. 7.14 Mass-analysed Ion Kinetic Energy (MIKE) spectra obtained from collisions between helium and (a) Fe(III)–heme⁺ (*m*/*z* 616) or (b) Fe(III)–heme⁺(His) (*m*/*z* 771) [31]. Fragmentation spectra acquired at ELISA immediately after photoexcitation with 532-nm light of (c) Fe(III)–heme⁺ or (d) Fe(III)–heme⁺(His), and after storage of the photoexcited ions for one revolution (e) Fe(III)–heme⁺ (100 μs) or (f) Fe(III)–heme⁺(His) (112 μs) [31]. As the spectra taken at ELISA have low resolution, the MIKE spectra were used to identify fragments

absorption of a single photon in agreement with the low energy needed for dissociation. The width in the internal energy distribution of the ions was, however, insufficient to account for the decay, and instead it was suggested that the necessity of two exponential functions to describe the data meant that there are two pathways

Fig. 7.15 Photodissociation mass spectrum of Fe (III)–heme⁺(NO) after 560-nm irradiation. The dominant fragment is heme⁺ formed by the loss of NO. There was no discernible signal from NO⁺ (*m*/*z* 30)

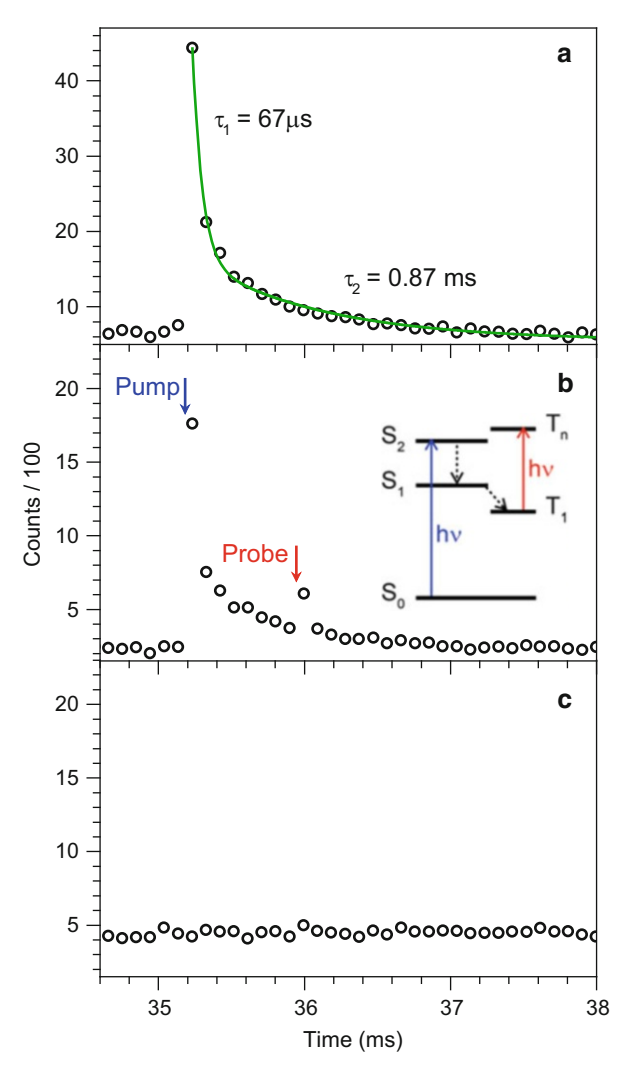


after photon absorption. One is internal conversion to the electronic ground state producing vibrationally excited ions that dissociate on the shorter time scale. The other is intersystem crossing to a long-lived triplet state that acts as a bottleneck for the dissociation process. The probability of the latter pathway is about 60 % based on the areas under the decay spectrum associated with each decay (Fig. 7.17).

It is well-known from solution-phase experiments that porphyrins have high triplet quantum yields [46]. Indeed, photodynamic therapy for cancer treatment exploits this fact in order to generate highly reactive singlet-oxygen ($^{1}O_{2}$) in reactions between triplet-state porphyrins and molecular oxygen ($^{3}O_{2}$) [47–51]. Triplet quantum yields are often more than 50 % and triplet-state lifetimes are hundreds of microseconds, dependent on the solvent [46]. That the gas-phase experiment provided similar numbers supports the above discussed interpretation for the two time constants.

In order to further support the idea that the ions decaying on the longer timescale had crossed into a triplet state, Støchkel et al. [45] carried out pump-probe experiments on the PP anions in the ELISA ring using two pulsed ns-laser systems (Figs. 7.16b, c and 7.18). The first laser pulse (430 nm light) excited the ions, and after 0.67 ms corresponding to seven revolutions in the ring, the ions were irradiated with the second laser pulse (684 nm). Most of the ions belonging to the short time component had dissociated at this time. Neutral fragments were measured on the other side of the ring to the laser interaction region. An increased yield of photofragments due to the absorption of 684-nm light was clearly seen (Fig. 7.16b). Importantly, the red light did not produce photofragments if the 430-nm pump laser beam was switched off (Fig. 7.16c). Absorption of red light is expected for triplet-state PP ions; for comparison triplet-state excited protoporphyrins in solution have been reported to absorb above 550 nm, and in benzene solution the triplet state of PP dimethyl ether has a very small band centred around 700 nm [52].

Fig. 7.16 (a) Time spectrum of PP anions that were photoexcited after 35.19 ms by 430-nm light (pump) [45]. (b) Same as (a) but a probe laser pulse (684 nm) was fired 0.67 ms after the pump laser pulse [45]. A simplified Jablonski diagram is shown to illustrate the photophysical processes: After excitation to the S₂ state, internal conversion to S₁ occurs followed by intersystem crossing to the T_1 triplet state. Ions in this state absorb red light. (c) Time spectrum of PP anions that were photoexcited by the probe laser (684 nm) at 35.86 ms [45]. No prior pump pulse was used and, consequently, no absorption was seen after firing the probe laser. The revolution time of the ions in the ring is $95.2 \mu s$ (the separation between the points)



In other experiments, 535-nm light was used as the pump, and the probe laser wavelength was scanned. Furthermore, results for two different time delays between the laser pulses were obtained (Fig. 7.19). Action spectra were then compiled by analysing the increased yield of photofragments induced by the second laser pulse. From both thus obtained spectra, it is evident that absorption is strong at 650 nm, and that it decreases as the wavelength increases, with little or no absorption seen above 800 nm. Moreover, the band appears sharper after the longer time delay (0.57 ms) than after the shorter one (0.19 ms), which may be due to a colder population at longer delay times. Experiments at lower probe wavelengths were complicated by ground-state absorption (see Fig. 7.19a), which means that it is difficult to exclude that there is some contribution from the Q_0 band, estimated to be maximal at 630 nm, to the pump-probe absorption spectrum at the lowest wavelengths.

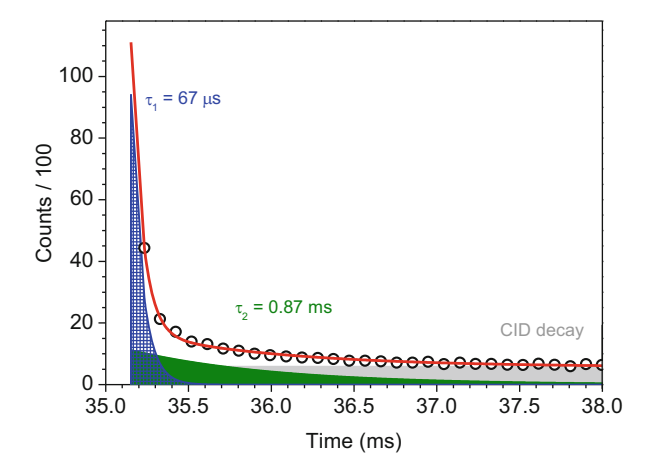


Fig. 7.17 From the areas under the decay spectrum associated with each decay (indicated by *blue* and *green*), the branching ratios of photoexcited PP anions can be found. Values of 40% and 60% were found for the fast and slow decays, respectively

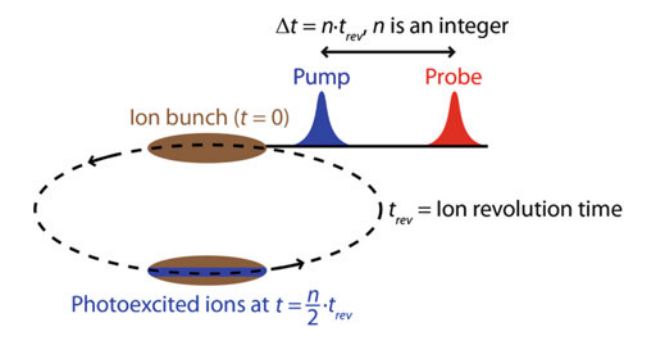


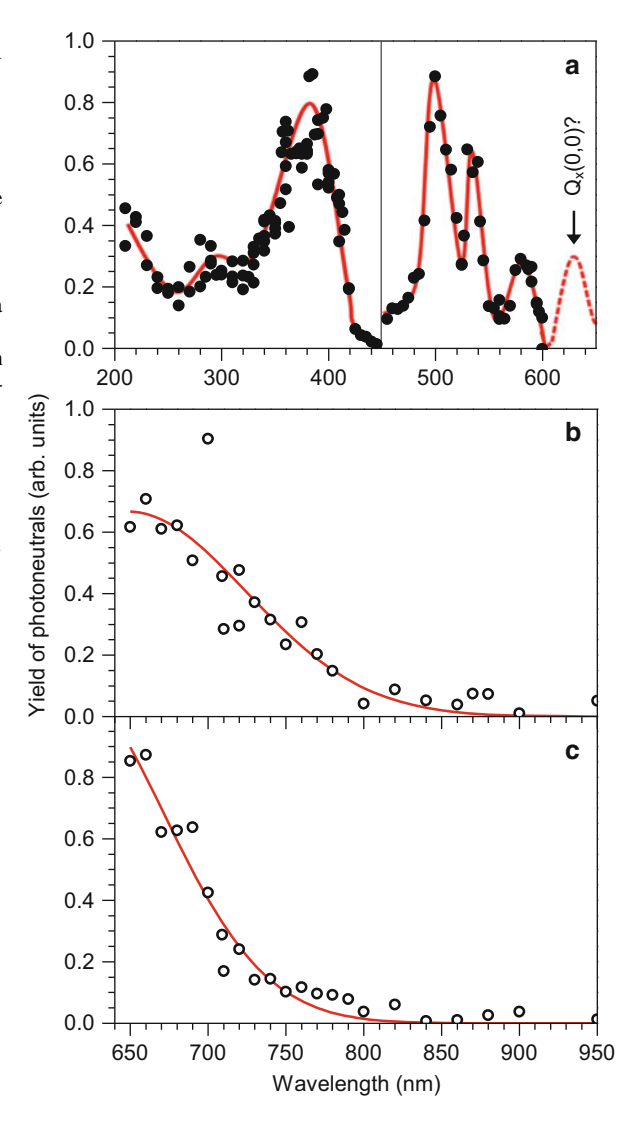
Fig. 7.18 Schematic illustration of pump-probe experiments at the ELISA storage ring. Ions are photoexcited with one laser pulse, and then after a certain number of revolutions in the ring, they are photoexcited once more by another laser pulse. The time delay between the two laser pulses corresponds to one or more revolutions in the ring

Conclusions and Outlook

Gas-phase action spectroscopy of porphyrin and heme ions has given a wealth of data that shed light on the intrinsic electronic properties of these highly important biomolecules. With these data at hand, it is possible to better understand how a microenvironment such as amino acids or single water molecules perturbs the electronic structure of a heme buried inside a hydrophobic pocket. Moreover, the data provide a natural testing ground for future benchmarking of advanced theoretical calculations on these ions.

There are still many more relevant questions to address. All the data until now have concentrated on ferric heme, but it would be worthwhile to do similar

Fig. 7.19 (a) Action spectrum of ground-state PPions in vacuo [44]. In the Qband region the bands are split due to the asymmetry in the ring. Low statistics prevented measurement of the fourth O band, but it was estimated to be at ~630 nm based on a vibronic splitting of 1.350 cm⁻¹. Band maxima were observed at 291 nm. 375-386 nm, 499 nm, 535 nm and 581 nm. (b) and (c) Twolaser experiment: Action spectra of photoexcited PP anions obtained from the vield of photoneutrals due to the probe laser pulse as a function of probe wavelength [45]. The pump laser was set to produce light at 535 nm. Time delays between the pump and probe were (a) 0.19 ms and (b) 0.57 ms



experiments for ferrous heme (Fig. 7.20). Ferrous heme can bind CO and O_2 in addition to NO, and a comparison between ferric heme–NO and ferrous heme–CO would be particularly interesting as they are isoelectronic. However, to produce a charged species, which is needed for mass spectrometric investigations, one or both of the carboxylic acid groups of ferrous heme have to be deprotonated. This is of course not an obstacle since protoporphyrin IX anions were easily brought into gas phase and subjected to investigations. Gradually building up the microenvironment of both ferrous and ferric heme

Fig. 7.20 Schematic drawing of Fe(II)—heme anion with a deprotonated carboxylic acid group

complexes in a controlled way, mimicking the heme protein pocket, is still a dream but certainly worth pursuing.

How the absorption changes upon cooling is another interesting direction to take. Not only will such work provide better data for benchmarking theory, it may also directly shed light on excited state lifetimes, *i.e.*, information on the time-evolution of the electronically excited states.

Finally, gas-phase spectroscopy of whole protein anions allows one to test the much debated issue of whether or not the original protein structure is preserved when transferred from solution phase to gas phase. The constituent heme is an excellent reporter on protein unfolding as its absorption spectrum strongly depends on its microenvironment. In short, there are many unanswered questions relating to gas-phase spectroscopy of heme and we hope to give the answers to some of these.

References

- 1. Berg, J.M., Tymoczko, J.L., Stryer, L.: Biochemistry, 6th edn. W.H. Freeman, New York (2007)
- Makinen, M.W., Churg, A.K.: Structural and analytical aspects of the electronic spectra of heme proteins. In: Lever, A.B.P., Gray, H.B. (eds.) Iron Porphyrins, Part 1. Addison-Wesley, Reading, MA (1983)
- 3. Kalyanasundaram, K.: Photochemistry of polypyridine and porphyrin complexes. Academic Press, London (1997)
- Gouterman, M.: Optical spectra and electronic structure of porphyrins and related rings. In: Dolphin, D. (ed.) The Porphyrins. Physical Chemistry, Part A, vol. III. Academic Press, London (1978)
- Edwards, L., Dolphin, D.H., Gouterman, M., Adler, A.D.: Porphyrins. 17. Vapor absorption spectra and redox reactions - Tetraphenylporphins and porphin. J. Mol. Spectrosc. 38, 16–32 (1971)
- 6. McCleverty, J.A.: Chemistry of nitric oxide relevant to biology. Chem. Rev. **104**, 403–418 (2004)
- Murad, F.: Discovery of some of the biological effects of nitric oxide and its role in cell signaling (Nobel lecture). Angew. Chem. Int. Ed. 38, 1856–1868 (1999)
- 8. Richter-Addo, G.B., Legzdins, P., Burstyn, J.: Introduction: Nitric oxide chemistry. Chem. Rev. 102, 857–859 (2002)

- Goodrich, L.E., Paulat, F., Praneeth, V.K.K., Lehnert, N.: Electronic structure of hemenitrosyls and its significance for nitric oxide reactivity, sensing, transport, and toxicity in biological systems. Inorg. Chem. 49, 6293–6316 (2010)
- Shimizu, H., Obayashi, E., Gomi, Y., Arakawa, H., Park, S.Y., Nakamura, H., Adachi, S., Shoun, H., Shiro, Y.: Proton delivery in NO reduction by fungal nitric-oxide reductase – cryogenic crystallography, spectroscopy, and kinetics of ferric-NO complexes of wild-type and mutant enzymes. J. Biol. Chem. 275, 4816–4826 (2000)
- 11. Paulat, F., Lehnert, N.: Electronic structure of ferric heme nitrosyl complexes with thiolate coordination. Inorg. Chem. **46**, 1547–1549 (2007)
- Rich, A.M., Armstrong, R.S., Ellis, P.J., Lay, P.A.: Determination of the Fe-ligand bond lengths and Fe-N-O bond angles in horse heart ferric and ferrous nitrosylmyoglobin using multiple-scattering XAFS analyses, J. Am. Chem. Soc. 120, 10827–10836 (1998)
- Lanucara, F., Chiavarino, B., Crestoni, M.E., Scuderi, D., Sinha, R.K., Maitre, P., Fornarini, S.: Naked five-coordinate Fe-III(NO) porphyrin complexes: vibrational and reactivity features. Inorg. Chem. 50, 4445–4452 (2011)
- Wyer, J.A., Nielsen, S.B.: Absorption by isolated ferric heme nitrosyl cations in vacuo. Angew. Chem. Int. Ed. 51, 10256–10260 (2012)
- Soldatova, A.V., Ibrahim, M., Olson, J.S., Czernuszewicz, R.S., Spiro, T.G.: New light on NO bonding in Fe(III) heme proteins from resonance Raman spectroscopy and DFT modeling. J. Am. Chem. Soc. 132, 4614–4625 (2010)
- 16. Olson, J.S., Phillips, G.N.: Myoglobin discriminates between O₂, NO, and CO by electrostatic interactions with the bound ligand. J. Biol. Inorg. Chem. **2**, 544–552 (1997)
- 17. Spiro, T.G., Soldatova, A.V., Balakrishnan, G.: CO, NO and O₂ as vibrational probes of heme protein interactions. Coord. Chem. Rev. **257**, 511–527 (2013)
- Laverman, L.E., Wanat, A., Oszajca, J., Stochel, G., Ford, P.C., van Eldik, R.: Mechanistic studies on the reversible binding of nitric oxide to metmyoglobin. J. Am. Chem. Soc. 123, 285–293 (2001)
- Sage, J.T., Morikis, D., Champion, P.M.: Spectroscopic studies of myoglobin at low pH heme structure and ligation. Biochemistry 30, 1227–1237 (1991)
- Fang, M., Wilson, S.R., Suslick, K.S.: A four-coordinate Fe(III) porphyrin cation. J. Am. Chem. Soc. 130, 1134–1135 (2008)
- Wyer, J.A., Brøndsted Nielsen, S.: Absorption in the Q-band region by isolated ferric heme⁺ and heme⁺(histidine) in vacuo. J. Chem. Phys. 133, 084306 (2010)
- 22. Lykkegaard, M.K., Ehlerding, A., Hvelplund, P., Kadhane, U., Kirketerp, M.-B.S., Brøndsted Nielsen, S., Panja, S., Wyer, J.A., Zettergren, H.: A soret marker band for four-coordinate ferric heme proteins from absorption spectra of isolated Fe(III)-heme⁺ and Fe(III)-heme⁺(His) ions in vacuo. J. Am. Chem. Soc. 130, 11856–11857 (2008)
- 23. Nonose, S., Tanaka, H., Okai, N., Shibakusa, T., Fuke, K.: Photo-induced reactions of hemin⁺(DMSO)_n clusters (n=0-3) produced with electrospray ionization. Eur. Phys. J. D **20**, 619–626 (2002)
- Adar, F.: Electronic absorption spectra of hemes and hemoproteins. In: Dolphin, D. (ed.) The Porphyrins. Physical Chemistry, Part A, vol. III. Academic Press, London (1978)
- Filsinger, F., Ahn, D.S., Meijer, G., von Helden, G.: Photoexcitation of mass/charge selected hemin⁺, caught in helium nanodroplets. Phys. Chem. Chem. Phys. 14, 13370–13377 (2012)
- Brunet, C., Antoine, R., Lemoine, J., Dugourd, P.: Soret band of the gas-phase ferricytochrome c. J. Phys. Chem. Lett. 3, 698–702 (2012)
- Bogumil, R., Maurus, R., Hildebrand, D.P., Brayer, G.D., Mauk, A.G.: Origin of the pHdependent spectroscopic properties of pentacoordinate metmyoglobin variants. Biochemistry 34, 10483–10490 (1995)
- 28. Cao, W.X., Christian, J.F., Champion, P.M., Rosca, F., Sage, J.T.: Water penetration and binding to ferric myoglobin. Biochemistry **40**, 5728–5737 (2001)

- Boffi, A., Das, T.K., della Longa, S., Spagnuolo, C., Rousseau, D.L.: Pentacoordinate hemin derivatives in sodium dodecyl sulfate micelles: model systems for the assignment of the fifth ligand in ferric heme proteins. Biophys. J. 77, 1143–1149 (1999)
- 30. Eaton, W.A., Hochstrasser, R.M.: Single-crystal spectra of ferrimyoglobin complexes in polarized light. J. Chem. Phys. **49**, 985–995 (1968)
- 31. Lykkegaard, M.K., Zettergren, H., Kirketerp, M.-B.S., Ehlerding, A., Wyer, J.A., Kadhane, U., Brøndsted Nielsen, S.: Photodissociation of isolated ferric heme and heme-His cations in an electrostatic ion storage ring. J. Phys. Chem. A 113, 1440–1444 (2009)
- 32. Charkin, O.P., Klimenko, N.M., Nguyen, P.T., Charkin, D.O., Mebel, A.M., Lin, S.H., Wang, Y.S., Wei, S.C., Chang, H.C.: Fragmentation of heme and hemin⁺ with sequential loss of carboxymethyl groups: a DFT and mass-spectrometry study. Chem. Phys. Lett. 415, 362–369 (2005)
- Charkin, O.P., Klimenko, N.M., Charkin, D.O., Chang, H.C., Lin, S.H.: Theoretical DFT study of fragmentation and association of Heme and Hemin. J. Phys. Chem. A 111, 9207–9217 (2007)
- 34. Siu, C.K., Guo, Y.Z., Hopkinson, A.C., Siu, K.W.M.: How large is the [Fe-III(protoporphyrin IX)]⁺ ion (hemin⁺) in the gas phase? J. Phys. Chem. B **110**, 24207–24211 (2006)
- 35. Andersen, J.U., Hvelplund, P., Brøndsted Nielsen, S., Tomita, S., Wahlgreen, H., Møller, S.P., Pedersen, U.V., Forster, J.S., Jørgensen, T.J.D.: The combination of an electrospray ion source and an electrostatic storage ring for lifetime and spectroscopy experiments on biomolecules. Rev. Sci. Instrum. 73, 1284–1287 (2002)
- 36. Angelelli, F., Chiavarino, B., Crestoni, M.E., Fornarini, S.: Binding of gaseous Fe(III)-heme cation to model biological molecules: direct association and ligand transfer reactions. J. Am. Soc. Mass Spectrom. 16, 589–598 (2005)
- Jee, J.E., van Eldik, R.: Mechanistic studies on the nitrite-catalyzed reductive nitrosylation of highly charged anionic and cationic Fe-III porphyrin complexes. Inorg. Chem. 45, 6523–6534 (2006)
- 38. Ellison, M.K., Scheidt, W.R.: Synthesis, molecular structures, and properties of six-coordinate [Fe(OEP)(L)(NO)] plus derivatives: elusive nitrosyl ferric porphyrins. J. Am. Chem. Soc. **121**, 5210–5219 (1999)
- 39. Chiavarino, B., Crestoni, M.E., Fornarini, S., Lanucara, F., Lemaire, J., Maitre, P., Scuderi, D.: Direct probe of NO vibration in the naked ferric heme nitrosyl complex. Chem. Phys. Chem. 9, 826–828 (2008)
- 40. Negrerie, M., Cianetti, S., Vos, M.H., Martin, J.L., Kruglik, S.G.: Ultrafast heme dynamics in ferrous versus ferric cytochrome c studied by time-resolved resonance Raman and transient absorption spectroscopy. J. Phys. Chem. B 110, 12766–12781 (2006)
- 41. Praneeth, V.K.K., Paulat, F., Berto, T.C., George, S.D., Nather, C., Sulok, C.D., Lehnert, N.: Electronic structure of six-coordinate iron(III)-porphyrin NO adducts: the elusive iron(III)-NO (radical) state and its influence on the properties of these complexes. J. Am. Chem. Soc. 130, 15288–15303 (2008)
- 42. Park, J., Lee, T., Park, J., Lim, M.: Photoexcitation dynamics of NO bound ferric myoglobin investigated by femtosecond vibrational spectroscopy. J. Phys. Chem. B (2013). doi:10.1021/jp400055d
- 43. Petrich, J.W., Lambry, J.C., Kuczera, K., Karplus, M., Poyart, C., Martin, J.L.: Ligand-binding and protein relaxation in heme-proteins a room-temperature analysis of NO geminate recombination. Biochemistry **30**, 3975–3987 (1991)
- 44. Wyer, J.A., Jensen, C.S., Brøndsted Nielsen, S.: Gas-phase action spectroscopy of protoporphyrin IX (PP) and zinc-PP anions from 210 nm to 720 nm. Int. J. Mass Spectrom. 308, 126–132 (2011)
- Støchkel, K., Wyer, J.A., Kirketerp, M.B.S., Brøndsted Nielsen, S.: Laser pump-probe experiments on microsecond to millisecond timescales at an electrostatic ion storage ring: Triplet-triplet absorption by protoporphyrin-IX anions. J. Am. Soc. Mass Spectrom. 21, 1884–1888 (2010)

- 46. Sinclair, R.S., Tait, D., Truscott, T.G.: Triplet-states of protoporphyrin-IX and protoporphyrin-IX dimethyl ester. J. Chem. Soc. Faraday Trans. I 76, 417–425 (1980)
- 47. Dougherty, T.J., Gomer, C.J., Henderson, B.W., Jori, G., Kessel, D., Korbelik, M., Moan, J., Peng, Q.: Photodynamic therapy. J. Natl. Cancer Inst. 90, 889–905 (1998)
- 48. Cox, G.S., Krieg, M., Whitten, D.G.: Photochemical reactivity in organized assemblies. 30. Self-sensitized photo-oxidation of protoporphyrin-IX derivatives in aqueous surfactant solutions product and mechanistic studies. J. Am. Chem. Soc. **104**, 6930–6937 (1982)
- 49. Brown, J.E., Brown, S.B., Vernon, D.I.: Photodynamic therapy new light on cancer treatment. J. Soc. Dye. Colour **115**, 249–253 (1999)
- 50. Sharman, W.M., Allen, C.M., van Lier, J.E.: Photodynamic therapeutics: basic principles and clinical applications. Drug Discov. Today **4**, 507–517 (1999)
- Fuchs, J., Thiele, J.: The role of oxygen in cutaneous photodynamic therapy. Free Radic. Biol. Med. 24, 835–847 (1998)
- Chantrell, S.J., McAuliffe, C.A., Munn, R.W., Pratt, A.C., Land, E.J.: Excited-states of protoporphyrin-IX dimethyl ester - reaction of triplet with carotenoids. J. Chem. Soc. Faraday Trans. I 73, 858–865 (1977)

UV-Visible Absorption Spectroscopy of Protein Ions

Rodolphe Antoine and Philippe Dugourd

Abstract

Optical spectroscopy has contributed enormously to our knowledge of the structure and dynamics of atoms and molecules and is now emerging as a cornerstone of the gas-phase methods available for investigating biomolecular ions. This chapter focuses on the UV and visible spectroscopy of peptide and protein ions stored in ion traps. First, we discuss experimental set-ups, deexcitation mechanisms following photo-excitation in electronically excited states and principles of action spectroscopy. Then, we report action spectra for different classes of gas-phase peptides and proteins. The optical activity of proteins in the near UV is directly related to the electronic structure and optical absorption of aromatic amino acids (Trp, Phe and Tyr). Some proteins also show absorption in the visible range due to the presence of a prosthetic group. Influence of protein charge state, formation of radical aromatic amino acids and solvation on proteins' visible and UV spectra is discussed.

8.1 Introduction

UV-Vis excitation entails the electronic excitation of a molecular species. The resulting spectra reflect the density of vibronic states and, depending on the type of excitation, UV-Vis excitation can probe, for example, charge-transfer mechanisms, the excitation of delocalised electrons and even ionisation processes. The first UV spectrum of a gas-phase amino acid was reported in 1985 by Levy and co-workers [1], using a cold molecular beam, and was rapidly followed by spectra for small neutral peptides [2]. Peptides display strong absorption bands in the vacuum ultraviolet (VUV) associated in particular with backbone peptide bond excitation.

R. Antoine (⋈) • P. Dugourd

Institut Lumière Matière, UMR5306 Université Lyon 1-CNRS Université de Lyon, 69622

Villeurbanne Cedex, France

e-mail: rodolphe.antoine@univ-lyon1.fr; philippe.dugourd@univ-lyon1.fr

For peptides, absorption above 220 nm occurs through specific chromophores provided by the side chains of aromatic amino acids. In nature, only three amino acids (tryptophan, tyrosine and phenylalanine) have an aromatic ring system and are thus accessible to near-UV excitation [3]. Spectroscopy of peptides and proteins has mainly focused on sequences containing one of these three amino acids using different laser schemes (UV, IR–UV, UV–UV and even IR–IR–UV multiple-resonance methods. For a review see [4]). In addition to the absorption by aromatic amino acids, different classes of proteins are coloured due to the presence of prosthetic groups containing visible chromophores. The groups of S. Brøndsted Nielsen and L.H. Andersen have pioneered the spectroscopy and photophysics of isolated natural biochromophores [5, 6]. While the absorbance of coloured proteins is highly sensitive to the prosthetic environment and absorption spectroscopy is an essential tool to monitor the conformational changes and the associated dynamics of proteins in solution, spectra of chromophores embedded in gas-phase proteins have only been reported recently [7].

This chapter focuses on UV spectroscopy of peptide and protein ions. After a short discussion of experimental setups and mechanisms, it explores the influence of biomolecule conformation, chromophore environment, chromophore electronic structure, and solvation on optical spectra.

8.2 Implementation of UV-Vis Action Spectroscopy

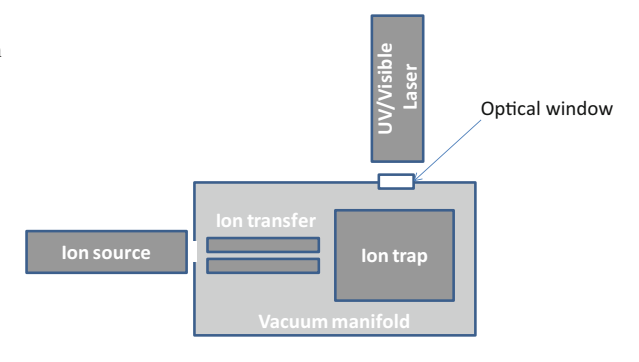
Ion-trap mass spectrometers, in which ions are stored in a specific place for a period of time, are particularly well-suited for action-spectroscopy experiments. Trapped ions are irradiated by a laser beam introduced to the instrument through a window or access holes (see Fig. 8.1).

Results shown in this chapter were obtained using nanosecond-pulsed tuneable optical parametric oscillators, with frequency doubling provided by barium borate (BBO) crystals which allows us to scan the photon wavelength from 215 nm to 2 μm .

In order to record action spectra, mass spectra were recorded as a function of laser wavelength. The yield of fragmentation at each laser wavelength is given by ln $((parent + \sum frag)/parent)/\phi$, where ϕ is the laser fluence, parent is the intensity of the parent peak and $\sum frag$ represents the total intensity of the photofragment peaks.

Quadrupole ion traps allow the use of hybrid activation that combines photoexcitation, possibly with different laser beams, and collisional excitation. Different schemes can be designed that combine the different excitations in the same or different mass spectrometry stages. In addition to the instruments developed in our laboratory [8, 9], different light sources can be used, including dye lasers and synchrotron radiation [10]. Different ion-storage devices were also used for action spectroscopy. Early experiments were performed with an FT-ICR instrument [11] and an electrostatic storage ring [5]. A direction being taken at present is the implementation of multipole ion traps for spectroscopy of cooled ions [4, 12].

Fig. 8.1 Generic instrument diagram for photodissociation experiments in ion traps



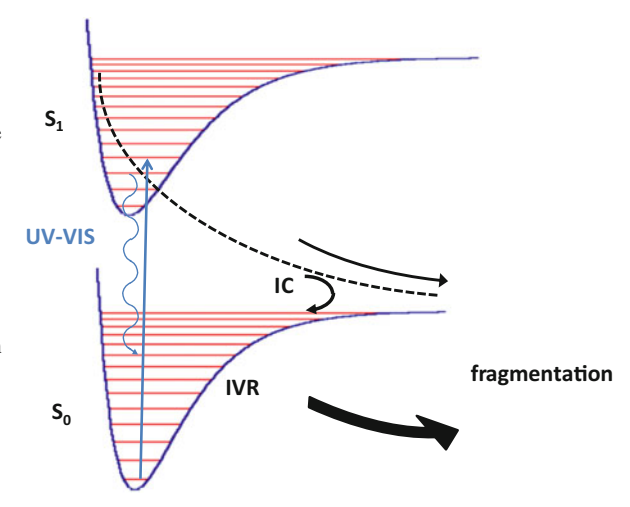
8.3 Photofragmentation and Optical Spectroscopy of Trapped Polypeptide and Protein Ions

Due to very low ion concentrations, absorption [13] and fluorescence [14] spectroscopies of trapped ions have been reduced to a few examples, and gasphase spectroscopy most often relies on action spectra [11]. The principle is to use the dissociation that follows photon absorption to monitor the optical properties of the selected ion. A common assumption is that the photodissociation yield is proportional to the absorption cross section.

The quest to perform spectroscopy on large systems in the gas phase, required to ensure the biological relevance of gas-phase studies, was slowed down by the bottleneck of action spectroscopy. As the size of the system and then the number of degrees of freedom increases, the redistribution of vibrational energy that follows internal conversion leads to a very small increase in temperature without fragmentation in the time window of the experiment. The possibility of fragmentation from electronic excited states prior to internal vibrational energy redistribution (IVR) [15] (see Fig. 8.2) may lead to the measurement of optical spectra for large systems. A possible drawback of this method may be the strong dependence of the fragmentation rate on the structure of the ions and/or on the initial electronic excited states, leading to a poor match between fragmentation yields and absorption cross sections.

An alternative which was developed in Lyon is to work with polyanions. The mass spectrum obtained after UV-laser irradiation at 260 nm of the doubly deprotonated $[M-2H]^{2-}$ gramicidin anion is shown in Fig. 8.3a. The main daughter ion corresponds to the oxidised $[M-2H]^{-\bullet}$ ion generated by electron detachment from the $[M-2H]^{2-}$ precursor ion. This electron loss is a typical de-excitation pathway for polyanions [16, 17]. Figure 8.3b presents the electron photodetachment efficiency as a function of wavelength for the gramicidin peptide dianions. The detachment can be seen below 300 nm where the absorption occurs in solution (inset in Fig. 8.3b) due to $\pi\pi^*$ excitations of aromatic residues. Thus, the first step in this electron loss was a resonant electronic excitation of the precursor ion. Absorption of a 260-nm photon by the peptide corresponds to an increase in energy

Fig. 8.2 Simplified diagram of photoexcitation and deexcitation pathways. The absorption of a UV/VIS photon (solid line) leads to the promotion of electrons to an excited electronic state. Possible relaxation pathways include: photon emission (wavy line), internal conversion (IC), or coupling to a dissociative state (dotted line). Statistical redistribution after internal conversion can be followed by unimolecular dissociation in the ground electronic state



of 4.77 eV. This energy is above the lowest electron-binding energy in the gramicidin dianion. Crossing from the electronic excited state to an auto-ionising state leads to electron detachment (see Scheme 8.1) [16].

We observed that the electron detachment yield is linear as a function of both laser power and irradiation time, showing that the electron loss results from the absorption of a single photon. The electron detachment yield can be used to record linear action spectra and monitor the excited electronic spectrum of the trapped ions.

8.4 UV Spectroscopy of Protein Anions

We present the electronic spectra of gas-phase deprotonated proteins with different charge states [18]. First results are reported for insulin [19]. Insulin is a small protein which consists of 51 amino acids distributed in two chains (chain A with 21 amino acids and B with 30 amino acids) linked by two disulfide bonds with an extra disulfide bond in chain A. Insulin contains four acidic [Glu] residues and four tyrosines. As a comparison, the gas-phase spectrum for [Tyr+H]⁺ is shown in Fig. 8.4a and is dominated by one band at 275 nm. This band is due to the excitation of π electrons within the phenol group. Action spectra for the $[M-4H]^{4-}$ and [M-6H]⁶⁻ insulin ions are compared in Fig. 8.4 and display similarities with the tyrosine spectrum. The two curves are, however, spectrally shifted. This is due to a change in the ionisation state of the chromophores [19]. This bathochromism represents a signature of the ionisation state of tyrosine in a protein and was also observed in solution for tyrosine-containing proteins. The red-shift reflects the destabilisation of the molecular orbitals due to the negative charge on the phenolate oxygen, leading to a smaller HOMO-LUMO gap in phenolate in comparison to phenol.

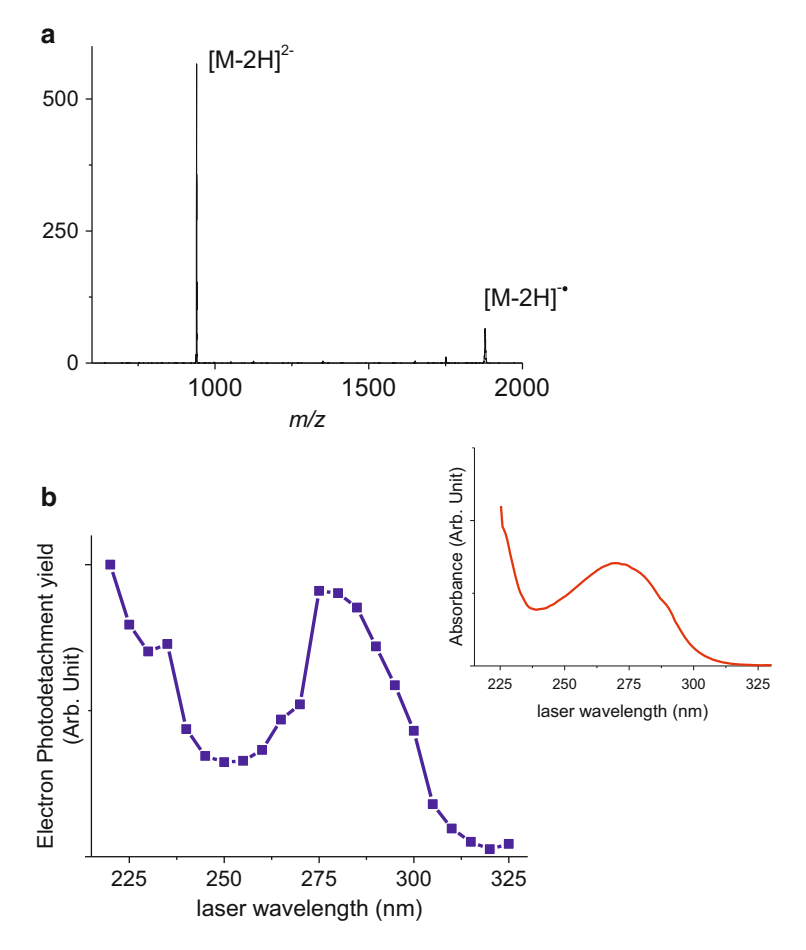
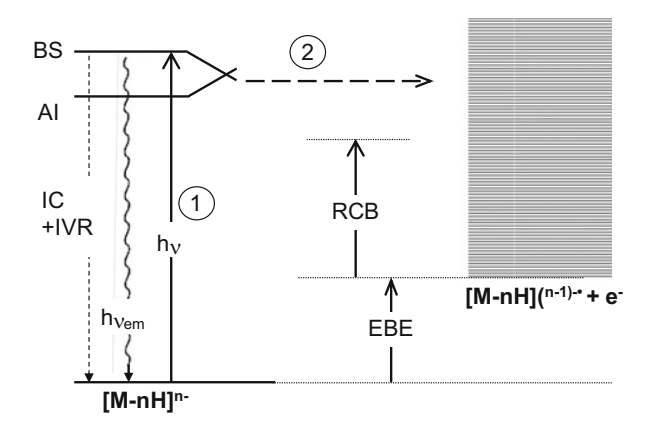


Fig. 8.3 (a) UV-photoinduced dissociation (UV-PID) spectrum (at 260 nm) obtained for doubly deprotonated $[M-2H]^{2-}$ gramicidin A peptide (sequence: formyl-L-Val-Gly-L-Ala-D-Leu-L-Ala-D-Val-L-Val-D-Val-L-Trp-D-Leu-L-Trp-D-Leu-L-Trp-D-Leu-L-Trp-ethanolamine). The main ion product results from electron detachment. (b) Electron photodetachment efficiency as a function of wavelength for the gramicidin A peptide dianion. *Inset*: Normalised absorption spectrum of gramicidin A in solution [100 μM of peptides in H_2O/CH_3CN (50/50, volume/volume)]

The question that comes to mind is that of the sensitivity of these action spectra to the intrinsic properties of the protein ions and to environmental factors. In order to address the question of the influence of the 3D organisation of the protein on its UV spectrum, the photodetachment yield spectra of myoglobin proteins electrosprayed from different solution conditions were recorded. Figure 8.5 presents the UV photodetachment yield of myoglobin in its native form (charge state 7—) and in its denatured form (charge state 11—). In its native form, the protein has a heme group at the centre around which the remaining apoprotein folds. In its denatured form, the apoprotein (*i.e.*, without the heme group) is observed.



Scheme 8.1 Proposed mechanisms for electron detachment through a two-step process: Resonant electronic excitation of the precursor ion (1). Crossing from the electronic excited state (BS) to an auto-ionising state (AI) leads to electron detachment (2). *RCB* repulsive Coulomb barrier, *EBE* electron binding energy. Other relaxation pathways include internal conversion followed by IVR and photon emission

The $\pi\pi^*$ band observed for the denatured myoglobin is red-shifted by 10 nm in comparison to the corresponding native form. Charge states are different, and the red-shift observed may be explained in part by the increase in negative charges in the denatured form. Note that in this case, contrary to our insulin example, no deprotonation of chromophores was expected due to the change in the charge states (there are 21 acidic residues in myoglobin). Note also that gas-phase spectra are blue-shifted in comparison to the solution spectrum of myoglobin under native conditions. The prediction of the shifts due to the solvent results from a subtle balance between different mechanisms resulting in opposite effects. The theoretical efforts that are necessary to predict the optical properties of entire proteins with influence of conformation and solvation are still out of reach.

8.5 Visible Spectroscopy of Protein Anions

Heme proteins, like myoglobin and cytochrome proteins, are metalloproteins containing a heme prosthetic group, either covalently or noncovalently bound to the protein. Heme molecules absorb in the visible range. The absorption of heme-containing moieties in the blue is commonly labelled as the "Soret band". Protein chromophores have been extensively studied both in solution and in the gas phase at the electrostatic heavy-ion storage ring, ELISA, in Aarhus and is discussed in this volume in Chap. 5 by Andersen and Bochenkova and Chap. 7 by Wyer and Brøndsted Nielsen [5, 6, 20]. There was evidence that in terms of absorption there are almost vacuum-like conditions in the hydrophobic interior of certain proteins like the green fluorescent protein (GFP), as there were no shifts between the gas-phase spectrum of the bare chromophore and the protein absorption

Fig. 8.4 Photofragmentation yield of protonated tyrosine [Tyr+H]⁺ as a function of laser wavelength (a). Photodetachment yield as a function of wavelength for the gas-phase [M-4H]⁴⁻ (b) and [M-6H]⁶⁻ (c) insulin ions. Schematic structures of tyrosine and insulin are given in *insets*

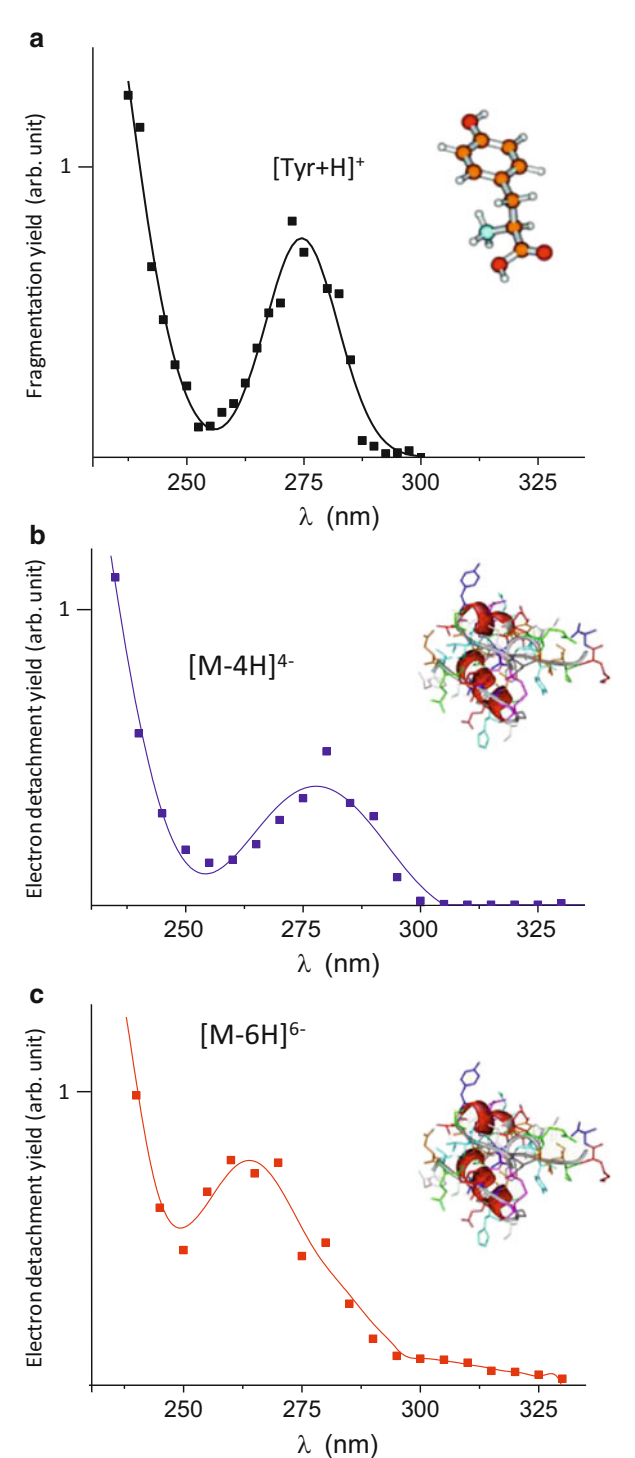


Fig. 8.5 (Top) Absorption spectrum for the myoglobin protein in native solution (10 uM, 50/50 MeOH/H₂O). (Bottom) Electron photodetachment yield measured as a function of the laser wavelength for holomyoglobin (charge state 7–) and apo-myoglobin (charge state 11-) (holo-myoglobin: with the heme group; apomyoglobin: without the heme group). The electron photodetachment yield for holo-myoglobin was recorded using the native solution $(10 \mu M, 50/50 \text{ MeOH/H}_2\text{O}),$ while that for apo-myoglobin was recorded using a denaturated solution (10 µM, 80/20 MeOH/H₂O)

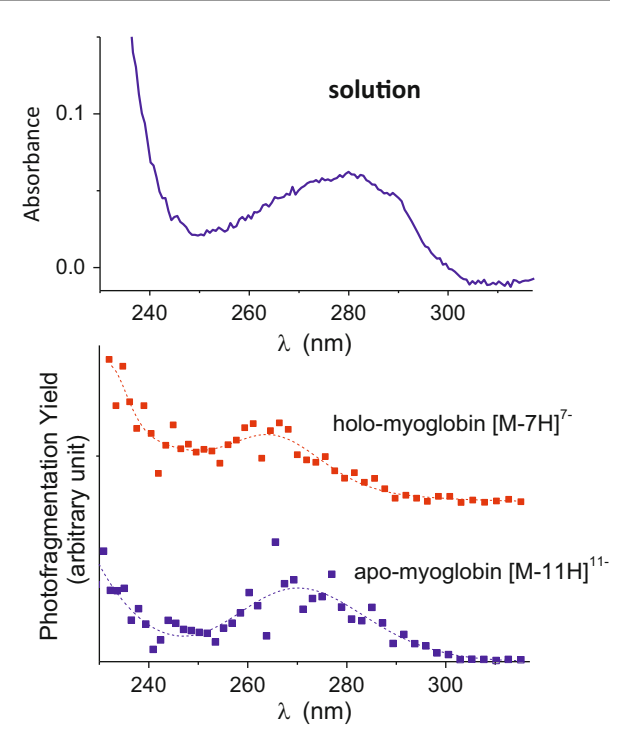
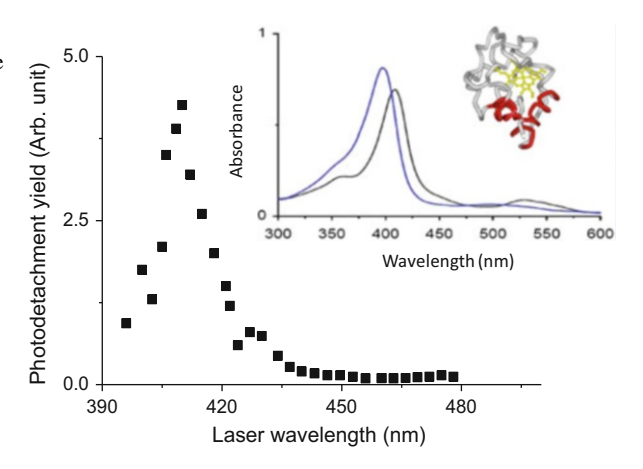


Fig. 8.6 Photodetachment yield of cytochrome c (charge state 6—) recorded as a function of the laser wavelength in the visible range. *Inset*: Visible part of the absorption spectrum for native (*black*) and unfolded (*blue*) cytochrome c in solution at pH 5. The X-ray structure of cytochrome c is shown with the heme group highlighted in *yellow*



spectrum in solution. Colour tuning was observed for other examples, such as visual opsins. In this section, we discuss spectra of chromophores within their protein hosts. We directly address the effect of the protein environment on the optical properties of the heme group without any external factors. The photodetachment yield of cytochrome c (charge state 6-) was recorded as a function of the wavelength in the visible range, from 400 nm to 550 nm and is shown in Fig. 8.6 [7]. A broad band centred at 410 nm was observed and attributed to the Soret band of the

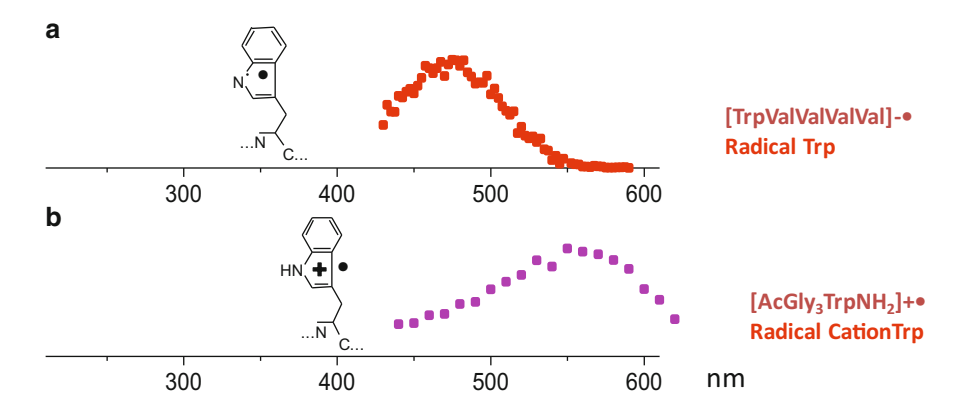


Fig. 8.7 Photofragmentation yield as a function of the laser wavelength for the gas phase (a) TrpValValVal oxidised anions $[M-2H]^{-\bullet}$ and (b) $[AcGly_3TrpNH_2]^{+\bullet}$ radical cations. The indole residue is in a neutral radical form in (a) and in a radical cation form in (b)

heme group covalently attached to the cytochrome c protein. The maximum of the band for the native structure in solution is very close to the value reported for the gas-phase protein (see inset in Fig. 8.6). However, when the protein is denatured in solution, the Soret band redshifts (see inset in Fig. 8.6), which demonstrates how sensitive the Soret band is to the local environment. The present result constitutes a benchmark for simulating the absorption of prosthetic chromophores within a protein environment without having to take into account solvent molecules.

8.6 Spectroscopy of Peptide Radical Ions

Radical centres present in peptides and proteins draw considerable interest for two major reasons: they play critical roles as intermediates in a variety of biological electron-transfer processes, and they provide a wealth of fragmentation pathways that are relevant to protein sequencing. Whereas the optical properties of closed-shell tryptophan in the environment of a protein is well documented, direct observations of radicals—and particularly radical cations—have been ailed by their high, environment-modulating reactivity.

Electron detachment from the doubly deprotonated TrpValValValVal peptide ([M-2H]²⁻) leads to the formation of an indolyl radical (see inset in Fig. 8.7a). The photogenerated radical was stable and could be isolated for several tens of milliseconds. In a two-colour experiment (see Scheme 8.2), the long-lived radical ions were isolated and, after isolation, irradiated with a second tuneable visible laser pulse (MS³ experiments) [21].

The fragmentation spectrum of the radical was systematically recorded as a function of the wavelength of the second laser in the 430–590 nm range. The resulting experimental photofragmentation spectrum is shown in Fig. 8.7a. It displays a single absorption band centred at 473 nm. This band is in the visible

$$[M-2H]^{2-} + hv_1 \xrightarrow{266 \text{ nm UV light}} [M-2H]^{-\bullet} + e^{-}$$

$$[M-2H]^{-\bullet} + hv_2 \xrightarrow{\text{tunable light visible}} \text{fragment ions}$$

Scheme 8.2 Spectroscopy of radical peptides. The first photon $(h\nu_I)$ is used to produce the radical. Optical properties of this radical are probed by using a tuneable visible laser $(h\nu_2 photon)$

part of the spectrum, which corresponds to a ~200 nm red-shift in comparison to the first transition observed for neutral or deprotonated tryptophan-containing peptides [1, 22]. This is due to a transition from an inner π orbital to the singly occupied π HOMO [23].

Radical cations are conveniently formed *in vacuo* by electron transfer occurring during collision-induced dissociation of ternary complexes composed of copper(II) [24], a ligand and the peptide of interest. Capped AcGly₃TrpNH₂ was used as a model for small tryptophan-containing peptides. The optical spectrum of the radical ion presented in Fig. 8.7b displays a broad absorption with maximum at 560 nm [25]. This constitutes a redshift of about 300 nm as compared to molecular tryptophan, and a redshift of about 100 nm as compared to the neutral tryptophan radical (Fig. 8.7a). The band is due to a leading electronic transition of type $\pi_{-2}\pi_0$.

Conclusion and Perspectives

One of the central results reported in this chapter is that among the multiple possible de-excitation pathways after photoexcitation to electronic excited states, relaxation of biomolecular polyanions is mainly achieved by electron emission. Electron photodetachment is a fast process that occurs prior to relaxation into vibrational degrees of freedom. The electron photodetachment yield can then be used to record gas-phase action spectra for systems as large as entire proteins, without limitation of size due to energy redistribution into a large number of modes.

Absorption spectra of peptides and proteins are sensitive to the electronic configuration of the chromophores and to their environment. While UV–Vis optical spectra directly depend on the electronic structure of chromophores, the sensitivity of these spectra to protein conformation is more delicate to assess. The results obtained on holo- and apo-myoglobin proteins are not conclusive. A full interpretation of these spectra would require extensive theoretical efforts that are beyond the scope of this chapter. A global strategy for the structural characterisation of proteins and their complexes should involve different experimental approaches as well as theory. The action spectroscopy described here could be complemented by ion mobility spectrometry (IMS) [26, 27], an approach that we are now developing.

Another important aspect is the relationship between the dynamics of relaxation of the chromophore and its peptide or protein environment [28]. While electron loss is the dominant process observed for polyanions, different relaxation channels were observed for cations [28, 29]. After photoexcitation, direct dissociation in the excited state competes with internal conversion to the electronic ground state and with radiative de-excitation. Control of the fragmentation pathways by photon activation would open new perspectives from the fundamental as well as analytical viewpoint. This could possibly be achieved through wavelength tuning [30]. A more general control of the dynamics will certainly involve optimal control, using shaped femtoseconds laser pulses [31] to drive the chosen process.

All the results discussed in this chapter rely on the electronic excitation of natural protein chromophores to the first excited states ($\pi\pi^*$ or charge-transfer type of excitations). Other electronic excitations can be explored by increasing the energy of the photons. In the vacuum ultra-violet range, excitation of peptides and proteins arises from $\pi\pi^*$, $n\pi$, ... excitations of different functional groups as well as photoionisation processes (see Chap. 11 by Schlathölter and Hoekstra) [10, 32, 33]. Another approach for exploring different types of excitations is to modify the optical properties of proteins. Proteins can be tagged with covalently or non-covalently bound chromophores, in particular to allow excitations in the near-UV or visible range. We have shown one example for cytochrome c with visible excitation of the prosthetic heme group. Tagging specific amino acids with dyes has also been used in the literature [34–36].

In parallel to these spectroscopic investigations, UV and visible lasers can be used to create new reactive intermediates that can be stored and manipulated in ion traps [37]. Electron photodetachment, which was the main focus of this chapter, leads to the formation of radical anions [38, 39]. The isolation of the oxidised radical anions and subsequent fragmentation initiated by collision-induced dissociation (Activated-EPD) [9] leads to high sequence coverages. This new technique is complementary to electron detachment dissociation (EDD) and reverse-electron transfer dissociation (ETD) for peptide and protein polyanions [40, 41].

References

- 1. Rizzo, T.R., Park, Y.D., Peteanu, L., Levy, D.H.: Electronic spectrum of the amino acid tryptophan cooled in a supersonic molecular beam. J. Chem. Phys. 83, 4819–4820 (1985)
- Cable, J.R., Tubergen, M.J., Levy, D.H.: Electronic spectroscopy of small tryptophan peptides in supersonic molecular beams. J. Am. Chem. Soc. 110, 7349–7355 (1988)
- Creighton, T.E.: Proteins: Structures and Molecular Properties, 2nd edn. W. H. Freeman, New York (1992)
- Rizzo, T.R., Stearns, J.A., Boyarkin, O.V.: Spectroscopic studies of cold, gas-phase biomolecular ions. Int. Rev. Phys. Chem. 28, 481–515 (2009)
- Nielsen, S.B., Lapierre, A., Andersen, J.U., Pedersen, U.V., Tomita, S., Andersen, L.H.: Absorption spectrum of the green fluorescent protein chromophore anion in vacuo. Phys. Rev. Lett. 87, 228102 (2001)
- Nielsen, I.B., Boye-Peronne, S., El Ghazaly, M.O.A., Kristensen, M.B., Nielsen, S.B., Andersen, L.H.: Absorption spectra of photoactive yellow protein chromophores in vacuum. Biophys. J. 89, 2597–2604 (2005)

- 7. Brunet, C., Antoine, R., Lemoine, J., Dugourd, P.: Soret band of the gas-phase ferricytochrome c. J. Phys. Chem. Lett. 3, 698–702 (2012)
- 8. Talbot, F.O., Tabarin, T., Antoine, R., Broyer, M., Dugourd, P.: Photo-dissociation spectroscopy of trapped protonated tryptophan. J. Chem. Phys. **122**, 074310 (2005)
- Larraillet, V., Antoine, R., Dugourd, P., Lemoine, J.: Activated-electron photodetachment dissociation for the structural characterization of protein polyanions. Anal. Chem. 81, 8410–8416 (2009)
- Brunet, C., Antoine, R., Allouche, A.R., Dugourd, P., Canon, F., Giuliani, A., Nahon, L.: Gas phase photo-formation and vacuum UV photofragmentation spectroscopy of tryptophan and tyrosine radical-containing peptides. J. Phys. Chem. A 115, 8933–8939 (2011)
- Dunbar, R.C.: Photodissociation of CH₃Cl⁺ and N₂O⁺ cations. J. Am. Chem. Soc. 93, 4354–4358 (1971)
- 12. Fujihara, A., Matsumoto, H., Shibata, Y., Ishikawa, H., Fuke, K.: Photodissociation and spectroscopic study of cold protonated dipeptides. J. Phys. Chem. A 112, 1457–1463 (2008)
- 13. Terasaki, A., Majima, T., Kondow, T.: Photon-trap spectroscopy of mass-selected ions in an ion trap: optical absorption and magneto-optical effects. J. Chem. Phys. 127, 231101 (2007)
- Iavarone, A.T., Duft, D., Parks, J.H.: Shedding light on biomolecule conformational dynamics using fluorescence measurements of trapped ions. J. Phys. Chem. A 110, 12714–12727 (2006)
- 15. Sobolewski, A.L., Domcke, W., Dedonder-Lardeux, C., Jouvet, C.: Excited-state hydrogen detachment and hydrogen transfer driven by repulsive (1)pi sigma* states: a new paradigm for nonradiative decay in aromatic biomolecules. Phys. Chem. Chem. Phys. 4, 1093–1100 (2002)
- Joly, L., Antoine, R., Broyer, M., Lemoine, J., Dugourd, P.: Electron photodetachment from gas phase peptide dianions. Relation with optical absorption properties. J. Phys. Chem. A 112, 898–903 (2008)
- 17. Wang, L.-S., Wang, X.-B.: Probing free multiply charged anions using photodetachment photoelectron spectroscopy. J. Phys. Chem. A **104**, 1978–1990 (2000)
- Bellina, B., Compagnon, I., Joly, L., Albrieux, F., Allouche, A.R., Bertorelle, F., Lemoine, J., Antoine, R., Dugourd, P.: UV spectroscopy of entire proteins in the gas phase. Int. J. Mass Spectrom. 297, 36–40 (2010)
- Joly, L., Antoine, R., Allouche, A.R., Broyer, M., Lemoine, J., Dugourd, P.: Ultraviolet spectroscopy of peptide and protein polyanions in vacuo: signature of the ionization state of tyrosine. J. Am. Chem. Soc. 129, 8428–8429 (2007)
- Andersen, L.H., Nielsen, I.B., Kristensen, M.B., El Ghazaly, M.O.A., Haacke, S., Nielsen, M. B., Petersen, M.A.: Absorption of schiff-base retinal chromophores in vacuo. J. Am. Chem. Soc. 127, 12347–12350 (2005)
- Joly, L., Antoine, R., Allouche, A.-R., Dugourd, P.: Formation and spectroscopy of a tryptophan radical containing peptide in the gas phase. J. Am. Chem. Soc. 130, 13832–13833 (2008)
- Compagnon, I., Allouche, A.-R., Bertorelle, F., Antoine, R., Dugourd, P.: Photodetachment of tryptophan anion: an optical probe of remote electron. Phys. Chem. Chem. Phys. 12, 3399–3403 (2010)
- Crespo, A., Turjanski, A.G., Estrin, D.A.: Electronic spectra of indolyl radicals: a timedependent DFT study. Chem. Phys. Lett. 365, 15–21 (2002)
- 24. Siu, C.-K., Ke, Y., Guo, Y., Hopkinson, A.C., Siu, K.W.M.: Dissociations of copper(II)-containing complexes of aromatic amino-acids: radical cations of tryptophan, tyrosine, and phenylalanine. Phys. Chem. Chem. Phys. 10, 5908–5918 (2008)
- Bellina, B., Compagnon, I., Houver, S., Maitre, P., Allouche, A.-R., Antoine, R., Dugourd, P.: Spectroscopic signatures of peptides containing tryptophan radical cations. Angew. Chem. Int. Ed. 50, 11430–11432 (2011)
- Bowers, M.T., Kemper, P.R., von Helden, G., van Koppen, P.A.M.: Gas-phase ion chromatography: transition metal state selection and carbon cluster formation. Science 260, 1446–1451 (1993)
- Clemmer, D.E., Jarrold, M.F.: Ion mobility measurements and their applications to clusters and biomolecules. J. Mass Spectrom. 32, 577–592 (1997)

- 28. Antoine, R., Broyer, M., Chamot-Rooke, J., Dedonder, C., Desfrançois, C., Dugourd, P., Grégoire, G., Jouvet, C., Onidas, D., Poulain, P., Tabarin, T., van der Rest, G.: Comparison of the fragmentation pattern induced by collisions, laser excitation and electron capture. Influence of the initial excitation. Rapid Commun. Mass Spectrom. 20, 1648–1652 (2006)
- Reilly, J.P.: Ultraviolet photofragmentation of biomolecular ions. Mass Spectrom. Rev. 28, 425–447 (2009)
- Kang, H., Dedonder-Lardeux, C., Jouvet, C., Martrenchard, S., Gregoire, G., Desfrancois, C., Schermann, J.P., Barat, M., Fayeton, J.A.: Photoinduced dissociation of protonated tryptophan TrpH+: a direct dissociation channel in the excited states controls the hydrogen atom loss. Phys. Chem. Chem. Phys. 6, 2628–2632 (2004)
- Lozovoy, V.V., Zhu, X., Gunaratne, T.C., Harris, D.A., Shane, J.C., Dantus, M.: Control of molecular fragmentation using shaped femtosecond pulses. J. Phys. Chem. A 112, 3789–3812 (2008)
- 32. Dodonova, N.Y.: Vacuum UV photophysics and photochemistry of biomolecules. J. Photochem. Photobiol. B Biol. 18, 111–121 (1993)
- Bari, S., Gonzalez-Magana, O., Reitsma, G., Werner, J., Schippers, S., Hoekstra, R., Schlatholter, T.: Photodissociation of protonated leucine-enkephalin in the VUV range of 8–40 ev. J. Chem. Phys. 134, 024314 (2011)
- 34. Gardner, M.W., Brodbelt, J.S.: Ultraviolet photodissociation mass spectrometry of bis-aryl hydrazone conjugated peptides. Anal. Chem. **81**, 4864–4872 (2009)
- 35. Tecklenburg Jr., R.E., Miller, M.N., Russell, D.H.: Laser ion beam photodissociation studies of model amino acids and peptides. J. Am. Chem. Soc. 111, 1161–1171 (1989)
- Wilson, J.J., Brodbelt, J.S.: Ms/ms simplification by 355 nm ultraviolet photodissociation of chromophore-derivatized peptides in a quadrupole ion trap. Anal. Chem. 79, 7883–7892 (2007)
- 37. O'Hair, R.A.J.: The 3d quadrupole ion trap mass spectrometer as a complete chemical laboratory for fundamental gas-phase studies of metal mediated chemistry. Chem. Commun. **14**, 1469–1481 (2006)
- 38. Antoine, R., Joly, L., Tabarin, T., Broyer, M., Dugourd, P., Lemoine, J.: Photo-induced formation of radical anion peptides. Electron photodetachment dissociation experiments. Rapid Commun. Mass Spectrom. 21, 265–268 (2007)
- 39. Gabelica, V., Tabarin, T., Antoine, R., Rosu, F., Compagnon, I., Broyer, M., Pauw, E.D., Dugourd, P.: Electron photodetachment dissociation of DNA polyanions in a quadrupole ion trap mass spectrometer. Anal. Chem. **78**, 6564–6572 (2006)
- Coon, J., Shabanowitz, J., Hunt, D., Syka, J.E.P.: Electron transfer dissociation of peptide anions. J. Am. Soc. Mass Spectrom. 16, 880–882 (2005)
- Kjeldsen, F., Silivra, O.A., Ivonin, I.A., Haselmann, K.F., Gorshkov, M., Zubarev, R.A.: Cα-c backbone fragmentation dominates in electron detachment dissociation of gas-phase polypeptide polyanions. Chem. Eur. J. 11, 1803–1812 (2005)

Excited-State Dynamics of Protonated Aromatic Amino Acids

Claude Dedonder, Géraldine Féraud, and Christophe Jouvet

Abstract

The electronic spectroscopy and the electronic excited state dynamics of the three protonated aromatic amino acids (PAAAs) phenylalanine (Phe), tyrosine (Tyr) and tryptophan (Trp) are presented in this chapter. *Ab-initio* calculations combined with various experimental techniques such as coincidence experiments, pump-probe spectroscopy and photo-fragmentation of cold trapped ions have been implemented to work out the complex photophysical processes involved in these AAs. The results include photo-fragmentation spectra, excited-state lifetimes, full fragmentation patterns at fixed excitation energies and specific fragmentation channels as a function of the excitation energy. Fragmentation patterns depending on the electronic excited state are detailed.

9.1 Introduction

There are three aromatic amino acids: phenylalanine (Phe) with benzene as the aromatic chromophore, tyrosine (Tyr) for which phenol is the aromatic moiety, and tryptophan (Trp) for which it is indole (Fig. 9.1). These are responsible for the absorption of UV light by proteins. The oscillator strength of the electronic transition in Trp is one order of magnitude larger than that of Tyr and two orders of magnitude larger than the Phe transition [1–3]. Thus, Trp is the amino acid mostly responsible for the optical properties of proteins in the UV-B (315–260 nm) spectral region. Trp has an emission band centre that strongly depends on the local environment, and this property is used to follow the folding/unfolding processes in proteins; Trp residues that are buried in the hydrophobic core of proteins can have spectra shifted by tens of nm compared to Trp on the surface of the protein

C. Dedonder (🖂) • G. Féraud • C. Jouvet Laboratoire de Physique des Interactions Ioniques et Moléculaires, CNRS UMR 7345, Aix Marseille Université. Centre de Saint-Jérôme, 13397 Marseille Cedex 20, France e-mail: Christophe.jouvet@univ-amu.fr

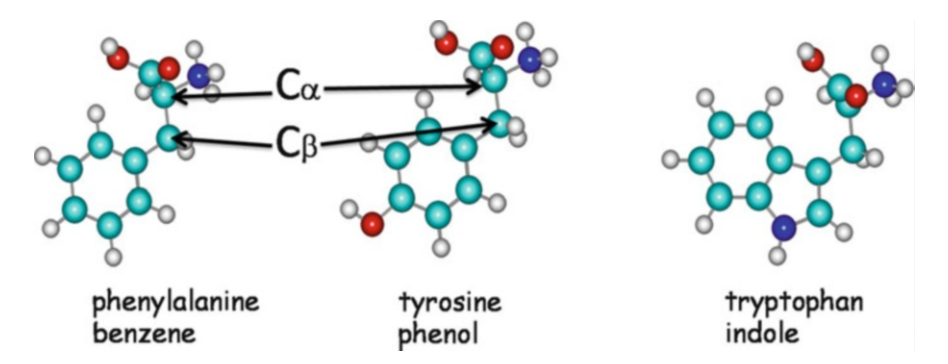


Fig. 9.1 The three protonated aromatic amino acids with C atoms in *cyan*, H in *white*, O in *red* and N in *blue*. The aromatic chromophore for each is indicated under its name

[1–3]. The Trp excited state lifetime is also strongly dependent on the environment, *i.e.*, on the protein structure [1, 4-6].

The emission shift in proteins seems quite well understood [7] but the variation of the excited state lifetime by more than two orders of magnitude is still not totally elucidated [1, 8, 9]. In particular, it has been shown that Trp at low pH, in its protonated form, has a very short lifetime [10]. To understand the basic properties of the molecule, gas-phase studies along with ab-initio calculations are necessary steps. The neutral aromatic amino acids have been characterised in the gas phase, cooled in supersonic expansions where their spectroscopy is recorded using fluorescence [11, 12] or multi-photon ionisation detection schemes [5, 13–15]. These molecules are very floppy species, and for example 12 conformers have been detected for tyrosine, which all seem to have nanosecond excited state lifetimes. It should be noted that conformers with very short lifetimes would not be detected using nanosecond laser, and it has recently been shown in the case of neutral Phe that the lifetime can change by one order of magnitude depending on the conformer [16]. The variation of the lifetime is not due to variations of the oscillator strength of the transition but to the appearance of non-radiative processes such as intersystem crossing, internal conversion or excited state photo-dissociation.

For the neutral systems, the spectroscopy of the excited states and the lifetimes are well documented but the non-radiative processes are largely unknown. As an example, it has been shown that phenol [17], the Tyr chromophore, loses an H atom upon optical excitation but this reaction has not yet been investigated for tyrosine.

As will be seen in the following sections, a more complete story of the processes following optical excitation can be tracked for protonated aromatic amino acids (PAAAs), starting with spectroscopy with a tunable laser, to the excited states dynamics, and followed by the primary and secondary fragmentations.

Double resonance IR/UV spectroscopy [11, 18] and *ab-initio* calculations unambiguously show that the proton is located on the amino group. These molecules have two (approximate) symmetry planes, the aromatic plane and the amino acid ("glycine") part, which are linked by the C_{α} – C_{β} bond. These local symmetries will be useful for labelling the electronic orbitals.

Ten years ago nothing was known about the excited states of these protonated species isolated in the gas phase since they were not easily produced; the development of electrospray sources was a necessary step for their easy production. Besides, these molecules are floppy so that an efficient cooling is required to record clear spectroscopy. Warm molecules display congested spectra [19, 20], and thus the spectroscopic information is not as good as that for cold species. In this chapter, we will mainly focus on protonated Tyr (TyrH⁺) and Trp (TrpH⁺), which have been more extensively studied because their oscillator strengths are larger than that of protonated Phe (PheH⁺).

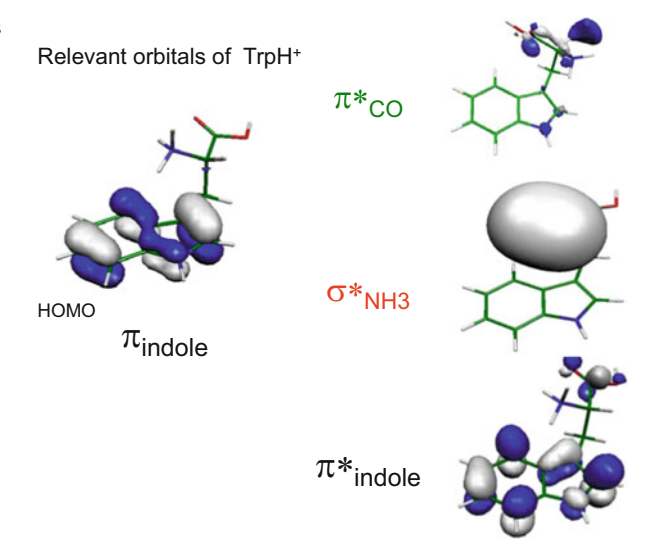
9.2 Ab-initio Calculations

While many papers have dealt with the excited-state properties of neutral amino acids [21–23], less has been done on the protonated species [19, 24, 25]. The recent improvements of ab-initio methods and in particular the Resolution-of-the-Identity [26] approximation in association with the Coupled Cluster method as implemented in the Turbomole package [27] gives results which compare very well with experiments. In particular, it is possible with this method to perform excited-state optimisations followed by excited-state vibrational analysis. Although the systems are quite complex, the excited states which play very important roles in the excitedstate dynamics of the PAAAs can be calculated quite accurately. We will see that the fragmentation pattern can be understood by considering three excited states, which are basically the same for the three PAAAs and are built on four molecular orbitals (shown in Fig. 9.2 for TrpH⁺). The HOMO, which is a π orbital localised on the indole aromatic part, and three unoccupied orbitals play a crucial role. First, there is the π^* orbital localised on the indole ring with which it is possible to build the $\pi\pi^*$ state responsible for the optical absorption and carrying the oscillator strength (for Trp there are two π^* orbitals responsible for the so-called L_a and L_b states of indole) [2]. The second important orbital is a Rydberg-type orbital localised on the protonated amino group. This orbital has σ^* symmetry with respect to the glycine plane (σ^*_{NH3}). The third one is more localised on the carbonyl group and has π^* type symmetry with respect to the glycine plane (π^*_{CO}).

To a first approximation, the excited states are built by promoting one electron from the HOMO to one of these three unoccupied orbitals. Note that we are presenting here a schematic view and one should not forget that the reality is more complex, and that the excited states are not built with just two orbitals. *Ab-initio* calculations have shown that excitation to any one of these states triggers the dynamics of a proton/hydrogen through a very small barrier.

- In the $\pi\pi^*$ state, the dominant process is a transfer from the ammonium group towards the indole/phenol aromatic part.
- In the $\pi\sigma^*_{NH3}$ state, the C-NH₃ part becomes hypervalent (as in the case of NH₄) and can very easily lose one H atom.
- In the $\pi\pi^*_{CO}$ state, the H atom of NH₃ which is hydrogen bonded to the carbonyl group can be transferred nearly barrier-less to the CO.

Fig. 9.2 Molecular orbitals involved in the electronic absorption of protonated tryptophan



The variation of the energy gap between $\pi\pi^*$ and $\pi\sigma^*$ (or $\pi\pi^*_{CO}$) states can be understood with simple arguments [24, 25, 28]. Basically, the fast dynamics occurs when the electron initially localised on the indole $\pi\pi^*$ state (or phenol for Tyr) jumps to one of the two states for which the excited orbital is localised on the protonated glycine part. The energy of these excited states depends on the chromophore: in a simple approximation to reach these states, one electron has to be removed from the aromatic part and added on the protonated glycine part. The energies of these states then strongly depend on the ionisation energy (IE) of the aromatic moiety, which is lower for Trp than for Tyr; thus the electron transfer is easier in Trp than in Tyr. Calculations have confirmed this crude model; the energy gap between the $\pi\pi^*$ state and the states localised on the glycine part is in the order of 0.3 eV for Trp while it is 0.9 eV in Tyr and 1.1 eV in Phe (Fig. 9.3). It should also be noticed that the ordering of the three excited states strongly depends on the conformer structure and in particular on the rotation around the C_{α} - C_{β} bond. For example, in Tyr, the $\pi\sigma^*_{NH3}$ state is lower in energy than the $\pi\pi^*_{CO}$ state for the A isomer while it is the opposite for the B isomer (in the ground-state geometry) but the $\pi\pi^*$ state is always the lowest. In Trp the ordering of the three states changes upon C_{α} – C_{β} rotation, but they stay very close in energy.

9.3 The General Method: Photo-fragmentation

From an experimental point of view, the general method to detect protonated ions relies on the fragmentation of these ions. Indeed the concentrations that can be achieved in most ion experiments are very small. This precludes absorption methods and makes fluorescence techniques difficult, although they are possible for ions that have a high fluorescence quantum yield (see Chap. 6), which is not the

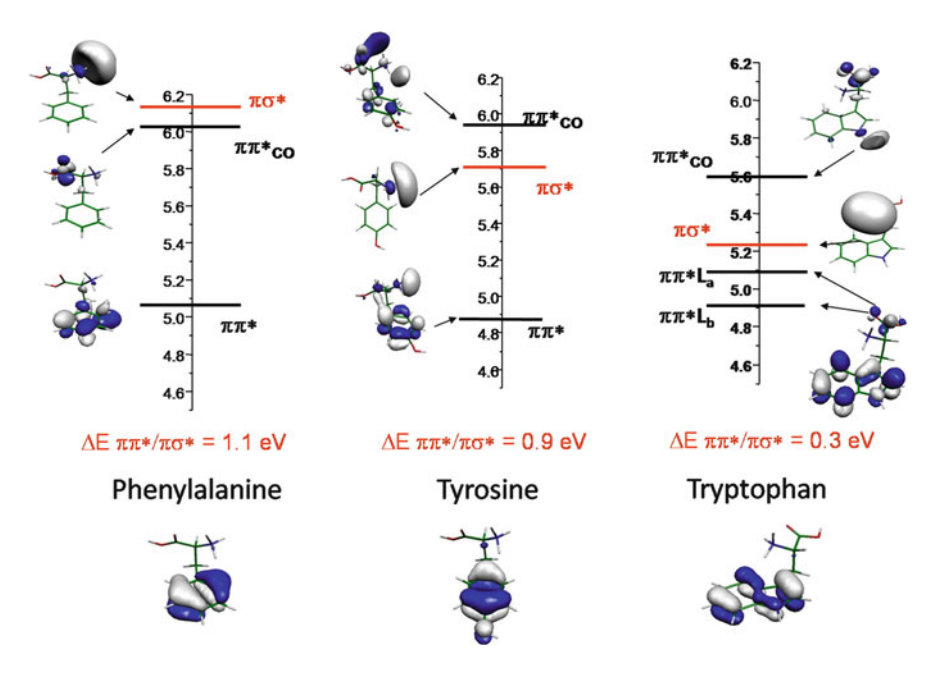


Fig. 9.3 Vertical energies calculated for the three protonated aromatic amino acids. The energy gap between the $\pi\pi^*$ and the $\pi\sigma^*$ levels differs greatly for the different protonated amino acids

case for protonated aromatic amino acids since their excited-state lifetimes are very short. Electron photo-detachment of these ions has been tried but has been unsuccessful even with powerful femtosecond lasers. This is probably due to the very high *IE* for producing doubly charged species, so that electron detachment is likely not competitive with fragmentation. (It should be mentioned that this is also the case for neutral molecules for which the ionisation quantum yield at threshold is quite small, typically 10 %) [29].

Thus in all spectroscopic experiments on protonated aromatic amino acids, the excited-states properties are obtained by detecting fragment ions as the laser wavelength is changed for absorption spectra, or as a function of the delay between pump and probe lasers for lifetime measurements. One can notice that since the electronic excitation is around 4 eV, the photon energy is large enough to induce some fragmentation, *i.e.*, a one-photon process is enough to induce bond dissociation. The fragmentation dynamics is very complex and not yet fully understood. It can be divided into two parts: the evolution of the excited state (electrons), and the evolution of the nuclei on a longer time scale.

The primary fragmentation process is linked to the dynamics in the excited state. Photo-excitation can lead to direct fragmentation in the excited state, which often occurs after an electron transfer, or to ground-state fragmentation after internal conversion, *i.e.*, the electronic energy is converted into vibrational energy in the ground state. Internal conversion produces very hot ions that are expected to fragment in a very similar way as fragmentation induced by low-energy collisions,

i.e., via statistical fragmentation schemes. It should be noticed that in the case of photo-fragmentation, the energy content of an ion is relatively well defined as the thermal energy of the ion before excitation plus the photon energy.

Primary fragments can still contain a lot of energy and can fragment further. However, the primary fragment does not contain a well-defined internal energy. Indeed in the first fragmentation process, the initial energy is shared between the neutral fragments, the ionic fragments and the translational kinetic energy. Thus, among the primary fragments, the ones that have more internal energy will fragment rapidly while those that have an internal energy just above the fragmentation barrier will take a very long time to break up. The entire succession of events occurs on different time scales ranging from the hundred of femtoseconds [28] to seconds [30], *i.e.*, over more than 12 orders of magnitude and thus different experimental techniques have to be used to characterise the complete process.

9.4 Fragmentation Pathways and Time Evolution

To disentangle the fragmentation processes induced by optical excitation, a lot of information is required: the fragmentation time, the nature and the number of fragments, and the energy distribution (internal and kinetic) of the fragments.

In most experiments only fragment ions are detected, whereas a complete analysis of the fragmentation mechanism requires the detection of both ionic and neutral species. In a few experiments, the neutral fragments have been detected through electron-impact ionisation or electron capture from an alkali gas [1], but there is no link between a given ion and a neutral product since these fragments are not detected in coincidence, and the neutral fragment may undergo additional fragmentation in the re-ionisation process, complicating the analysis. In particular, it is important to know how many neutral fragments are produced together with a fragment ion: if more than one neutral fragment is produced, are they produced together or sequentially and in which order?

Understanding the fragmentation mechanisms also involves analysing the energetics and kinetics of the reaction. For the energetics, this means that one has to control the initial energy of the system before the fragmentation; then a UV photon is well suited for exciting the system as long as the thermal energy is not too high, *i.e.*, small compared to the photon energy. As we will see, information on the fragment kinetic energies can be obtained, but the internal energy (vibrational and rotational energy distribution) has not yet been obtained in such large systems.

The fragmentation time is also a very important information. It can help to differentiate fragmentation occurring in the excited states (very fast sub nanosecond) from processes occurring after internal conversion in the ground state or secondary fragmentation (*i.e.*, fragmentation of hot fragments).

9.4.1 The Method: Coincidence Experiments

Photo-fragmentation of protonated Trp and Tyr has been investigated in a unique experimental setup (Arc en Ciel setup in Orsay), in which ionic and neutral fragments from photo-fragmentation are detected in coincidence, in time and in position. From these data the kinetic energy, the number of neutral fragments associated with a fragment ion, their masses, and the order of the fragmentation steps are extracted. Moreover the fragmentation time scale ranging from tens of nanoseconds to milliseconds is obtained. Longer time scales (in the hundred of millisecond range) have been studied at the ELISA setup in Aarhus [30]. From all these data a comprehensive fragmentation mechanism has been proposed.

A detailed description of the experimental set-up and data analysis can be found in [31–33]. In order to get the number of neutral fragment(s) produced with one ionic fragment, coincidence techniques have to be used, which means that one and only one parent ion is photo-dissociated each time the laser is fired, and that the ionic and neutral fragments are detected individually. To ensure that no more than one ion is excited for each laser shot, the number of ions detected per laser pulse has to be a lot smaller than the repetition rate: for example if one ion is detected every 100 laser shots, the probability of exciting two ions (false coincidences) is 10^{-4} (assuming a detection efficiency of 100 %). Experimentally, the ions produced by an electrospray ion source (ESI) are bunched in packets of 50-ns duration, containing about 1,000 ions at a repetition rate of 1 kHz. The ion bunch is accelerated up to 2.5 kV. When one parent ion is photo-dissociated, the neutral species reach a position sensitive detector (PSD), while the ionic fragment is deflected in a 45° electrostatic parallel-plate analyser before reaching another PSD. For each laser shot, the arrival times and positions of the neutral and ionic fragments are recorded. This experimental set-up allows recording the fragmentation time in the range of ns to ms, the number of neutral fragments produced from each ion detected, and the order of the fragmentation steps.

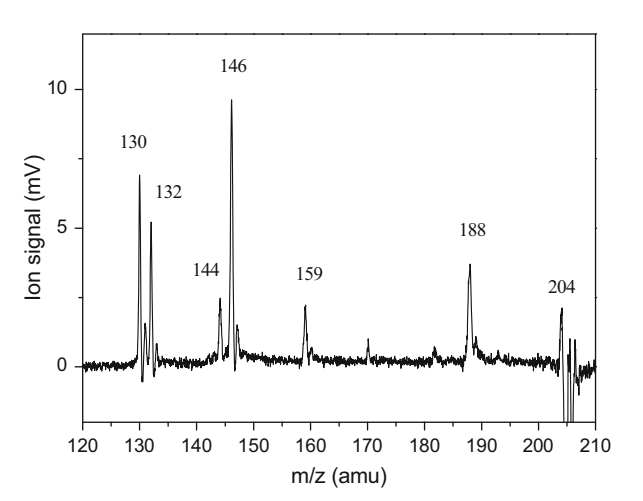
9.4.2 Results: The Tryptophan Case

The photo-dissociation mass spectrum of protonated tryptophan (Fig. 9.4) has been recorded by many groups [20, 34–36]. Some fragments are the same as those obtained from Collision Induced Dissociation (CID) [37] and some are specific to the photo-dissociation process, namely the loss of H (m/z = 204) and the C_{α} – C_{β} bond rupture (m/z = 130). This is already an indication that the optical excitation induces some dynamics in the excited state, and that not everything is governed by internal conversion followed by statistical fragmentation.

The coincidence experiments allow to go further, the main results being: [32]

- (1) Among the fragmentation channels, the ion at m/z = 204 reveals the H-loss reaction is specific to UV photo-excitation.
- (2) Except for the m/z = 130 fragments due to secondary fragmentations after H-loss ion, all fragmentation processes are finished in 10 μ s after 266-nm

Fig. 9.4 Photo-fragmentation mass spectrum of protonated tryptophan (m/z= 205) after excitation at 266 nm. The negative signal at m/z = 205 shows the depletion of the parent ion [34]



photon excitation. The primary fragmentation events leading to the formation of m/z = 188 (NH₃ loss), 159 (H₂O + CO loss), and 132 (dehydrogenated glycine loss) take place within 10 ns. Secondary fragmentations leading to m/z = 146 and 144 occur in less than 10 μ s.

- (3) Fragmentation of the tryptophan radical cation obtained after H loss (m/z = 204) takes times of up to the ms range and leads to C_{α} – C_{β} bond rupture (m/z = 130). The absorption of a probe photon by the radical cation will increase the reaction rate and the m/z = 130 detection. This is the explanation for the plateau observed at long times in the decay of Trp in the femtosecond pump-probe experiment (*vide infra*).
- (4) From the coincidence experiment, the relationship between the parent ion and the daughter ion can be tracked without ambiguity.

(a) m/z = 205
$$\rightarrow$$
 m/z = 188 + NH₃ (in less than 10 ns) \rightarrow m/z = 146 +CH₂CO + NH₃ (μ s) \rightarrow m/z = 144 + CO₂ + NH₃ (μ s)

Ammonia loss occurs in the ground state after a complex rearrangement [38] and has a barrier of 1 eV [39, 40]. It is the lowest-energy channel. The energy content after the NH₃ loss is such that fragmentation can continue on a longer time scale and end up with the formation of m/z = 144 or 146.

(b) $m/z = 205 \rightarrow m/z = 187 + H_2O \rightarrow m/z = 159 + CO + H_2O$ (in less than 10 ns)

This process probably occurs in the ground state after proton transfer from the ammonium group to the carboxylic acid group. The first step is water loss, and the CO loss occurs immediately after since the dissociation barrier for CO loss is less than 0.1 eV after water loss.

(c) $m/z = 205 \rightarrow m/z = 132 + NH_2CHCOOH$ (less than 10 ns) [32]. This fragmentation was quite unexpected. From Collision Induced Dissociation (CID) experiments, this fragment was expected to be produced by HCN loss (m/z = 27) from m/z = 159. The coincidence experiment

demonstrates, however, that this fragment is produced in only one step. A mechanism has been proposed to rationalise this observation: proton transfer from the NH₃ group to the indole ring, followed by C_{α} – C_{β} bond rupture, and in the ionic complex an hydrogen transfer from the amino group of the glycine towards the nitrogen of the pyrrol group [32].

- (d) $m/z = 205 \rightarrow m/z = 204 + H \rightarrow m/z = 130 + NH₂CH₂COOH (very slow)$
- (e) $m/z = 205 \rightarrow m/z = 130 + NH_2CH_2COHOH$ (less than 10 ns, excited state) [41].

m/z=130 corresponds to the C_{α} – C_{β} bond rupture. It is produced by two mechanisms, fragmentation after H loss or through a direct fragmentation in the excited state. The coincidence experiments have shown that this fragmentation channel occurs on two time scales: a fast one (less than 10 ns) which is observed in tyrosine and tryptophan and not in tyramine and tryptamine and a slow one (tens of μ s or ms) observed for all four species. On one hand, a direct barrier-less mechanism has been found through *ab-initio* calculations: the first step is hydrogen transfer from the amino group toward the carbonyl group and then a direct (barrier-less) dissociation along the C_{α} – C_{β} bond in the excited state occurs [32, 41]. On the other hand, the fragmentation after H loss leads to a very long time dynamics: after H loss, the radical cations have a broad internal energy distribution, and the cations having just enough energy to dissociate are going to take a very long time (up to ms) to fragment as shown by the experiments in the storage ring [30].

9.5 Spectroscopy in Cold Ion Traps

The PAAAs are very flexible molecules due to the rotational motions of the protonated amino group and of the C–C single bonds, in particular the C_{α} – C_{β} bond, which will give rise to low vibrational frequencies. The rotational barrier around the C_{α} – C_{β} bond is only 0.4 eV [24] leading to vibrations as low as 30 cm⁻¹. Thus, precise spectroscopic information requires very cold molecules (less than 50 K) to avoid spectral congestion. The experimental method was pioneered by O. Boyarkin and T.R. Rizzo in Lausanne [35, 36, 42] using a cold 22-pole ion trap developed by D. Gerlich [43]. Since then, several experimental set-ups using this technique have been built and a simplified version with lower performance using a commercial Paul trap [44, 45] has been developed in particular by Wang et al. [43].

In brief, the experiment consists in sending ions into a trap filled with helium buffer gas held at a few K. The ions are trapped for some time (ms) to ascertain thermalisation before they are fragmented with a laser beam. All ions are then extracted from the trap, a particular fragment ion is mass selected, and its signal recorded as a function of the laser wavelength. If the fragmentation yield and branching ratio are independent of the wavelength, the photo-fragmentation spectrum is similar to an absorption spectrum.

9.5.1 Spectroscopy

Spectroscopy of protonated aromatic amino acids has been done by Rizzo's group [18, 36] at very low temperatures (around 12 K) in the case of phenylalanine and tyrosine and by Fuke's group in Kobe at a slightly higher temperature [46, 47]. At high temperatures, the spectrum becomes unresolved due to spectral congestion [19, 45] but 50 K seems to be enough to get nice spectroscopic information (see below). The S_0 – S_1 transition energy is very similar to that of the neutral molecule (shift of 50 cm⁻¹ and 400 cm⁻¹ to the red for Phe and Tyr, respectively). This is a good indication that the protonation site is not on the chromophore, which would have perturbed the electronic transition much more [48].

9.5.1.1 Phenylalanine

The Phe spectrum was first recorded [18] detecting the fragment masses $m/z = 74 \pm 1$ or 92 ± 1 on a limited range of excitation energy, *i.e.*, from the S_1 band origin up to 800 cm^{-1} above. The spectrum is nicely resolved, and two conformers with different rotations around the C_{α} – C_{β} bond were identified. A similar experiment at lower spectral resolution, over a larger energy range (developed in two set-ups in Orsay and in Marseille) has shown that for low photon energies the fragments are m/z = 75 and 92 (this fragment corresponds to the C_{α} – C_{β} bond rupture after proton transfer to the benzene ring), and that the fragmentation channel changes to the m/z = 120 fragment (CO + H_2 O loss) at higher energies as shown in Fig. 9.5. The bands observed at this resolution are the 0–0 transition at ~266 nm and a vibronic transition associated with deformation of the benzene ring (~262 nm). Vibrational structures are also observed at higher energies when the m/z = 120 fragment is produced. The experimental results could be indicative of a conical intersection between two different electronic states.

9.5.1.2 Tyrosine

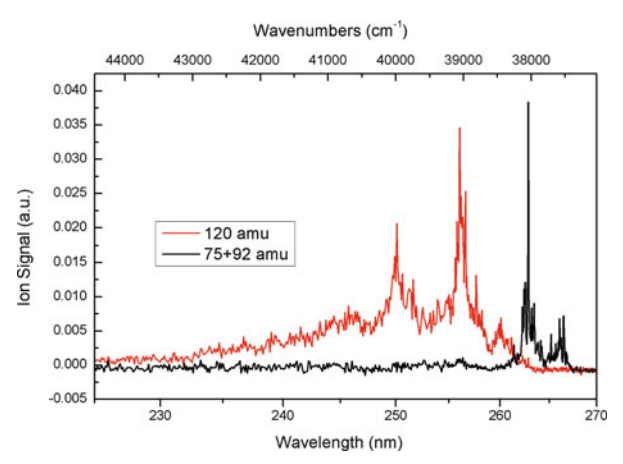
A high resolution spectrum of protonated tyrosine was first obtained at a very low temperature in a 22-pole trap [18]. Recently, a wider spectral range has been recorded at lower spectral resolution and higher temperature around 50 K (Fig. 9.6).

At low energy the dominant dissociation channel produces the m/z =108 fragment which corresponds to C_{α} – C_{β} bond rupture after a proton transfer to the phenol ring. The m/z = 107 fragment, which corresponds to C_{α} – C_{β} rupture but without proton transfer, is very weak at low energies but becomes quite important at high energies (below 240 nm) when the H-loss channel giving the m/z = 181 ion is appearing.

Below 275 nm, the m/z = 108 fragment decreases in abundance while the m/z = 136 and 147 fragments (not shown here) are growing: these two channels are $H_2O + CO$ loss and $NH_3 + H_2O$ loss, respectively, which are the most important ones in collision induced dissociation.

Below 240 nm, at the appearance of the H loss channel, the m/z = 119 (NH₃ loss from m/z = 136) and the m/z = 123 (NH₃ + CH₂CO loss) fragments increase in

Fig. 9.5 Photo-fragmentation spectra of protonated phenylalanine over a large spectral range: at low energies the fragmentation results in m/z = 75 and 92 (*red curve*), while at higher energies these fragments disappear and m/z = 120 is produced (*black curve*)

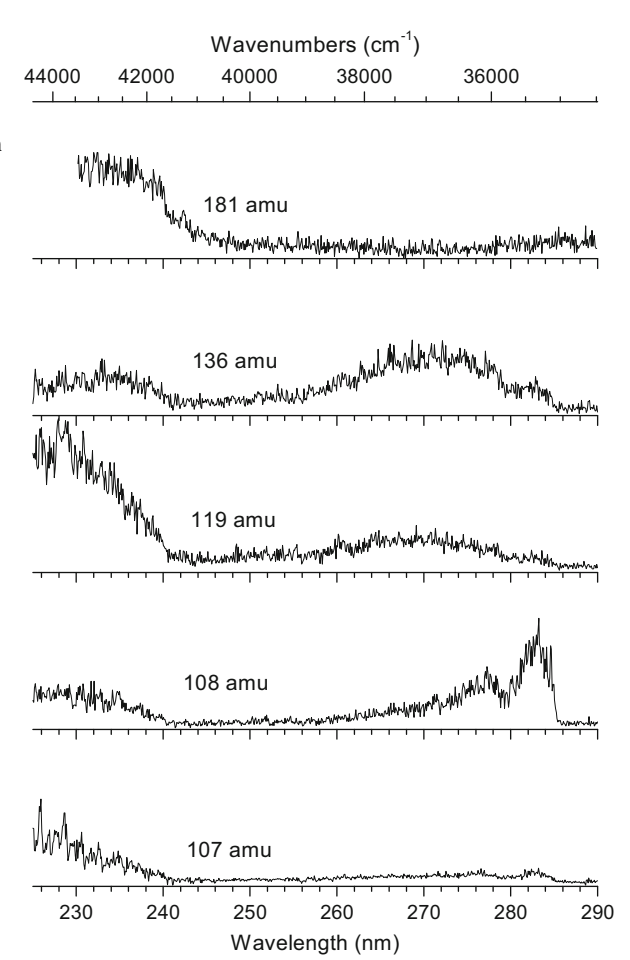


abundance. These fragments are secondary fragments and are obtained in CID when the collision energy is increased.

The change in fragmentation channels, not all observed in CID, shows that the initially excited state has a strong influence on the fragmentation dynamics, and that the dynamics is more complex than internal conversion followed by statistical dissociation. More information is needed to explain these fragmentations.

At higher spectral resolution, one can see that conformer A of Tyr (the conformer with the lowest transition energy) does not have the same fragmentation pattern as isomer B. This is reflected in Fig. 9.7 in which the observed spectrum depends on the fragment detected. This is a very important observation, which shows that the fragmentation process is not at all statistical: the energy brought by the laser for all the isomers is the same within 0.1 \% since the electronic transitions are very similar and isomer B (and D) are leading more efficiently to the m/z = 107or 108 fragment. As seen in the experiment of Fig. 9.6, the fragment is m/z = 108which corresponds to the side-chain bond rupture after a proton transfer from the ammonium group towards the phenol ring (a simple C_{α} – C_{β} bond rupture would lead to m/z = 107). The fragmentation is driven by the initial structure, which also implies that the electronic properties and the mechanisms are strongly dependent on small changes of geometry. The structures of these isomers were identified from IR/ UV [18] double resonance spectra in combination with ab-initio ground state calculations (see Fig. 9.8). In isomer A and C, both the NH₃⁺ and CO groups are above the phenol ring whereas in isomer B and D (B is the most stable isomer by only 2.7 kJ/mol) only the ammonium group is above the ring. A and C are quite similar with respect to the rotation around the C_{α} – C_{β} bond, they differ only by the flipping of the OH bend of the phenol moiety and it is similar for isomers B and D.

Fig. 9.6 Photo-fragmentation spectrum of protonated tyrosine as a function of excitation wavelength obtained in an ion trap at around 50 K. The spectrum changes with the detected fragment



9.5.1.3 Tryptophan

The case of tryptophan (Trp) is different because no vibrationally resolved spectra could be realised under similar experimental conditions. This is due to the very short excited-state lifetime, in the femtosecond range (between 10 and 100 fs), which is indicative of a very efficient non-radiative process in Trp as will be discussed in the next sections.

9.5.2 Comparison Between Spectroscopic Results and *Ab-initio* Calculations

Since the experimental spectroscopy of protonated molecules has made tremendous progress, it is worthwhile to compare with the results from recent *ab-initio* methods. This will give some confidence in the calculations, which is particularly necessary to

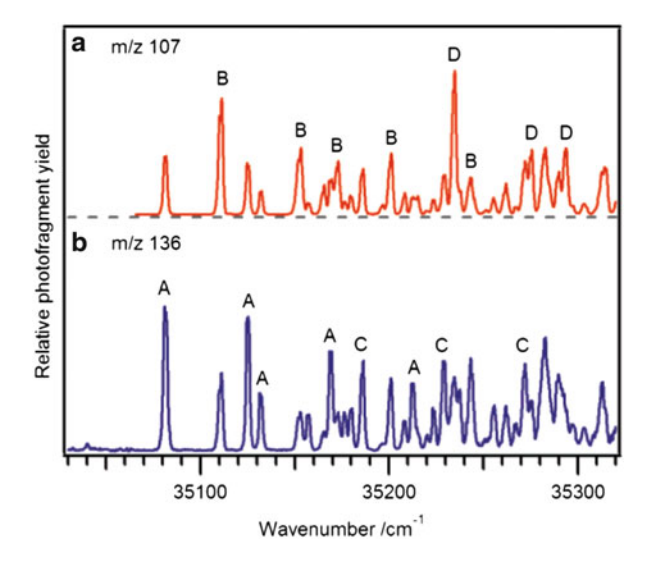


Fig. 9.7 Photo-excitation spectra of cold protonated tyrosine taken from Stearns et al. [18]. Different isomers are labelled A, B, C, and D. Isomers B and D preferentially give the fragment at m/z=107 or 108 (C_{α} - C_{β} bond rupture). Reprinted with permission from [18]. Copyright (2007) American Chemical Society

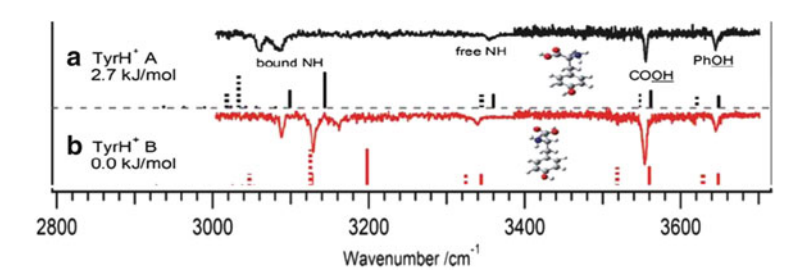


Fig. 9.8 Infrared/UV spectra of protonated tyrosine in an ion trap selecting the band origin of either isomer A or isomer B from the work of Stearns et al. [18]. The most stable isomer is isomer B. The *full sticks* are the calculated scaled harmonic vibrations and the *dotted sticks* are the unscaled anharmonic ones. Reprinted with permission from [18]. Copyright (2007) American Chemical Society

understand the dynamical aspects of the excited-state relaxation processes. In Fig. 9.9, the calculated electronic spectra of the three lowest conformers of TyrH⁺ are presented in comparison with the experimental spectrum taken from the work of Stearns et al. [18]. The spectra are calculated using the pgopher software [49]. In this figure, the scale is normalised to the 0–0 transition of conformer A. The absolute transition energy for conformer A has been calculated to be at 35,345 cm⁻¹ whereas the experimental transition origin is 35,083 cm⁻¹, *i.e.*, the calculated value is 262 cm⁻¹ too high (calculation at the ri-cc2/cc-pVDZ level including S₀ and S₁ optimisation as well as variation of the zero-point energy, performed with the Turbomole package

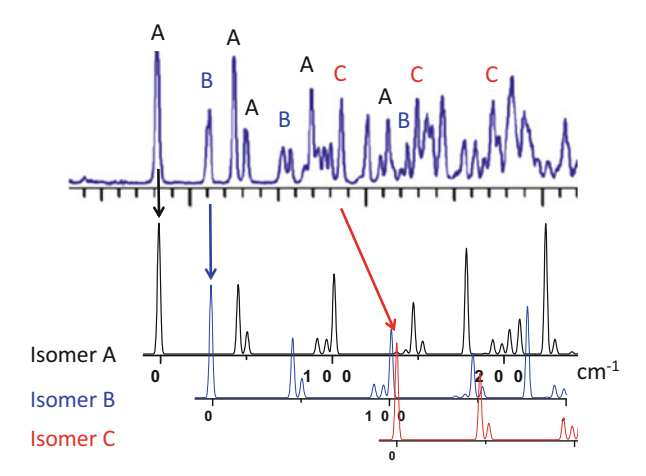


Fig. 9.9 Comparison between the experimental spectrum of Stearns et al. [18]. and calculated spectra (unpublished). In this figure the spectra calculated for all the isomers have been shifted by 262 cm⁻¹ so that the calculated spectral origin of isomer A is in coincidence with the experimental 0–0 transition. Both the low-frequency vibrations and the 0–0 origin of the electronic transition for each isomer are quite well calculated. For Isomer C, the calculation is slightly worse but it is still quite impressive that the energy order of the isomer transitions is reproduced with an error less than 100 wavenumbers. Adapted with permission from [18]. Copyright (2007) American Chemical Society

[27]), which is an error of less than 1 %. The transition energy for isomer B is calculated to be 30 cm⁻¹ higher in energy than isomer A (as in the experiment) and isomer C is calculated to be 132 cm⁻¹ higher than isomer A (instead of 105 cm⁻¹ in the experiment). The calculated frequencies and Franck-Condon factors are in good agreement with the observed ones. Such a good agreement between experimental data and calculations is quite impressive and gives some confidence in the potential energy surface region which cannot be probed experimentally, *i.e.*, far from the Franck-Condon accessible region. This quality of the calculations is quite typical nowadays as can be seen in the recent benchmark study of Send et al. [50].

9.5.2.1 Vibrational Analysis

The excited state vibrational analysis of protonated Phe has not been published yet. For protonated Tyr the low-frequency modes observed are due to a combination of rotation along the C_{α} – C_{β} bond and butterfly vibrations of the two planes (glycine and phenol). If one compares the conformers in the protonated species and in the neutral [12, 51], one can see that the number of conformers observed is quite smaller in the protonated species. This is due to the presence of a charge which creates a dominant charge–dipole interaction. As often in protonated systems the 0–0 transition is not the strongest band as it is for the neutral molecule. This is due to the larger change in the equilibrium geometry between the ground and the excited state due, as mentioned above, to the presence of the nearby charge-transfer states ($\pi\sigma^*$ or $\pi\pi^*_{CO}$) and their coupling with the locally excited state, which

induces an important modification of the charge distribution between the ground and excited states.

9.6 Excited-State Dynamics

The excited-state dynamics at very short times have been obtained for ions directly issued from an electrospray source, thus from hot ions (how hot nobody knows!). The method to obtain information on the excited-state dynamics is to perform pump/probe femtosecond spectroscopy. This is a standard technique in which the first photon promotes the system to the excited state while the second photon probes the evolution of the excited state by re-exciting the parent and monitoring the fragments. In the case of ions for which the fragmentation pattern is the only observable, the second laser should change the fragmentation pathways. It is in fact a complex phenomenon to disentangle since fragmentation can be affected in two ways, either by a change in the fragmentation rate or by a change in the fragmentation branching ratio.

To a first approximation, one can assume that the probe laser is bringing some additional energy to the system, and that this will change (increase) the reaction rates and the branching ratio when there are many fragments. Indeed, the observed signal depends strongly upon what the experiment is measuring:

- (a) The experiment is measuring fragmentation times.
 - Fragmentation-time sensitive experiments can be achieved by photofragmenting a fast ion in an electric field parallel to the propagation axis and by selecting the observed fragment ions produced at a given position in this field, which is equivalent to selecting the ion produced at a given time [52, 53]. If one selects experimentally fragment ions produced in a time interval [0–20 ns for example] and if these photo-fragment ions are produced with a time constant T [as an example 100 ns], the absorption of the probe-laser photon will increase the internal energy and thus increase the fragmentation rate k' = 1/T' [as an example to $T' \sim 1$ ns], so that more fragment ions are produced in the observation window. The absorption of the probe photon will be seen as an increase of the ion signal, and the excited-state lifetime is seen as a decay of this ion signal when the delay between the pump and the probe is increased. At the opposite, if the observation temporal window selects ions produced at long time delay, the probe laser will produce a depopulation of the ion signal. This is one of the reasons why the pump/probe signals recorded on the TrpH⁺ fragments in Fig. 9.10 are so complex.
- (b) If the experiment is not set up for such a time sensitive detection scheme, *i.e.*, if the analysis of the fragmentation process occurs a long time after the fragmentation has occurred (in an ion trap for example), then only the variation of the branching ratio between the fragment ions can be detected. This implies that no pump/probe signal can be detected when only one fragment is produced since only the rate is changing, which the experiment is not measuring. It may be interesting to revise the above deduction. If one ion (TrpH⁺ for example) gives

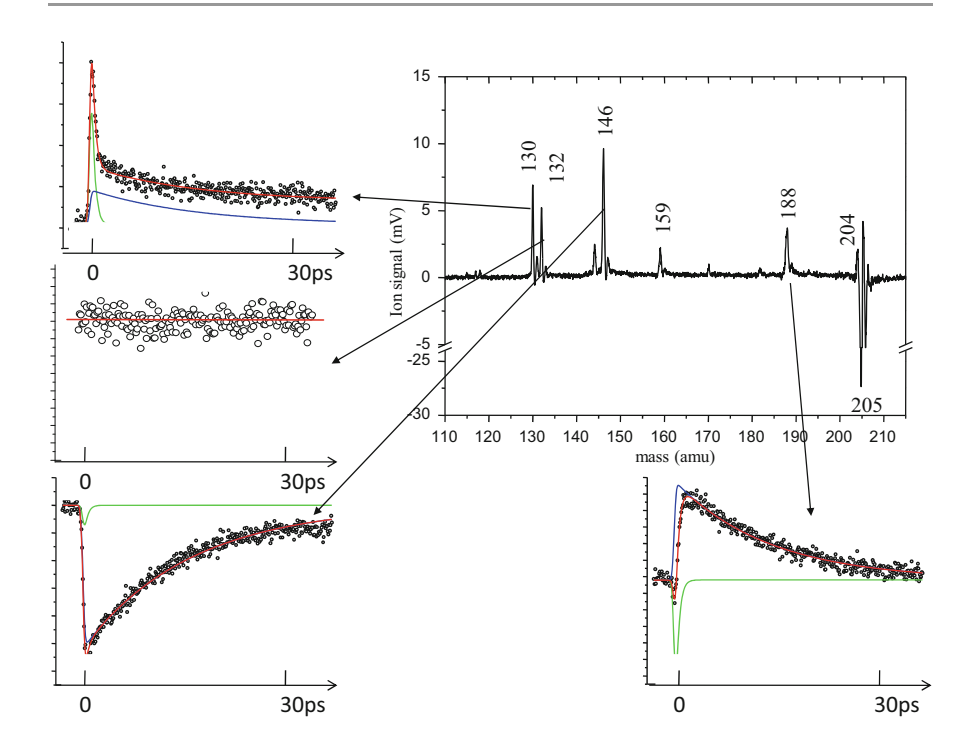


Fig. 9.10 *Upper right*: mass spectrum obtained after photo-excitation of protonated tryptophan (m/z = 205) with 4.66-eV (266-nm) light. Around the mass spectrum: pump/probe signals from different fragment ions. For the m/z = 132 fragment (*middle left*) the signal is flat. This fragment is issued from species (conformer/excited states) which specifically lead to this fragment only [33, 54] (see above). For all the fragments, the *coloured lines* are the fits of the time-resolved signals by bi-exponential decays (*red lines*) with time constants of 400 fs (*green lines*) and 15 ps (*blue lines*). For each fragment the decomposition is different, reflecting that the dynamics on the excited state have a profound influence on the fragmentation occurring at a much longer time

five fragments ions, and if the intensity of four of these fragments is changing when the probe laser is added while the intensity of the fifth fragment does not change, one can deduce that this fifth fragment is not in competition with the others and is a result of a totally different fragmentation mechanism or that a specific conformer is producing this particular ion.

9.6.1 Tryptophan fs Dynamics

In Fig. 9.10 we present the pump/probe signals obtained by optically changing the delay between the pump and the probe lasers while recording the intensity of the fragment ions for the best characterised system, protonated Trp. The first obvious observation is that the time-dependent signal is different for each fragment. If the

fragmentation was purely statistical, all the decay curves should be the same whatever the fragment, which clearly is not the case. The fastest decay time observed in the excited-state dynamics is a few hundreds of femtoseconds, which is the fastest that could be measured with the laser. This is in line with the absence of well-defined vibronic bands in the spectroscopic experiment in a cold ion trap, which suggests even faster dynamics (in the order of 10 fs) to wipe out the vibrational spectrum [35]. This was rather surprising since the first excited-state lifetime of neutral Trp is in the ns range [5]. The presence of an excess proton does not change the energetics of the transition much but it strongly affects the non-radiative processes in the excited state.

One should also note that the probe photon is changing the branching ratio between fragments, in particular increasing the signal of m/z = 130 (C_{α} – C_{β} bond rupture) at very short times. This experimental result is a clear evidence that one can control the fragmentation channels and branching ratios using appropriate femtosecond laser pulses with the right delay between the pump and the probe laser.

To be able to understand such complex time-dependent signals, more information is necessary, in particular the fragmentation mechanism and the parent/daughter ion relationship as well as the fragmentation time (from coincidence experiments).

9.6.2 Bi-exponential Decays

For all the fragments (except m/z = 132), the observed time-dependent signals could be fitted by a bi-exponential decay. It is a good opportunity to discuss the danger of over-interpreting experimental results, and we want to spend a few lines considering the case of bi-exponential decays. As already mentioned, the pumpprobe signals for TrpH⁺ fragmentation were obtained with hot ions directly extracted from the electrospray source, and thus the UV photon is exciting many conformers. Theoretical calculations indicate that some conformers should have a very short lifetime and others should have long lifetimes since the energies of the dissociative states ($\pi\sigma^*$) and stable state ($\pi\pi^*$) are changing quite a lot upon rotation around the C_{α} – C_{β} bond. Since the excited ions are hot, the signal observed should be the sum of all these lifetimes ranging from a few femtoseconds to some nanoseconds. Although not mathematically exact, the signal produced by such an ensemble of molecules can be fitted nicely with a bi-exponential decay function [55]. However, the two time constants obtained have no physical meaning, and in particular they should not be assigned to the excitation of two species nor to two excited states as is so often done in the literature. Basically, if the only information on a system is a bi-exponential decay, one can only deduce that there are some species that have a short lifetime and some with longer lifetimes, that's all!

172 C. Dedonder et al.

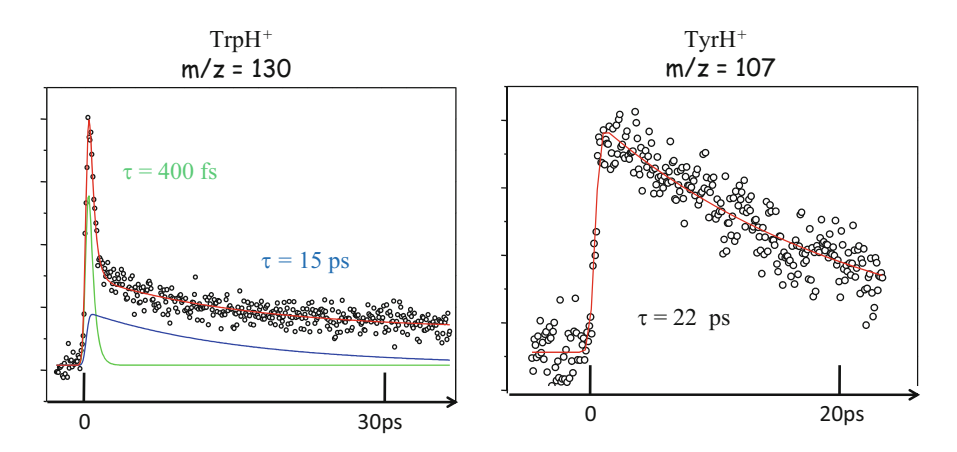


Fig. 9.11 Comparison of the excited-state lifetimes of protonated tryptophan and tyrosine recorded on the same fragmentation channel: the C_{α} - C_{β} bond cleavage

9.6.3 Comparison between TrpH⁺ and TyrH⁺

The pump probe signals presented in Fig. 9.11 are obtained by photo-excitation of TrpH⁺ and TyrH⁺ at 266 nm and detection of similar fragments issued from the C_{α} – C_{β} bond rupture (m/z = 130 for Trp and m/z = 107 for Tyr).

Without going into the details, the basic feature is that the lifetime of TrpH⁺ is short (hundreds of fs) whereas the TyrH⁺ lifetime is in the order of 20 ps (100 times longer), which means that the non-radiative processes are much more efficient in TrpH⁺ than in TyrH⁺. The observation of the very short lifetime of TrpH⁺ as compared to TyrH⁺ can be understood from the calculations: the $\pi\sigma^*$ and $\pi\pi^*_{CO}$ states, leading to dissociation, are very close in energy to the $\pi\pi^*$ state for TrpH⁺ whereas the gap is quite significant in TyrH⁺. There is a very simple reason why the excited states of protonated amino acid molecules are expected to have short excited state lifetimes. The extra proton is carrying the positive charge, and it will tend to attract the electrons. Thus one of the first excited states which will be quite low in energy is a charge transfer (CT) state in which the electron is coming from the HOMO towards the protonated group. Upon the addition of an electron on this protonated C-NH₃⁺ group, it becomes hypervalent and thus very unstable, and this is going to induce fast dynamics: as an example NH₄⁺ is stable but the lifetime of NH₄ is in the 13 ps range [56, 57]. In the case of TrpH⁺, this will trigger either loss of hydrogen or its transfer to the carboxylic group. When the extra proton is far from the chromophore, these CT states are changing the excited-states dynamics but not so much the spectroscopy. On the contrary, these charge-transfer states have been shown to play a key role in the energetics of the electronic transition in protonated aromatic molecules for which the proton is attached to the aromatic ring [58].

The dynamics observed in Figs. 9.10 and 9.11 for TrpH⁺ is more complex than the simple picture described above since the time-resolved signals have to be fitted by multi-exponential decays (400 fs and 15 ps). This is mainly due to the presence

of many conformers in the source. Indeed the calculations show that the energy gaps between the excited states are strongly dependent on the conformation of the ion, in particular through the rotation around the C_{α} – C_{β} bond, thus the lifetime of each conformer can be quite different [33] and some conformers have a longer lifetime. The full interpretation of the pump-probe signals can be found in Grégoire et al. [33].

9.7 The General Picture

9.7.1 Tryptophan

From the *ab-initio* calculations and experimental data, one can make a good connection between the excited state, *i.e.*, on which orbital the excited electron is localised, and the fragmentation pathway. The overall picture of the excited-state dissociation pathways is presented in Fig. 9.12 and summarised in the following:

The $\pi\pi^*_{CO}$ state leads to a barrier-less H transfer from the NH_3^+ group towards the carboxyl group. The concerted electron–proton transfer to the carboxyl weakens the C_α – C_β bond and will lead to the fragment ion at mass m/z = 130. After internal conversion and since the proton is on the acidic group, this channel leads easily to the loss of water and CO (m/z = 159).

The $\pi\sigma^*$ state leads to H loss or internal conversion through a small barrier. The H-loss channel leads to the formation of the radical cation at mass m/z = 204 that can further fragment into its secondary fragment ion at mass m/z = 130. The internal-conversion channel leads to ammonia loss (m/z = 188) followed by secondary fragmentations (CO₂ or C₂H₂O loss leading to m/z = 144 and 146, respectively).

The $\pi\pi^*$ state leads to a proton transfer from the NH_3^+ group towards the indole ring. The fragment ion associated with this proton-transfer reaction is m/z=132. This is the only channel insensitive to the probe laser with a pump/probe signal completely flat. One might expect that the other fragmentation channels would enter the competition, in particular in the mobile proton model framework [59]. The absence of a pump/probe signal in this channel clearly indicates that this is not the case, and that the kinetics of fragmentation is faster than the proton exchange and total energy redistribution.

9.7.2 Tyrosine

The overall picture for the TyrH⁺ dynamics, presented in Fig. 9.13, is basically the same as for TrpH⁺, except that the $\pi\pi^*-\pi\sigma^*_{NH3}$ energy gap is larger in tyrosine and is given in terms of the potential energy surface instead of electron localisation. Experimentally, it has been seen that the C_{α} – C_{β} bond rupture is conformer dependent. At low energies the ionic fragment is not the m/z = 107 fragment (C_{α} – C_{β} direct rupture) as thought initially but m/z = 108 (C_{α} – C_{β} bond breaks after proton transfer from the amino group toward the phenol ring). This mechanism has been

174 C. Dedonder et al.

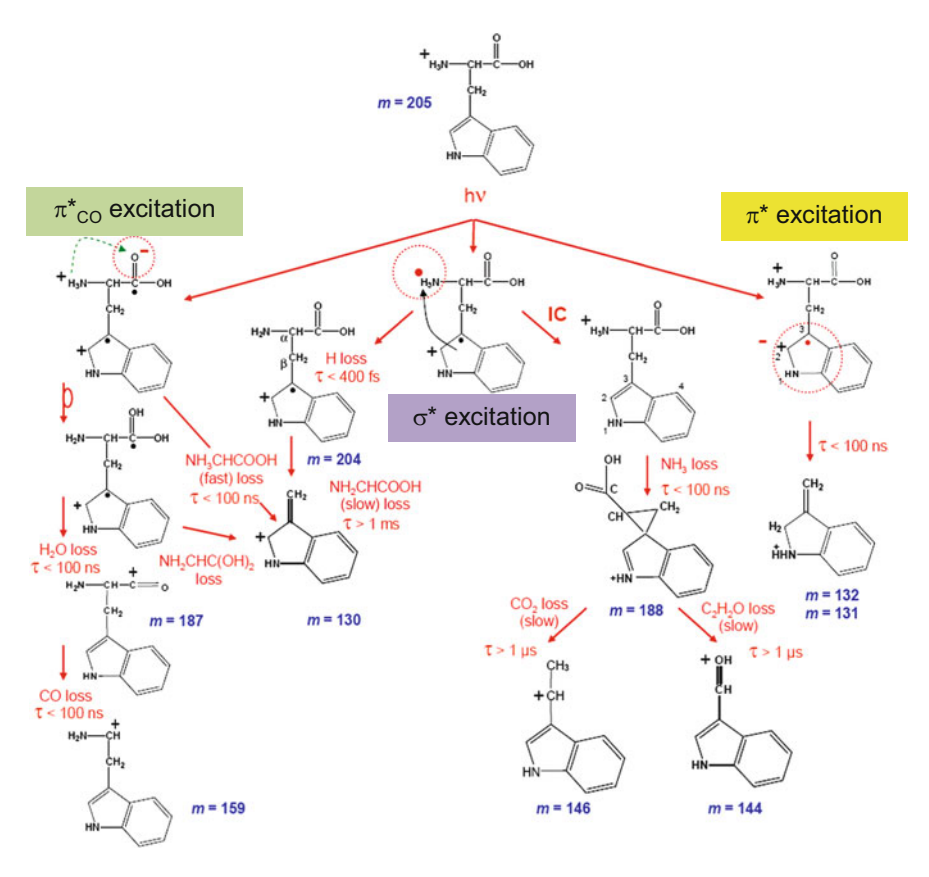
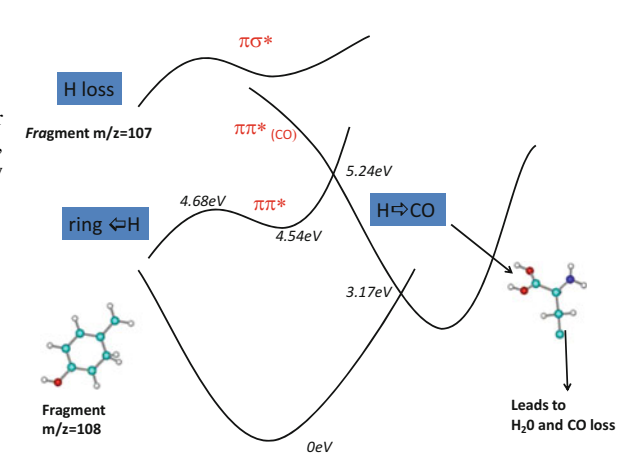


Fig. 9.12 General scheme showing the connection between the electron localisation (*i.e.*, excited state) and the fragmentation channels in protonated tryptophan. Reprinted with permission from [32]. Copyright [2007], American Institute of Physics

predicted theoretically: optimisation of the S_1 ($\pi\pi^*$) state, in which one H is pointing toward the ring induces a strong puckering of the phenol chromophore. The barrier to the proton transfer (PT) toward the phenol ring has been calculated to be of the order 0.15 eV and is isomer independent. In this process the excited state crosses the ground state, and the dynamics in this hot ground state leads to C_{α} – C_{β} bond rupture after the proton transfer. This channel, dominant at low excitation energies, is in competition with a second channel: the proton transfer from the NH₃⁺ to the carbonyl, which is due to a crossing between S_1 and S_2 . Indeed the second excited state ($\pi\pi^*_{CO}$) leads without barrier to a proton transfer to the carbonyl group. Along this proton-transfer coordinate, S_2 crosses S_1 at around 0.7 eV above the $\pi\pi^*$ optimised energy and a second crossing with S_0 occurs below the $\pi\pi^*$ state (–1.37 eV). This triggers the dynamics on the ground-state surface leading to the H₂O+CO loss (m/z = 136) and H₂O+NH₃ loss (m/z = 147). The initial $\pi\pi^*$ state decays through this channel by the S_1/S_2 avoided crossing. This is the dominant channel at higher energies (+1,000 cm⁻¹ see Fig. 9.6).

Fig. 9.13 Schematic potential energy functions of protonated tyrosine as a function of the proton transfer towards CO (*right hand side*), towards the phenol ring at low energy (*left*) and for the H-loss channel at higher energy (see text)



Theoretical calculations predicted that the $\pi\sigma^*$ state could be excited at higher energies, which should lead to H loss. Indeed above 5 eV (below 240 nm), the H-loss channel opens up leading to the formation of the radical cation, which subsequently fragments through the C_{α} – C_{β} bond dissociation leading to the m/z = 107 fragment (Fig. 9.13). As in many aromatic molecules containing NH or OH [17], the NH $\pi\sigma^*$ dissociative state crosses the ground state, and then part of the population is found in a ground state which decays along the high energy CID (statistical) channels (m/z = 123/119).

From this scheme and *ab-initio* calculations, the observation that two isomers (isomer A and B) do not have the same fragmentation branching ratio [18] can be understood. In isomer B, which gives more efficiently m/z = 108, the barrier to the proton transfer from NH_3^+ to the carboxyl is higher; thus the proton transfer towards the phenol ring is favoured.

9.7.3 Phenylalanine

The photo-dissociation processes are very similar in phenylalanine. At low energies fragmentation occurs through $C_{\alpha}\!\!-\!\!C_{\beta}$ bond rupture leading either to the glycine ion m/z=75 or to the m/z=92 fragment through proton transfer to the phenyl ring. These channels are the equivalent of the ions observed from fragmentation of the radical cation (m/z = 74 and 91). At higher energies (>800 cm^{-1}) these channels close, while a new one opens up, leading to the m/z = 120 fragment. This channel (loss of H₂O+CO) is associated with crossing the barrier to proton transfer towards the carboxyl group as in tyrosine. The $\pi\sigma^*$ state leading to the H-loss channel has not been reported up to now but can be expected at higher energies.

The role of the triplet states in these processes has been postulated on the basis that the chromophores (indole, phenol) have an intersystem crossing rate of the same order of magnitude as the fluorescence one. This rate has no obvious reason to change in the protonated system but since the excited-state lifetime due to

176 C. Dedonder et al.

photo-dissociation processes is in the picosecond range, the intersystem crossing in the protonated PAAAs is no longer competitive.

9.8 Small Peptides

These kinds of studies (spectroscopy, fs pump/probe, coincidence and *ab-initio* calculations) have been pursued on small peptides containing an aromatic residue. In the spectroscopic work, spectra have been obtained up to 20 amino acids, and the spectra are still very clean and well resolved [60]. This means that the number of conformers formed in a cold trap is quite small, and that these peptides fold into a very limited number of conformers. One alternative, however, is that only a small part of the population can dissociate after optical excitation. These large molecules contain so many degrees of freedom that they cannot fragment during the experimental time window (ms) if the process is statistical in the ground state, so that the detection scheme requires some non-statistical fragmentations.

It has been shown that for some pseudo-random peptide sequences containing either Tyr or Trp, some peptides were fragmenting through C_{α} – C_{β} bond rupture while others did not [61]. This rupture seems to be much more efficient for Tyr than for Trp.

So the non-statistical fragmentation schemes have clearly to be understood. Some pieces of information have emerged from studies on small peptides (di- and tripeptide), and basically the scheme is similar to the one presented for the PAAAs. The excited lifetime for Trp-containing peptides is shorter (100 fs) than for the Tyr (ps) ones [53, 62]. The fragmentation pathway could be interpreted in the same manner as for PAAAs. The localisation of the electron on the peptide chain triggers some specific fragmentations. In a very simple approximation, for Trp-containing peptides, the $\pi\pi^*$ state is heavily mixed with excited states localised on the peptide chain and the excitation may extend along the chain. In Tyr-containing peptides, the energy gap between the $\pi\pi^*$ state and other excited states is larger, the transfer of excitation is more difficult, and it requires some rearrangements such as proton transfer between the amide group and the carbonyl group in order to induce the fragmentation which will stay localised near the initial excitation and then lead more efficiently to C_{α} – C_{β} rupture.

Conclusions

The excited-state dynamics of protonated aromatic amino acids is very complex. Some understanding of the phenomena involved in the fragmentation processes seems to have been reached. It has required a huge effort from high quality spectroscopy giving information on the structural landscape, dynamical studies on more than 10 orders of magnitude from femtoseconds to seconds (for comparison 10¹⁰ is the age of the universe in years). Quite interestingly, dynamical events are occurring on the whole temporal scale. Coincidence experiments have given the number and sequence of neutral fragments and the fragmentation times for each ion. Last, but not least, high level *ab-initio*

calculations, which are in very good agreement with the experimental data, have given the conceptual framework needed to rationalise the results.

These protonated aromatic amino acids are probably the molecules that have the most complete experimental description. Indeed, for dynamics of neutral molecules of this size the processes after internal conversion are totally unknown, the branching ratio between different fragmentation channels are not known and are very difficult to obtain and no study has ever reached the temporal scale needed to properly describe the processes.

The general picture obtained for the protonated aromatic amino acids seems to be useful for understanding the photo-fragmentation of small peptides containing aromatic residues, but a complete understanding of the processes in larger peptides is still lacking. The present results are opening a fascinating possibility using lasers, changing their energy and time, to selectively break a bond in proteins which have a given sequence or secondary structure. This may lead to a kind of laser controlled therapy!

References

- Lakowicz, J.R.: Invited review on spectral relaxation in proteins. Photochem. Photobiol. 72, 421–437 (2000)
- 2. Lakowicz, J.R.: Principles of Fluorescence Spectroscopy, 2nd edn. Springer, New York (1999)
- Schermann, J.-P.: Spectroscopy and Modelling of Biomolecular Building Blocks. Elsevier, Amsterdam (2008)
- Katarzyna, G., Szabelsk, M., Rzeska, A., Karolczak, J., Sulowska, H., Wiesław, W.: Photophysical properties of tyrosine at low pH range. Chem. Phys. Lett. 362, 519–526 (2002)
- Philips, L.A., Webb, S.P., Martinez, S.J., Fleming, G.R., Levy, D.H.: Time-resolved spectroscopy of tryptophan conformers in a supersonic jet. J. Am. Chem. Soc. 110, 1352–1355 (1988)
- Robbins, R.J., Fleming, G.R., Beddard, G.S., Robinson, G.W., Thistlethwaite, P.J., Woolfe, G. J.: Photophysics of aqueous tryptophan: pH and temperature effects. J. Am. Chem. Soc. 102, 6271–6279 (1980)
- 7. Vivian, J.T., Callis, P.R.: Mechanisms of tryptophan fluorescence shifts in proteins. Biophys. J. **80**, 2093–2109 (2001)
- Callis, P.R., Petrenko, A., Muin, P.L., Tusell, J.R.: Ab initio prediction of tryptophan fluorescence quenching by protein electric field enabled electron transfer. J. Phys. Chem. B 111, 10335–10339 (2007)
- Dedonder-Lardeux, C., Jouvet, C., Perun, S., Sobolewski, A.L.: External electric field effect on the lowest excited states of indole: ab initio and molecular dynamics study. Phys. Chem. Chem. Phys. 5, 5118–5127 (2003)
- 10. Marquezin, A., Hirata, I.Y., Juliano, L., Ito, A.S.: Tryptophan as a probe for acid-base equilibria in peptides. Biopolymers **71**, 569–576 (2003)
- 11. Rizzo, T.R., Park, Y.D., Peteanu, L.A., Levy, D.H.: The electronic spectrum of the amino acid tryptophan in the gas phase. J. Chem. Phys. **84**, 2534–2541 (1986)
- Inokuchi, Y., Kobayashi, Y., Ito, T., Ebata, T.: Conformation of L-tyrosine studied by fluorescence-detected UV-UV and IR-UV double-resonance spectroscopy. J. Phys. Chem. A 111, 3209–3215 (2007)
- Hünig, I., Seefeld, K.A., Kleinermanns, K.: REMPI and UV–UV double resonance spectroscopy of tryptophan ethylester and the dipeptides tryptophan–serine, glycine–tryptophan and proline–tryptophan. Chem. Phys. Lett. 369, 173–179 (2003)

 Snoek, L.C., Kroemer, R.T., Hockridge, M.R., Simons, J.P.: Conformational landscapes of aromatic amino acids in the gas phase: infrared and ultraviolet ion dip spectroscopy of tryptophan. Phys. Chem. Chem. Phys. 3, 1819–1826 (2001)

- 15. Shimozono, Y., Yamada, K., Ishiuchi, S.-I., Tsukiyama, K., Fujii, M.: Revised conformational assignments and conformational evolution of tyrosine by laser desorption supersonic jet laser spectroscopy. Phys. Chem. Chem. Phys. 15, 5163–5175 (2013)
- Mališ, M., Loquais, Y., Gloaguen, E., Biswal, H.S., Piuzzi, F., Tardivel, B., Brenner, V., Broquier, M., Jouvet, C., Mons, M., Došlić, N., Ljubić, I.: Unraveling the mechanisms of nonradiative deactivation in model peptides following photoexcitation of a phenylalanine residue. J. Am. Chem. Soc. 134, 20340–20351 (2012)
- 17. Sobolewski, A.L., Domcke, W., Dedonder-Lardeux, C., Jouvet, C.: Excited-state hydrogen detachment and hydrogen transfer driven by repulsive $\pi\sigma^*$ states: a new paradigm for nonradiative decay in aromatic biomolecules. Phys. Chem. Chem. Phys. **4**, 1093–1100 (2002)
- Stearns, J.A., Mercier, S., Seaiby, C., Guidi, M., Boyarkin, O.V., Rizzo, T.R.: Conformationspecific spectroscopy and photodissociation of cold, protonated tyrosine and phenylalanine. J. Am. Chem. Soc. 129, 11814–11820 (2007)
- 19. Nolting, D., Marian, C., Weinkauf, R.: Protonation effect on the electronic spectrum of tryptophan in the gas phase. Phys. Chem. Phys. 6, 2633–2640 (2004)
- Talbot, F.O., Tabarin, T., Antoine, R., Broyer, M., Dugourd, P.: Photodissociation spectroscopy of trapped protonated tryptophan. J. Chem. Phys. 122, 074310 (2005)
- Serrano-andres, L., Roos, B.O.: Theoretical study of the absorption and emission spectra of indole in the gas phase and in a solvent. J. Am. Chem. Soc. 25, 185–195 (1996)
- 22. Gindensperger, E., Haegy, A., Daniel, C., Marquardt, R.: Ab initio study of the electronic singlet excited-state properties of tryptophan in the gas phase: the role of alanyl side-chain conformations. Chem. Phys. **374**, 104–110 (2010)
- 23. Blancafort, L., González, D., Olivucci, M., Robb, M.A.: Quenching of tryptophan 1 (π , π *) fluorescence induced by intramolecular hydrogen abstraction via an aborted decarboxylation mechanism. J. Am. Chem. Soc. **124**, 6398–6406 (2002)
- Grégoire, G., Jouvet, C., Dedonder, C., Sobolewski, A.L.: Ab initio study of the excited-state deactivation pathways of protonated tryptophan and tyrosine. J. Am. Chem. Soc. 129, 6223–6231 (2007)
- 25. Grégoire, G., Jouvet, C., Dedonder, C., Sobolewski, A.L.: On the role of dissociative $(\pi, \sigma)^*$ states in the photochemistry of protonated tryptamine and tryptophan: an ab initio study. Chem. Phys. **324**, 398–404 (2006)
- 26. Hattig, C.: Geometry optimizations with the coupled-cluster model CC2 using the resolution identity approximation. J. Chem. Phys. **118**, 7751–7761 (2003)
- 27. TURBOMOLE V6.2 2011, a development of U. of K. and; Forschungszentrum Karlsruhe GmbH, 1989–2007; TURBOMOLE GmbH, since 2007. http://www.turbomole.com
- 28. Kang, H., Jouvet, C., Dedonder-Lardeux, C., Martrenchard, S., Gregoire, G., Desfrancois, C., Schermann, J.P., Barat, M., Fayeton, J.A.: Ultrafast deactivation mechanisms of protonated aromatic amino acids following UV excitation. Phys. Chem. Chem. Phys. 7, 394–398 (2005)
- 29. Jochims, H.W., Baumgärtel, H., Leach, S.: Photoionization quantum yields of polycyclic aromatic hydrocarbons. Astron. Astrophys. **314**, 1003–1009 (1996)
- Andersen, J.U., Cederquist, H., Forster, J.S., Huber, B.A., Hvelplund, P., Jensen, J., Liu, B., Manil, B., Maunoury, L., Nielsen, S.B., Pedersen, U.V., Rangama, J., Schmidt, H.T., Tomita, S., Zettergren, H.: Photodissociation of protonated amino acids and peptides in an ion storage ring. Determination of Arrhenius parameters in the high-temperature limit. Phys. Chem. Chem. Phys. 6, 2676–2681 (2004)
- Lepere, V., Lucas, B., Barat, M., Fayeton, J.A., Picard, Y.J., Jouvet, C., Çarçabal, P., Nielsen, I.B., Dedonder-Lardeux, C., Grégoire, G., Fujii, M.: Characterization of neutral fragments issued from the photodissociation of protonated tryptophane. Phys. Chem. Chem. Phys. 9, 5330–5334 (2007)

- Lepere, V., Lucas, B., Barat, M., Fayeton, J.A., Picard, Y.J., Jouvet, C., Çarçabal, P., Nielsen, I.B., Dedonder-Lardeux, C., Grégoire, G., Fujii, M.: Comprehensive characterization of the photodissociation pathways of protonated tryptophan. J. Chem. Phys. 127, 134313 (2007)
- Grégoire, G., Lucas, B., Barat, M., Fayeton, J.A., Dedonder-Lardeux, C., Jouvet, C.: UV photoinduced dynamics in protonated aromatic amino acid. Eur. Phys. J. D 51, 109–116 (2009)
- 34. Kang, H., Dedonder-Lardeux, C., Jouvet, C., Martrenchard, S., Grégoire, G., Desfrançois, C., Schermann, J.-P., Barat, M., Fayeton, J.A.: Photo-induced dissociation of protonated tryptophan TrpH+: a direct dissociation channel in the excited states controls the hydrogen atom loss. Phys. Chem. Chem. Phys. 6, 2628–2632 (2004)
- Mercier, S.R., Boyarkin, O.V., Kamarioti, A., Guglielmi, M., Tavernelli, I., Cascella, M., Rothlisberger, U., Rizzo, T.R.: Microsolvation effects on the excited-state dynamics of protonated tryptophan. J. Am. Chem. Soc. 128, 16938–16943 (2006)
- Boyarkin, O.V., Mercier, S.R., Kamariotis, A., Rizzo, T.R.: Electronic spectroscopy of cold protonated tryptophan and tyrosine. J. Am. Chem. Soc. 128, 2816–2817 (2006)
- 37. Rogalewicz, F., Hoppilliard, Y., Ohanessian, G.: Fragmentation mechanisms of alpha-amino acids protonated under electrospray ionization: a collisional activation and ab initio theoretical study. Int. J. Mass Spectrom. **195–196**, 565–590 (2000)
- 38. Lioe, H., O'Hair, R.A.J., Reid, G.E.: Gas phase ion chemistry of biomolecules. Part 37 Gasphase reactions of protonated tryptophan. J. Am. Soc. Mass Spectrom. **15**, 65–76 (2004)
- Grewal, R.N., El Aribi, H., Harrison, A.G., Siu, K.W.M., Hopkinson, A.C.: Fragmentation of protonated tripeptides: the proline effect revisited. J. Phys. Chem. B 108, 4899–4908 (2004)
- El Aribi, H., Orlova, G., Rodriquez, C.F., Almeida, D.R.P., Hopkinson, A.C., Siu, K.W.M.: Fragmentation mechanisms of product ions from protonated tripeptides. J. Phys. Chem. B 108, 18743–18749 (2004)
- Lucas, B., Barat, M., Fayeton, J.A., Perot, M., Jouvet, C., Grégoire, G., Brøndsted Nielsen, S.: Mechanisms of photoinduced C-alpha-C-beta bond breakage in protonated aromatic amino acids. J. Chem. Phys. 128, 164302 (2008)
- Svendsen, A., Lorenz, U.J., Boyarkin, O.V., Rizzo, T.R.: A new tandem mass spectrometer for photofragment spectroscopy of cold gas-phase molecular ions. Rev. Sci. Instrum. 81, 073107 (2010)
- Wang, Y.S., Tsai, C.H., Lee, Y.T., Chang, H.C., Jiang, J.C., Asvany, O., Schlemmer, S., Gerlich, D.: Investigations of protonated and deprotonated water clusters using a low-temperature 22-pole ion trap. J. Phys. Chem. A 107, 4217–4225 (2003)
- 44. Wang, X.-B., Wang, L.-S.: Development of a low-temperature photoelectron spectroscopy instrument using an electrospray ion source and a cryogenically controlled ion trap. Rev. Sci. Instrum. 79, 073108 (2008)
- 45. Choi, C.M., Choi, D.H., Kim, N.J., Heo, J.: Effective temperature of protonated tyrosine ions in a cold quadrupole ion trap. Int. J. Mass Spectrom. 314, 18–21 (2012)
- Fujihara, A., Matsumoto, H., Shibata, Y., Ishikawa, H., Fuke, K.: Photodissociation and spectroscopic study of cold protonated dipeptides. J. Phys. Chem. A 112, 1457–1463 (2008)
- Fujihara, A., Noguchi, N., Yamada, Y., Ishikawa, H., Fuke, K.: Microsolvation and protonation effects on geometric and electronic structures of tryptophan and tryptophan-containing dipeptides. J. Phys. Chem. A 113, 8169–8175 (2009)
- 48. Rode, M., Sobolewski, A.L., Dedonder, C., Jouvet, C., Dopfer, O.: Computational study on the photophysics of protonated benzene. J. Phys. Chem. A 113, 5865–5873 (2009)
- 49. PGOPHER, a program for simulating rotational structure. C. M. Western, University of Bristol. http://pgopher.chm.bris.ac.uk
- 50. Send, R., Kühn, M., Furche, F.: Assessing excited state methods by adiabatic excitation energies. J. Chem. Theory Comput. 7, 2376–2386 (2011)
- Grace, L.I., Cohen, R., Dunn, T.M., Lubman, D.M., De Vries, M.S.: The R2PI spectroscopy of tyrosine: a vibronic analysis. J. Mol. Spectrosc. 215, 204–219 (2002)

180 C. Dedonder et al.

 Grégoire, G., Kang, H., Dedonder-Lardeux, C., Jouvet, C., Desfrançois, C., Onidas, D., Lepere, V., Fayeton, J.: Statistical vs. non-statistical deactivation pathways in the UV photofragmentation of protonated tryptophan-leucine dipeptide. Phys. Chem. Chem. Phys. 8, 122–128 (2006)

- 53. Lucas, B., Barat, M., Fayeton, J.A., Jouvet, C., Çarçabal, P., Grégoire, G.: Statistical versus non-statistical photo-fragmentation of protonated GWG tri-peptide induced by UV excitation. Chem. Phys. **347**, 324–330 (2008)
- Kang, H., Dedonder-Lardeux, C., Jouvet, C., Grégoire, G., Desfrançois, C., Schermann, J.-P., Barat, M., Fayeton, J.A.: Control of bond-cleaving reactions of free protonated tryptophan ion by femtosecond laser pulses. J. Phys. Chem. A 109, 2417–2420 (2005)
- 55. Grégoire, G., Jouvet, C., Dedonder, C.: What is the meaning of lifetime measurement? http://hal.archives-ouvertes.fr/hal-00023586/fr/ (2006), 2-4
- 56. Fuke, K., Takasu, R., Misaizu, F.: Photoionization of hypervalent molecular clusters: electronic structure and stability of NH₄(NH₃)n. Chem. Phys. Lett. **229**, 597–603 (1994)
- 57. Park, J.K.: Stability of the Rydberg H₃O radical. Bull. Korean Chem. Soc. 20, 734–736 (1999)
- Alata, I., Dedonder, C., Broquier, M., Marceca, E., Jouvet, C.: Role of the charge-transfer state in the electronic absorption of protonated hydrocarbon molecules. J. Am. Chem. Soc. 132, 17483–17489 (2010)
- Rodriquez, C.F., Cunje, A., Shoeib, T., Chu, I.K., Hopkinson, A.C., Siu, K.W.M.: Proton migration and tautomerism in protonated triglycine. J. Am. Chem. Soc. 123, 3006–3012 (2001)
- Nagornova, N.S., Rizzo, T.R., Boyarkin, O.V.: Highly resolved spectra of gas-phase gramicidin S: a benchmark for peptide structure calculations. J. Am. Chem. Soc. 132, 4040–4041 (2010)
- 61. Poulain, P.: Structure et dynamique de proteines isolees: approches statistiques. PhD Universite Claude Bernard -Lyon 1 (2006)
- Nolting, D., Schultz, T., Hertel, I.V., Weinkauf, R.: Excited state dynamics and fragmentation channels of the protonated dipeptide H₂N-Leu-Trp-COOH. Phys. Chem. Chem. Phys. 8, 5247–5254 (2006)

UV Photophysics of DNA and RNA Nucleotides *In Vacuo*: Dissociation Channels, Time Scales, and Electronic Spectra

10

J. Mathias Weber, Jesse Marcum, and Steen Brøndsted Nielsen

Abstract

This chapter deals with the UV-induced fragmentation of mononucleotide and oligonucleotide ions isolated *in vacuo*. We review gas-phase photodissociation spectra of mononucleotides, single strands, double strands and quadruplexes, and compare these with the corresponding spectra in solutions to consider solvatochromic shifts. The role of multiple bases is considered within the Frenkel exciton model that describes the electronic coupling between two or more bases, which is relevant to understand photoexcitation. We discuss relaxation of the excited states and the time scales for nucleotide dissociation when there is no solvent quenching of the excess energy. Finally, the photophysical behaviour of DNA with respect to electron ejection will be discussed with an emphasis on the functional groups involved in electron loss.

10.1 Introduction

The photohysics of DNA is important for the understanding of deleterious processes that can ultimately cause skin cancer. Fortunately, this outcome of UV exposure of skin is relatively unlikely due to the high photostability of DNA with

J.M. Weber (\subseteq)

JILA and Department of Chemistry and Biochemistry, University of Colorado, Boulder, CO 80309-0440, USA

e-mail: weberjm@jila.colorado.edu

I Marcum

Department of Chemistry and Food Science, Framingham State University, 100 State Street, Framingham, MA 01701-9101, USA

S. Brøndsted Nielsen

Department of Physics and Astronomy, Aarhus University, Ny Munkegade 120, 8000 Aarhus C, Denmark

e-mail: sbn@phys.au.dk

respect to UV-induced reactions and the highly efficient repair mechanisms for DNA damage. In the prebiotic era, the protective stratospheric ozone layer had not yet developed, leading to high UV radiation flux on the surface of the young Earth. The high photostability of DNA and RNA must have been a key factor for the evolution of life and is in fact one of the reasons why DNA can be used to encode genetic information in the first place. It is the nucleobases (adenine, thymine, cytosine, guanine, and uracil) that absorb the UV light transmitted through the atmosphere, so it comes as no surprise that their photophysics has been studied extensively. Indeed, it has been realised that the particular chemical structures of DNA bases serve several roles: They account beautifully for DNA replication, RNA transcription and translation according to the specific pairing of bases (Watson-Crick base pairs) and the genetic code, and they are the reason for the extraordinary photostability of DNA, protecting against UV induced damage [1, 2]. Still, photoinduced modification of the bases through photodamage can lead to mutations which ultimately may compromise cell function and result in cell death or cancer.

Single bases absorb most strongly around 260 nm. The corresponding electronic transitions are due to excitations into π^* orbitals from either π orbitals (denoted as $\pi\pi^*$ transitions) or non-bonding orbitals (denoted as $\pi\pi^*$ transitions) [3–5]. The oscillator strength for $\pi\pi^*$ transitions is significantly higher than that for $\pi\pi^*$ transitions. Relaxation of excited electronic states can occur by internal conversion (IC) via conical intersections (where electronic potential energy surfaces touch) within a few hundred femtoseconds [1, 2, 6]. Consequently, fluorescence quantum yields are very small, 10^{-4} or less, and intersystem crossing to lower-lying triplet states is negligible [7]. Initially, vibrational energy resulting from the conversion of electronic excitation is deposited in the base, but intramolecular vibrational redistribution (IVR) is assumed to occur rapidly, followed by dissipation of the excess energy to surrounding water molecules within a few picoseconds. This scheme protects the molecules as the electronic excitation that generates transient reactive species is (mostly) converted to harmless heat.

The situation is more complicated for multichromophore DNA and RNA strands, where each base is connected to a furanose sugar and two sugars are linked by a negatively-charged phosphate group. The building blocks, each of which is composed of (at least) a nucleobase, a sugar and a phosphate group, are called nucleotides. In double strands, the distance between two adjacent bases is short (3.4 Å), and their aromatic rings are parallel, which leads to the interaction of their π -electron systems. Because the stacked bases are electronically coupled when photoexcited, deexcitation times can span tens of picoseconds to nanoseconds [8–10], and the energy is therefore not always distributed rapidly to the surrounding medium. The characteristics of the bright excited states, such as the number of bases that are collectively excited and the quantum dynamics involving dark charge-transfer states, have been much debated (see [11] and references therein for examples). The interbase electronic coupling depends on conformation and environmental perturbations, which makes theoretical descriptions inherently complicated. Whether such superposition states are actually of importance in the context of photoreactivity of nucleic acids and their protection from radiation damage is still an open question.

While the base (i.e., the chromophore) itself is not charged in its native state, a nucleic acid can be easily charged by deprotonation of phosphate groups, producing a nucleotide. In addition, protonated species can be produced at low pH values (<4). The focus of this chapter is on ionic systems isolated in vacuo that can be studied in experiments based on mass-spectrometry techniques. One motivation for gas-phase investigations is to shed light on the electronic properties and the energytransfer processes in DNA at the molecular level in the absence of perturbations from chemical environments (e.g., other biomolecules, solvent molecules or ions). The effect of water molecules can then be disentangled through comparisons with the behaviour of solutions. Also, since most excited-state calculations are performed on isolated molecules, gas-phase reference data are needed as benchmarks for electronic structure theory [12–16]. In particular, the description of multibase systems is nontrivial due to the electronic couplings between two or more bases in the excited state. Last but not least, gas-phase experiments on DNA strands are important for the understanding of bioanalytical techniques such as mass spectrometric sequencing of oligonucleotides. These techniques rely predominantly on collisional activation of electrosprayed DNA strands, but more recent approaches combine UV excitation with collisions to obtain better sequence coverage.

10.2 Photodissociation Mass Spectra and Fragmentation Mechanisms

Nucleotide ions can be conveniently prepared *in vacuo* by both electrospray ionisation (ESI) and matrix-assisted laser desorption/ionisation (MALDI). However, photodissociation experiments have been carried out mainly with ions starting from ESI sources [17–32], both as native anions and as cations in the form of protonated nucleic acids.

UV-excitation of DNA [26, 28] and RNA mononucleotides, abbreviated [M–H]⁻ (M = neutral mononucleotide, see also Table 10.1), as well as cyclic derivatives [27, 28] leads to the same fragments as those found in collision-induced dissociation (CID) experiments. The observed fragment ion masses are collected in Table 10.1.

Fragment ion species can be grouped into two general classes according to the primary fragmentation sites. The first group consists of products that are based on breaking the phosphate-sugar link, which results in the formation of PO_3^- and $H_2PO_4^-$. The second class involves fragments formed after cleavage of the relatively weak CN glycosidic bond between the nucleobase and sugar subunits and a number of subsequent reactions. Cleavage of this bond can result in formation of the deprotonated base, B^- (B = A, C, G, T), or an ion of the form [M–H–BH]⁻ that corresponds to the loss of neutral, intact base (BH) from the parent mononucleotide. Another fragment ion formed at lower abundance is the species [M–H–BH–H₂O]⁻, which is thought to arise from unimolecular dissociation of the primary fragment ion [M–H–BH]⁻ [33].

Table 10.1 Observed masses and assignments for mononucleotide photofragments (reproduced with permission from [28])

	;							
Parent [M-H]	dAMP		AMP		cAMP		dCMP	
Fragments	z/w	Assignment	z/m	Assignment	z/m	Assignment	z/m	Assignment
	79	PO ₃ -	79	PO_3^-	62	PO ₃ -	79	PO ₃ -
	76	$\mathrm{H_2PO_4}^-$	76	$\mathrm{H_2PO_4}^-$	ı	ı	76	$\mathrm{H_2PO_4}^-$
	134	A ⁻	134	A_	134	A_	ı	ı
	1	ı	139	See text	ı	I	ı	I
	151	See text	151	See text	ı	ı	ı	I
	177	$[M-H-BH-H_2O]^-$	193	$[M-H-BH-H_2O]^-$	175	$[M-H-BH-H_2O]^-$	177	$[M-H-BH-H_2O]^-$
	195	[M-H-BH]	211	[M-H-BH]	193	[M-H-BH]	195	[M-H-BH]
	M = M							
Parent [M-H]	dGMP	_	GMP		cGMP		dTMP	
Fragments	z/w	Assignment	z/m	Assignment	z/m	Assignment	z/m	Assignment
	62	PO ₃ -	79	PO ₃ -	79	PO ₃ -	62	PO ₃ -
	26	$\mathrm{H}_{2}\mathrm{PO}_{4}^{-}$	26	$\mathrm{H_2PO_4}^-$	26	$\mathrm{H_2PO_4}^-$	26	$\mathrm{H_2PO_4}^-$
	150	D	150	 	150	 	125	_L_
	ı	ı	ı	I	ı	I	I	ı
	ı	ı	151	See text	ı	ı	151	See text
	177	$[M-H-BH-H_2O]^-$	193	$[M-H-BH-H_2O]^-$	175	$[M-H-BH-H_2O]^-$	177	$[M-H-BH-H_2O]^-$
	195	[M-H-BH]	211	[M-H-BH]	193	[M-H-BH]	195	$[M-H-BH]^-$

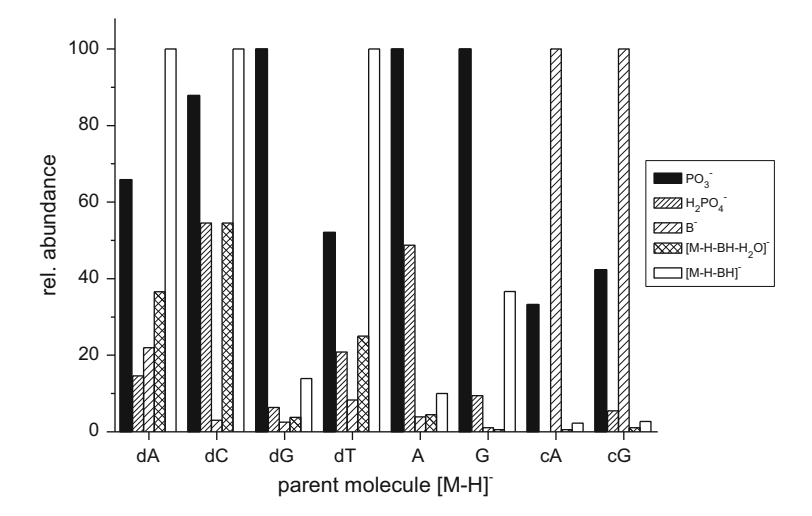


Fig. 10.1 Branching ratios for fragmentation channels of mononucleotide ions after photon absorption at 4.77 eV (dA), 4.28 eV (dC), 4.59 eV (dG), 4.77 eV (dT), and close to the peak absorbance for A, G, cA and cG [26, 27]

An additional fragment ion that is base-independent, but is not observed for all parent ions, has m/z = 151. This fragment was also found in CID experiments [34] but has not yet been identified. Its independence of the identity of the nucleobase indicates that it is a phosphate/sugar fragment. Finally, a fragment ion that was seen only for the parent ion [AMP–H]⁻, has m/z = 139 [27, 28, 31]. The low abundance of this ion, combined with the fact that it is not common to any other parent ion, suggests that it may not be of much significance. No assignment has been offered for this fragment ion so far.

Branching ratios for all fragment channels of all parent ions are summarised in Fig. 10.1 [26–28]. All observed fragmentation reactions would give rise to loss of genetic information. Cleavage of the CN glycosidic bond results in base loss, while phosphate-sugar bond cleavage corresponds to backbone fragmentation for oligonucleotides. Cleavage of the phosphate-sugar bond is particularly important for the mass-spectrometric determination of nucleotide sequence.

The fragment mass spectra of oligonucleotide anions following UV absorption have been studied by several groups [22, 24, 25, 30, 32, 35]. At photon energies around 4.7 eV and lower, photodetachment is the only observed decay process, but hybrid activation methods such as employing CID after UV photodetachment lead to dissociation with high fragmentation yield and good sequence coverage [22]. In contrast, UV excitation by 193-nm photons (6.42 eV) produces extensive fragmentation without any additional activation, again very similar to fragments from CID [30, 32, 35]. As we focus on the photophysics involving the lower-lying $\pi\pi^*$ and $\pi\pi^*$ excitation region here, we will refrain from a more detailed review of these higher energy UV fragmentations.

Scheme 10.1 H₂PO₄⁻ fragment formation [27]

Following excitation, most nucleotide fragmentation processes involve extensive molecular rearrangement. All fragment channels observed following UV excitation are also observed upon the activation of gas-phase nucleotides and oligonucleotides using a number of other activation methods including CID, infrared multiphoton dissociation (IRMPD), post-source decay (PSD) and blackbody infrared radiative dissociation (BIRD) [36–40]. Many of these methods involve thermal excitation of the parent ions, suggesting that direct bond cleavage from an electronically excited state does not occur, and the molecule instead fragments due to a large amount of vibrational energy.

Work in both the condensed phase and *in vacuo* indicates that nucleobases and nucleotides may undergo fast internal conversion through conical intersections via ring-puckering motion leading to pyramidalisation of the base geometry to reach a vibrationally excited ground electronic state [1, 6, 17, 18, 41]. This is in agreement with the interpretation that nucleotides undergo fragmentation on the electronic ground-state surface. The electronic energy that is converted into vibrational energy in the molecule (up to 5.8 eV in the experiments by Marcum et al. [26–28]) can then be used to induce unimolecular fragmentation. Only the deprotonated base anion, B⁻, could in principle result from direct heterolytic bond cleavage on a repulsive curve in an excited electronic state. While this is generally viewed as an unlikely possibility, there are no experimental data suited to completely exclude this process, even though the majority of B⁻ ions produced are probably generated by "thermal" decay from vibrationally hot ions in the electronic ground state [29].

In general, the molecular level details of the fragmentation mechanisms are not well understood. Ho and Kebarle [42] used CID under single-collision conditions to dissociate mononucleotide parent ions and determined threshold enthalpies for the various fragment channels, comparing them with threshold enthalpies from semi-empirical calculations and transition-state theory. Based on these data, they proposed fragmentation mechanisms for the major fragment channels. They suggested that $H_2PO_4^-$ fragment formation occurs as the phosphate group abstracts a proton from the 4' carbon of the sugar in an E2-type elimination (see Scheme 10.1). The proposed mechanism for PO_3^- generation is transfer of a proton from a phosphate OH group to the phosphoric acid ester oxygen with concomitant PO bond cleavage (see Scheme 10.2). These mechanisms are now generally accepted and are in accord with many processes assumed to be active in nucleotide backbone cleavage [43].

Scheme 10.2 PO₃⁻ fragment formation [27]

Scheme 10.3 Glycosidic CN bond cleavage with formation of a reactive encounter complex [27]

The processes underlying the formation of fragments based on glycosidic bond cleavage are not as clear. Based on work by Rodgers et al. [44], Ho and Kebarle [42] proposed a mechanism involving proton transfer from the 2' carbon of the sugar to the phosphate group (see Scheme 10.3) concomitant with the loss of the base in an E2-type elimination process. The B⁻ ion formed in this way forms a weakly-bound encounter complex with the phosphate-sugar fragment. This complex can subsequently dissociate forming B⁻ fragment ions, or a second proton transfer step may occur prior to dissociation of the complex, resulting in BH fragments and [M–H–BH]⁻ fragment ions where the negative charge is on the phosphate-sugar fragment.

All non-cyclic mononucleotides exhibit very low abundances of B^- fragments [26–28], while B^- is the dominant fragment for cyclic mononucleotides [27, 28] (see Fig. 10.1). The reason for this behaviour is probably a small survival chance for the B^- anions in the presence of sufficiently acidic protons, as proton transfer to B^- will result in the formation of [M–H–BH] $^-$ fragment ions and neutral BH. This is consistent with the complete absence of C^- ions from UV photodissociation of [dCMP-H] $^-$ parent ions [26] as the proton affinity of C^- is ca. 0.4 eV higher than those of the other bases, which are within 0.1 eV of each other [26, 45, 46].

In cyclic nucleotides, the phosphate group has two phosphate ester bridges to the furanose ring (see Fig. 10.2). These two connections hinder formation of phosphate-based products as well as the conformational rearrangement necessary for the E2-mechanism that leads to glycosidic bond cleavage. As mentioned above,

Fig. 10.2 Structures of adenosine cyclic-3',5'-monophosphate (*left*) and guanosine cyclic-3',5'-monophosphate (*right*)

formation of B⁻ was found to be the dominant fragmentation process for the cyclic mononucleotides. This presents several questions as to the mechanisms that are involved. If the previously proposed E2-type mechanism (Scheme 10.3) is still at play, one of the two phosphoric acid ester bridges must be broken first to allow glycosidic bond cleavage and concomitant proton transfer. In addition, the observed formation of PO₃⁻ and H₂PO₄⁻ fragments means that at least two bonds between the phosphate and sugar groups must be cleaved. If one of the phosphate ester bridges is first broken so that the phosphate group can participate in an E2-type reaction, the preference of B⁻ loss over BH could be explained by the smaller number of acidic protons available for transfer to the nucleobase in cyclic nucleotides. Alternative mechanisms are discussed in more detail in [27, 28], but no single reaction scheme can consistently explain all observations, similar to the complex processes encountered in CID [43].

10.3 Time Scales for Dissociation

An interesting question is whether or not photoproduct formation, as described in the preceding section, can compete with relaxation by energy transfer to solvent when the nucleotide is solvated. If prompt dissociation processes are possible, they would be hazardous to biological systems. However, if dissociation occurs on long time scales, the more rapid energy transfer to solvent (typically within a few picoseconds [1]) will most likely preclude significant amounts of fragmentation. Thus, to determine whether or not fragmentation is important in biological systems, it is necessary to switch off energy dissipation to the solvent and elucidate the intrinsic dissociation times of nucleotides so that they can be compared to time scales for other relaxation mechanisms. Measurement of such intrinsic dissociation timescales can be accomplished in vacuo using mass spectrometric experiments. We note that the measurement of decay times on the scale of 10^{-8} to 10^{-3} s is difficult, since they are too long for typical optical delay line techniques and too short to employ ion trapping approaches, e.g., in Paul traps or Fourier-transform ion-cyclotron resonance mass spectrometers. Such experiments are best performed using ion optical approaches and ion storage devices (see, e.g., [47-50]).

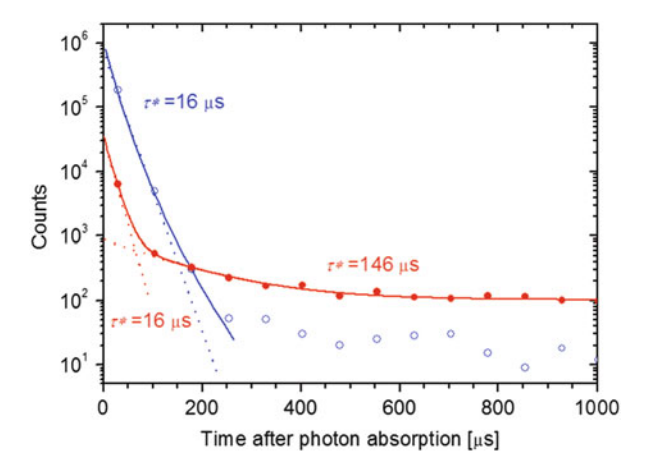


Fig. 10.3 The yield of neutral fragments *versus* time after photoexcitation of AMP anions and cations with 266-nm light in an electrostatic ion storage ring. The time between each point corresponds to the revolution time in the ring. Photoexcited anions dissociate with a time constant of 16 μ s; at very long times (milliseconds) and longer the decay is due to collision-induced dissociation in the ring. Photoexcited cations dissociate with two time constants of 16 μ s and 146 μ s; the short time constant was established from experiments where the ions were excited at different places in the ring. Taken from [17]. Copyright 2003 by The American Physical Society

The first experiments to investigate the intrinsic time scale of nucleotide photofragmentation were performed on the storage ring ELISA in 2003 by Brøndsted Nielsen and co-workers [17]. Photoexcitation of adenosine 5'-monophosphate anions ([AMP+H]⁺) and cations ([AMP+H]⁺) with 266-nm light led to dissociation on the microsecond time scale (see Fig. 10.3). Dissociation time constants were approximately 16 µs for both anions and cations. This finding implies that "thermal" fragmentation of the isolated ions occurs on a much slower time scale than vibrational relaxation in solution, despite the fact that a single UV photon heats the molecule to a temperature equivalent of more than 1,000 K. Furthermore, these comparatively long timescales imply that photodissociation occurs via predominately statistical processes, meaning that dissociation could be accounted for by rate constant expressions derived from statistical methods such as Rice-Ramsperger-Kassel-Marcus (RRKM) and Arrhenius-like models. Interestingly, a larger dissociation time constant of 146 µs was found for the cations in addition to the initial faster decay (see Fig. 10.3). This longer time constant may be due to a different fragmentation channel or even the formation of long-lived triplet states (which is thought to be negligible for processes in solution [7]); it should be noted, however, that the importance of this channel is much less than 1 %. At present, there is no experimental evidence to pinpoint the origin of this longer decay time.

The storage-ring technique only allows for determination of the time scale for slow processes. However, indirect measurements indicate that, while decay on the µs time scale is dominant for the anions, such slow decay processes can only account for a minor fraction of the observed cation fragments. This conclusion

was based on comparisons of the total ion beam depletion with a statistical decay model. The total beam depletion for the anions was essentially explained by completely statistical decay, while for the cations the ion beam depletion due to statistical decay was less than 1 % of the total. Similarly, for singly-protonated DNA dinucleotides (dA₂, dG₂, and dC₂) where light is absorbed by either a protonated or a neutral base, only 2-3 % of the ions decayed statistically after 260-nm photoexcitation [21]. Interestingly, in the case of protonated dT₂, the propensity of statistical decay is higher (10 %), which is attributed to the lower proton affinity of thymine compared to the other bases, and that the phosphoric acid group can compete with the thymine base for the excess proton. In this picture, a protonated-base nucleotide is more prone to prompt dissociation than a neutral one. For deprotonated dinucleotides (dA₂ and dT₂) where both bases are neutral, about 20 % of the decay could be accounted for by statistical dissociation, which is much less than that seen for the mononucleotide. The reason for this is unclear. Experiments were also carried out on a series of singly-protonated DNA homopolymers of adenine (dA₂, dA₃, dA₄, and dA₅) using 266-nm light [19]. Here the importance of nonstatistical dissociation decreased with the size of the oligonucleotide or, in other words, with the number of neutral adenines. Taken together, the overall picture is that photoexcitation of neutral bases causes more dissociation on a long time scale (microseconds) than photoexcitation of protonated bases does.

Additionally, we note that calculations by Brøndsted Nielsen and Sølling [18] on neutral and protonated adenine indicate that the conical intersection between the S_1 and S_0 states reached after out-of-plane deformation is located significantly lower in energy for the cation than for the neutral, which may provide an explanation for the very different photodissociation chemistry of nucleotide anions and cations. Femtosecond pump-probe experiments by Nolting et al. [51] on protonated adenine, monitoring fragment ion formation as a function of time, revealed that internal conversion takes place in less than 161 fs for protonated adenine, but that it takes place on longer time scales (picoseconds) for neutral adenine, as reported by others [52, 53]. This difference was ascribed to the intermediate $n\pi^*$ state that is spectroscopically not accessible for the cation, and that traps the excited-state population in the neutral adenine case. It is possible that the lack of this intermediate trapping state leads to population of a repulsive electronic curve, which could explain the increase in non-statistical decay with the size of the nucleotide [19]. However, this is a hypothesis that remains to be tested more thoroughly.

To further explore the occurrence of rapid dissociation processes, Andersen and co-workers in Aarhus [31] and Fayeton and co-workers in Orsay [29] performed photoexcitation experiments on AMP and dAMP nucleotide anions, respectively, in an electric field and using time-of-flight mass spectrometry. After light absorption, the ions would spend up to one hundred nanoseconds in the electric field. Fragment ions formed within this field have different energies and velocities than those formed outside of the field. By simply measuring the arrival times of the neutral fragments to the detector, the groups could disentangle rapid dissociation from slow, statistical dissociation. The Orsay group observed, in addition to neutral fragments, ionic fragments formed in coincidence [29]. An electrostatic analyser

was used for mass analysis of the ions. Andersen and co-workers found that [AMP-H] anions dissociate with two different time constants of 95 ns and 2.4 µs, with branching ratios of 54 % and 46 %, respectively [31]. The 2.4-us time constant is likely associated with statistical dissociation, although it is significantly shorter than that measured at ELISA (16 µs) [17]. It is difficult to explain this behaviour unless the internal energy distributions of the ion populations are different in the two experiments. Also, the 94-ns decay is hard to reconcile with the results from the ELISA experiment, where decay was observed to be predominantly on the microsecond time scale. The authors exclude the possibility of two-photon absorption based on measurements of the yield of photoneutrals as a function of laser power. However, such a conclusion is difficult to draw if there are too few ions in the interaction region. Indeed, Fayeton and co-workers [29] found no such short lifetime component for the similar [dAMP-H] anion using 263-nm light. Instead, they found that all dissociation took place with a time constant of 1 µs, which is not substantially different than the 2.4-µs constant measured by Andersen and co-workers but is significantly shorter than that obtained from the ELISA experiment. In the case of [AMP+H]⁺ cations, Andersen and co-workers [31] found two short dissociation times of 85 ns and 640 ns, which would both be too short to be measured in the delayed dissociation experiment at ELISA and are therefore in accordance with the conclusion from the beamdepletion results [17]. On the other hand, these times are much longer than expected for dissociation from electronically excited states as well as after IC but prior to IVR. However, we caution that this result does not exclude prompt bond ruptures since the ionic fragment and the neutral fragment may stick together as a long-lived, ionmolecule encounter complex. Such complexes are often formed and may dissociate on time scales of up to tens of nanoseconds [54]. The only way to fully exclude prompt fragmentation would be to perform pump-probe experiments on the same time scale as the initial energy conversion processes (i.e., the 10^{-13} to 10^{-11} s time scale). More work is clearly needed to fully understand the different results obtained from various experimental setups. In this regard, storage-ring experiments with shorter revolution times of about five microseconds would be valuable.

Brøndsted Nielsen and co-workers [19] also performed lifetime experiments on singly deprotonated DNA homopolymers of adenine, dA₂, dA₃, and dA₄ (all with one deprotonated phosphate group) and on doubly deprotonated dA₄ (two deprotonated phosphate groups). Decay curves obtained after photoexcitation at 210 nm and 250 nm are shown in Fig. 10.4. The decay behaviour of dA₂ and dA₃ is ascribed to one-photon absorption, while that of dA₄ is due to two-photon absorption. Not surprisingly, the decay is faster at the higher photon energy, being complete within half a millisecond at 210 nm and about 2.5 ms at 250 nm for the dA₂ anion. It is noteworthy that, even with 210-nm light (5.9 eV) where the photon energy is above the adiabatic electron detachment energies (5.72 eV and 5.62 eV for dA₂ and dA₃ monoanions, respectively [55]), delayed dissociation is still observed. This indicates that internal conversion back to the ground state is quick enough to compete with the crossing from the electronically excited state to a state in the electron detachment continuum, where an electron is liberated. Unfortunately, the measurement did not provide direct information on the branching ratio between the two deexcitation

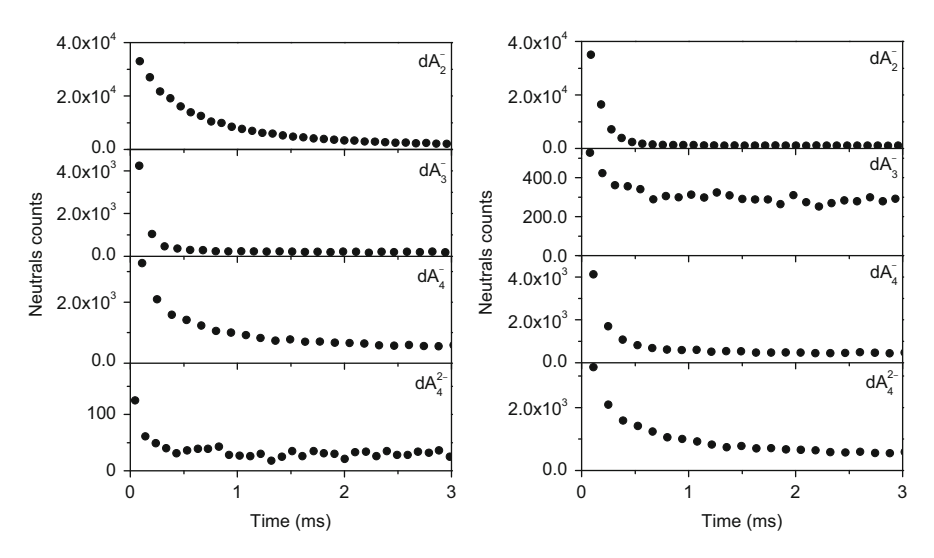


Fig. 10.4 Decay curves of $[dA_n-H]^-$ (n=2,3, and 4) and $[dA_4-2H]^{2-}$ anions after 250-nm (**a**) and 210-nm (**b**) photoexcitation. The decay is due to the absorption of one photon for n=2 and two photons for n=3,4. Reprinted with permission from [19]. Copyright 2012, American Institute of Physics

schemes. In line with the observed competition between detachment and relaxation, Gabelica et al. [24] found that there were two deexcitation pathways following 260-nm excitation of DNA multianions, one involving IC and subsequent dissociation and the other being electron detachment. However, a repulsive Coulomb barrier present in the multianions can hinder electron detachment (which would require electron tunnelling through the barrier), causing IC to be a more favourable process. Furthermore, it is also possible that dissociation of the radical anions can occur following electron detachment. For more discussion on the competition between electron detachment and internal conversion, we refer to Chap. 5 by Andersen and Bochenkova.

Finally, we note that, by comparing the time scales for dissociation (tens of μs) and solvent cooling (ca. 10 ps), one can estimate a quantum yield of ca. 10^{-6} for "thermal" dissociation of nucleotides in the condensed phase, which could still lead to low levels of DNA photodamage. Of course, it is likely that solvent reorientation for such large molecules would be the rate-limiting step for condensed-phase fragmentation, which would slow this process even further, rendering photodamage by vibrational predissociation an even rarer event.

10.4 Optical Properties of Nucleotides In Vacuo: Action Spectra

The difference in absorption between single bases and oligonucleotides containing stacked bases is limited [19, 26], which at first seems to indicate that the bases do not electronically couple in the excited states. In the case of electronic coupling

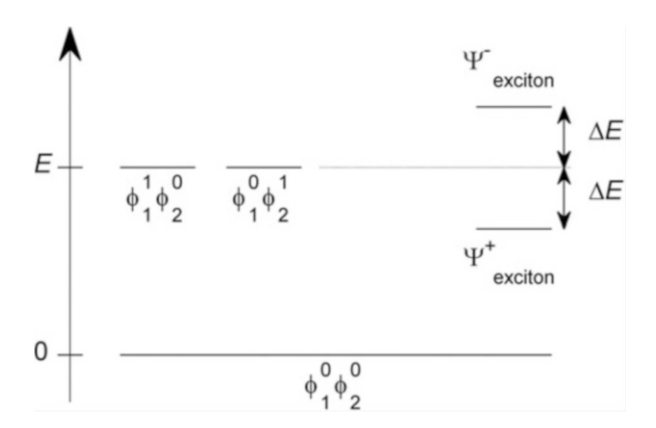


Fig. 10.5 Energy level diagram for two adjacent identical bases. *Left*: No coupling between the bases. $\varphi_m^{\ \ i}$ is the *i*th excited state (0 = ground state and 1 = first excited state) of the *m*th base (1 or 2). *Right*: Exciton coupling resulting in two exciton states, $\Psi_{exciton}^{\pm} = \frac{1}{\sqrt{2}} \left(\phi_1^0 \phi_2^1 \pm \phi_1^1 \phi_2^0 \right)$. The two bases are collectively excited, *i.e.*, they share the excitation energy between them. The oscillator strengths for the two exciton states are often different. Adapted from [11]. Copyright 2013, Royal Society of Chemistry

between two bases, there will be two excited-state wavefunctions that can be approximated by linear combinations of the two wavefunctions from the uncoupled bases. This is illustrated in Fig. 10.5. In the absence of coupling, either base 1 or base 2 is excited and the other is in its electronic ground state. In this particular example, the individual excitation energies are the same, E. Coupling results in new eigenfunctions of the excited states that consist of in-phase and out-of-phase superpositions of the uncoupled eigenstates (denoted Frenkel exciton states). These new eigenstates are split by $2\Delta E$, where ΔE is the energy difference between the energies of the coupled and uncoupled states. As a result, the absorption spectrum is expected to broaden, but a splitting of the characteristic absorption band measured at 260 nm for solvated DNA is not observed.

Nevertheless, calculations of DNA excited states [12–16, 56–61] have all indicated significant electronic coupling between stacked bases, and that the length of the exciton could extend over several bases. However, the change in absorption is limited when compared to the absorption by monomer bases. Thus, Markovitsi and co-workers [58] performed calculations on (dA)₂₀:(dT)₂₀ model duplexes and found that higher-energy exciton states carry larger oscillator strengths than lower ones, which causes only a small blueshift (3 nm) in the absorption when compared to that of the monomers. In other work, calculations by Lange and Herbert [16] indicated that adenine monomers assembled in a B-DNA configuration should display a slight blueshift and a red tail relative to isolated monomers (see Fig. 10.6). Recent theoretical work by Markovitsi, Improta and co-workers on two to five stacked adenines in a B-DNA configuration support these conclusions [62].

It should be kept in mind that intra- and inter-strand microenvironments of the bases in aqueous solution differ, which may cause an inhomogeneous broadening of the absorption band and, as a result, make it hard to identify slightly blue-shifted

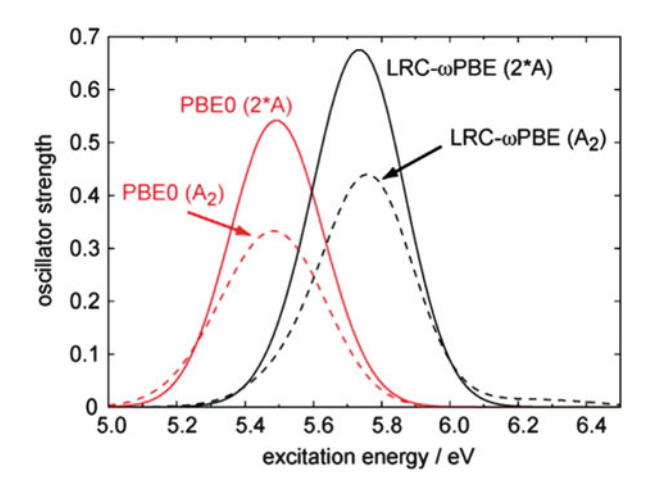


Fig. 10.6 Calculated absorption spectra of the adenine monomer (*solid curves*, two non-interacting monomers labelled as "2*A") and the adenine dimer in the canonical B-DNA geometry (*broken curves*). A 0.3-eV Gaussian broadening was applied to the gas-phase vertical excitation energies that were weighted by their respective oscillator strengths. Reprinted with permission from [16]. Copyright 2009 American Chemical Society

exciton states. A way to avoid the complication of different base microenvironments is to do spectroscopy of isolated systems *in vacuo*.

The first gas-phase spectra of mononucleotides were published by Weber and co-workers [26–28] (see Fig. 10.7). Strictly speaking, these spectra do not represent the energy-dependent absorption cross section $\sigma_{abs}(E)$ as they were obtained measuring photodissociation. Therefore, they represent the absorption cross section multiplied by the photodestruction probability $p_d(E)$ (in ion depletion spectra) or multiplied by the fragmentation probability $p_f(E)$ for a specific fragment ion (in fragment action spectra). These probabilities are not constant across the spectrum and can lead to large variations of the fragment branching ratios for different energies. We note that these photodissociation spectra are still often referred to as absorption spectra in the literature. This terminology is only applicable in a very limited number of cases, e.g., for ion depletion spectra if all absorption events lead to the destruction of the parent ion with unit probability across the range of photon energies under study.

The photodissociation spectra for B = A, C, and T show a broad peak at photon energies below ca. 5.5 eV and increasing photodissociation cross sections at the high energy side of the window of observation for all fragments formed [26]. The latter is largely missing from the spectra of guanine-containing mononucleotides, probably because the next-higher absorption band for this base is at higher energies, outside of the accessible photon-energy range. The overall shape of the spectra is independent of the phosphate-sugar configuration [27], but depends on the threshold energies and survival probabilities of the fragment ions in different decay channels [26]. The shapes of the fragment spectra are very similar for the fragments

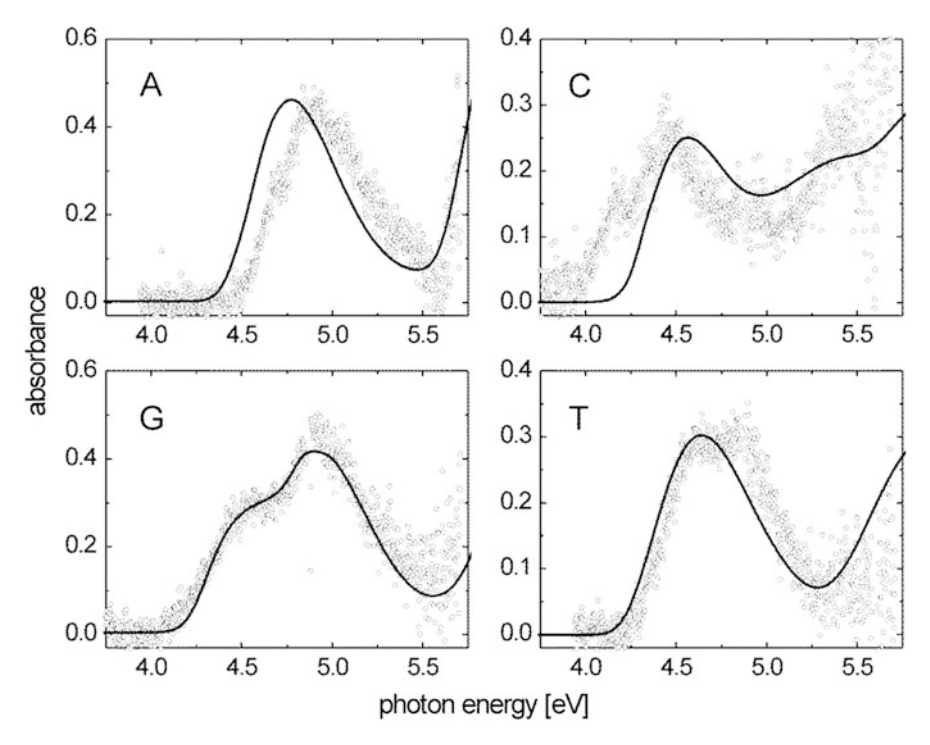


Fig. 10.7 Parent ion depletion spectra (*open circles*) and aqueous solution absorption spectra (*solid lines*) of the DNA mononucleotides (the base is indicated in each panel). Depletion data (in arbitrary units) have been normalised to the peaks of the aqueous solution absorption spectra in each case for easier comparison. Reprinted from [26]. Copyright 2009, Royal Society of Chemistry

belonging to the same parent ion in most cases [26–28]. Part of the spectral congestion observed is certainly due to the parent ions being at room temperature [63] but if the relaxation of the electronically excited state proceeds at sub-picosecond time scales [1, 18], lifetime broadening could play a role as well.

With these spectra at hand, it is now possible to elucidate the role of base-stacking effects from gas-phase spectroscopy of DNA strands. Brøndsted Nielsen and co-workers [19] studied small DNA homopolymers of adenine, and their fragmentation induced by photon absorption was monitored from the yield of neutral fragments formed as a function of time. An example for the spectrum of the [dA₄–H]⁻ anion is shown in Fig. 10.8 together with that of the [dAMP–H]⁻ mononucleotide. It is evident that the two have quite similar photodestruction spectra. The maximum of the strand spectrum is slightly blueshifted by 3 nm from the peak at 253 nm reported for [dAMP–H]⁻ anions, which is indicative of exciton coupling between interacting adenine bases. However, there is no tail to the red as predicted by Lange and Herbert [16]. It should be mentioned that the interpretation of the experimental results is complicated by the fact that different

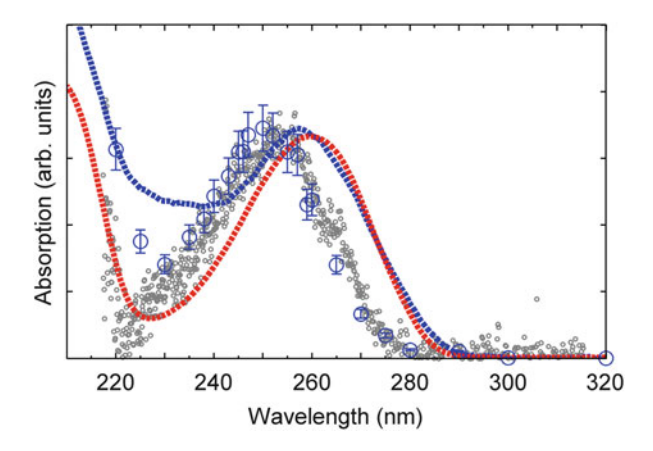


Fig. 10.8 UV spectra of dA_4 and dAMP in gas phase and aqueous solution. *Blue circles*: Ion-depletion spectrum of $[dA_4-H]^-$ anions *in vacuo* reproduced from [19]. *Grey points*: Ion-depletion spectrum of $[dAMP-H]^-$ anions *in vacuo* reproduced from [26]. *Blue curve*: Absorption spectrum of dA_4 in solution. *Red curve*: Absorption spectrum of dAMP in solution. Each spectrum is normalised to the band maximum at ca. 250 nm (gas phase) and ca. 260 nm (solutions). Reprinted from [11]. Copyright 2013, Royal Society of Chemistry

structural motifs of the strands in the ion beam are likely being sampled. For example, in the case of dinucleotides, Gidden and Bowers [64] identified three families of conformations from ion-mobility experiments, stacked, hydrogen-bonded, and open conformations (see representative examples on Fig. 10.9). However, the propensity of stacking is expected to increase with the number of bases for singly-charged strands. Nonetheless, even though theory and experiment seem to agree that the base–base interactions result in slightly blue-shifted absorption bands, more work is needed to better establish the details.

Next, we consider how solvation affects the spectra. The overall shapes of the absorption spectra of solutions of the disodium salts of mononucleotides are very similar to their gas-phase photodissociation spectra (see Fig. 10.7). The bands of the solution spectra exhibit small solvatochromic shifts of up to 0.22 eV [26] (about 10 nm in this wavelength range), a shift that is also seen for the adenine base itself [65]. In Fig. 10.8 the solution spectra of dAMP and dA₄ are included together with the gas-phase spectra for comparison. Solvation of the strand also causes a significant redshift of about 10 nm, but the red end of the absorption band is very similar in shape for the gaseous and the solvated ions. The valley on the high energy side of the band maximum is less deep in the gas-phase spectrum, which may be due to less overlap with the band with maximum below 210 nm. In solution, this band has a maximum at 190 nm. The data indicate that different environments of each adenine residue are less important for the band width compared to conformational disorder and vibrational broadening. The role played by individual water molecules on the absorption spectrum would be an interesting question for future studies monitoring the red-shift in absorption.

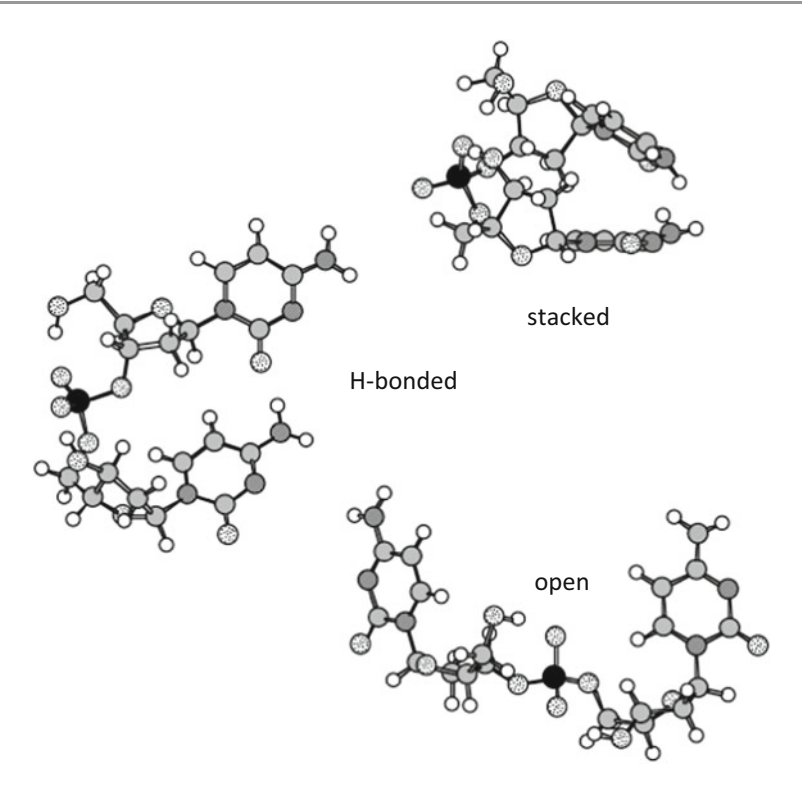
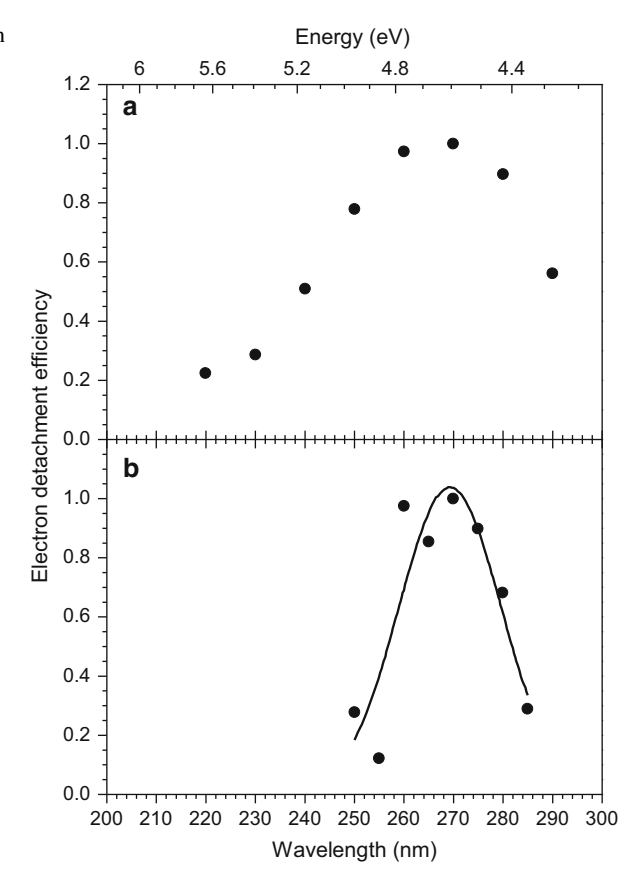


Fig. 10.9 Conformations of DNA dinucleotides, $[dB_2-H]^-$, can be represented by three families. Carbon is *grey*, oxygen *spotted*, nitrogen *striped*, hydrogen *white*, and phosphor *black*. Reproduced with kind permission from Springer Science + Business Media: [64], Figure 5

Gas-phase spectroscopy of larger multiply charged DNA oligonucleotide strands *in vacuo* has been studied by Gabelica et al. [22–24] based on electron detachment. They found that the neutral base is the site of detachment in agreement with the idea that the highest occupied molecular orbital (HOMO) is located on the base [55, 66, 67], and that guanine strands had the highest electron detachment yield in accordance with the fact that it has the lowest ionisation energy among the four canonical DNA bases. Importantly, plots of the electron detachment cross section as a function of excitation wavelength showed that highest values were obtained in the region of base absorption. This is illustrated for single-stranded $[dG_6-3H]^{3-}$ and double-stranded [dsC-5H]⁵⁻ in Fig. 10.10. These results indicate that the involved electronic states (resonance states) act as doorway states to the detachment continuum, and base excitation enhances electron detachment. In other work, Rosu et al. [25] used wavelength-dependent electron-detachment efficiencies to shed light on the difference in absorption by single strands, double strands and quadruplexes in vacuo. The systems chosen for study are shown in Fig. 10.11 together with the corresponding spectra. It is clearly evident that the duplexes and the quadruplex

Fig. 10.10 Relative electron photodetachment yield as a function of excitation energy for (a) $[dG_6-3H]^{3-}$ single strands (adapted with permission from [24]. Copyright 2007 American Chemical Society) and (b) $[dsC-5H]^{5-}$ double strands, $dsC = (5'-CGCGGGCCCGCG-3')_2$ (adapted with permission from [22]. Copyright 2006 American Chemical Society)



display red-shifted absorption bands compared to the single strands, which implies that such spectroscopy can be useful to obtain information on folding motifs.

No absorption spectra have been reported for protonated nucleotides or oligonucleotides. However, work has been done on protonated adenine (AdeH⁺) by Weinkauf and co-workers [68]. Their spectrum of the isolated ion *in vacuo* formed by electrospray ionisation is shown in Fig. 10.12. It was recorded from the yield of ions that had lost ammonia after photoexcitation in a Paul trap. The onset for absorption is red-shifted compared to that for neutral adenine by about 10 nm. After the smooth onset there is a broad band at higher energies. It is not possible to tell the band maximum as the scan did not extend over the whole absorption profile. The authors also calculated relative energies of the most important tautomers based on a combined density functional theory and multi-reference configuration interaction approach. The two lowest-energy structures are shown in Fig. 10.12. The associated S_1 state energies were calculated to provide vertical excitation energies. The best match between theory and experiment was obtained for the lowest-lying tautomer 1 but contributions from the tautomer 2 to the experimental spectrum could not be excluded. In other work by Cheong et al. [69], the 3 isomer was formed from

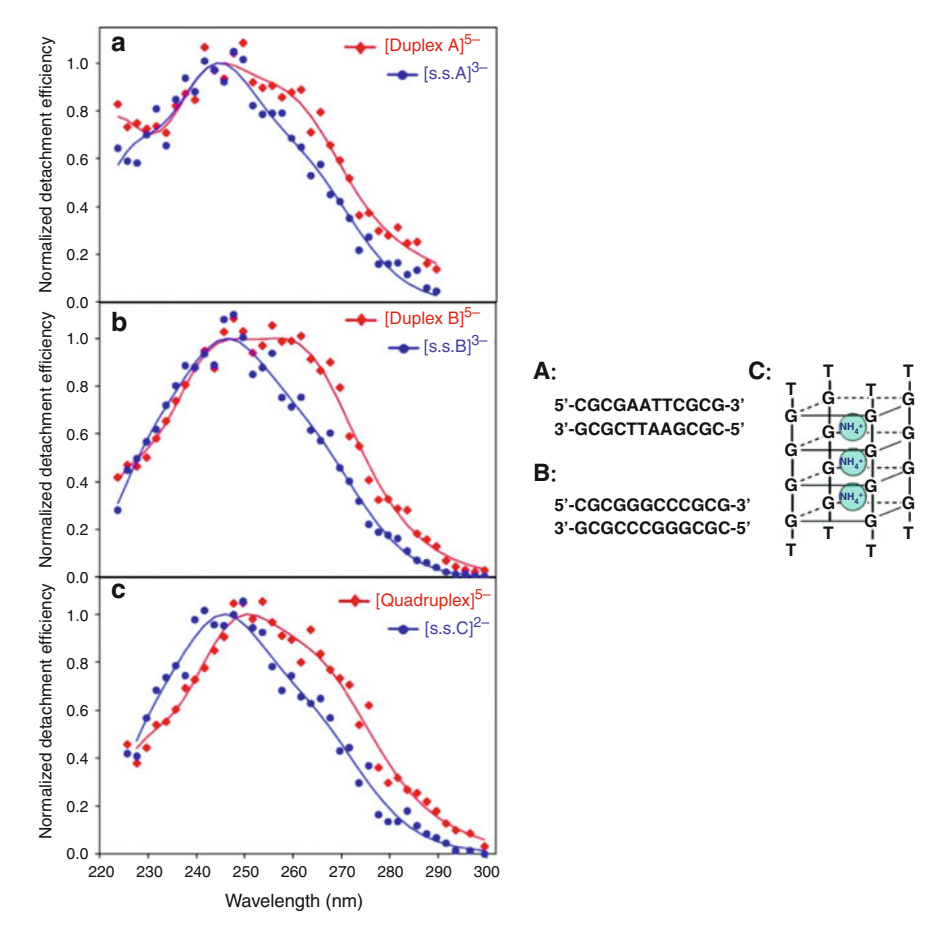


Fig. 10.11 Relative electron photodetachment yields as a function of excitation energy for (a) [dCGCGAATTCGCG–3H]³⁻ single strand (s.s.A) and the corresponding duplex⁵⁻ (duplex A); (b) [dCGCGGGCCCGCG–3H]³⁻ single strand (s.s.B) and duplex, and (c) [dTGGGGT–2H]²⁻ single strand (s.s.C), and G-quadruplex⁵⁻ (quadruplex). Reprinted with permission from [25]. Copyright 2012 American Chemical Society

dissociation of the adenine dimer after ionisation, and its action spectrum was found to be significantly redshifted compared to that reported by Weinkauf and co-workers (Fig. 10.12).

10.5 Photoelectron Spectroscopy of Nucleotide Anions

If the photon energy becomes greater than the binding energies of the most weakly bound electrons, electrons can be ejected from nucleotide anions. The photophysics of anionic mono- and oligonucleotides has been investigated by a number of

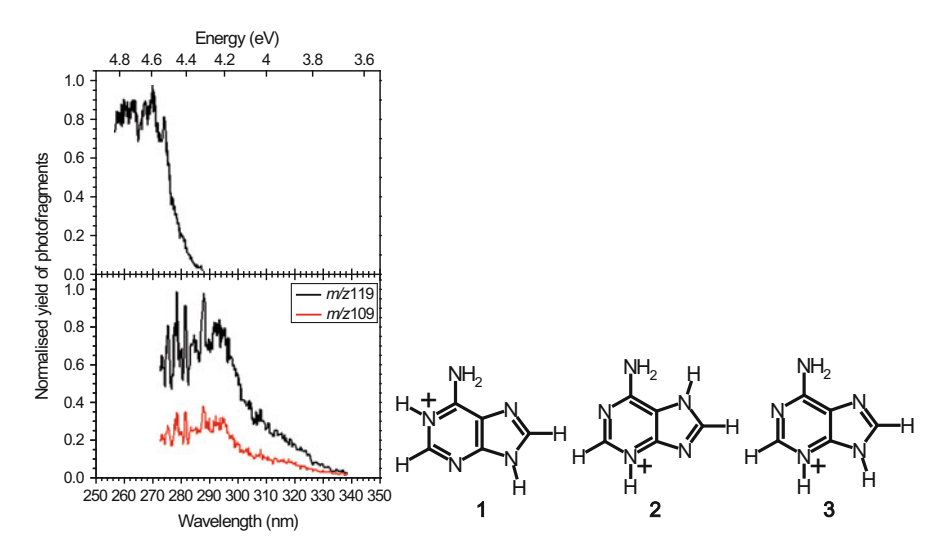
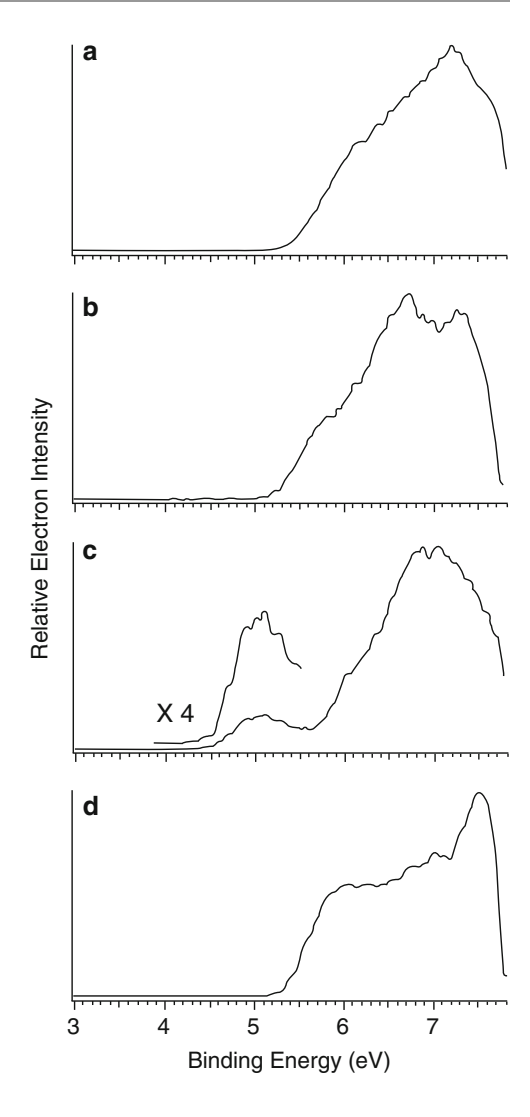


Fig. 10.12 *Left*: Gas-phase action spectra of protonated adenine (AdeH⁺). (a) AdeH⁺ (1) was formed by electrospray ionisation, and the fragment ion $(m/z \ 119)$ that had lost ammonia was sampled. Data taken from [68] (b) AdeH⁺ (3) was formed after ionisation of the adenine dimer. Spectra were obtained by monitoring either the m/z-119 fragment ion or the m/z-109 one (loss of HCN). The ratio between the yields of m/z-119 and m/z-109 ions is 2.5. Data taken from [69]. *Right*: The three lowest-energy tautomers of protonated adenine. 2 and 3 are higher in energy than 1 by 0.02 eV and 0.07 eV

groups. The photoelectron spectra of singly charged DNA nucleotide anions were first studied by Wang and co-workers [55]. The electron-binding energies in mononucleotides are slightly above 5 eV, except [dGMP–H] $^-$, which has an electron-binding energy ca. 0.7 eV lower than any of the others (see Fig. 10.13). Likewise, the presence of guanine in DNA di- and trinucleotides significantly lowers the electron-binding energies in these species. This indicates that the HOMO of guanine-containing nucleotide anions resides on the guanine base (in a π orbital) rather than on the phosphate group. Of the other di- and trinucleotides investigated by Wang and co-workers, only the singly charged [dA3–H] $^-$ ion shows features at similarly low binding energies, suggesting that adenine also has a propensity towards accommodating excess electrons. The low electron-binding energies of guanine-containing nucleotides are consistent with evidence from condensed-phase studies indicating that ionisation of DNA predominantly leads to holes localised on poly-G sequences (so-called guanine runs), particularly GGG [24, 70, 71].

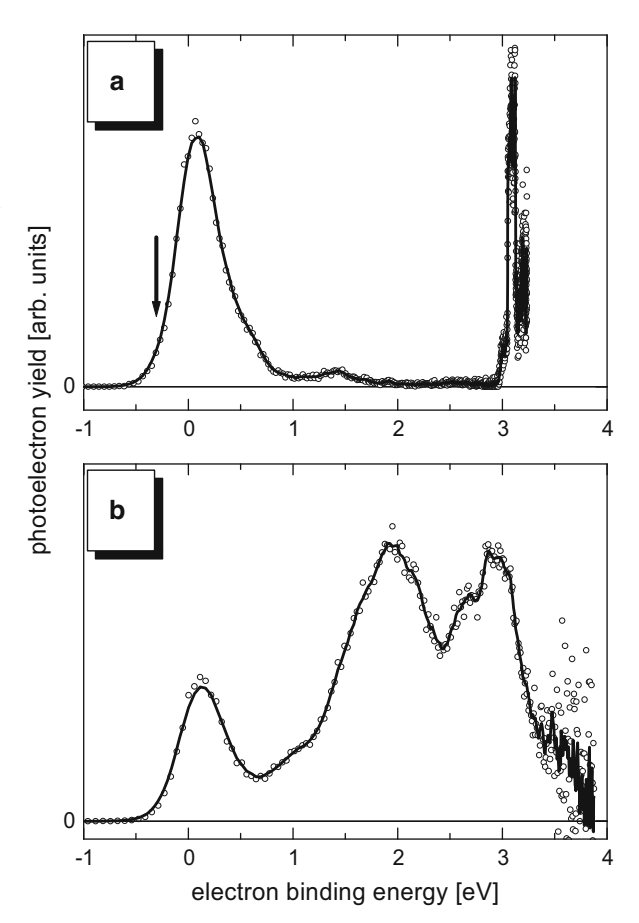
In principle, every phosphate group can be deprotonated to carry a negative excess charge, allowing oligonucleotides to be multiply-charged negative ions. Multiply-charged oligonucleotide anions were first studied by Weber et al. [67], who reported photoelectron spectra of $[dB_5-4H]^{4-}$ ions (B=A,T). They observed

Fig. 10.13 Photoelectron spectra of deprotonated DNA mononucleotide anions dAMP⁻ (a), dCMP⁻ (b), dGMP⁻ (c), and dTMP⁻ (d) at 157 nm (7.866 eV). Reproduced with permission from [55]. Copyright (2004) National Academy of Sciences, USA



that the adenine-containing species were much less stable with respect to electron loss than the thymine-containing ions (see Fig. 10.14). In fact, the electron binding energy in $[dA_5-4H]^{4-}$ was found to be slightly negative, the tetra-anion being stabilised only through the presence of a repulsive Coulomb barrier that dominates the long-range electron-molecule potential in multiply charged anions [72–75]. Although direct detachment is possible for photon energies above the electron-binding energies, the wavelength dependence for photodetachment from hexanucleotide trianions $[dB_6-3H]^{3-}$ measured by Gabelica and co-workers [23] suggests that excitation of the base significantly enhances the photodetachment efficiency (as discussed above).

Fig. 10.14 Photoelectron spectra of $[dA_5-4H]^{4-}$ at 3.49 eV (a) and 4.66 eV (b) photon energy. The *arrow* marks the estimated value of the adiabatic electron detachment energy. The *open circles* are raw data points, the *solid lines* are five-point-averaged curves to guide the eye. Reprinted with permission from [67]. Copyright 2004 American Chemical Society



10.6 Concluding Remarks

The last 10 years have provided a wealth of information on the behaviour of isolated nucleotides *in vacuo* after UV photoexcitation, but there are still many issues that need to be properly addressed. It seems that base protonation leads to more prompt photodissociation, but different experiments have provided quite different results regarding the importance and the time scales of statistical and nonstatistical dissociation processes. Additionally, no spectroscopic data are available for these ions. There is also a lack of data when it comes to the photodissociation channels of protonated oligonucleotides. With respect to spectroscopy of strands where exciton coupling plays a role, it would be interesting to freeze out the structural fluctuations. If the frozen structures increase base stacking, this would also increase the corresponding electronic coupling. Spectroscopy of cold nucleic acids in ion traps would provide important data to benchmark the nontrivial problem of carrying out electronic-structure calculations of excited states. In addition to information on

single-site energies and electron coupling terms, absorption-band widths could directly give excited-state lifetimes. To bridge the gap between experiments *in vacuo* and in solution, work on partially-hydrated ions is needed. Gradually building up the solvation environment by the attachment of one water molecule at a time would establish how many water molecules are needed to obtain the absorption of DNA in bulk solution. In conclusion, there is much more to be done in the future relating to mass spectrometry and UV spectroscopy of isolated DNA and RNA nucleotides.

References

- Crespo-Hernandez, C.E., Cohen, B., Hare, P.M., Kohler, B.: Ultrafast excited-state dynamics in nucleic acids. Chem. Rev. 104, 1977–2019 (2004)
- Middleton, C.T., de La Harpe, K., Su, C., Law, Y.K., Crespo-Hernandez, C.E., Kohler, B.: DNA excited-state dynamics: from single bases to the double helix. Annu. Rev. Phys. Chem. 60, 217–239 (2009)
- 3. Clark, L.B.: Transition moments of 2'-deoxyadenosine. J. Phys. Chem. 99, 4466–4470 (1995)
- Matsuoka, Y., Nordén, B.: Linear dichroism studies of nucleic-acid bases in stretched polyvinyl-alcohol film - molecular-orientation and electronic-transition moment directions. J. Phys. Chem. 86, 1378–1386 (1982)
- Petke, J.D., Maggiora, G.M., Christoffersen, R.E.: Ab initio configuration-interaction and random phase approximation calculations of the excited singlet and triplet-states of adenine and guanine. J. Am. Chem. Soc. 112, 5452–5460 (1990)
- Domcke, W., Yarkony, D.R., Köppel, H.: Conical Intersections: Electronic Structure, Dynamics & Spectroscopy. In: Ng, C.-Y. (ed.) Advanced Series in Physical Chemistry, vol. 15. World Scientific, Singapore (2004)
- Longworth, J.W., Rahn, R.O., Shulman, R.G.: Luminescence of pyrimidines purines nucleosides and nucleotides at 77 degrees K. Effect of ionization and tautomerization. J. Chem. Phys. 45, 2930–2939 (1966)
- 8. Markovitsi, D., Gustavsson, T., Banyasz, A.: Absorption of UV radiation by DNA: spatial and temporal features. Mutat. Res. Rev. Mutat. **704**, 21–28 (2010)
- Markovitsi, D., Gustavsson, T., Vaya, I.: Fluorescence of DNA duplexes: from model helices to natural DNA. J. Phys. Chem. Lett. 1, 3271–3276 (2010)
- Vaya, I., Gustavsson, T., Miannay, F.A., Douki, T., Markovitsi, D.: Fluorescence of natural DNA: from the femtosecond to the nanosecond time scales. J. Am. Chem. Soc. 132, 11834–11835 (2010)
- Nielsen, L.M., Hoffmann, S.V., Nielsen, S.B.: Electronic coupling between photo-excited stacked bases in DNA and RNA strands with emphasis on the bright states initially populated. Photochem. Photobiol. Sci. 12, 1273–1285 (2013)
- Ghosh, D., Isayev, O., Slipchenko, L.V., Krylov, A.I.: Effect of solvation on the vertical ionization energy of thymine: from microhydration to bulk. J. Phys. Chem. A 115, 6028–6038 (2011)
- Ghosh, D., Kosenkov, D., Vanovschi, V., Williams, C.F., Herbert, J.M., Gordon, M.S., Schmidt, M.W., Slipchenko, L.V., Krylov, A.I.: Noncovalent interactions in extended systems described by the effective fragment potential method: theory and application to nucleobase oligomers. J. Phys. Chem. A 114, 12739–12754 (2010)
- 14. Bravaya, K.B., Kostko, O., Ahmed, M., Krylov, A.I.: The effect of π-stacking, H-bonding, and electrostatic interactions on the ionization energies of nucleic acid bases: adenine-adenine, thymine-thymine and adenine-thymine dimers. Phys. Chem. Chem. Phys. 12, 2292–2307 (2010)

 Alexandrova, A.N., Tully, J.C., Granucci, G.: Photochemistry of DNA fragments via semiclassical nonadiabatic dynamics, J. Phys. Chem. B 114, 12116–12128 (2010)

- 16. Lange, A.W., Herbert, J.M.: Both intra- and interstrand charge-transfer excited states in aqueous B-DNA are present at energies comparable to, or just above, the $^1\pi\pi^*$ excitonic bright states. J. Am. Chem. Soc. **131**, 3913–3922 (2009)
- 17. Nielsen, S.B., Andersen, J.U., Forster, J.S., Hvelplund, P., Liu, B., Pedersen, U.V., Tomita, S.: Photodestruction of adenosine 5'-monophosphate (AMP) nucleotide ions in vacuo: statistical versus nonstatistical processes. Phys. Rev. Lett. **91**, 048302 (2003)
- Nielsen, S.B., Sølling, T.I.: Are conical intersections responsible for the ultrafast processes of adenine, protonated adenine, and the corresponding nucleosides? ChemPhysChem 6, 1276–1281 (2005)
- Nielsen, L.M., Pedersen, S.O., Kirketerp, M.B.S., Nielsen, S.B.: Absorption by DNA single strands of adenine isolated in vacuo: the role of multiple chromophores. J. Chem. Phys. 136, 064302 (2012)
- Nielsen, J.B., Thogersen, J., Jensen, S.K., Nielsen, S.B., Keiding, S.R.: Vibrational dynamics of deoxyguanosine 5'-monophosphate following UV excitation. Phys. Chem. Chem. Phys. 13, 13821–13826 (2011)
- Worm, E.S., Andersen, I.H., Andersen, J.U., Holm, A.I.S., Hvelplund, P., Kadhane, U., Nielsen, S.B., Poully, J.C., Støchkel, K.: Photodissociation of dinucleotide ions in a storage ring. Phys. Rev. A 75, 042709 (2007)
- Gabelica, V., Tabarin, T., Antoine, R., Rosu, F., Compagnon, I., Broyer, M., De Pauw, E., Dugourd, P.: Electron photodetachment dissociation of DNA polyanions in a quadrupole ion trap mass spectrometer. Anal. Chem. 78, 6564–6572 (2006)
- 23. Gabelica, V., Rosu, F., De Pauw, E., Antoine, R., Tabarin, T., Broyer, M., Dugourd, P.: Electron photodetachment dissociation of DNA anions with covalently or noncovalently bound chromophores. J. Am. Soc. Mass. Spectrom. 18, 1990–2000 (2007)
- Gabelica, V., Rosu, F., Tabarin, T., Kinet, C., Antoine, R., Broyer, M., De Pauw, E., Dugourd,
 P.: Base-dependent electron photodetachment from negatively charged DNA strands upon
 260-nm laser irradiation. J. Am. Chem. Soc. 129, 4706–4713 (2007)
- Rosu, F., Gabelica, V., De Pauw, E., Antoine, R., Broyer, M., Dugourd, P.: UV spectroscopy of DNA duplex and quadruplex structures in the gas phase. J. Phys. Chem. A 116, 5383–5391 (2012)
- Marcum, J.C., Halevi, A., Weber, J.M.: Photodamage to isolated mononucleotidesphotodissociation spectra and fragment channels. Phys. Chem. Chem. Phys 11, 1740–1751 (2009)
- Marcum, J.C., Kaufman, S.H., Weber, J.M.: UV-photodissociation of non-cyclic and cyclic mononucleotides. Int. J. Mass Spectrom. 303, 129–136 (2011)
- Marcum, J.C.: Electronic photodissociation spectroscopy of electrosprayed anions. Doctoral Dissertation, Department of Chemistry and Biochemistry, University of Colorado, Boulder (2011)
- 29. Kumar, S.S., Perot-Taillandier, M., Lucas, B., Soorkia, S., Barat, M., Fayeton, J.A.: UV photodissociation dynamics of deprotonated 2'-deoxyadenosine 5'-monophosphate [5'-dAMP-H]. J. Phys. Chem. A 115, 10383–10390 (2011)
- 30. Smith, S.I., Brodbelt, J.S.: Hybrid activation methods for elucidating nucleic acid modifications. Anal. Chem. 83, 303–310 (2011)
- 31. Aravind, G., Antoine, R., Klaerke, B., Lemoine, J., Racaud, A., Rahbek, D.B., Rajput, J., Dugourd, P., Andersen, L.H.: Sub-microsecond photodissociation pathways of gas phase adenosine 5'-monophosphate nucleotide ions. Phys. Chem. Chem. Phys 12, 3486–3490 (2010)
- 32. Smith, S.I., Brodbelt, J.S.: Characterization of oligodeoxynucleotides and modifications by 193 nm photodissociation and electron photodetachment dissociation. Anal. Chem. 82, 7218–7226 (2010)

- Habibigoudarzi, S., McLuckey, S.A.: Ion-trap collisional activation of the deprotonated deoxymononucleoside and deoxydinucleoside monophosphates. J. Am. Soc. Mass Spectrom. 6, 102–113 (1995)
- Cerny, R.L., Gross, M.L., Grotjahn, L.: Fast-atom-bombardment combined with tandem massspectrometry for the study of dinucleotides. Anal. Biochem. 156, 424

 –435 (1986)
- Guan, Z.Q., Kelleher, N.L., Oconnor, P.B., Aaserud, D.J., Little, D.P., McLafferty, F.W.: 193 nm photodissociation of larger multiply-charged biomolecules. Int. J. Mass Spectrom. Ion Proc. 158, 357–364 (1996)
- Phillips, D.R., McCloskey, J.A.: A comprehensive study of the low-energy collision-induced dissociation of dinucleoside monophosphates. Int. J. Mass Spectrom. Ion Proc. 128, 61–82 (1993)
- McLuckey, S.A., Goeringer, D.E.: Slow heating methods in tandem mass spectrometry.
 J. Mass Spectrom. 32, 461–474 (1997)
- Klassen, J.S., Schnier, P.D., Williams, E.R.: Blackbody infrared radiative dissociation of oligonucleotide anions. J. Am. Soc. Mass Spectrom. 9, 1117–1124 (1998)
- Wan, K.X., Gross, M.L.: Fragmentation mechanisms of oligodeoxynucleotides: effects of replacing phosphates with methylphosphonates and thymines with other bases in T-rich sequences. J. Am. Soc. Mass Spectrom. 12, 580–589 (2001)
- Yang, J., Hakansson, K.: Characterization of oligodeoxynucleotide fragmentation pathways in infrared multiphoton dissociation and electron detachment dissociation by Fourier transform ion cyclotron double resonance. Eur. J. Mass Spectrom. 15, 293–304 (2009)
- 41. Marian, C.M.: A new pathway for the rapid decay of electronically excited adenine. J. Chem. Phys. **122**, 104314 (2005)
- Ho, Y.H., Kebarle, P.: Studies of the dissociation mechanisms of deprotonated mononucleotides by energy resolved collision-induced dissociation. Int. J. Mass Spectrom. Ion Proc. 165, 433–455 (1997)
- Wu, J., McLuckey, S.A.: Gas-phase fragmentation of oligonucleotide ions. Int. J. Mass Spectrom. 237, 197–241 (2004)
- 44. Rodgers, M.T., Campbell, S., Marzluff, E.M., Beauchamp, J.L.: Low-energy collision-induced dissociation of deprotonated dinucleotides - determination of the energetically favored dissociation pathways and the relative acidities of the nucleic-acid bases. Int. J. Mass Spectrom. Ion Proc. 137, 121–149 (1994)
- 45. Huang, Y.Q., Kenttämaa, H.: Theoretical estimations of the 298 K gas-phase acidities of the pyrimidine-based nucleobases uracil, thymine, and cytosine. J. Phys. Chem. A **107**, 4893–4897 (2003)
- 46. Huang, Y.Q., Kenttämaa, H.: Theoretical estimations of the 298 K gas-phase acidities of the purine-based nucleobases adenine and guanine. J. Phys. Chem. A 108, 4485–4490 (2004)
- 47. Lammich, L., Andersen, L.H., Aravind, G., Pedersen, H.B.: Experimental characterization of the metastable D₂⁻ ion by photofragment imaging. Phys. Rev. A **80**, 023413 (2009)
- Lepère, V., Lucas, B., Barat, M., Fayeton, J.A., Picard, V.J., Jouvet, C., Carcabal, P., Nielsen, I., Dedonder-Lardeux, C., Gregoire, G., Fujii, A.: Comprehensive characterization of the photodissociation pathways of protonated tryptophan. J. Chem. Phys. 127, 134313 (2007)
- Møller, S.P.: ELISA, an electrostatic storage ring for atomic physics. Nucl. Instrum. Methods 394, 281–286 (1997)
- Dahan, M., Fishman, R., Heber, O., Rappaport, M., Altstein, N., Zajfman, D., van der Zande, W.J.: New type of electrostatic ion trap for storage of fast ion beams. Rev. Sci. Instrum. 69, 76–83 (1998)
- 51. Nolting, D., Weinkauf, R., Hertel, I.V., Schultz, T.: Excited-state relaxation of protonated adenine. ChemPhysChem 8, 751–755 (2007)
- 52. Lührs, D.C., Viallon, J., Fischer, I.: Excited state spectroscopy and dynamics of isolated adenine and 9-methyladenine. Phys. Chem. Chem. Phys. 3, 1827–1831 (2001)
- 53. Kang, H., Lee, K.T., Jung, B., Ko, Y.J., Kim, S.K.: Intrinsic lifetimes of the excited state of DNA and RNA bases. J. Am. Chem. Soc. 124, 12958–12959 (2002)

54. DePuy, C.H., Bierbaum, V.M.: Gas-phase reactions of organic-anions as studied by the flowing afterglow technique. Acc. Chem. Res. 14, 146–153 (1981)

- Yang, X., Wang, X.B., Vorpagel, E.R., Wang, L.S.: Direct experimental observation of the low ionization potentials of guanine in free oligonucleotides by using photoelectron spectroscopy. Proc. Natl. Acad. Sci. USA 101, 17588–17592 (2004)
- Nachtigallova, D., Hobza, P., Ritze, H.H.: Electronic splitting in the excited states of DNA base homodimers and -trimers: an evaluation of short-range and Coulombic interactions. Phys. Chem. Chem. Phys. 10, 5689–5697 (2008)
- 57. Ritze, H.H., Hobza, P., Nachtigallova, D.: Electronic coupling in the excited electronic state of stacked DNA base homodimers. Phys. Chem. Chem. Phys. 9, 1672–1675 (2007)
- Bouvier, B., Dognon, J.P., Lavery, R., Markovitsi, D., Millié, P., Onidas, D., Zakrzewska, K.: Influence of conformational dynamics on the exciton states of DNA oligomers. J. Phys. Chem. B 107, 13512–13522 (2003)
- Tonzani, S., Schatz, G.C.: Electronic excitations and spectra in single-stranded DNA. J. Am. Chem. Soc. 130, 7607–7612 (2008)
- 60. Improta, R., Santoro, F., Barone, V., Lami, A.: Vibronic model for the quantum dynamical study of the competition between bright and charge-transfer excited states in single-strand polynucleotides: the adenine dimer case. J. Phys. Chem. A 113, 15346–15354 (2009)
- Santoro, F., Barone, V., Improta, R.: Influence of base stacking on excited-state behavior of polyadenine in water, based on time-dependent density functional calculations. Proc. Natl. Acad. Sci. USA 104, 9931–9936 (2007)
- 62. Banyasz, A., Gustavsson, T., Onidas, D., Changenet-Barret, P., Markovitsi, D., Improta, R.: Multi-pathway excited state relaxation of adenine oligomers in aqueous solution: a joint theoretical and experimental study. Chem. Eur. J. 19, 3762–3774 (2013)
- Boyarkin, O.V., Mercier, S.R., Kamariotis, A., Rizzo, T.R.: Electronic spectroscopy of cold, protonated tryptophan and tyrosine. J. Am. Chem. Soc. 128, 2816–2817 (2006)
- Gidden, J., Bowers, M.T.: Gas-phase conformational and energetic properties of deprotonated dinucleotides. Eur. Phys. J. D 20, 409–419 (2002)
- Li, L., Lubman, D.M.: Ultraviolet visible absorption-spectra of biological molecules in the gas-phase using pulsed laser-induced volatilization enhancement in a diode-array spectrophotometer. Anal. Chem. 59, 2538–2541 (1987)
- 66. Zakjevskii, V.V., King, S.J., Dolgounitcheva, O., Zakrzewski, V.G., Ortiz, J.V.: Base and phosphate electron detachment energies of deoxyribonucleotide anions. J. Am. Chem. Soc. 128, 13350–13351 (2006)
- 67. Weber, J.M., Ioffe, I.N., Berndt, K.M., Löffler, D., Friedrich, J., Ehrler, O.T., Danell, A.S., Parks, J.H., Kappes, M.M.: Photoelectron spectroscopy of isolated multiply negatively charged oligonucleotides. J. Am. Chem. Soc. 126, 8585–8589 (2004)
- 68. Marian, C., Nolting, D., Weinkauf, R.: The electronic spectrum of protonated adenine: theory and experiment. Phys. Chem. Chem. Phys. 7, 3306–3316 (2005)
- 69. Cheong, N.R., Nam, S.H., Park, H.S., Ryu, S., Song, J.K., Park, S.M., Perot, M., Lucas, B., Barat, M., Fayeton, J.A., Jouvet, C.: Photofragmentation in selected tautomers of protonated adenine. Phys. Chem. Chem. Phys. 13, 291–295 (2011)
- Zhu, Q.Q., LeBreton, P.R.: DNA photoionization and alkylation patterns in the interior of guanine runs. J. Am. Chem. Soc. 122, 12824–12834 (2000)
- 71. Giese, B.: Electron transfer in DNA. Curr. Opin. Chem. Biol. **6**, 612–618 (2002)
- 72. Wang, L.S., Ding, C.F., Wang, X.B., Nicholas, J.B., Nicholas, B.: Probing the potential barriers and intramolecular electrostatic interactions in free doubly charged anions. Phys. Rev. Lett. **81**, 2667–2670 (1998)
- Wang, X.B., Ding, C.F., Wang, L.S.: Photodetachment spectroscopy of a doubly charged anion: direct observation of the repulsive Coulomb barrier. Phys. Rev. Lett. 81, 3351–3354 (1998)

- Wang, X.B., Nicholas, J.B., Wang, L.S.: Intramolecular Coulomb repulsion and anisotropies of the repulsive Coulomb barrier in multiply charged anions. J. Chem. Phys. 113, 653–661 (2000)
- 75. Wang, X.B., Wang, L.S.: Observation of negative electron-binding energy in a molecule. Nature 400, 245–248 (1999)

Action Spectroscopy of Gas-Phase Peptide lons with Energetic Photons

11

Thomas Schlathölter and Ronnie Hoekstra

Abstract

Photodissociation studies on free complex protonated peptides and other biomolecular ions have long been limited to the UV wavelength range and longer wavelengths which are accessible by intense lasers. By interfacing tandem mass spectrometry with synchrotron beamlines, it is possible to overcome this limitation. We have thoroughly studied the interaction of vacuum ultraviolet (VUV) and soft X-ray photons with gas phase protonated peptides. Molecular fragmentation patterns, unobserved in conventional mass spectrometry, can be observed experimentally. Instead of relatively slow statistical fragmentation along the peptide backbone, much faster formation of fragment ions related to sidechains of aromatic amino acids is observed. The underlying process most likely involves fast charge migration. A previously unobserved dissociation scheme, in which photoabsorption leads to a fast loss of a tyrosine side chain can be observed for the VUV and soft X-ray range. This loss process leads to the formation of a residual peptide that is remarkably cold internally.

11.1 Introduction

For many decades, optical spectroscopy approaches have been amongst the most important experimental tools for the exploration of molecular structure and dynamics. The dynamics of complex (bio-)molecular systems lie at the very heart of functionality in nature. The driving force of structural dynamics in biomolecular systems are changes in the molecular electronic structure which subsequently couple to atomic motion. For example, structural changes of biomolecular complexes upon absorption of a visible-light photon are at the basis of natural

Atomic and Molecular Physics Group, University of Groningen, Zernikelaan 25 9747AA

Groningen, The Netherlands

e-mail: tschlat@kvi.nl; r.a.hoekstra@rug.nl

T. Schlathölter (⋈) • R. Hoekstra

biological functions such as vision and photosynthesis. Even though cis-trans isomerisation of the retinal chromophore is known as the molecular basis of human vision, the electronic and structural dynamics underlying this process and the subsequent coupling to the protein environment by charge transfer are still ambiguous. The same is true for the molecular basis of photosynthesis: for instance, femtosecond absorption spectroscopy was recently employed to show that structural changes in the light harvesting complex II play a role in the photo protection processes [1]. Such photophysical studies are typically done in the liquid phase, because this is where most complex biomolecular systems perform. Even genuine quantum processes such as propagation of a coherent superposition of electronic-vibrational eigenstates over long distances have been spectroscopically observed in light harvesting complexes under biological conditions [2, 3].

Over the last years, however, there has also been enormous interest in the physics of gas-phase biomolecular systems. De Vries and Hobza [4] give three major motivations for spectroscopic gas-phase studies, namely i) the importance to distinguish intrinsic molecular properties from effects of the chemical environment; ii) the possibility to investigate fundamental interactions and microsolvation; and iii) the need of gas-phase data to test quantum chemical calculations. Most experiments have focused on the infrared (IR) [5], visible and ultraviolet (UV) ranges. Only a few recent studies have been performed in the near vacuum ultraviolet (VUV) [6]. In the following, the focus will be on even higher photon energies, i.e. the entire VUV range and soft X-rays. In that spectral range, experimental studies in the condensed phase additionally suffer from radiation damage and poor transparency.

Until very recently, spectroscopy with energetic photons was limited to biomolecular systems in the condensed phase with the exception of comparably small systems (nucleobases, amino acids etc.) for which gas-phase studies have been performed. Many amino acids are relatively easy to investigate, as these molecules can be brought into the gas-phase by mere evaporation. A number of experimental VUV and soft X-ray spectroscopy studies have been performed and electronic transitions were assigned to the various spectral features, and used for instance to investigate conformational effects [7–9]. Only a few specific small peptides such as glycyl-glycine can be evaporated without thermal decomposition [10]. However, there are also some classes of small peptides, which possess unusually high stability due to e.g. ring structure [11] that can be evaporated.

Most larger peptides and proteins and a number of amino acids disintegrate upon evaporation. Alternative techniques based on desorption of neutral molecules, e.g. matrix assisted laser desorption ionisation (MALDI [12]) or laser induced acoustic desorption (LIAD [13]) have already been successfully applied. A particularly powerful method for production of pure targets of gas-phase complex molecular ions is electrospray ionisation (ESI [14]). The use of ionic rather than neutral molecules has the benefit of allowing for straightforward manipulation. Radiofrequency (RF) techniques can thus be used for mass selection, transport and accumulation of the ions in traps.

We have demonstrated in a number of recent studies that RF-trapping of mass-selected electrosprayed protonated peptides or oligonucleotides can provide targets sufficiently dense for VUV [15, 16], and soft X-ray [17, 18], photofragmentation studies. A similar technique has also been applied to VUV [19] and soft X-ray [20] photoionisation of larger multiply protonated proteins. Dugourd and coworkers have focused on deprotonated peptides and their radicals [21, 22]. Peptides and proteins are particularly interesting for photoionisation studies. The fact that peptides are built up from a construction kit of 20 canonical amino acids which are chemically very different, allows the synthesis of systems for virtually any experimental purpose.

In this chapter, we will first describe the experimental technique, i.e. the home-built tandem mass-spectrometer featuring an RF ion trap and how it is interfaced with third generation synchrotron beamlines for VUV and soft X-ray photons. After this, the response of protonated peptides after VUV and soft X-ray photoabsorption will be discussed.

11.2 Experimental Technique

To generate beams of singly or multiply protonated peptides, a home-built electrospray ionisation (ESI) source is fed with the respective peptide solution. Typically, ~30 μmol methanol solutions with 1 % formic acid are used for a peptide such as leucine enkephalin (YGGFL, m = 555.62). The electrosprayed particles enter the vacuum chamber through a capillary which is 20 cm in length and has an inner diameter of 0.125–0.5 mm (see Fig. 11.1, bottom left). An RF ion-funnel is used for phase-space compression of the positive ions and focuses into an RF-only quadrupole, which acts as a second phase-space compressor. A quadrupole mass filter discriminates undesirable masses before a clean beam of mass selected biomolecular ions enters the 3D RF trap through one of the hyperbolic end caps until sufficient ion density is reached. Continuous injection into the trap is only possible, when the injected ions are collisionally cooled before they can escape the trap. To this end, a He-buffer gas pulse is injected into the trap through a bore in the ring electrode. The pressure in the trap increases to about 10^{-3} mbar. Typically injection periods are a couple of 100 ms. At the end of the loading cycle, the ESI beam is deflected by means of a static electric field. The resulting trapped target typically has a diameter of about 300 µm and contains a few 1,000 protonated peptides.

For exposure of the target to a beam of energetic photons, the apparatus is interfaced with an appropriate synchrotron beamline. For the VUV photoionisation experiments presented in this chapter, the U125/2 beamline and the 10 m focal length normal incidence monochromator (NIM) at the BESSY II facility in Berlin (Germany) were used [23]. The soft X-ray studies were performed using the U49/2 beamline and a plane grating monochromator (PGM) at the BESSY II facility and the i411 beamline at MAXlab in Lund (Sweden). In all cases, relatively low resolution gratings were employed in order to have maximum photon fluxes of the order of 10^{13} s⁻¹. The photon beam crosses the RF-trap centre through two bores in the ring-electrode. Typical photon beam diameters in the centre of the trap

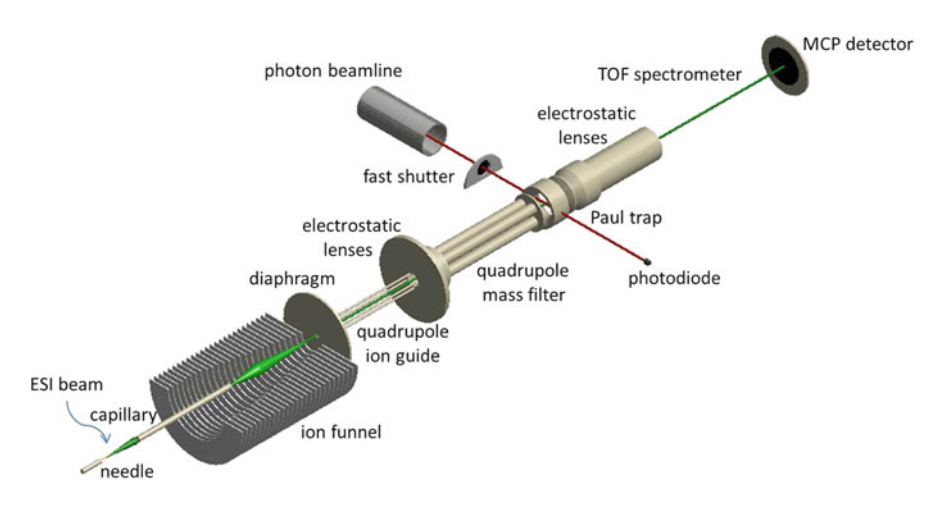


Fig. 11.1 Sketch of the experimental setup

were 100 µm or smaller. The photon flux through the trap is monitored using an SXUV-type silicon p-n junction photodiode (IRD, Newbury Park, USA) mounted about 30 cm downstream.

For typical photon fluxes and trap densities, the protonated peptides need to be exposed for periods between few 100 and 2,000 ms, depending on the photoabsorption cross section. The photon beam is controlled by means of a mechanical shutter. Typically, the open period is chosen such that less than 10 % of the peptides are ionised, implying that less than 10 % of the ionised peptides were subjected to multiple photon absorption. Ions stemming from photofragmentation processes often have relatively high kinetic energies and need to be cooled down with a second buffer gas pulse.

A bias voltage of ± 200 V is then applied to the end caps of the RF-trap to extract the trap content into a linear time-of-flight (TOF) mass spectrometer (M/ Δ M = 200). The ions are detected on a silhouette type micro channel plate detector operated in analog mode and read out by a 1 GHz digitiser. Typically 500–1,000 such mass scans are averaged to obtain a high quality mass spectrum. For each scan, a subsequent mass-scan obtained with an empty trap is subtracted to compensate for the residual gas. A third scan of the native trap content without photon exposure is subtracted as a reference for the trap content. Figure 11.2a shows the structure of the neurotransmitter leucine enkephalin. In Fig. 11.2b, VUV photofragmentation mass spectra for protonated leucine enkephalin obtained at three difference spectra, there is a cut off at 500, i.e. below the precursor mass of 555. At the precursor mass, a large negative peak is observed, which reflects the loss of precursor ions from the trap. The cutoff at low masses is due to the settings of the RF trap. Typically, fragments with masses below 70 are not trapped and accordingly do not contribute to the mass

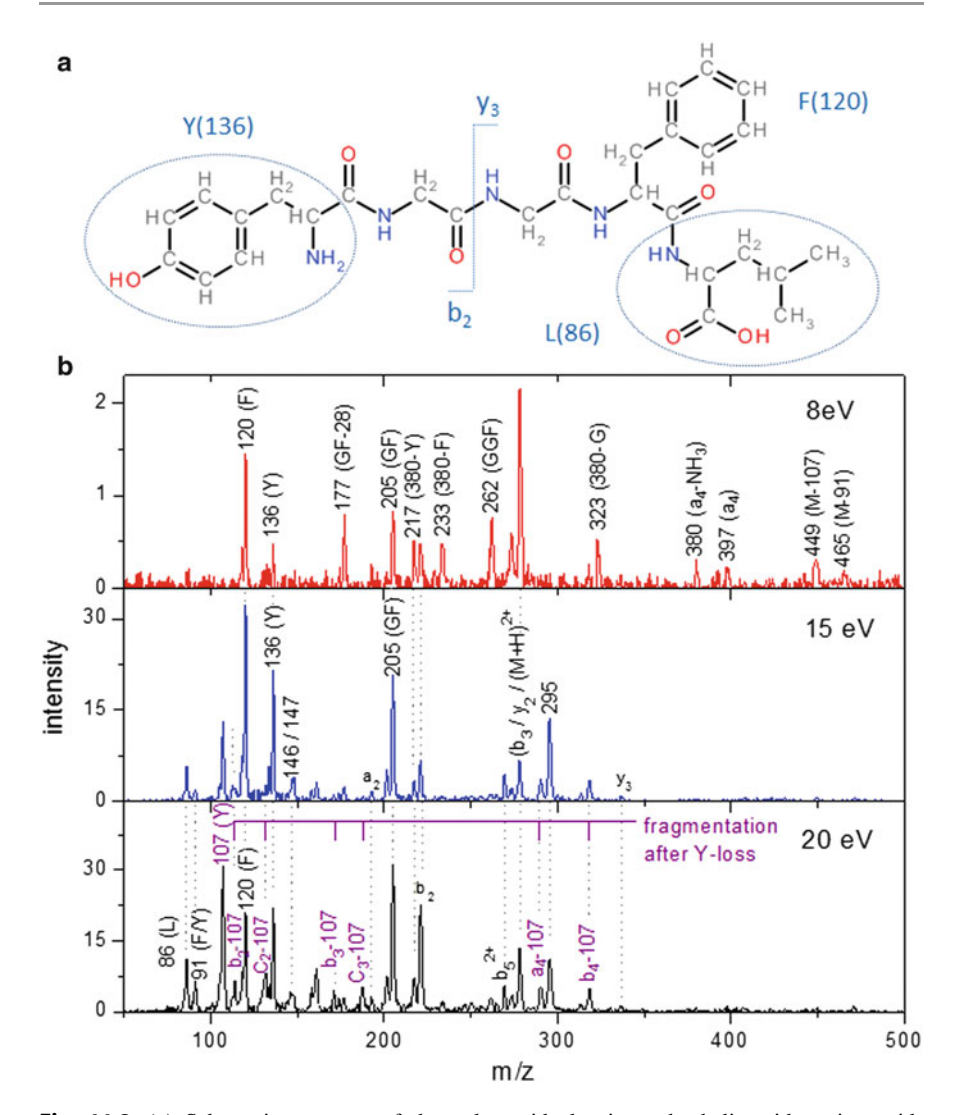


Fig. 11.2 (a) Schematic structure of the polypeptide leucine enkephalin with amino acids sequence tyrosine-glycine-phenylalanine-leucine (YGGFL). (b) VUV photofragmentation mass spectra of (YGGFL+H)⁺ obtained at 8 eV, 15 eV and 20 eV [15]. Reprinted with permission from [15]. Copyright 2011, AIP Publishing LLC

spectra. The details of the spectra will be discussed later. It is however obvious at first glance that a strong dependence on the photon energy is observed.

Native trap content and photon flux are known parameters. In an action spectroscopy approach, the loss of precursor molecules from the trap can thus be used to directly determine the relative total photoionisation cross section. Similarly, relative partial ion yields can be determined, which are directly linked to the total photoionisation cross section.

11.3 VUV Photofragmentation of Protonated Polypeptides

11.3.1 Leucine Enkephalin as a Model System

In the previous section, three photofragmentation mass spectra for leucine enkephalin were displayed (see Fig. 11.2). It is important to note, that at 8 eV, intensities are about a factor of 15 smaller than for 15 and 20 eV. This is due to the fact that the ionisation energy of the lowest energy conformer of leucine enkephalin amounts to 8.87 eV [24]. Dissociative photoexcitation rather than photoionisation manifests itself in the mass spectrum. The strongest peaks are observed at m/z 278/279 and at m/z 120 and can be assigned to b₃ or y₂ fragments and the F immonium ion, respectively. For the rest, the observed peaks are mainly due to regular backbone scission and internal fragments, as also observed by low excitation energy techniques such as collision induced dissociation (CID [25]) or surface induced dissociation (SID [26]) with intensities shifted to smaller fragments.

For photon energies exceeding the ionisation energy, the spectra are dominated by fragments with m/z = 80–240 amu (see spectra for 15 eV and 20 eV in Fig. 11.2b). The immonium ions (see Fig. 11.2a) at 86 (L), 120 (F), 136 (Y) and the common fragments of these groups (91 and 107) are strongest. This is at variance from what is observed with CID or SID but resembles results obtained by keV ion impact (KID [27]). At 20 eV the fragmentation pattern observed is richer than at 15 eV. Of particular interest is a series of a, b and c fragments which have lost the Y side chain.

From a series of mass spectra such as the ones displayed in Fig. 11.2b, it is possible to obtain partial ion yields curves as a function of photon energy by peak integration. For the four strongest (YGGFL+H)⁺ fragmentation channels, the results are displayed in Fig. 11.3e–h. All curves feature a broad peak with a typical full width at half maximum of about 10 eV. Only for m/z = 120 (F) is there an absolute maximum at $h\nu = 15$ eV, whereas the maximum is around $h\nu = 20$ eV for the remaining fragments. Some fragments feature a local maximum at 15 eV.

The general shape of the partial ion yields in Fig. 11.3 is very similar to what has been observed for neutral gas phase amino acids by Jochims et al. [29, 30] for neutral gas phase amino acids. In the amino acids data, clear inflections are observable at each energy, where a deeper lying molecular orbital becomes accessible. The photofragment yield curves thus depend directly on the energetic ordering of the valence molecular orbitals, i.e., the molecular density of states.

Experimentally, the density of valence states manifests in photoelectron emission spectra, which are displayed in Fig. 11.3a—c for three of the amino acids present in leucine enkephalin [7, 28]. The spectra are dominated by intense peaks due to valence electrons at binding energies between 10 and 19 eV. For glycine (Fig. 11.3a) the three lowest states are due to the N lone pair n_N (HOMO), the hydroxyl O lone pair n_O and the bonding carbonyl orbital π_{CO} . Only the aromatic amino acids (here tyrosine and phenylalanine, Fig. 11.3b,c) have a slightly different valence structure since the π orbitals on the phenyl (phenylalanine) and phenol (tyrosine) rings have lower ionisation energies than the n_N orbitals. Last but not

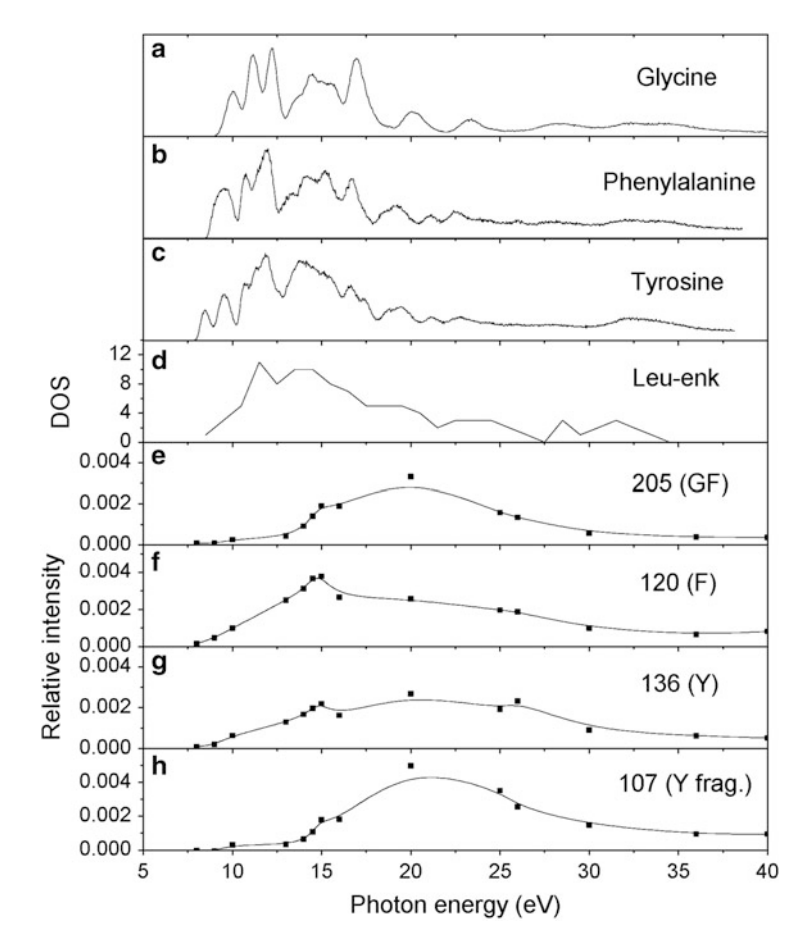


Fig. 11.3 Comparison of the photoelectron data for the amino acids glycine [7] (a), phenylalanine [28] (b), and tyrosine [28] (c) with the calculated molecular valence orbital density of leu–enk (d) and the fragment yields of GF (e), F (f), Y (g) and m = 107 (h). Reprinted with permission from [15]. Copyright 2011, AIP Publishing LLC

least, Fig. 11.3d displays the density of molecular valence orbitals for leucine enkephalin as determined by density functional theory calculations. Clearly the peptide electronic structure overall resembles those of the amino acids. The calculations prove that the highest occupied molecular orbitals are indeed localised on the aromatic rings.

Ionisation of the highest occupied molecular orbitals leads to a resulting dication with low excitation energies. This regime has been probed before using a two-photon absorption approach and neutral peptides. Only negligible fragmentation was found [31]. In (YGGFL+H)⁺, fragmentation is known to set in at internal energies between 3 and 4 eV (when timescales of 1 s are involved [26], as is the case here). If we assume, that the electronic excitation energy is efficiently transferred

into vibrational energy by internal vibrational redistribution (IVR), then only states with binding energies exceeding ~13 eV can lead to appreciable dissociation. This is the case for GF, m=107 (Fig. 11.3e,h) and many other fragments. For the immonium ions with m=120 (F) and m=136 (Y), the situation is clearly different. These fragments are not formed following simple IVR. The yields of both immonium ions peak at $h\nu\approx\!15$ eV which for (F) even is the absolute maximum in yield. The π orbitals from the aromatic side chains have mostly low binding energies up to around 12 eV so a large fraction of the ionisation processes in this photon energy range will certainly originate from the aromatic groups. Here, fast dissociation via repulsive molecular states seems to be more efficient than dissociation following IVR.

The dominating fragment well above the ionisation threshold is the Y sidechain with m=107. This fragment has not been observed in conventional fragmentation studies of leucine enkephaline but is dominant in dissociative photoionisation of neutral gas-phase tyrosine [28]. Below the ionisation threshold, loss of the neutral m=107 tyrosine side chain is evident from the observed peak M-107 at m=449. In the case of ionisation at higher photon energies, the additional charge can give rise to a charge separation process. Also here, the process underlying the dissociation cannot be IVR but probably involves a repulsive molecular state.

The dominating m = 107 fragment ion is accompanied by a series of N-terminal fragments. These fragments are formed by backbone scission of the remaining peptide $((b_2 - 107)^+, (c_2 - 107)^+, (b_3 - 107)^+, (c_3 - 107)^+, (a_4 - 107)^+, and$ (b₄ - 107)⁺)—a process which is not observed in conventional fragmentation experiments. A tentative scheme for this process is shown in Fig. 11.4. In this scheme the photoionisation from the tyrosine (Y) sidechain leads to a non-adiabatic scission of the Y Cα-Cβ bond. The cationic sidechain appears as a dominant feature in the mass spectrum. The remaining protonated peptide cation then undergoes IVR before the excess excitation energy induces backbone scission according to the mobile proton model [32]: Upon an increase of vibrational excitation energy, the proton is mobilised and samples various sites in the molecule. Eventually, a CID-like fragmentation pattern of the system lacking the sidechain is observed. In the mass spectrum, the ratio between the a₄-107 and b₄-107 peaks is about 1 which hints at an excitation energy of about 4.8 eV [26]. The fast loss of the charged tyrosine side chain after 20 eV photoabsorption is thus an efficient mechanism to cool the remaining peptide. It is conceivable, that such loss processes facilitate survival of functional peptide substructures after absorption of very energetic photons.

11.3.2 Peptide Length Effects and Cross Sections

For a systematic investigation of VUV photoionisation as well as charge and energy migration, it is beneficial to look into a slightly simpler type of peptide. Synthetic systems of the type $(YG_nF+H)^+$ (for a sketch, see Fig. 11.5) still feature the two aromatic amino acids tyrosine (Y) and phenylalanine (F), but now both are in terminal positions. In between the termini, a variable number of (sidechain-less)

Fig. 11.4 The three step process of leu–enk dissociation. After ionisation (**a**) the peptide loses the Y fragment (107) non-adiabatically (**b**) and the remaining peptide breaks at the backbone following IVR (**c**). Reprinted with permission from [15]. Copyright 2011, AIP Publishing LLC

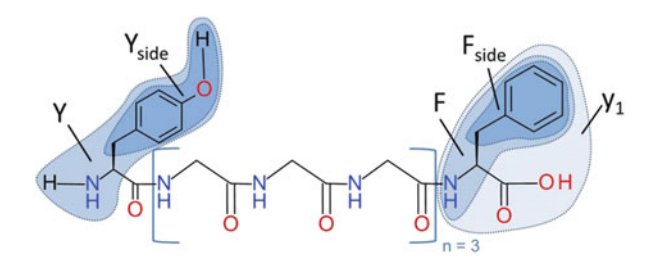


Fig. 11.5 Structure of the YG_nF peptides for the example n=3. The aromatic amino acids tyrosine (Y) and phenylalanine (F) enclose n=0,1,3,5 or 10 glycine units (G) indicated by brackets. Sidechain-related fragments are highlighted [16]. Reproduced by permission of the PCCP Owner Societies

glycine moieties allows controlled variation of photoabsorption cross section and charge/energy migration distance. Figure 11.6 shows a comparison of spectra obtained at $h\nu=20$ eV for $n=0,\,1,\,3,\,5,\,$ and 10. The mass of the protonated peptides increases from 329 to 899, which is why the mass range is increasing. For all peptides except $[YG_{10}F+H]^+$ fragments related to the aromatic sidechains are almost exclusively observed. Even though the fragment distribution strongly varies with n, in all cases the spectra are dominated by masses smaller than 200, as found for leucine enkephalin. These fragments all stem from the two termini, indicating that not only photoabsorption in an aromatic sidechain leads to formation of the respective ion. Rather, the same fragments can also be produced upon photoabsorption by the peptide backbone, possibly after fast charge or energy transfer towards the termini.

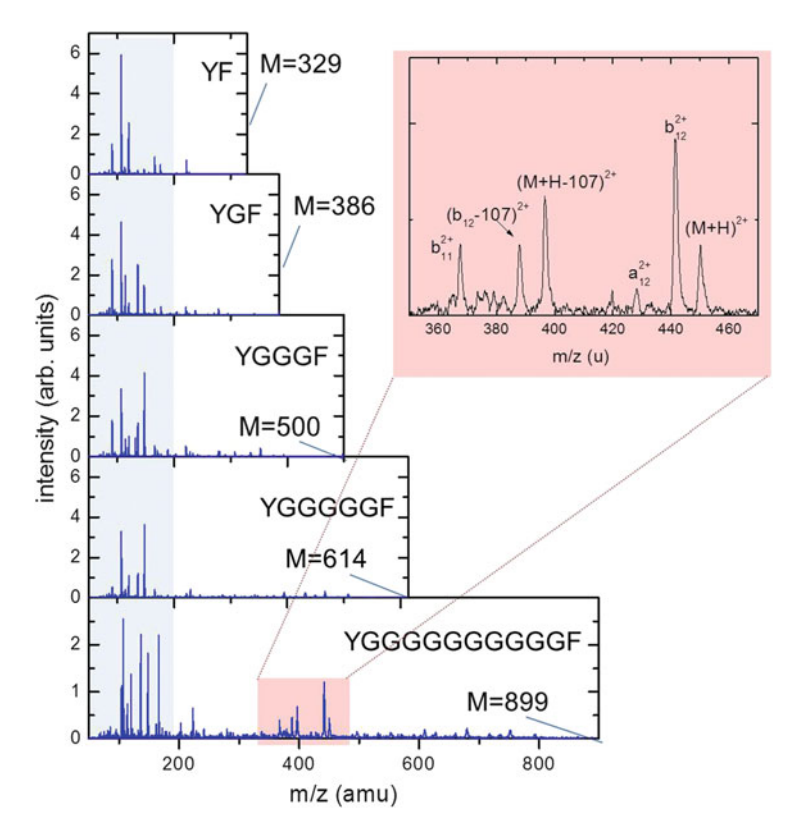


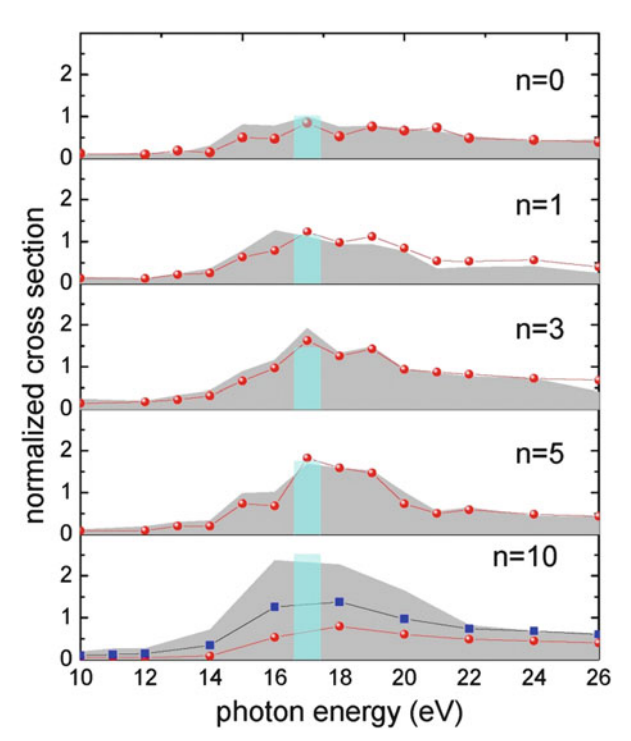
Fig. 11.6 Photofragmentation spectra for $[YG_nF + H]^+$ and n = 0, 1, 3, 5, 10 at $h\nu = 20$ eV. The *inset* displays a zoom in the m = 350–470 region of the n = 10 spectrum, where a series of dication peaks are observed [16]. Reproduced by permission of the PCCP Owner Societies

For n=10, however, a strong contribution from dications is observed (see zoom in Fig. 11.6) and larger fragments due to backbone scission also occur. Instead of charge separation and formation of small fragments, the dication de-excites e.g. by loss of a neutral tyrosine sidechain with m=107—similar to what was observed for sub-threshold photoabsorption in leucine enkephalin. Also, backbone scission and loss of small neutral fragments from the carboxyl-terminal is observed. It is clear that the fast loss of aromatic sidechains is quenched in the largest system.

A more detailed insight into the fragmentation process can be obtained from the (relative) total photoabsorption cross sections $\sigma_{tot,exp}(n)$ as a function of photon energy (see shaded area in Fig. 11.7). At 17 eV $\sigma_{tot,exp}(0)$ is arbitrarily set to 1. The overall shape of the photoabsorption cross section is very similar to the case of leucine enkephalin partial ion yields in Fig. 11.3e–h with a strong increase at about 13 eV and a broad feature with a width of about 9 eV.

The absolute $(YG_nF+H)^+$ photoabsorption cross section can be estimated from available experimental data for the constituent amino acids glycine σ_G and

Fig. 11.7 *Shaded area*: σ_{tot} . $_{\rm exp}$ (n)for $[YG_nF + H]^+$ as a function of photon energy for n = 0, 1, 3, 5, 10. The bars indicate $\sigma_{tot,amino}(n)$ at 16.7 eV and scaled to the experimental data for n = 0. Circles: cross sections $\sigma_{\rm Y}$ F,exp (n) for production of Y, F related fragment ions. Squares (n = 10): sum of σ_{Y} Frexp (n) and the cross section for production of doubly charged fragments odication [16]. Reproduced by permission of the PCCP Owner Societies



phenylalanine σ_F . It can be assumed that σ_{F^*} σ_{Y} because of the similar molecular structure of phenylalanine and tyrosine. For $h\nu=16.7$ eV, the total cross sections then amount to $\sigma_{tot.amino}=\sigma_{Y}+n\sigma_{G}+\sigma_{F}$ and can be found in Table 11.1.

The $\sigma_{tot.amino}$ (n) are displayed in Fig. 11.7 as bars. From Fig. 11.7 and the cross section ratios in Table 11.1, it is clear that the observed total photoabsorption cross sections follow the trend expected from the amino acid data. This implies that unlike the case of UV energies, where photoabsorption is often related to chromophores and thus site specific [6], in the VUV range photoabsorption scales with the peptide length with the aromatic sidechain not playing a special role. However, from Fig. 11.6 it is already clear that for n = 10 the fragmentation pattern changes dramatically. How does this manifest in the cross sections? Besides the total cross sections, Fig. 11.7 also includes the sum of the partial ion yields for Y and F immonium ions and their fragments ($\sigma_{Y,F,exp}(n)$, red dots). Clearly, up to $n = 5 \sigma_{Y,F,exp}(n)$ roughly equals $\sigma_{tot,exp}(n)$. This implies that one Y or F immonium related ion is produced for every photoabsorption process. Clearly, to some extent holes created on the G moieties need to migrate towards one of the termini for this to occur. Hole migration towards Y and F is energetically favourable because of the lower ionisation potentials of Y and F as compared to G, even when initial protonation on the N-terminal is assumed. In the latter case however formation of Y-related cations does not necessarily require hole migration towards Y. The expected protonation on the N-terminal even hinders hole migration towards Y

n	$\sigma_{tot,amino}(n)$	$\sigma_{tot,amino}(n)\!/\!\sigma_{tot,amino}(0)$	$\sigma_{tot,exp}(n)/\sigma_{tot,exp}(0)$	$\sigma_{Y,F,exp}(n)/\sigma_{Y,F,exp}(0)$
0	5	1	1	1
1	5.8	1.15	1.11	1.31
3	7.3	1.45	1.93	1.91
5	8.8	1.75	1.82	2.16
10	12.6	2.5	2.32	0.78

Table 11.1 Photoabsorption cross sections at $h\nu = 16.7$ eV (in 10^{-16} cm²) from summation of amino acid cross sections [33] ($\sigma_{\text{tot.amino}}(n)$)

The remaining columns display cross section ratios between YG_nF and YF

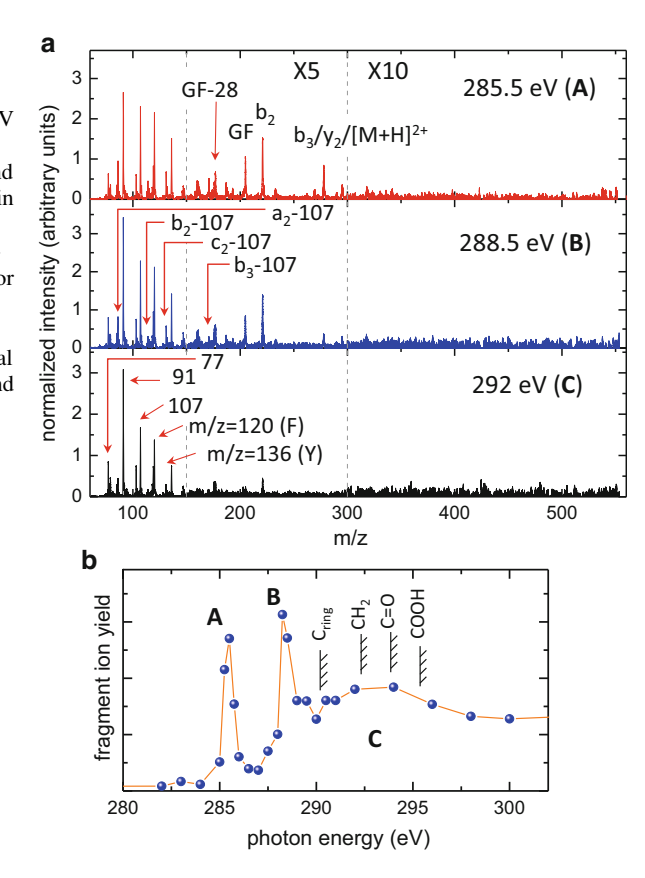
and accordingly, Y related yields always exceed the F related ones, with their ratio increasing with n.

The underlying hole migration process must be different from (and thus much faster than) IVR because i) for fixed n, the fragmentation pattern is only weakly dependent on $h\nu$ and thus on the excitation energy and ii) for a given $h\nu$, the fragmentation pattern only weakly depends on n. In an IVR/statistical fragmentation scenario, an increase in system size and thus phase space would necessarily lead to an exponential decrease in dissociation rates for given channels. The fragmentation pattern would have to change dramatically.

However, in case of the largest peptide under study, $\sigma_{Y,F,exp}(10) < \sigma_{Y,F,exp}(0)$ (see Table 11.1), i.e. even on an absolute scale, less immonium related ions are formed than in a peptide without G moieties. Instead, for $h\nu=14$ –16 eV the yield of doubly charged cations (see inset Fig. 11.6) exceeds $\sigma_{Y,F,exp}$ (in Fig. 11.7, the square indicates the sum of dication cross section and $\sigma_{Y,F,exp}$). The case for much larger proteins such as cytochrome c (m ~ 12,000) has been investigated by Milosavljevic et al. [20] using a similar approach. They solely observed intact parent dications or dications that lost a CO_2 unit. $(YG_{10}F+H)^+$ clearly marks a transition size to the large peptide/protein regime. Here, photoinduced holes do not efficiently migrate towards aromatic sites anymore.

From the existing data, it is very difficult to draw conclusions about the actual charge migration process at play in VUV photoionisation of protonated peptides. Possibilities include charge transport along the peptide due to fast and almost barrierless dihedral rotation occurring before IVR—a process involving timescales of the order of a few 100 fs [34]. Another option would be electron correlation driven ultrafast charge migration which is expected to happen on sub fs to few fs timescales [35, 36]. Future studies are needed to clarify this issue, possibly by pump-probe type approaches using coincident detection of photofragments and photoelectrons. For such experiments, however, it would be advantageous to have the possibility of localised ionisation. This can be achieved by increasing the photon energy into the soft X-ray regime.

Fig. 11.8 (a) Photofragmentation mass spectra for $h\nu = 285.5 \text{ eV}$ (A), 288.5 eV (B), and 292 eV (C). The intensities in the mass region between 150 and 300 are multiplied by 5 and in the region between 300 and 560 by 10. (b) Typical C Kedge photoionisation yield for the fragment with m/z 120 (phenylalanine immonium ion). The dominating spectral features are labeled A, B, and C. Indicated are the C 1s ionisation energies for ring (C_{ring}) [9], amino group (CH₂), peptide bond (C=O) and carboxyl (COOH) [10] site [17]. Reprinted with permission from [17]. Copyright 2012. American Chemical Society



11.4 Soft X-Ray Photofragmentation of Protonated Polypeptides

Figure 11.8 displays mass spectra of $(YGGFL+H)^+$ products after photoabsorption at three photon energies close to the C K-edge. Again, the mass spectra are dominated by fragments with m/z 80–150 u. It is clear that virtually no fragments with masses exceeding m/z 300 are observed. As for the VUV photoionisation case (see Fig. 11.2b), strongest yields are observed for the immonium ions at m=120 (F), 136 (Y) and the fragments of these groups with m=91 and 107. However, whereas for VUV photons at 15 eV and at 20 eV, intermediate size fragments of masses between 200 and 350 contribute with appreciable intensity, this mass range is relatively weaker for 285.5 eV and 288.5 eV and almost fully absent at 292 eV. Furthermore, the series of fragments due to backbone scission (a_2 , b_2 , b_3 , and c_2) which removed excess energy by losing the tyrosine side chain (m=107) (see sketch in Fig. 11.4) is present as well.

Peak integration of these mass spectra gives partial cation yields as a function of photon energy. Fig. 11.8b displays such a cation yield for m/z 120, i.e., the

phenylalanine (F) immonium ion, which we will refer to as a near edge X-ray absorption mass spectrometry (NEXAMS) spectrum. Qualitatively, very similar NEXAMS spectra are observed for all fragments. The spectrum in Fig. 11.8b is dominated by two sharp peaks at 285.4 (A) and 288.4 eV (B) with full widths at half-maximum (fwhm) of 0.6 and 0.7 eV, respectively. A broader structure (C) starts approximately at 290 eV and extends far beyond 300 eV. Very recently, photoionisation of the large protein cytochrome c was studied, and very similar partial ion yields have been observed [20]. However, whereas for cytochrome c, the structure C dominates the spectrum, here highest intensities are observed for A or B.

Transitions can be assigned to the NEXAMS peaks, by comparison to existing near edge X-ray absorption data for the gas-phase amino acids tyrosine (Y), phenylalanine (F) [7] and glycine (G) [9]. Peak A (285.4 eV) is solely due to C 1s excitations into the π^* -orbitals of the Y and F aromatic rings. This transition therefore is a good candidate for localised ionisation in future pump-probe studies.

Peak B (288.4 eV) is due to C 1s $-\pi_{C=O}^{*}$ transitions in the amino group and thus not site specific, regarding single amino acids. A small contribution on the low energy side of B is due to C 1s $\rightarrow\sigma^{*}$ excitations in the Y and F aromatic rings.

Structure C is partly due to C 1s ionisation of the peptide. The respective binding energies have been determined experimentally for glycylglycine as 292.32 eV (C bonded to amino groups), 293.85 eV (peptide bond C), and 295.37 eV (carboxyl terminal C) [10]. The ionisation energies of the aromatic side chains are 290.2 eV (Y) and 290.3 eV (F) [9] which is exactly at the onset of the broad structure C (see Fig. 11.8). Structure C is thus partly due to K-shell ionisation, which, in light elements such as C, rapidly decays nonradiatively by Auger de-excitation [37]. Here, a triply charged [YGGFL+H]³⁺ is formed, whereas below threshold, resonant Auger decay leads to the formation of [YGGFL+H]²⁺ intermediates, which may contribute to a peak at m = 278. Peak C also includes contributions from various C 1s σ^* and Rydberg transitions. In the high energy tail of C, mainly shape resonances contribute [9, 10].

In the context of the VUV results, it is of particular interest to have a closer look into the NEXAMS spectra for the immonium ions of the aromatic amino acids and their fragments, as well as into the spectra for the fragments related to the two-step fragmentation mechanism.

Figure 11.9 displays the results for the immonium related ions. It is again obvious that these fragments are formed for absorption along the backbone (B), the aromatic sidechains (A) and in case of double ionisation and other transitions (C). The Y immonium ion with m=136 has a relatively large cross section for photoabsorption on the aromatic rings—peak A is high. For the F immonium ion (m=120), A is relatively smaller, probably due to the fact that for a non-terminal immonium ion, two rather than one bonds need to be disrupted. With decreasing size of immonium fragments, A is getting relatively smaller and C increases, i.e. ionisation becomes more dominant. This decrease of peak A is intuitively expected as higher initial charge and/or excitation energy in the system usually shifts the fragmentation pattern toward smaller masses.

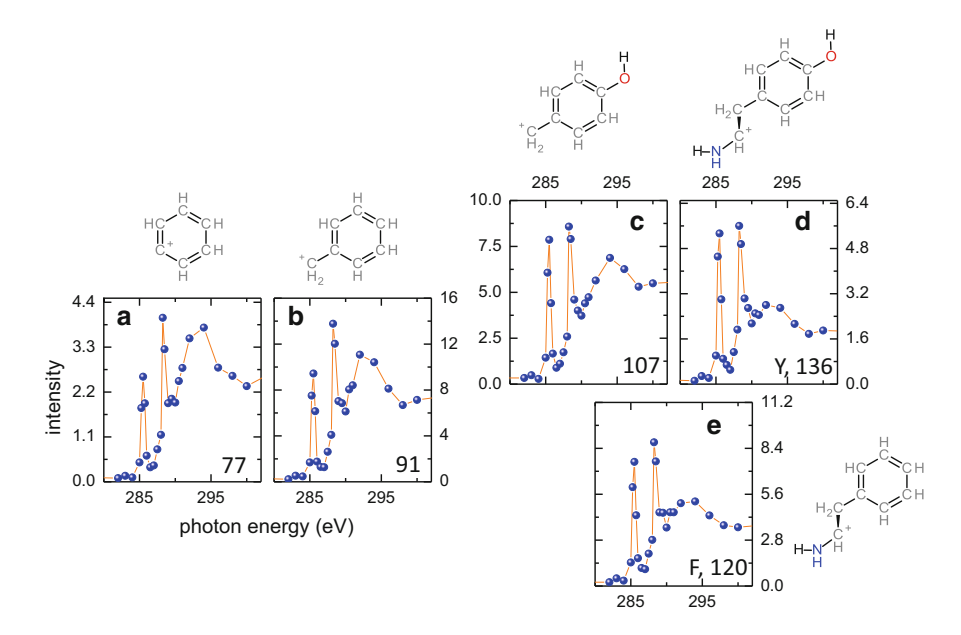


Fig. 11.9 C K-edge NEXAMS spectra of [YGGFL+H]⁺ for Y and F immonium ions and related fragments of (*right*) intact Y (d) and F (e) immonium ion and (*left*) related fragments common to both amino acids (a, b). The sketches next to the spectra display the structure of the respective fragment in the parent molecule. Intensities are given in arbitrary units on the same relative scale as the other NEXAMS spectra in this article [17]. Reprinted with permission from [17]. Copyright 2012. American Chemical Society

Figure 11.10 shows the NEXAMS data for the fragmentation channels involving backbone scission. These channels are usually associated with lower activation energies than formation of immonium ions and immonium ion fragments because scission of fewer or weaker bonds is involved. Here, for all observed channels, peak A is strongest, i.e. the process is preferably triggered by absorption by the aromatic rings. This is most pronounced for the largest b3–107 fragment.

In summary, C 1s $\to \pi^*$ excitations in the aromatic rings appear to be softest X-ray absorption channels protonated leucine enkephalin at the C K-edge. C 1s excitation along the peptide backbone on the other hand, contributes strongly to the formation of smaller fragments and is a more destructive channel. C 1s ionisation (above threshold) always induces extensive fragmentation and is not site selective.

Conclusions

In this chapter we have shown how the combination of tandem mass spectrometry and VUV and soft X-ray photoabsorption can be used to investigate charge dynamics in small gas-phase peptides. The absorption of energetic photons predominantly leads to formation of fragments related to the side-chains of aromatic amino acids—a finding that is not observed in conventional mass spectrometry. It is also clear that photon induced holes along the peptide

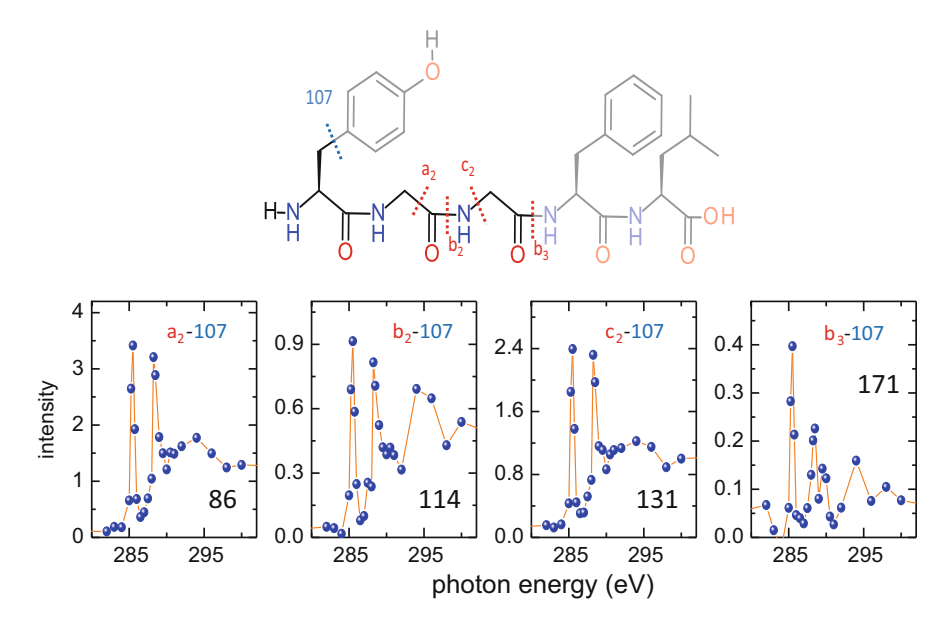


Fig. 11.10 C K-edge NEXAMS spectra of [YGGFL+H]⁺ for fragments stemming from backbone scission followed by Y-side chain loss. Intensities are given in arbitrary units on the same relative scale as the other NEXAMS spectra in this article [17]. Reprinted with permission from [17]. Copyright 2012. American Chemical Society

backbone are efficiently transferred to terminal and non-terminal aromatic sidechain. This process starts to be quenched, however, for larger peptides. Instead, large dications and large singly charged fragments are observed.

Soft X-ray absorption close to the C K-edge allows to site-selectively ionise protonated peptides. Clearly, this implies great potential for charge migration studies in synthetic model systems.

For the entire photon energy range under study, a new two-step fragmentation process is identified, where the photoionised system first cools off excitation energy by fast loss of an aromatic side-chain. In a second step the remaining system is subject to conventional statistical fragmentation along the backbone.

Acknowledgements All experiments have been performed at the Helmholtz-Zentrum Berlin—Electron storage ring BESSY II. We thank for provision of synchrotron radiation from the beamlines U49/2-PGM-1 and U125/2-NIM.

References

 Ruban, A.V., Berera, R., Ilioaia, C., van Stokkum, I.H.M., Kennis, J.T.M., Pascal, A.A., van Amerongen, H., Robert, B., Horton, P., van Grondelle, R.: Identification of a mechanism of photoprotective energy dissipation in higher plants. Nature 450, 575–578 (2007)

- Collini, E., Wong, C.Y., Wilk, K.E., Curmi, P.M.G., Brumer, P., Scholes, G.D.: Coherently wired light-harvesting in photosynthetic marine algae at ambient temperature. Nature 463, 644–647 (2010)
- Van Grondelle, R., Novodereshkin, V.I.: Photosynthesis: quantum design for a light trap. Nature 463, 614–615 (2010)
- de Vries, M.S., Hobza, P.: Gas-phase spectroscopy of biomolecular building blocks. Annu. Rev. Phys. Chem. 58, 585–612 (2007)
- Laskin, J., Futrell, J.H.: Activation of large ions in FT-ICR mass spectrometry. Mass Spectrom. Rev. 24, 135–167 (2005)
- Reilly, J.P.: Ultraviolet photofragmentation of biomolecular ions. Mass Spectrom. Rev. 28, 425–447 (2009)
- Plekan, O., Feyer, V., Richter, R., Coreno, M., de Simone, M., Prince, K.C., Carravetta, V.: Investigation of the amino acids glycine, proline, and methionine by photoemission spectroscopy. J. Phys. Chem A 111, 10998–11005 (2007)
- Feyer, V., Plekan, O., Richter, R., Coreno, M., Prince, K.C., Carravetta, V.: Core level study of alanine and threonine. J. Phys. Chem A 112, 7806–7815 (2008)
- Zhang, W., Carravetta, V., Plekan, O., Feyer, V., Richter, R., Coreno, M., Prince, K.C.: Electronic structure of aromatic amino acids studied by soft x-ray spectroscopy. J. Chem. Phys. 131, 035103 (2009)
- Feyer, V., Plekan, O., Richter, R., Coreno, M., Prince, K.C., Carravetta, V.: Photoemission and photoabsorption spectroscopy of glycyl-glycine in the gas phase. J. Phys. Chem. A 113, 10726–10733 (2009)
- Arachchilage, A.P.W., Wang, F., Feyer, V., Plekan, O., Prince, K.C.: Correlation of electronic structures of three cyclic dipeptides with their photoemission spectra. J. Chem. Phys. 133, 174319 (2010)
- 12. Zhang, L.D., Pan, Y., Guo, H.J., Zhang, T.C., Sheng, L.S., Qi, F., Lo, P.K., Lau, K.C.: Conformation-specific pathways of beta-alanine: a vacuum ultraviolet photoionization and theoretical study. J. Phys. Chem. A 113, 5838–5845 (2009)
- 13. Calvert, C.R., Belshaw, L., Duffy, M.J., Kelly, O., King, R.B., Smyth, A.G., Kelly, T.J., Costello, J.T., Timson, D.J., Bryan, W.A., Kierspel, T., Rice, P., Turcu, I.C.E., Cacho, C.M., Springate, E., Williams, I.D., Greenwood, J.B.: LIAD-fs scheme for studies of ultrafast laser interactions with gas phase biomolecules. Phys. Chem. Chem. Phys. 14, 6289–6297 (2012)
- Fenn, J.: Electrospray wings for molecular elephants (Nobel lecture). Angew Chem Int Ed 42, 3871–3894 (2003)
- Bari, S., Gonzalez-Magaña, O., Reitsma, G., Werner, J., Schippers, S., Hoekstra, R., Schlathölter, T.: Photodissociation of protonated leucine-enkephalin in the VUV range of 8–40 eV. J. Chem. Phys. 134, 024314 (2011)
- Gonzalez-Magaña, O., Reitsma, G., Bari, S., Hoekstra, R., Schlathölter, T.: Length effects in VUV photofragmentation of protonated peptides. Phys. Chem. Chem. Phys. 14, 4351–4354 (2012)
- González-Magaña, O., Reitsma, G., Tiemens, M., Boschman, L., Hoekstra, R., Schlathölter, T.: Near-edge x-ray absorption mass spectrometry of a gas-phase peptide. J. Phys. Chem. A 116, 10745–10751 (2012)
- Gonzalez-Magaña, O., Tiemens, M., Reitsma, G., Boschman, L., Door, M., Bari, S., Hoekstra, R., Lahaie, P.O., Wagner, J.R., Huels, M.A., Schlathölter, T.: Fragmentation of protonated oligonucleotides by energetic photons and Cq+ ions. Phys. Rev. A 87, 032702 (2013)
- Milosavljevic, A.R., Nicolas, C., Lemaire, J., Dehon, C., Thissen, R., Bizau, J.-M., Refregiers, M., Nahon, L., Giuliani, A.: Photoionization of a protein isolated in vacuo. Phys. Chem. Chem. Phys. 13, 15432–15436 (2011)
- Milosavljevic, A.R., Canon, F., Nicolas, C., Nahon, L., Giuliani, A.: Gas-phase protein innershell spectroscopy by coupling an ion trap with a soft x-ray beamline. J. Phys. Chem. Lett. 3, 1191 (2012)

- Brunet, C., Antoine, R., Allouche, A.-R., Dugourd, P.: Gas phase photo-formation and vacuum UV photofragmentation spectroscopy of tryptophan and tyrosine radical-containing peptides. J. Phys. Chem. A 115, 8933–8939 (2011)
- Brunet, C., Antoine, R., Dugourd, P., Canon, F., Giuliani, A., Nahon, L.: Formation and fragmentation of radical peptide anions: insights from vacuum ultra violet spectroscopy. J. Am. Soc. Mass Spec. 23, 274–281 (2012)
- Reichardt, G., Bahrdt, J., Schmidt, J., Gudat, W., Ehresmann, A., Müller-Albrecht, R., Molter, H., Schmoranzer, H., Martins, M., Schwentner, N., Sasaki, S.: A 10m-normal incidence monochromator at the quasiperiodic undulator U125-2 at BESSY. Nucl. Instrum. Methods A 467, 462 (2001)
- Polfer, N.C., Oomens, J., Suhai, S., Paizs, B.: Infrared spectroscopy and theoretical studies on gas-phase protonated leu-enkephalin and its fragments: direct experimental evidence for the mobile proton. J. Am. Chem. Soc. 129, 5887–5897 (2007)
- 25. Rakov, V., Borisov, O., Whitehouse, C.: Establishing low-energy sequential decomposition pathways of leucine enkephalin and its N- and C-terminus fragments using multiple-resonance CID in quadrupolar ion guide. J. Am. Soc. Mass Spectrom. 15, 1794–1809 (2004)
- Laskin, J.: Energetics and dynamics of fragmentation of protonated leucine enkephalin from time-and energy-resolved surface-induced dissociation studies. J. Phys. Chem. A 110, 8554–8562 (2006)
- Bari, S., Hoekstra, R., Schlathölter, T.: Peptide fragmentation by keV ion-induced dissociation. Phys. Chem. Chem. Phys. 12, 3376–3383 (2012)
- 28. Plekan, O., Feyer, V., Richter, R., Coreno, M., Prince, K.C.: Valence photoionization and photofragmentation of aromatic amino acids. Mol. Phys. 106, 1143–1153 (2008)
- 29. Jochims, H., Schwell, M., Chotin, J., Clemino, M., Dulieu, F., Baumgärtel, H., Leach, S.: Photoion mass spectrometry of five amino acids in the 6–22 eV photon energy range. Chem. Phys. **298**, 279–297 (2004)
- 30. Jochims, H., Schwell, M., Baumgärtel, H., Leach, S.: Photoion mass spectrometry of adenine, thymine and uracil in the 6–22 eV photon energy range. Chem. Phys. **314**, 263–282 (2005)
- 31. Walter, K., Lindner, J., Grotemeyer, J., Schlag, E.: Biomolecules in the gas phase 5. Small peptides investigated by multiphoton mass-spectrometry. Chem. Phys. 125, 155–163 (1988)
- Paizs, B., Suhai, S.: Fragmentation pathways of protonated peptides. Mass Spectrom. Rev. 24, 508–548 (2005)
- 33. Kamohara, M., Izumi, Y., Tanaka, M., Okamoto, K., Tanaka, M., Kaneko, F., Kodama, Y., Koketsu, T., Nakagawa, K.: Optical oscillator strength distribution of amino acids from 3 to 250 eV and examination of the Thomas-Reiche-Kuhn sum rule. Rad. Phys. Chem. 77, 1153–1155 (2008)
- 34. Schlag, E.W., Selzle, H.L., Schanen, P., Weinkauf, R., Levine, R.D.: Dissociation kinetics of peptide ions. J. Phys. Chem. A 110, 8497–8500 (2006)
- Remacle, F., Levine, R.D., Schlag, E.W., Weinkauf, R.: Electronic control of site selective reactivity: a model combining charge migration and dissociation. J. Phys. Chem. A 103, 10149–10158 (1999)
- Breidbach, J., Cederbaum, L.S.: Migration of holes: formalism, mechanisms, and illustrative applications. J. Chem. Phys. 118, 3983–3996 (2003)
- 37. Guillemin, R., Stolte, W.C.C., Piancastelli, M.N., Lindle, D.W.: Jahn-Teller coupling and fragmentation after core-shell excitation in CF₄ investigated by partial-ion-yield spectroscopy. Phys. Rev. A **82**, 043427 (2010)

A Ab initio calculations, 90, 156–158, 163, 166–169, 173, 175, 176	Collision induced, 22, 27, 150, 151, 161, 162, 164, 183, 189, 214 Complexation, 2, 31
Action spectroscopy, 15, 16, 21–38, 42, 70–81, 83, 93, 105, 106, 121, 134, 142–143, 150, 209–224	Conical intersection, 47, 48, 50, 58, 68, 70, 90–92, 99, 164, 182, 186, 190 Conjugation, 9, 71
Activation energy, 27, 76, 80, 93	Coulomb-attenuation method (CAM), 50
Adenine, 1, 3, 4, 12, 107, 182, 190, 191,	Coulomb barrier, 146, 192, 201
193–196, 198–201	Coupled cluster (CC), 50, 51, 113, 157
Adenosine, 29, 111, 188, 189	Crown ether (CE), 30, 31
Adenosine monophosphate (AMP), 29, 31,	Cryogenic, 41, 56
189, 190	Cytochrome c, 111, 125–127, 129, 148, 149,
Adiabatic detachment energy (ADE), 202	151, 220, 222
Alanine, 29	Cytosine (C), 1, 12, 107, 182
Amino acids, 3–6, 12, 13, 30, 45, 56, 68, 70, 71,	
108, 111, 118, 120–128, 141, 142, 144,	•
151, 155–176, 210, 211, 213–220,	D
222, 223	Degrees of Freedom, 27, 29, 58, 73, 74, 77,
AMP. See Adenosine mono phosphate (AMP)	126, 143, 150, 176
Aromatic amino acid, 3, 4, 12, 30, 142,	Delocalisation, 12, 14, 46
155–176, 214, 216, 217, 222	Density functional theory (DFT), 47, 48, 50,
Arrhenius rate constant, 80	55, 120, 198, 215
Autodetachment, 25, 67, 72, 76, 77, 83, 86,	Dipole moment, 47–49, 90
88, 99	Dispersed fluorescence, 106
	Dissociation, 15, 22, 23, 25, 27–34, 36–38, 41, 42, 73, 75, 80, 81, 106, 107, 120, 126,
В	128–134, 143–145, 150, 151, 156, 159,
Barrier height, 91, 94	161–165, 172, 173, 175, 176, 181–203,
Base pairing, 182	214, 216, 217, 220
Biochromophore, 12, 13, 15, 16, 45, 105, 142	DNA, 1, 3, 4, 17, 58, 107, 108, 181–203
Born Oppenheimer, 10, 94	Duplex, 3, 107, 108, 193, 197, 199
Bom Oppenhenner, 10, 94	Dye, 49, 50, 106–111, 142, 151
	Dyc, +7, 50, 100–111, 1+2, 151
C	
Charge transfer, 8, 13, 14, 17, 30, 31, 46, 47,	E
49, 54–55, 71, 91, 108, 109, 113, 120,	EBE. See Electron binding energy (EBE)
125, 141, 151, 168, 172, 182, 210	Electron affinity, 15, 75, 76, 87
Coincidence experiments, 161–163, 171	Electron binding energy (EBE), 89, 144, 146,
Cold ions, 16, 17, 40, 122	200, 201

Electron detachment, 22, 29, 72, 77, 83, 88, 92, 106, 121, 143–146, 149, 151, 159, 191, 192, 197, 202 Electronic transition, 7–10, 13, 15, 58, 74, 85, 94, 150, 155, 164, 165, 168, 172, 182, 210	Gramicidin A, 145 Green fluorescent protein (GFP), 12, 13, 51, 53, 58, 67–99, 146 Guanine, 1, 2, 12, 107, 182, 194, 197, 200
Electron transfer, 47, 68, 70, 99, 107, 108, 119, 149–151, 158, 159 Electrospray, 16, 22, 23, 33, 35–39, 74, 111, 121, 145, 157, 161, 169, 171, 183, 198, 200, 210, 211 Electrostatic fields, 1 Electrostatic ion storage ring in Aarhus (ELISA), 22–33, 72–74, 77–81, 83, 121, 123, 126, 127, 130–132, 134, 146, 161, 189, 191 Exchange correlation (XC), 48, 49 Excited state, 10, 12, 16, 22, 31, 40, 42, 46–55, 58, 68, 70, 72–74, 76, 77, 81, 82, 85–87, 89–96, 98, 99, 105, 108, 110, 111, 113, 121, 122, 124, 132, 136, 143, 144, 146, 150, 151, 155–176, 182, 183, 186,	H Hartree Fock (HF), 49, 50, 55 Heme, 12, 111, 117–136, 145, 146, 148, 149, 151 Hemoglobin (Hb), 118, 119 Highest occupied molecular orbital (HOMO), 7, 13, 15, 113, 150, 157, 172, 197, 200, 214 Histidine, 14, 118–120, 123–126, 128 HOMO. See Highest occupied molecular orbital (HOMO) Hund's rule, 7 Hydration, 106
190–193, 195, 202, 203 Excited state dynamics, 52, 53, 58, 90, 155–176 Exciton, 17, 193–195, 202	I Imidazole, 120 Indole, 149, 155, 157, 158, 163, 173, 175 Infrared (IR), 28, 81, 126, 167, 186, 210 Insulin, 144, 146, 147 Internal conversion (IC), 6, 8, 22, 24, 31, 70,
F Fluorescence, 6, 8, 10, 15, 17, 22, 38–42, 70, 85, 92, 94, 100, 105–114, 143, 156, 158, 175, 182	73, 74, 77, 78, 82–84, 86, 87, 90–94, 97, 99, 106, 132, 133, 143, 144, 146, 151, 156, 159–161, 165, 173, 177, 182, 186, 190–192
Fluorescent protein, 11–13, 51, 53, 58, 67–99, 146 Förster resonance energy transfer (FRET), 107–111 Fourier transform ion cyclotron resonance (FT-ICR), 32, 39–41, 142, 188 Frank Condon, 85, 86 Frenkel exciton model, 17 FRET. See Förster resonance energy transfer (FRET) FT-ICR. See Fourier Transform Ion Cyclotron Resonance (FT-ICR)	Intersystem crossing, 6, 27, 106, 132, 133, 156, 175, 176, 182 Intramolecular vibrational redistribution (IVR), 6, 74, 89, 182, 191, 216, 217, 220 Ion mobility, 15, 16, 150, 196 Ion trap, 16, 22, 33, 35–39, 41, 42, 72, 74, 81, 106, 142, 143, 151, 163, 166, 167, 169, 171, 202, 211 Isomerisation, 15, 91, 210 IVR. See Intramolecular vibrational redistribution (IVR)
G Generalised gradient approximation (GGA),	J Jabłoński diagram, 6, 7, 133
48, 49, 53, 55 GFP. See Green fluorescent protein (GFP) GGA. See Generalised gradient approximation (GGA) G-quartet, 2, 5	K Kasha's rule, 6 Kinetic shift, 23, 25, 27, 38, 41, 106 Kohn–Sham, 47–49

L Leucine enkephaline, 216 Lifetime, 6, 16, 22, 24–26, 29, 37, 40, 80–81, 86, 87, 90–94, 96, 106, 111, 112, 122, 132, 136, 154, 156, 159, 166, 169, 171–173, 175, 176, 191, 195, 203 Local density approximation (LDA), 48, 55 Lorentz force, 1 Lowest unoccupied molecular orbital (LUMO), 7, 15, 49, 113 Luciferase, 12, 13, 111 Luminescence, 27, 28, 121 Luminophore, 13, 106, 111 LUMO. See Lowest unoccupied molecular	P Peptide, 3–6, 13, 29–31, 54, 108–111,
orbital (LUMO)	147, 148, 150, 151, 159, 185, 198, 199, 201 Photodissociation 23, 28, 30–32, 34, 126, 129
M Magnetic fields, 1 Many-body perturbation theory (MBPT), 50 Mass spectrometry, 5, 15, 32, 106–108, 142, 183, 190, 203, 222 Matrix assisted laser desorption ionisation (MALDI), 22, 183, 210 Metalloporphyrin, 12, 118 Microenvironment, 106, 111, 120, 121, 127, 134–136, 193, 194 Molecular dynamics (MD), 46, 53, 56–58, 73 Molecular orbital (MO), 4, 7, 8, 12, 47, 51, 56, 144, 157, 158, 197, 214, 215 Multiphoton, 126, 156, 186 Multiply charged anions, 3, 106, 201 Myoglobin, 28, 118, 125, 145, 146, 148	Photodissociation, 23, 28, 30–32, 34, 126, 129, 132, 143, 156, 161, 175, 176, 183–190, 194, 196, 202 Photoelectron spectroscopy (PES), 47–50, 58, 68, 72, 76, 90, 99, 199–202 Photoexcitation, 5, 23, 25–27, 30–32, 34–36, 42, 72–73, 86, 90, 106, 110, 111, 121, 128–134, 142, 144, 150, 151, 159, 161, 167, 170, 172, 189–192, 198, 202, 214 Photofragmentation, 35, 37, 73, 143–144, 147, 149, 158–163, 165, 166, 177, 189, 211–221 Photophysical processes, 6–7, 133 Photostability, 181, 182 Photosynthesis, 17, 68, 118, 210 Polarisation, 46, 49, 53–56 Polyproline, 108, 109 Porphyrin, 12, 118, 120–125, 127, 129–134
N Nitric oxide (NO), 119–129, 132, 133, 135, 185, 193, 198 Nitrophenolate, 113, 144 Non-adiabatic excited-state dynamics, 58 Nonstatistical dissociation, 190, 202 Nucleic acid, 1–3, 12, 182, 183, 202 Nucleobase, 17, 182, 183, 185, 186, 188, 210 Nucleotide, 1, 181–203	Potential energy surface, 22, 42, 47, 71, 74, 88, 91, 94, 95, 105, 168, 173, 182 Prompt dissociation, 30, 32, 42, 188, 190 Prompt fragmentation, 191 Protein, 4, 5, 11–13, 15–17, 28, 29, 45, 49, 51, 53–58, 67–99, 106–109, 111, 113, 114, 118–121, 124–127, 129, 130, 136, 141–151, 155, 156, 177, 211, 220, 222 Protoporphyrin IX (PP), 117–136 Pump-probe, 93, 132–134, 162, 171, 173, 190, 191, 220, 222
O Oligonucleotide, 1, 107, 183, 185, 186, 190, 192, 197–200, 202, 211 Oscillator strength, 8, 14, 15, 90, 155–157, 182, 193, 194 Oxyluciferin, 12, 13, 111–114	Q Q band, 118–123, 125–127, 129, 135 QET. See Quasi-equilibrium theory (QET) Quadruplexes, 197

Quadrupole ion trap, 37-39, 72, 81, 142 Time constant, 26–28, 31, 32, 128–136, 169-171, 189, 191 Quasi-equilibrium theory (QET), 27, 89, 92 Time-dependent density functional theory (TD-DFT), 119 R Time of flight, 35-36, 41, 83, 190, 212 Radical, 30, 31, 34, 86, 90, 119, 129, 149-151, Time-resolved action spectroscopy, 72-81 162, 163, 173, 175, 192, 211 Triplet state, 7, 27, 106, 132, 133, 175, 182, 189 Rate constant, 27, 80, 81, 89, 92, 93, 108, 189 Trp-cage protein, 108, 109 Resonance structure, 13, 47 Tryptophan, 3, 5, 12, 34, 142, 149, 150, 155, Retinal, 12, 13, 15, 46, 53, 54, 57, 58, 210 158, 161-163, 166, 170-174 Rhodopsin (Rh), 12, 13, 46, 53, 54, 57 Tyrosine, 3, 5, 12, 29, 31, 70, 99, 142, 144, 147, Ribo nucleic acid (RNA), 1, 181-203 155, 156, 163, 164, 166, 167, 172-175, 213-219, 222 Rice Ramsperger Kassel Marcus (RRKM), 89, 92, 189 S Ultrafast, 68, 90, 92, 94, 220 Schiff base, 12, 13 Ultraviolet, 11, 16, 141, 210 Semiempirical methods, 52–53 Uracil, 1, 12, 182 Single-reference methods, 50, 52 Solvation, 16, 53, 142, 146, 196, 203 Solvatochromism, 196 Soret band, 118, 121, 122, 125, 129, 146, Vacuum ultraviolet (VUV), 141, 210-222 148, 149 Vertical detachment energy (VDE), 75, 76, 83, 86-88 Spin flip, 6, 27 Stacking, 196, 202 Vibration, 72, 88, 98, 163, 167, 168 Statistical dissociation, 27, 31, 32, 80, 165, Vibrational autodetachment (VAD), 77, 83, 86, 190, 191, 202 88-90, 93, 99 Stokes shift, 7, 9, 106 Vibrational cooling (VC), 6, 129 Storage ring, 16, 22–33, 41, 42, 72–74, 121, Visible, 11, 12, 16, 54, 68, 118, 125, 126, 128, 126, 134, 142, 146, 163, 189, 191, 224 142, 146–151, 209, 210 Vision, 12, 68, 90, 210, 224 T Tagging, 151 Tautomer, 198, 200 Watson Crick, 1, 107, 182 Tetracyanoquinodimethane (TCNQ), 24, 25 Thermionic emission, 76, 84, 85 Thymine, 1, 12, 107, 182, 190, 201 Z Zajfman trap, 36, 37, 41